Experimental constraints on rheology during eclogite-facies metamorphic reactions

Sarah Incel

To cite this version:

Sarah Incel. Experimental constraints on rheology during eclogite-facies metamorphic reactions. Earth Sciences. Université Paris sciences et lettres, 2017. English. NNT : 2017PSLEE020 . tel-01628809

HAL Id: tel-01628809
https://theses.hal.science/tel-01628809

Submitted on 4 Nov 2017

THÈSE DE DOCTORAT

de l'Université de recherche Paris Sciences et Lettres
PSL★ Research University

Préparée à l'École Normale Supérieure

Contrainte expérimentale sur la rhéologie au cours des réactions d'éclogitisation

Experimental constraints on rheology during eclogite-facies metamorphic reactions

Ecole doctorale n°560

Ecole Doctorale des Sciences de la Terre

Spécialité : Sciences de la Terre et de l'Environnement

COMPOSITION DU JURY :

M. SCHUBNEL Alexandre – Directeur de thèse
Laboratoire de Géologie de l'ENS – UMR8538

Mme HILAIRET Nadège – Co-encadrante de thèse
Unité Matériaux et Transformations – UMR8207

M. JOHN Timm – Co-directeur de thèse
Freie Universität Berlin

Mme BURNLEY Pamela – **Rapporteur**
University of Nevada, Las Vegas

M. JAMTVEIT Bjørn – **Rapporteur**
University of Oslo

Mme BOLFAN-CASANOVA Nathalie – **Examinatrice**
Université Blaise Pascal

M. CHOPIN Christian – **Président du jury**
École Normale Supérieure de Paris

M. LABROUSSE Loïc – **Invité**
Université Pierre et Marie Curie

M. AGARD Philippe – **Invité**
Université Pierre et Marie Curie

M. RENNER Jörg – **Invité**
Ruhr-Universität Bochum

Soutenue par :

Sarah INCEL

le 15 Mai 2017

Dirigée par :

Alexandre SCHUBNEL
Laboratoire de Géologie de l'ENS – UMR8538

Nadège HILAIRET
Unité Matériaux et Transformations – UMR8207

& **Timm JOHN**
Freie Universität Berlin

Laboratoire de Géologie, Ecole Normale Supérieure Paris

ED n° 560 Ecole doctorale des Science de la Terre et de l'Environnement

Thèse de Doctorat – Pétrologie & Géophysique

EXPERIMENTAL CONSTRAINTS ON RHEOLOGY DURING ECLOGITE-FACIES METAMORPHIC REACTIONS

Sarah Incel

Soutenance le 15 Mai 2017

Membres du jury :

Dr. Alexandre Schubnel	Directeur de thèse
Dr. Nadège Hilairet	Co-encadrante de thèse
Pr. Timm John	Co-directeur de thèse
Pr. Pamela Burnley	Rapporteur
Pr. Bjørn Jamtveit	Rapporteur
Pr. Christian Chopin	Président du jury
Dr. Nathalie Bolfan-Casanova	Examinatrice

Invités :

Pr. Loïc Labrousse

Pr. Philippe Agard

Pr. Jörg Renner

Still und eng und ruhig auferzogen,

Wirft man uns auf einmal in die Welt;

Uns umspülen hunderttausend Wogen,

Alles reizt uns, mancherlei gefällt,

Mancherlei verdrießt uns,

und von Stund' zu Stunden

Schwankt das leicht unruhige Gefühl;

Wir empfinden, und was wir empfunden,

Spült hinweg das bunte Weltgewühl.

- *Johann Wolfgang von Goethe*

ACKNOWLEDGEMENTS

Three years are over. Three years in which I grew with each task and challenge. Three years of experience that completely changed my life thanks to my colleagues, supervisors, my dear friends and family.

There are no words to express the degree of gratitude for these past years! Therefore, the following text will not nearly reflect how thankful I am.

I was very lucky that I had the chance to work and live in the most beautiful city in the world – Paris. But maybe I would see Paris differently if I had not met so many amazing people. Thanks to my dear colleagues at ENS, IPGP, and UPMC who took me out for beers after work. Thanks to them, I could really enjoy this city. Special thanks to Thomas for all the good times we had together and the interesting French expressions which he taught me! I would also like to thank Yves Pinquier for constructing several pieces for the experiments and the preparation of the sample assembly. Thanks to my colleagues and friends at FU Berlin. Every time I came back to the GeoCampus, it felt like coming home. I would also like to thank the group of Jörg Renner at Ruhr-Universiät Bochum, especially Frank Bettenstedt for his help and the nice discussions during the coffee break in the morning with the other Master and PhD students. Due to the warm atmosphere in this lab, the experimental work at RUB was one of the best experiences during my PhD.

There are also my dear colleagues from ZIP who became friends over the last years and who made me experience that Europe means home. At this point, I want to thank Philippe Agard for creating this project that completely changed my life. But I would also like to thank all other ZIP advisors and the scientists from the advisory board who made this project a wonderful experience for me.

Many, many thanks to my supervisors during the Bachelor, Master, and my PhD. Everything started with the lecture on magmatic petrology of Ralf Milke during my 3rd semester at university in which I discovered my passion for rocks and the stories they tell us about areas in the Earth where no one has ever been before. Ralf also made me discover my second great passion, the passion for experimental work. Thanks to his lectures, support and encouragement over all these years, I am now writing the acknowledgements of my PhD thesis on experimental petrology/geophysics. I am deeply thankful for all the great discussions and times with Timm. His belief in me and his persistence made me apply for this PhD position, which I finally got to work under the supervision of Alex with co-supervision of Nadège and Loïc. Many, many thanks to Nadège for the help and the support during the D-DIA experiments and the data treatment, but also for the reunions and discussions at ENS and elsewhere! The petrology part was mainly supervised by Loïc and I thank him so much for his help on the thermodynamic calculations and the discussions on the microstructures of the natural and

experimental samples. During the field trips to Norway and Corsica I did not only collect many rock samples, but also a lot of unforgettable moments! And finally Alex, who might not know how thankful I am to be one of his PhD students. Thanks to him, I rediscovered my enthusiasm and my curiosity for science, which I believe are one of the most important factors if you consider a scientific career. Alex has the gift to inspire people and he inspired me tremendously. Having him as supervisor was probably one of the best things that ever happened to me.

There are two other scientists I would like to thank: which are Christian Chopin and Jörg Renner. Many thanks to Christian Chopin for the discussions on the many petrological and mineralogical problems I had during the last years. As I already said, the stay in the geophysical lab in Bochum was always a pleasure particularly thanks to Jörg Renner, who helped and advised Thomas and me performing the experiments and the data treatment. But I would like to especially thank him for all the work he did in correcting several abstracts for conferences, posters, and finally my first paper.

The thesis you hold in your hands would not have been written without the mental support of my family and friends over all these years. Many thanks to my parents, for their love, their support, their advice, their trust, their belief in me, and for the freedom to take my own decisions – Tausend Dank, Mama und Papa! I also want to thank my two little brothers, Can and Levi, who I miss so much. Most of the mental support, especially during the last months, came from my beloved friends Luise, Hannah, Lucy, Johann, Lukas, Kathi, Damien, and Gianina who were always there for me. Special thanks to my best friends Bianca and François, for their patience, their humor, and their warmth, but particularly for preventing me from failure under stress. Lastly, I want to thank the most important person in my life, my little sister Jüly. She is my one and only – mein Lieblingsmensch– since the moment she was born. I am the luckiest person on Earth that I met all these people and to have such amazing friends, who pushed and supported me to realize my dreams!

CONTENT

I Introduction 1
II Methodology 21
III Eclogitization of blueschist 63
Paper
Laboratory earthquakes triggered during eclogitization of lawsonite-bearing blueschist 83
IV Eclogitization of granulite 125
V Thermodynamic constraints on the formation of intermediate and deep earthquakes 157
VI Final conclusion 183
VII Perspectives 185
References

“The hardest thing to learn in life is which
bridge to cross and which to burn”
- *Bertrand Russell*

I INTRODUCTION

1.1 INTERMEDIATE-DEPTH SEISMICITY

Most of intermediate (60-300 km depth) and deep (300-700 km) seismicity is recorded in subduction zones and makes up around a third of the total recorded seismicity on Earth (Frohlich, 2006). Intermediate and deep seismicity cannot be explained by classic models on fracture and frictional behavior of rocks, viable to understand the generation of shallow earthquakes in lower-crustal and cold rocks, Intermediate and deep earthquakes occur in regions of the Earth believed to be too warm and with large confining pressures. Under these conditions crystal plastic flow is expected to be active to favor ductile deformation. Earthquakes, the result of sudden stress release accompanied by the emission of elastic waves, should therefore not be able to nucleate under those conditions. The high confining pressures of around 1.8-90 GPa (60-300 km depth) at which these earthquakes are recorded, would also require an impossibly high shear stress to cause brittle fracture or friction according to the Coulomb-criterion or Byerlee’s law (Byerlee, 1978). Although many experimental, field, and theoretical studies have addressed this phenomenon, the underlying mechanisms behind intermediate and deep seismicity remain poorly understood. Geophysical observations coupled with thermodynamic calculations, but also some field evidence demonstrate a strong link between metamorphic reactions and the occurrence of intermediate-seismicity in lower crustal rocks (Peacock & Wang, 1999; Hacker et al., 2003; Kita et al., 2006; Hétenyi et al., 2007; Liang et al., 2011; Deseta et al., 2014).

1.2 LINK BETWEEN ECLOGITIZATION IN LOWER CRUSTAL ROCKS AND INTERMEDIATE-DEPTH SEISMICITY –GEOPHYSICAL OBSERVATIONS, THERMODYNAMIC MODELLING & FIELD OBSERVATIONS

1.2.1 Subduction zones – Eclogitization of the oceanic crust

Subduction zones play a fundamental role in Earth’s geodynamic system. The sinking of lithosphere into the mantle is believed to represent an important driving force for plate tectonics today. The lifecycle of the oceanic crust starts with its birth at mid-ocean ridges, where magma is generated in the mantle due to decompression melting and rises to form mid-ocean ridge basalt (MORB) at the ocean floor. At the end of its lifetime the oceanic crust returns into Earth’s mantle together with its lithospheric mantle slab during subduction. This recycling process is strongly linked to other chemical cycles influencing Earth’s surface and climate, e.g. carbon and water cycle, which in return highly affects fauna, flora, and mankind. Most of the subduction zones can be found along the Western coast of South and North America and along the Eastern coast of Asia to form the so-called “ring of fire” (circles in

Figure 1). This name derives from the pronounced volcanic activity in this region, which is related to subduction processes, and will not be further discussed in this thesis. Although most of the seismicity occurs at shallow depth shallow depths < 50 km a lot of events can also be recorded at much greater depth until around 700 km (Figure 2).

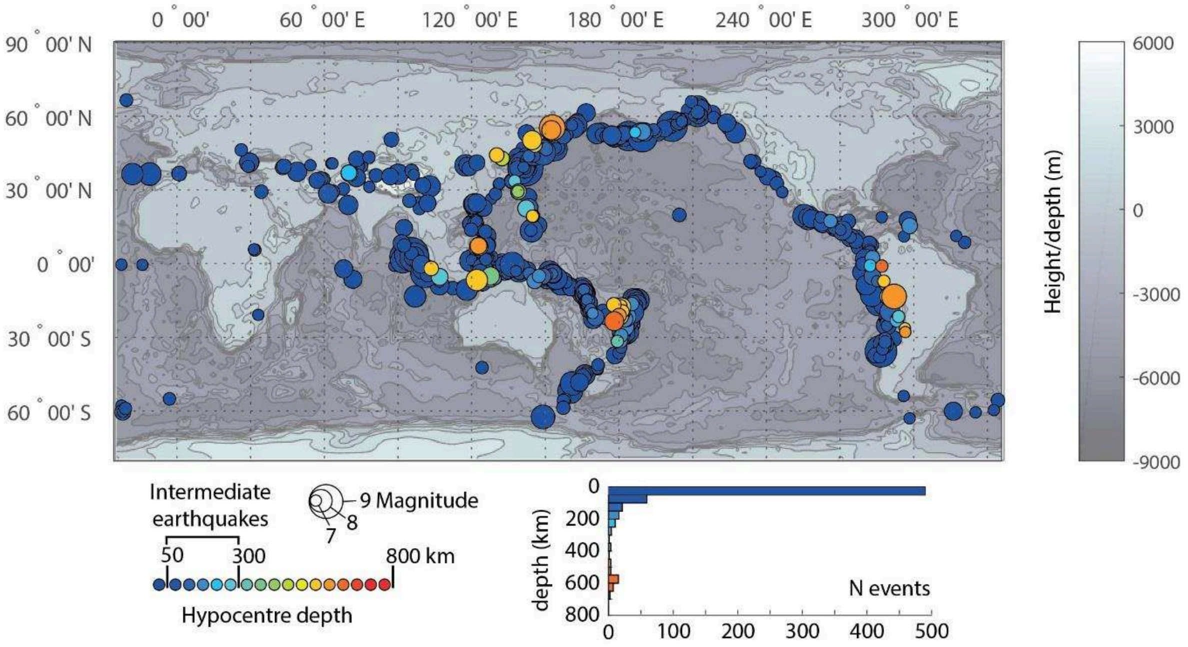

Figure 1: ANSS Catalogue Earthquakes Magnitude >7.0 (1900-2013) (Geomap App) showing the recorded seismic events in the Earth from 1900 to 2013. Dark blue circles represent

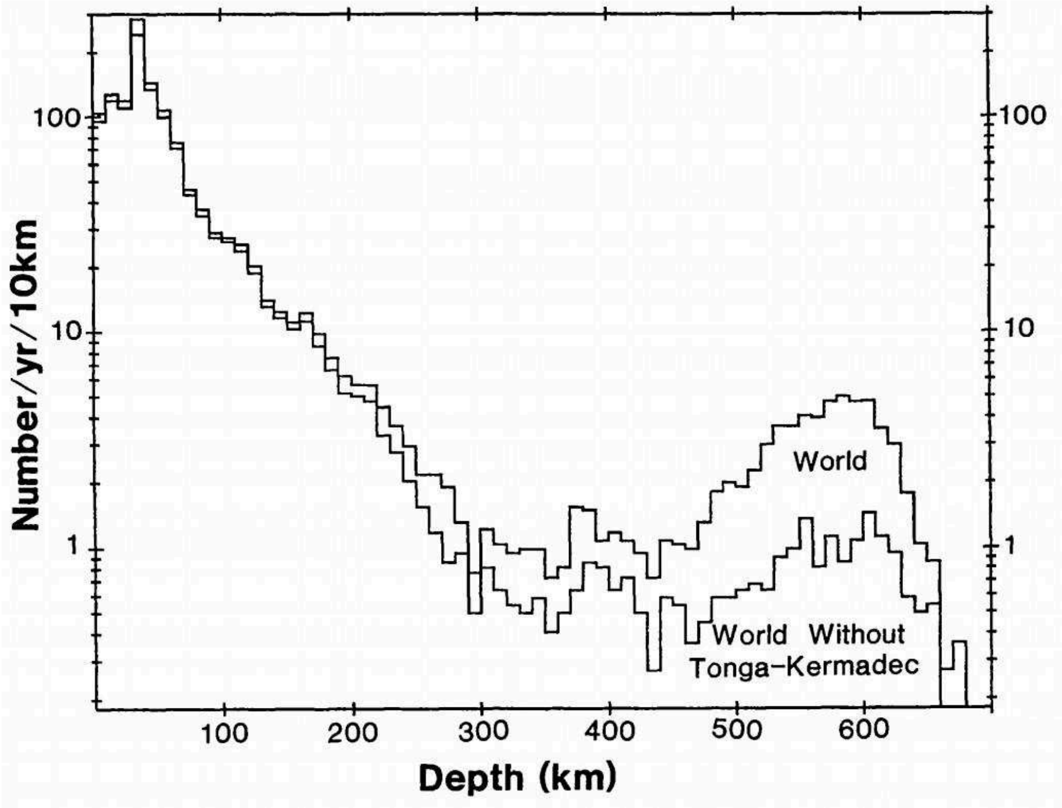

Figure 2: From Frohlich (1989). Bimodal distribution of earthquakes.

Although each subduction zone shows its own characteristics they can be roughly classified as either warm or cold depending on the convergence rate and the thermal structure of the incoming lithosphere (Peacock & Wang, 1999). The first chapter of this thesis focuses on the formation of intermediate-depth seismicity within the upper Wadati-Benioff plane in cold subduction zones. Therefore a cold subduction zone, with NE Japan as an example, will be introduced and further discussed in the following.

Cold Subduction below Northeast Japan

The Pacific plate descends under the northeastern Japan arc in Tohoku and beneath the Kuril Arc in Hokkaido (Figure 3; Kita et al., 2006). All epicenters (red circles in Figure 3) from the JMA earthquake catalog, which occurred in this area between January 2002 to August 2005 are shown in Figure 3 (Kita, et al., 2006). The corresponding number of earthquakes over depth histograms exhibit a peak in seismicity between 80 and 90 km depth representing the intermediate-depth earthquakes. A schematic cross section of the subduction below NE Japan clearly shows the upper and lower Wadati-Benioff planes formed by the intermediate-depth earthquakes (circles in Figure 3). During subduction, a jadeite lawsonite blueschist will first transform to lawsonite amphibole eclogite and finally to eclogite due to changing P-T conditions (Figure 4). A striking observation is the coincidence of the lawsonite-blueschist to eclogite transition and the seismicity distribution along the upper Wadati-Benioff plane.

These metamorphic reactions involve the breakdown of lawsonite and glaucophane, causing dehydration and densification of the rock due to the replacement of blueschist-facies minerals by a nominally anhydrous high-pressure eclogite-facies mineral assemblage (Figure 4). The good correlation between the breakdown of hydrous phases, as lawsonite (≈ 11.5 % H_2O; Hacker et al., 2003) and glaucophane (≈ 2.3 % H_2O; Hacker et al., 2003), and the relocation of intermediate-depth seismicity leads to the theory of dehydration embrittlement with lawsonite believed to act as a major player in causing brittle failure under high-pressure conditions.

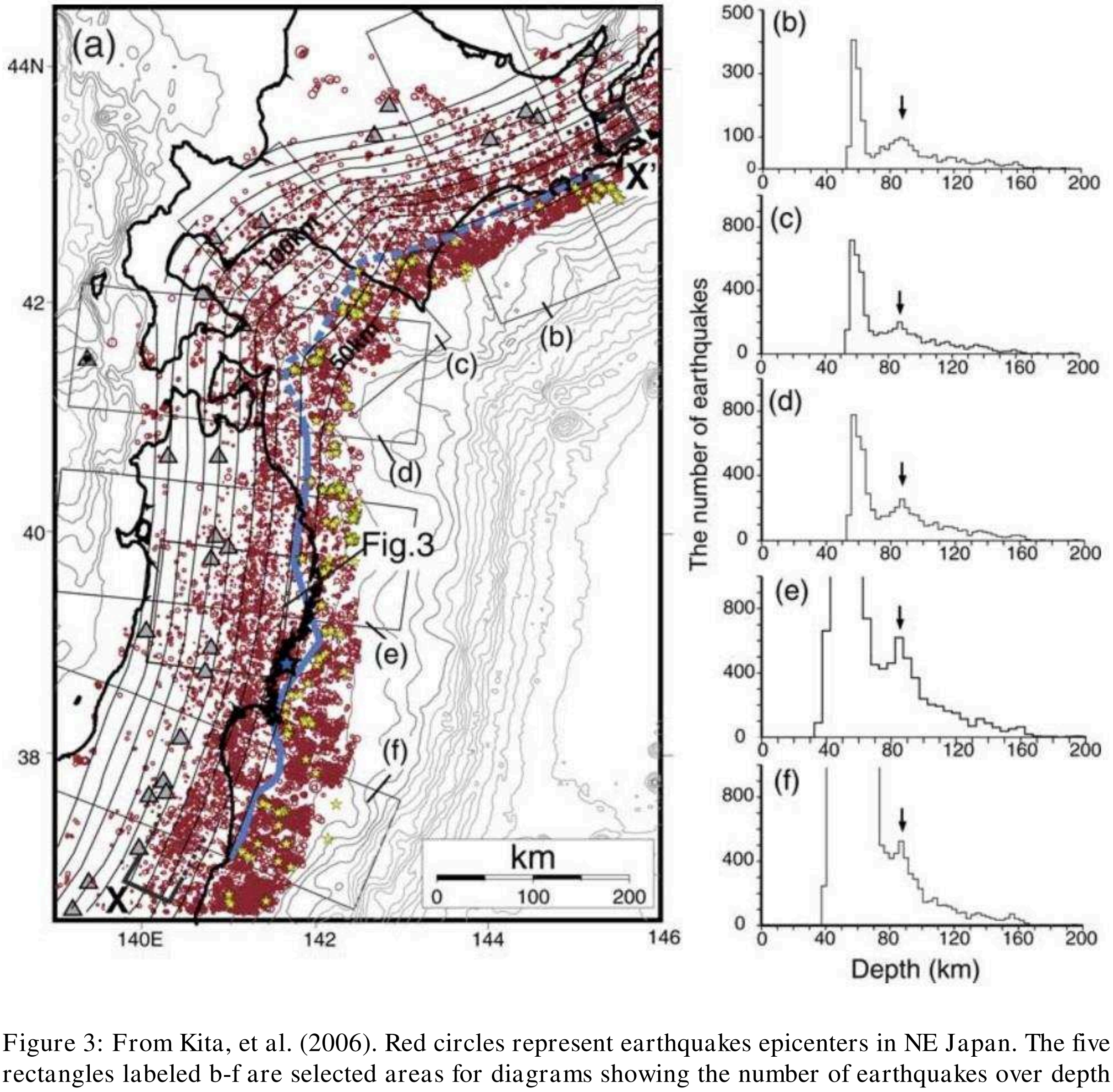

Figure 3: From Kita, et al. (2006). Red circles represent earthquakes epicenters in NE Japan. The five rectangles labeled b-f are selected areas for diagrams showing the number of earthquakes over depth (on the right).

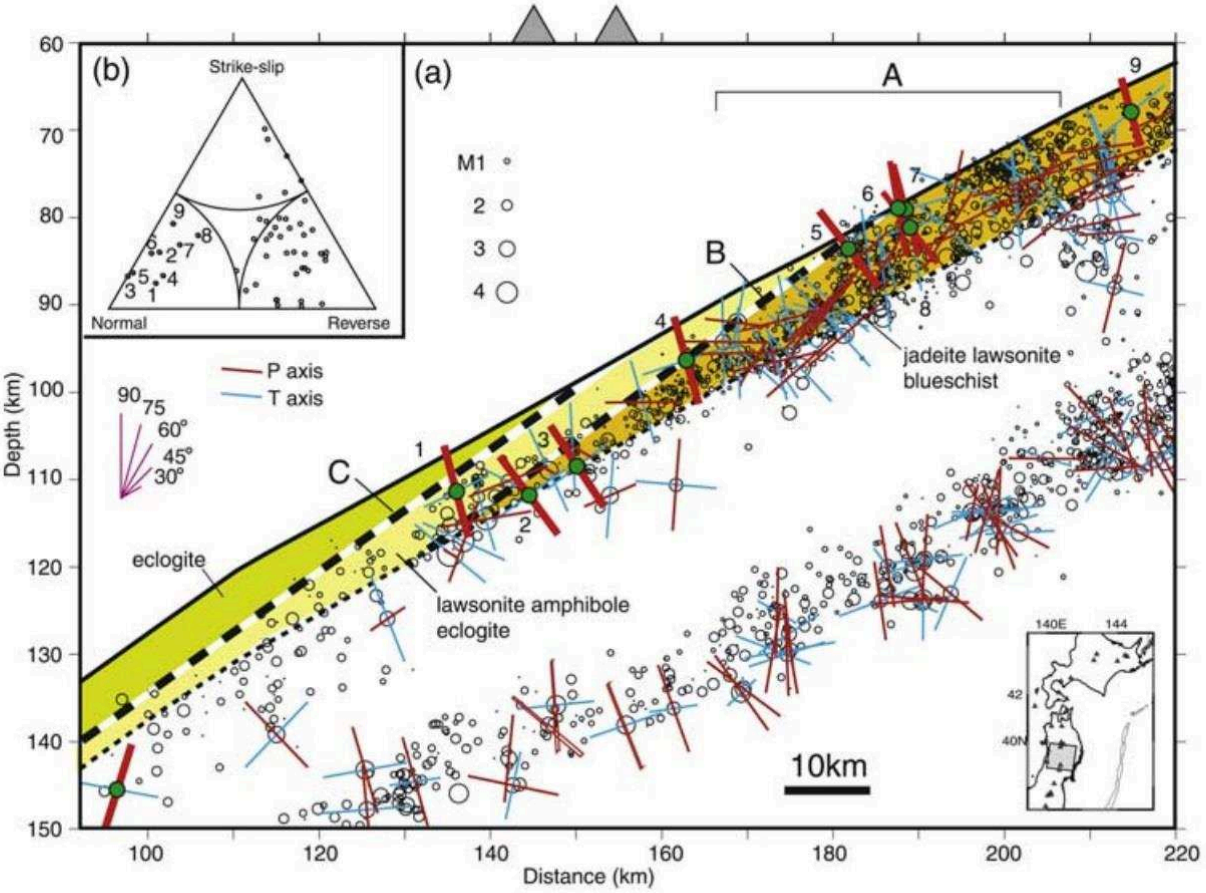

Figure 4: From Kita, et al. (2006). Schematic cross-sectional view of the area labeled in Figure 3. Circles represent earthquakes below NE Japan. Their size corresponds to their magnitude. They clearly form two different planes called the upper and lower Wadati-Benioff planes of seismicity. The upper plane is believed to represent the earthquakes within the subducting ocean crust. Colored areas show thermodynamically calculated stability fields of different metabasalts. During cold subduction the rock will transform from jadeite lawsonite blueschist to first lawsonite amphibole eclogite and finally to eclogite. This transformation is accompanied by dehydration and densification of the rock. A striking observation is the cessation of seismicity once rocks enter the stability field of eclogite.

1.2.2 Continent-continent collison zones – Eclogitization of the continental crust

Although almost all intermediate and deep earthquakes are recorded in subduction zones there are some events that occur in collision zones between two continental crusts, e.g. the Himalaya-Tibet collision zone (Figure 5). The combination of the relocation of seismic events below Nepal, geophysical observations, and thermodynamic modeling demonstrates that intermediate-depth earthquakes occur in regions of the lower continental crust that are partially eclogitized (Hétenyi et al., 2007, Liang et al., 2011; Figure 5). This observation suggests that there is a link between the transition from granulite to eclogite and the formation of intermediate-depth earthquakes (Jackson et al., 2004; Liang et al., 2011). In contrast to the previously presented case of eclogitization of blueschist of the oceanic crust, accompanied by dehydration reactions, the metamorphic reactions occurring during eclogitization of nominally anhydrous granulite are linked to fluid-related reactions within the rock (Goldsmith, 1981; Jamtveit et al., 1990).

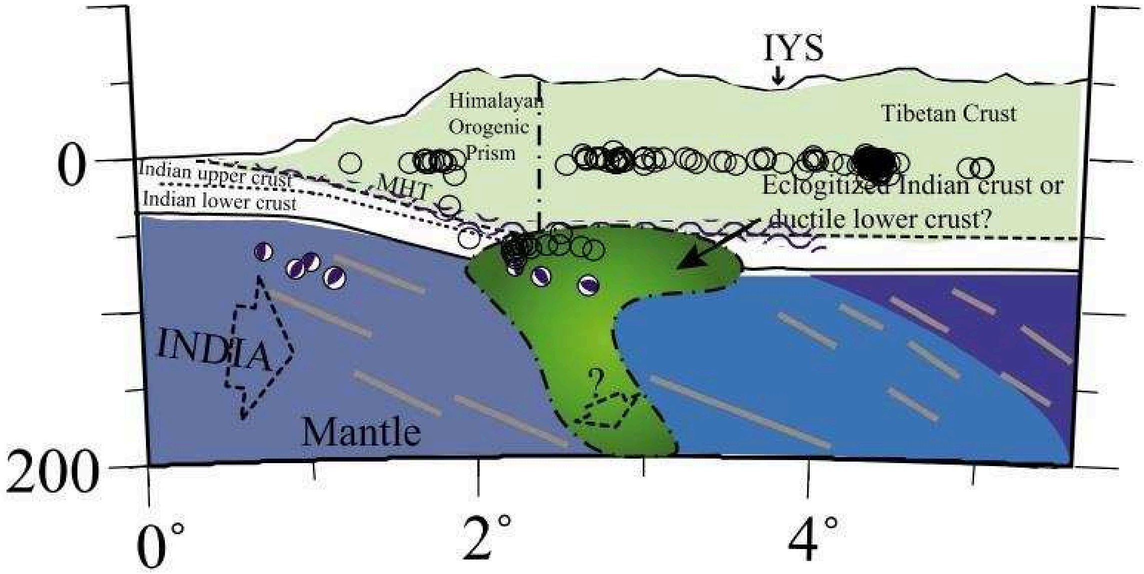

Figure 5: Modified from Liang et al. (2011). Intermediate-depth seismicity occurs in regions of the lower continental crust that are expected to be composed to partially eclogitized granulites.

1.2.3 Field evidence for intermediate-depth seismicity in lower crustal rocks

Pseudotachylites with high pressure quenching paragenesis are considered as natural evidence that seismic faulting occurred in rocks of the lower oceanic and continental crust. These structures are believed to represent the quenched frictional melt that was formed due to fast slip during a seismic event (Sibson, 1975).

Cima di Gratera in Cap Corse, France

In the Alpine part of Corsica in Cap Corse, field observations demonstrate that the mafic metagabbros of the oceanic crust underwent brittle failure at high-pressure/low-temperature (HP/LT) conditions (Andersen et al., 2008; Deseta et al., 2014). Complex pseudotachylite vein networks can be found in these rocks showing varying amounts of water from 0 to around 14 wt. % (Deseta et al., 2014). The occurrence of nominally anhydrous pseudotachylites leads the authors to conclude that primarily not the dehydration of hydrous phases, present in these metagabbros, triggered failure at intermediate-depth but another mechanism, e.g. brittle failure due to ductile shear instabilities.

Holsnøy in the Bergen Arcs, Norway

There is also field evidence that brittle failure at intermediate-depth occurred in nominally anhydrous rocks of the lower continental crust. On Holsnøy, an island in the Bergen Arcs, SW Norway, wide networks of pseudotachylites can be found in granulites that experienced high-pressure/high-temperature (HP/HT) metamorphism.

Both field observations demonstrate a link between metamorphic reactions occurring during the eclogitization of the either hydrous oceanic crust or the almost dry continental crust. This suggests that there might be a common mechanism during eclogite-facies metamorphic reactions in lower crustal rocks that could cause intermediate-depth earthquakes in both settings.

1.3 PROPOSED MECHANISMS THAT MIGHT TRIGGER INSTABILITIES AT ELEVATED PRESSURE-TEMPERATURE CONDITIONS

There are three main hypotheses in the literature try to explain the phenomenon of intermediate-depth and/or deep seismicity. Those are called dehydration embrittlement, ductile shear instabilities, and transformational faulting. Every theory has its strengths and weaknesses for deciphering the underlying mechanisms triggering earthquakes at deeper depths.

1.3.1 Dehydration embrittlement

The theory of dehydration embrittlement tries to explain the transition from ductile to brittle behavior with an increase in pore fluid pressure due to the onset of dehydration of hydrous phases. If the rock is rather impermeable, the liberated fluid during the breakdown of water-bearing minerals cannot dissipate fast enough. This will cause a pore fluid pressure increase that in return decreases the effective pressure on the system and could therefore enable faulting. This theory was first noted by Hubbert and Rubey (1959) and one year later also discussed by Griggs & Handin (1960).

Thermodynamic models combined with the relocation of seismic events in subduction zones also exhibit a good correlation with expected dehydration reactions and bursts in seismicity (Hacker et al. 2003, Kita et al. 2006). It is believed that the seismicity forming the upper Wadati-benioff plane of seismicity are earthquake ruptures in the down-going oceanic crust. Lower Wadati-Benioff plane seismicity is expected to be caused by processes in the partially serpentinized mantle lithosphere. For the upper plane a suit of dehydration reactions starts with the decomposition of clays at lower pressures and is followed by the dehydration of chlorite minerals as pressure and temperature increases. At even higher pressures and temperatures, in the depth range of intermediate-depth earthquakes, the breakdown of amphibole, mainly glaucophane, and in some cases additionally the breakdown of lawsonite during eclogitization of blueschist may trigger earthquakes (Schmidt & Poli, 1998, Okazaki & Hirth, 2016). Although this theory demonstrates some very convincing arguments there is still some trouble. Seismicity can be recorded until a depth of around 680 km where hydrous phases are no longer expected to be stable. Therefore either only small amounts of water (in the ppm range) are necessary to enable brittle failure (Zhang et al. 2004) or this theory can only explain intermediate-depth seismicity and there is another mechanism occurring at greater depth. Another conceptual model, called dehydration-driven stress transfer, has been recently proposed to explain embrittlement of olivine-antigorite mixtures (Ferrand et al., 2017). This model proposes that brittle failure accompanied by AEs can be triggered in the laboratory due to the breakdown of a hydrous and rheological weak phase (antigorite) surrounded by a stronger phase (olivine). The disappearance of the weaker load-bearing phase will charge the surrounding olivine and may enable failure depending on a critical ratio of both phases.

1.3.2 Ductile shear instabilities

Crystal plastic creep might induce structural changes which in return could accelerate further creep. This self-enhancing process could proceed and concentrate in thin layers in which high flow rates will develop. Heat will continuously be produced while plastic deformation occurs which could finally provoke shear melting if some conditions are fulfilled, e.g. poor heat conduction and a certain thickness of the developed shear zone. In the literature this process is called thermal runaway (Kelemen and Hirth, 2007). There are only very few experimental studies supporting this theory and most of the arguments on which this idea bases derive from physical models (Frohlich, 2006). Nevertheless, this mechanisms gained some attention to decipher the formation of pseudotachylites, believed to be the product of fast frictional melting during seismic slip, found in nominally anhydrous rocks of the Bergen Arcs and the Western Gneiss Region, Norway (Austrheim & Boundy, 1994; John et al., 2006). Although this theory could explain intermediate and deep seismicity in various rock types, there are at least three main weaknesses (Frohlich, 2006). Most of the models are based on geometries that initiate faulting along rupture parallel to the slab surface. This stands in contrast to seismic observations that faults seem to cut obliquely through the slab. Another problem this theory faces is how these instabilities could propagate at velocities fast enough to emit elastic waves over large areas of tens of kilometers in size. Lastly, if ductile shear instabilities represent the trigger for intermediate and deep seismicity, then the precursory creep (observed in the lab by Bridgeman, 1936) prior to brittle fracture should also be observable in nature, which is not the case.

1.3.3 Transformational faulting

The theory of transformational faulting includes different mechanisms that might occur during solid-solid transitions as grain size reduction, volume change and/or enthalpy (latent heat) release. Since the hypothesis of ductile shear instabilities also treats the mechanism of grain size reduction during creep there are some overlaps between both theories. However, the newly forming grains during transformational faulting will be the product of a reaction and therefore either chemically or structurally (polymorphic transitions) different from the reactant phase(s). Grain size reduction during intense shearing produces smaller grains that are not chemically different since those represent mechanically ground crystals. This decrease in grain size can cause a decrease in rock strength (Green & Burnely, 1989). Attractive forces between the atoms prevent the crystal lattice from falling apart, However within grain or interphase boundaries these forces are much weaker. Since the grain or interphase boundary density is much higher in small grain size domains those will be much weaker compared to surrounding regions with larger grains.

Another mechanism this theory includes is the change in thermodynamic parameters, e.g. volume and enthalpy, during metamorphic reactions. Assuming a complete phase transformation, the changes in pressure (P) and/or temperature (T) in a system causes a change in entropy (S), volume (V), and/or enthalpy (H) (Spear, 1995) following:

$$\left(\frac{\delta P}{\delta T}\right) = \frac{\Delta S_{(T,P,X)}}{\Delta V_{(T,P,X)}} = \frac{\Delta H_{(T,P,X)}}{T\Delta V_{(T,P,X)}}. \tag{1}$$

In order to create a mechanical instability that causes brittle failure the reactions has to involve a volume decrease and/or a heat release (Hodder, 1984) and occur fast enough to trigger dynamic rupture. The degree of metastability of the reactant phase(s), necessary for the transformation to occur suddenly enough, might therefore play an important role (Kirby et al., 1996). It is expected that this might be the case in subduction zones where a cold oceanic slab descents into the warmer mantle (Dennis & Walker, 1965; Kirby et al., 1995). This theory also faces some problems in explaining seismicity at greater depths. If earthquakes at elevated pressure and temperature are triggered by volume decrease then seismologists would expected implosive radiation pattern. Yet, intermediate and deep earthquakes show double couple focal mechanisms as their shallow counterparts (Honda, 1932; Randall & Knopoff, 1970). Ekström & Richards, 1994 conclude that the overall stress field of the tectonic setting governs the radiation pattern. It is also possible that the phase transformation nucleates at preexisting faults that would slip once reactivated and therefore also demonstrate a dominant shear character (Kirby, 1987). There is also a scale problem: these reactions unlikely occur suddenly over spatial ranges wide enough to trigger a seismic event (Vaisnys & Pilbeam, 1976); the degree in metastability required for this sudden energy release might also not be reached (Karato et al., 2001; Mosenfelder et al., 2001; Marton et al., 2005). Another problem is that once the transition starts the temperature rises together with a drop in pressure which shifts the system back to equilibrium conditions and therefore limits the reaction (Liu et al., 1998; Mosenfelder et al., 2000). Assuming that transformational faulting might be a possible candidate to trigger deep seismicity than it is also difficult to explain the observation that these earthquakes often occur repeatedly in the same place (Wiens & Snider, 2001). Despite all these difficulties, it is striking that once no further mineral transformations (below 680 km depth) are expected seismicity ceases.

1.4 METAMORPHIC REACTIONS UNDER ECLOGITE-FACIES CONDITIONS

This thesis is composed of three main chapter in which each part investigates the potential of eclogite-facies metamorphic reactions on the formation of intermediate-depth seismicity triggered in different geological settings and different rock types. The first chapter treats how intermediate-depth earthquakes of the upper Wadati-Benioff zone are generated during the eclogitization of blueschist in subduction zones. Although most of the intermediate-depth seismicity is recorded in subduction zones, there are continent-continent collision zones that also reveal seismic activity in lower crustal regions that are expected to be partially eclogitized, e.g. Himalaya-Tibet collision zone (Hétenyi et al., 2007; Liang et al., 2011). Therefore the second main part of this thesis will present the experimental work performed on the eclogitization of granulites. Finally the last chapter will present two deformation experiments on almost pure samples, either tremolite or glaucophane, that were performed to investigate the impact of the change of reaction thermodynamics on the production of mechanical instabilities enabling brittle failure.

1.4.1 Two amphiboles: glaucophane and tremolite, their structure and stability

Amphiboles are inosilicates, which are structurally built of double-chains of corner-connected SiO_4-tetrahedra (Figure 6, Deer, Howie & Zussman, 2013). The amphibole family contains many different amphibole minerals, which can all be represented by the general formula $A_{0-1}B_2C_5T_8O_{22}(OH)_2$. Depending on the cation radius and its oxidation state, various cations may occupy the four different cation sites A, B, C, and T. These substitutions, generate the numerous amphibole solid-solution series. The cation sites A, B, and C, are octahedraly coordinated and the T-site hosts tetrahedral coordinated cations (Figure 6; modified after Deer, Howie & Zussman, 2013). Octahedra sites are expressed as A, M1, M2, M3, and M4 (Figure 6) with M1 as smallest and M4 as largest cation site. Bigger cations, e.g. the alkali cations Na^+, K^+, and the large hydroxyl anions OH^- occupy the large cation site A; smaller cations, e.g. Mg^{2+}, Fe^{2+}/Fe^{3+}, the sites M1-M3. The occupation of each site not only determines the chemical composition of the amphibole but also its crystal structure (crystal symmetry) and the resulting chemical and physical properties of each amphibole mineral.

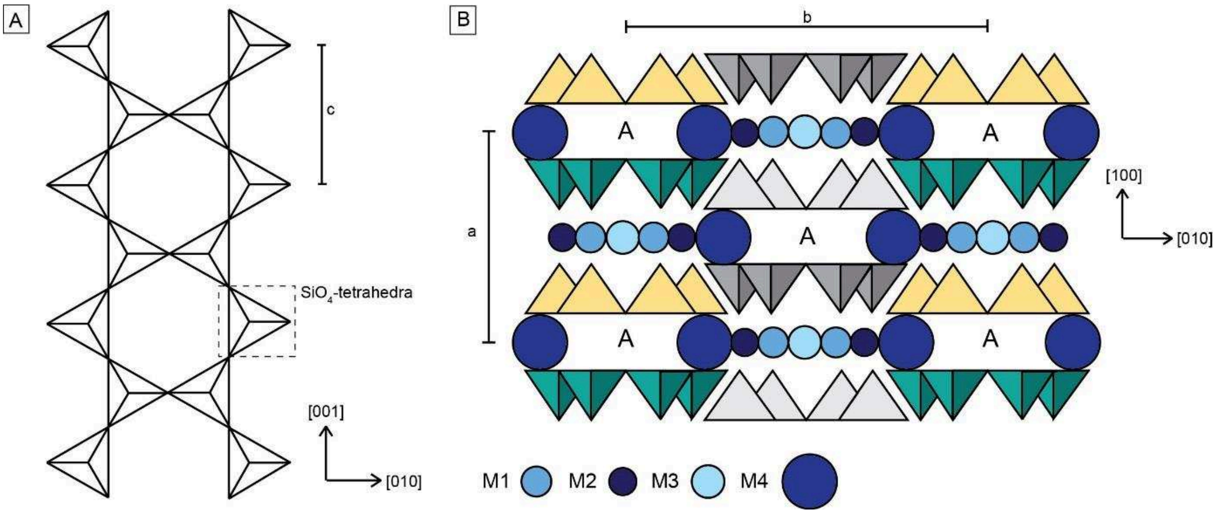

Figure 6: A) Double-chain structure of inosilicates. B) General structure of amphibole minerals showing the double-chains consisting of the tetrahedra-site cations and the octahedrally coordinated M-sites (M1-M4). The A site denotes the largest site, that can corporate K^+ and Na^+ cations, but also the large hydroxyl anion OH^-.

Tremolite as a member of the Ca-amphibole group (nomenclature after Leake et al., 1997) with the formula $Ca_2Mg_5Si_8O_{22}(OH)_2$ and glaucophane as representative of the Na-amphibole family with $Na_2Mg_3Al_2Si_8O_{22}(OH)_2$ are both monoclinic. The P-T diagram in Figure 7 (modified after Corona et al. 2013) demonstrates the thermodynamically calculated (Holland & Powell, 1998) and experimentally investigated (Koons 1982; Carman & Gilbert 1983; Corona et al., 2013) high-pressure stability of glaucophane. At elevated pressure (Koons, 1982) glaucophane decomposes to jadeite and talc according to

$$\text{glaucophane} \leftrightarrow 2\ \text{jadeite} + \text{talc} \tag{2}$$

$$\text{Gln} \leftrightarrow 2\ \text{Jd} + \text{Tlc}$$

$$Na_2Mg_3Al_2Si_8O_{22}(OH)_2 \leftrightarrow 2\ NaAlSi_2O_6 + Mg_3Si_4O_{10}(OH)_2.$$

In each of the three experimental studies (Koons 1982, Carman & Gilbert 1983, Corona et al., 2013) the Clapeyron slope of the high-pressure glaucophane breakdown reaction is positive and the slope for the thermodynamically calculated phase boundary (Holland & Powell 1998) is slightly negative in the presented P-T range (Figure 7). The high-pressure breakdown of glaucophane is an exothermic reaction, liberating around 8.9 $kJ.mol^{-1}$ (Holland, 1988) with a negative volume change of approx. 2.4 %.

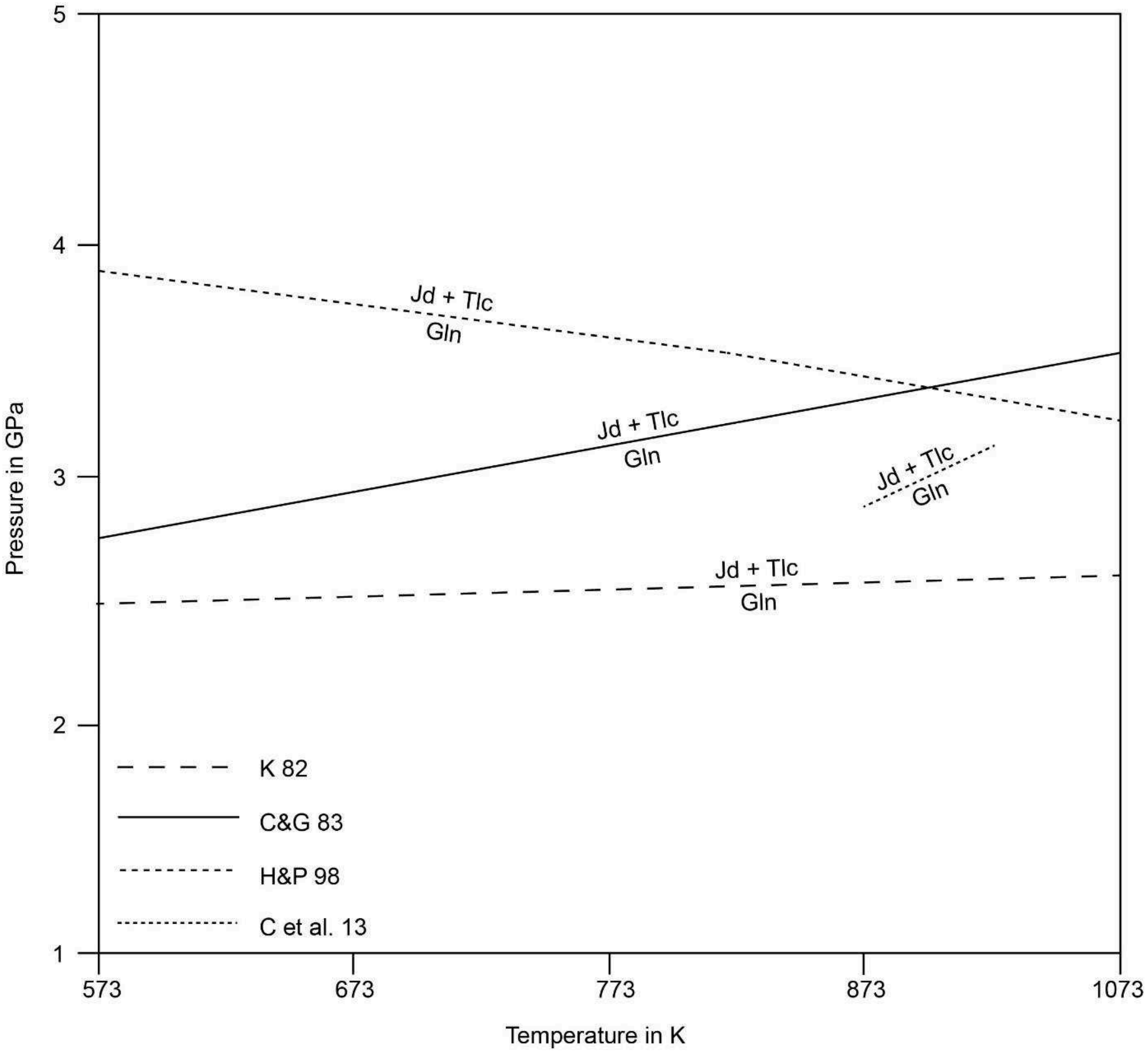

Figure 7: P-T pseudosection presenting the high-pressure stability of glaucophane either thermodynamically modelled (Holland & Powell, 1998 - H&P 98) or experimentally investigated (Koons, 1982 – K 82; Carman & Gilbert, 1983 – C&G 83; Corona et al., 2013 – C et al. 13) in the P-T range 1-5 GPa and 573-1073 K. Jd= jadeite; Tlc= talc; Gln= glaucophane.

As it is shown in Figure 8 the stability of tremolite is restricted to lower pressures relative to glaucophane stability. At higher pressure it decomposes to diopside and talc according to

$$\text{tremolite} \leftrightarrow 2\ \text{diopside} + \text{talc} \tag{3}$$

$$\text{Tr} \leftrightarrow 2\ \text{Di} + \text{Tlc}$$

$$Ca_2Mg_5Si_8O_{22}(OH)_2 \leftrightarrow 2\ CaMgSi_2O_6 + Mg_3Si_4O_{10}(OH)_2.$$

The slope of the high-pressure breakdown reaction of tremolite is positive in all experimental studies presented (Kirby, 1987; Jenkins et al., 1991; Chernosky et al., 1998). As with the high-pressure breakdown reaction of glaucophane the decomposition of tremolite is exothermic and releases an energy of around -7.5-7.8 kJ.mol^{-1} (Jenkins et al., 1991). The volume change, around -1.9 %, is also negative. The molar volumes of all reactant and product phases taken for the calculation of the volume changes as well as the reaction enthalpies for both breakdown reactions are listed in Table 1.

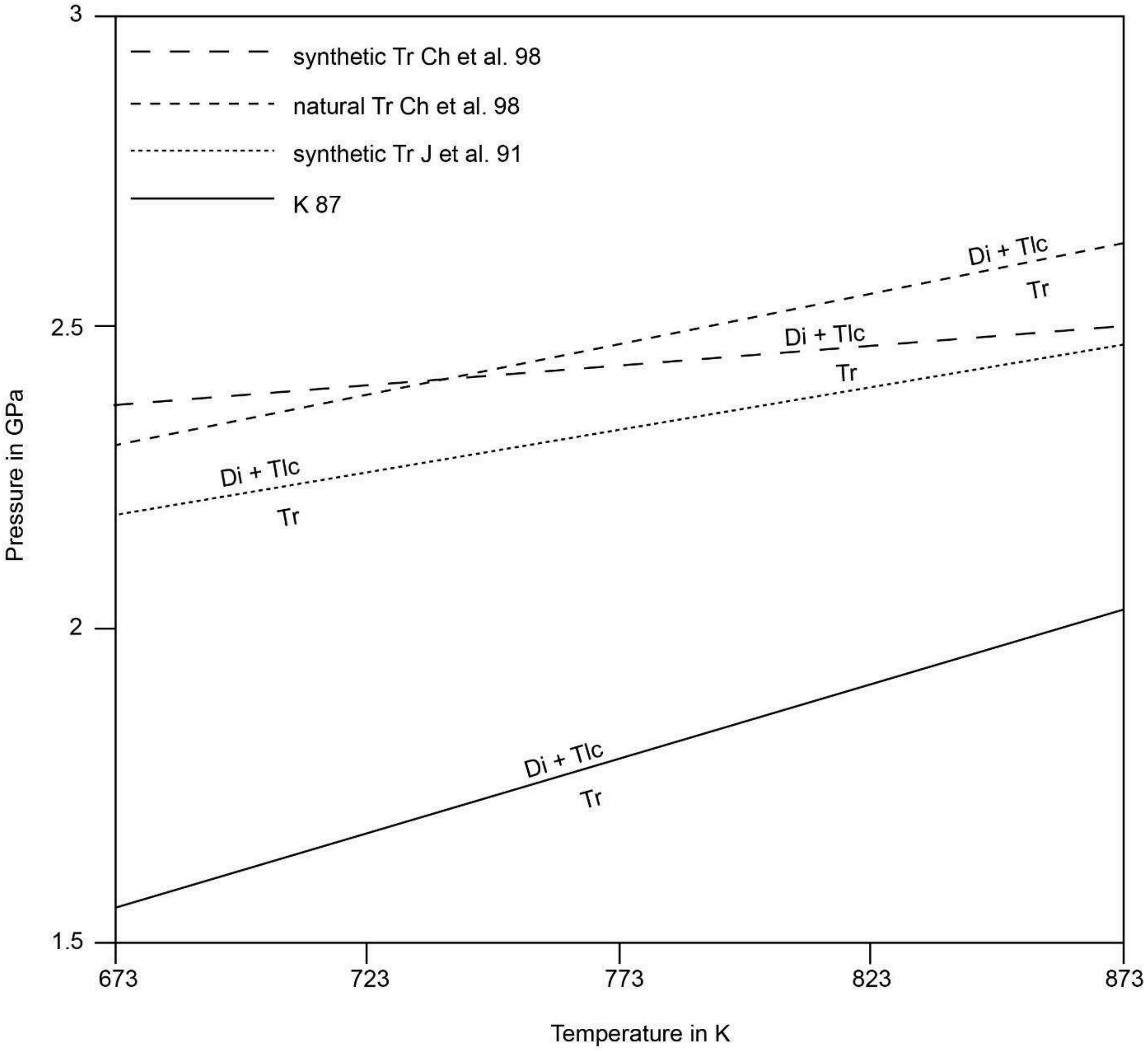

Figure 8: Compilation of high-pressure stability data on tremolite from Kirby (1987) (K 87), Jenkins et al. 1991 on synthetic tremolite (synthetic Tr J et al. 91), and Chernosky et al. (1998) on either synthetic or natural tremolite (synthetic/natural Tr Ch et al. 98) in the P-T range 1.5-3 GPa and 673-873 K. Di= diopside; Tlc= talc, Tr= tremolite.

Table 1: Thermodynamic data of glaucophane and tremolite and their reaction products at high-pressure, jadeite and talc or diopside and talc, respectively.

Phase	V_m (from Holland & Powell, 1998) [cm^3/mol]	Reaction	$\Delta_R H^0_{298}$ [kJ.mol^{-1}]	ΔV [%]
Gln, glaucophane	262.4	Gln= 2 Jd + Tlc[1]	≈ -8.9	≈ -2.4
Tr, tremolite	272.7	Tr= 2 Di + Tlc[2]	≈ -7.6	≈ -1.9
Jd, jadeite	60.4			
Di, diopside	66.2			
Tlc, talc	136.4			

[1]Koons, 1982 ; [2]Kirby, 1987

1.4.2 Lawsonite – a water carrier in cold subudution zones

Lawsonite is a metamorphic mineral stable under high-pressure/low-temperature (HP/LT) conditions with the structural formula $CaAl_2Si_2O_7(OH)_2 \cdot H_2O$. It is a mineral belonging to the group of sorosilicates where Al-O octahedra are corner-connected with a Si_2O_7 group (Figure 9). In the wide cavities, created by the arrangement of Al-O octahedra and Si_2O_7 groups, larger cations as Ca^{2+} and even water molecules can be incorporated into the lawsonite structure (Figure 9). Chemical analyses demonstrate that lawsonite contains 11.5 wt.% H_2O. At low pressures it decomposes to zoisite, kyanite, quartz, and H_2O and within the coesite stability field first to zoisite, kyanite, coesite, and H_2O and at even higher pressures to grossular, kyanite, coesite, and H_2O (Figure 10). Interestingly, calculated P-T paths of the subducting oceanic crust reveal that the metabasalts of the oceanic crust enter the lawsonite stability field during cold subduction as in the case of NE Japan discussed below (Figure 4). Therefore, it is assumed that larger amounts of water may be carried into Earth's mantle in cold subduction zones. Due to the breakdown of lawsonite at high temperature the crystal-bound water is liberated and participate in the upper plate mantle wedge metasomatism. It is also believed that the observed seismic wave anisotropy in the mantle wedge for some subduction zones, situated just above the P-T range where lawsonite is expected to break down, results from the liberation of water during dehydration reactions (Bostock & VanDecar, 1995).

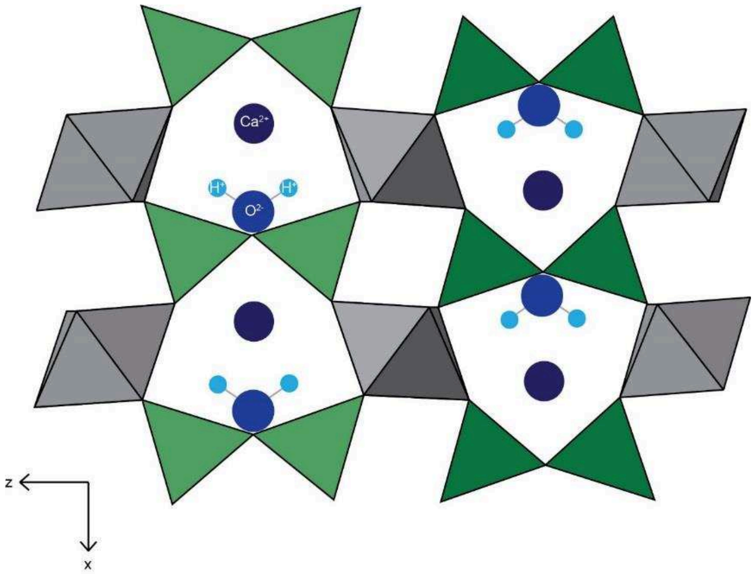

Figure 9: Lawsonite structure after Deer, Howie, Zussman (2013). Green triangles represent the corner-connected Si_2O_7 group. Togther with this structural group the Al-octahedrons (grey) build up wide cavities. In these cavities large Ca^{2+} cations (dark blue) and structurally-bound water molecules (light blue: H^+ and marine blue: O^{2-}*) are incorporated in lawsonite's structure.*

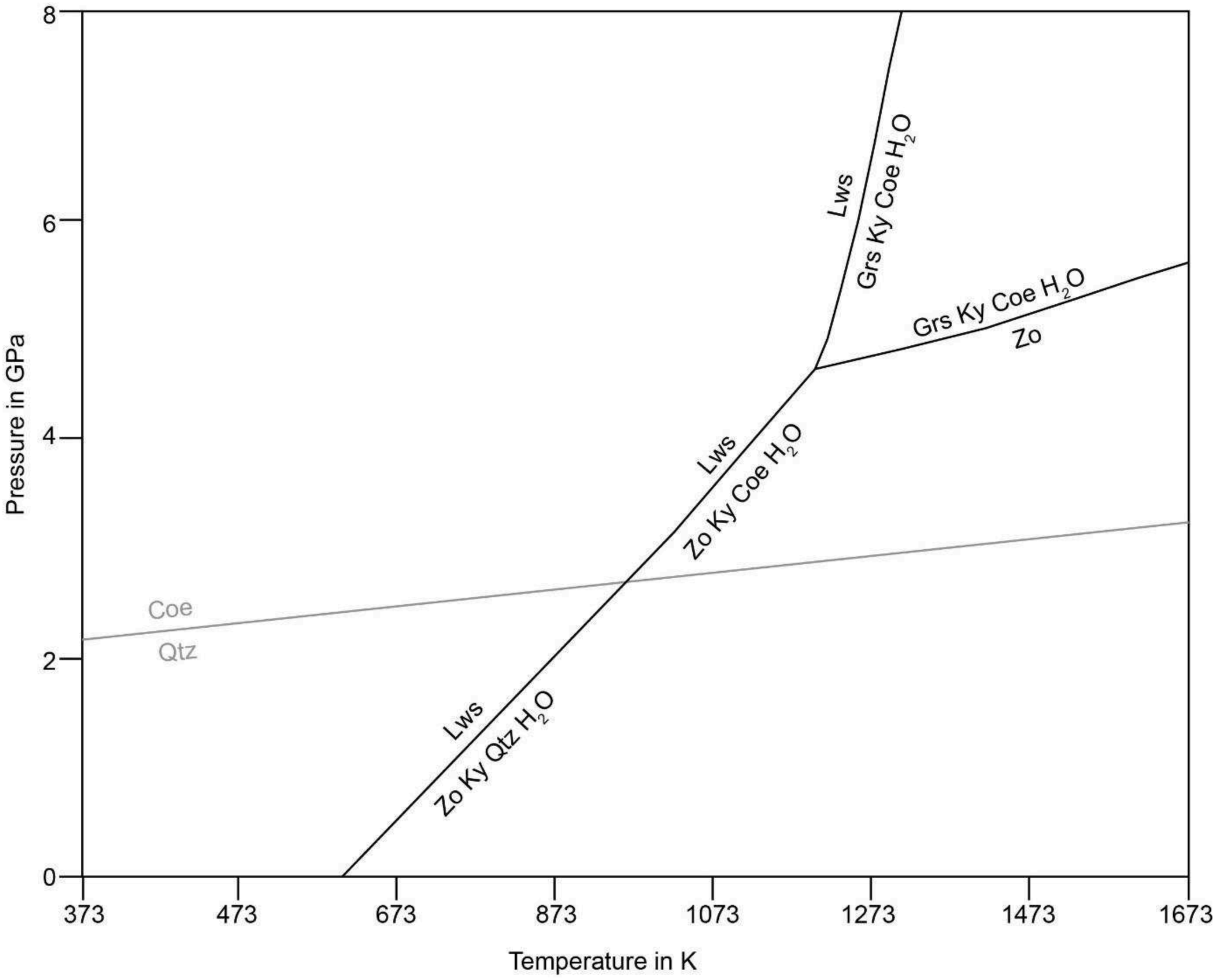

Figure 10: Modified after Pawley (1994). P-T pseudosection showing the stability of lawsonite (Lws) at high-pressure high-temperature conditions. At lower pressure it transforms to zoisite (Zo), kyanite (Ky), quartz (Qtz), and a water-rich fluid (H_2O) with increasing temperature. Under higher pressure, around 2-3 GPa coesite (Coe) instead of quartz will form. The stable mineral assemblage under even higher pressure will be grossular (Grs), Ky, and Coe. This reaction is also accompanied by the liberation of H_2O.

1.4.3 Plagioclase stability at high-pressure

Plagioclase feldspars are the most common rock-forming mineral species in the crust (Deer, Howie & Zussman, 2013). Therefore one of the most important metamorphic reactions in plagioclase bearing rocks are the breakdown reactions of albite, the Na-rich end-member, and anorthite, the Ca-rich end-member of plagioclase feldspars. Experimental work on the stability of plagioclase lead to the better understanding of these metamorphic reactions occurring at elevated pressure and temperature (Figure 11). The decomposition of the albite component in feldspar at high pressure can be written as (Goldsmith, 1980; 1981)

$$\text{Albite} \leftrightarrow \text{jadeite} + \text{quartz} \tag{4}$$

$$\text{Ab} \leftrightarrow \text{Jd} + \text{Qtz}$$

$$Na_2Si_3O_8 \leftrightarrow Na_2Si_2O_6 + SiO_2.$$

In the absence of water, the anorthite component of plagioclase transforms to

$$3 \text{ anorthite} \leftrightarrow \text{grossular} + \text{kyanite} + \text{quartz} \tag{5}$$

$$3 \text{ An} \leftrightarrow \text{Grs} + \text{Ky} + \text{Qtz}$$

$$3\, CaAl_2Si_2O_8 \leftrightarrow Ca_3Al_2(SiO_4)_3 + Al_2SiO_5 + SiO_2.$$

In the presence of a fluid phase at high pressure

$$4 \text{ An} + \text{fluid} \leftrightarrow 2 \text{ zoisite} + \text{kyanite} + \text{quartz} \tag{6}$$

$$4 \text{ An} + \text{fluid} \leftrightarrow 2 \text{ Zo} + \text{Ky} + \text{Qtz}$$

$$4\, CaAl_2Si_2O_8 + H_2O \leftrightarrow 2\, Ca_2Al_3Si_3O_{12}(OH) + Al_2SiO_5 + SiO_2.$$

The two reactions indicated as 1) and 2) in Figure 11 are

1) Anorthite + fluid ↔ liquid (7)
2) Zoisite + kyanite + quartz + fluid ↔ liquid (8)

and mark the onset of partial melting of anorthite at higher pressure in the presence of a water-rich fluid. The thermodynamics behind the albite breakdown at high-pressure are very well studied and listed in Table 2. This reaction involves a negative volume change of around 17 % and is, with – 12.8 kJ.mol^{-1}, an exothermic reaction (Holland, 1980), liberating heat as it progresses (Table 2).

Table 2: Thermodynamic data of albite, jadeite, and quartz.

Phase	V_m (from Holland & Powell, 1998) [cm^3/mol]	Reaction	ΔH_R [kJ.mol^{-1}]	ΔV [%]
Ab, albite	100.1	Ab ↔ Jd +Qtz[1]	≈ -12.8[1]	≈ -17
Jd, jadeite	60.4			
Qtz, quartz	22.7	3 An ↔ Grs + Ky + Qtz[2]	≈ -10*	≈ -36
An, anorthite	100.8			
Ky, kyanite	44.1	4 An + fluid ↔ 2 Zo + Ky+ Qtz + fluid[3]	≈ -10*	≈ -14
Zo, zoisite	135.8			
Grs, grossular	125.4			

[1] Holland (1980); [2] Goldsmith (1980) ; [3] Goldsmith (1981) ; * Calculated using Theriak Domino

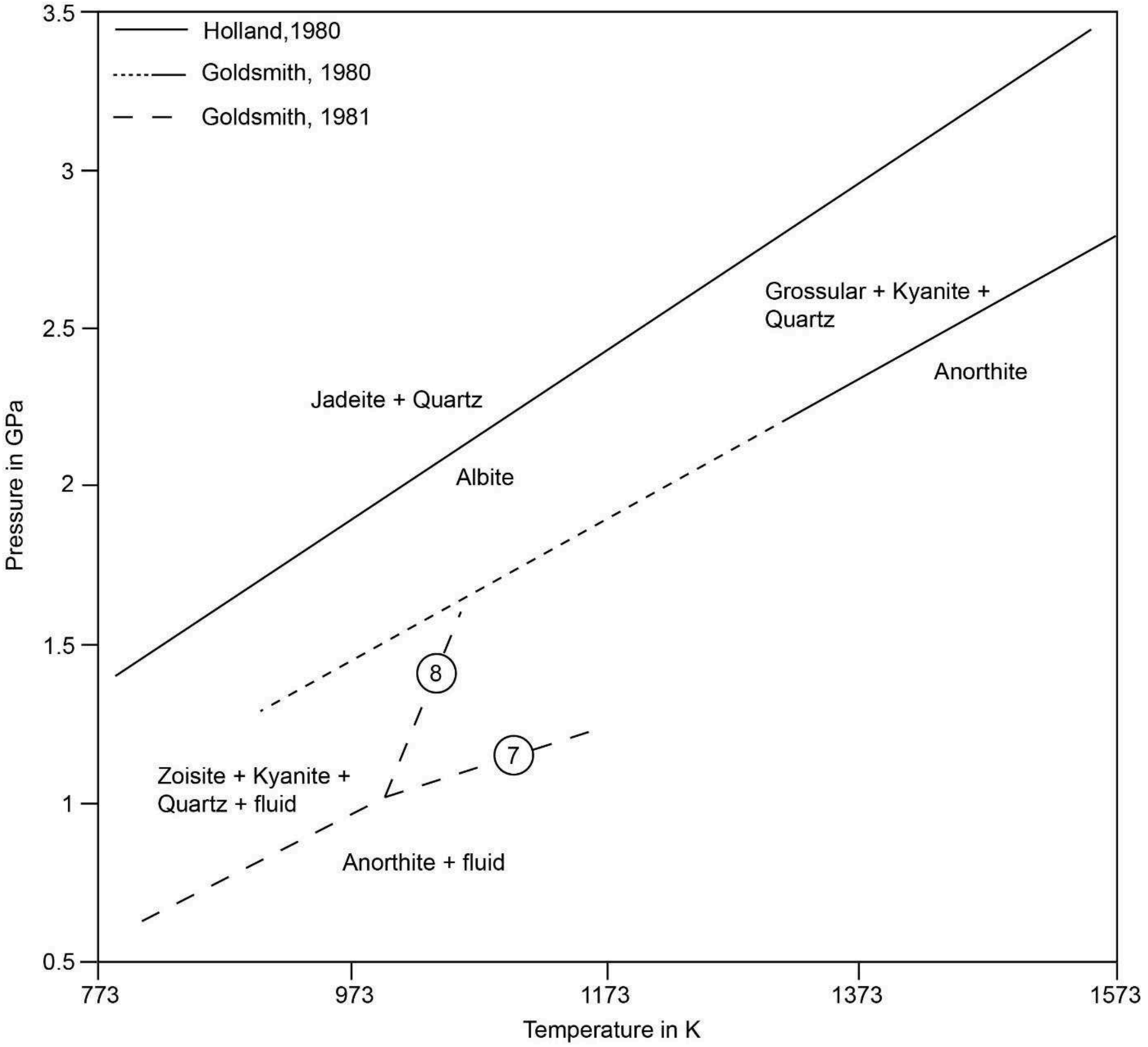

Figure 11: High-pressure stability of albite and anorthite.

1.5 EXPERIMENTAL STUDIES ON FAULTING TRIGGERED BY MINERAL REACTIONS

Much has been done in rock mechanic laboratory experiments to investigate the impact of mineral reactions on brittle failure. Most of the experimental work was performed using hydrous phases, e.g. serpentine minerals or gypsum that became unstable while deforming (Raleigh & Paterson, 1965; Raleigh, 1967; Dobson et al., 2002; Jung et al., 2004; Brantut et al., 2011; Gasc et al., 2011; Leclère et al., 2016). One of the first deformation experiments performed on serpentine samples was published by Raleigh & Paterson (1965) and Raleigh (1967). The authors observed that brittle failure occurred in samples undergoing syndeformational dehydration. They propose two mechanisms that may have weakened or embrittled the sample i) because of increasing pore pressure or ii) due to the loss of cohesive strength. Later the additional observation of acoustic emissions (AEs) during deformation of antigorite samples in a multi-anvil press at high-pressure/high-temperature (HP/HT) conditions also points to dehydration embrittlement as viable mechanism for subduction zone seismicity (Dobson et al., 2002). Shortly after, two experimental studies performed on serpentinite and eclogite, respectively, also came out with the same interpretation (Jung et al., 2004; Zhang et al., 2004). Interestingly, the experimental results on eclogite, which is a nominally dry rock, lead the authors to conclude that only minor amounts of water present in the rock are necessary to weaken it. Recently, experimental results on the deformation of almost pure lawsonite samples exhibits that it undergoes unstable slip accompanied by AEs due to dehydration (Okazaki & Hirth, 2016).

As previously mentioned there are only a few experimental results supporting the theory of ductile shear instabilities (Bridgeman, 1936; Meade & Jeanloz, 1991). It is also possible that the experimental results could be interpreted differently to favor transformation faulting as weakening process (Kirby et al., 1991).

Most of the experimental work that support the theory of transformational faulting were performed on the olivine germanate analog Mg_2GeO_4 to investigate the role of the olivine-spinel transition in deep seismicity. Though, one of the first experimental studies demonstrating transformational faulting leading to unstable slip under high-pressure conditions was performed on ice and tremolite samples (Kirby, 1987). In this study the author showed several experimental results on the transition ice I to ice II and on the mineral reaction tremolite ↔ 2 diopside + talc. Both materials, when deformed in the stability field of their high pressure polymorph/phase assemblage, reveal stick-slip behavior accompanied by audible bangs. He therefore concluded that volume decrease in conjunction with the liberation of heat during the transition from either ice I to ice II or the reaction tremolite to diopside and talc initiated brittle failure. Two years later a study on Mg_2GeO_4 also demonstrated high pressure faulting (Green & Burnley, 1989; Burnley et al., 1991). Samples after deformation exhibited microcracks filled with the nanocrystalline high-pressure phase – the germanate spinel. In contrast to “normal” Griffith cracks the microcracks they found in the samples were oriented with the opening direction parallel to the axis of maximum compression. Therefore the authors called these "anticracks". They state that the formation, growth and finally the connection of these anticracks, filled with the weaker and denser nanocrystalline product phase, formed the fracture plane. Some years later these Mg_2GeO_4 deformation experiments were re-performed by using a modern state-of-the-art D-DIA apparatus, which is mounted on a synchrotron beamline at the Advanced Photon Source (APS) in Chicago and equipped with a system that is able to record AEs (Schubnel et al., 2013). Brittle failure also occurred in those samples and was accompanied by AEs. After the deformation experiments the product phase, spinel (germanate), was found within the shear fractures of the sample implying a link between high-pressure (HP) failure and the transition from olivine to spinel. The authors additionally demonstrate that the total number of AEs, as lab-equivalent to natural earthquakes, follow the Gutenberg-Richter law. Since the small “lab-earthquakes” follow the same power-law distribution as natural earthquakes, they suggested that their laboratory observations might be scale up and the mechanics at the origin of the seismic instability at the laboratory scale applicable to natural earthquakes.

Geophysical, field, and experimental observations show that intermediate and deep seismicity might be linked to metamorphic reactions during the burial of lithospheric slabs. However, most of the experimental work was performed on material investigating the seismicity of the lithosphere mantle. Except from a very recent study (Okazaki & Hirth, 2016) the formation of intermediate-depth earthquakes generated in high-pressure crustal rocks has almost been completely disregarded.

The main goal of the present Ph.D. thesis is to fill this gap and to experimentally investigate the underlying mechanisms of intermediate-depth seismicity in either hydrous or anhydrous crustal rocks. Comparison of the microstructures obtained from the experiments with those observable in the field and comparison of acoustic emission pattern with the natural seismic record from intermediate depths are then considered as relevant tests for the upscaling of our experiment based models. The first part of this thesis will present the experimental results on the deformation of blueschist to examine if and how intermediate-depth seismicity forms in subduction zones. The end of the chapter tries to make a link between the microstructures from the lab to those of natural blueschist samples, collected during a field trip to Alpine Corsica. Afterward, the second chapter shows the preliminary experimental data on the eclogitization of granulite as representative for intermediate-depth seismicity in continent-continent collision zones. Again, the microstructures obtained from the experiments were compared to natural microstructures in granulites, sampled in the Bergen Arcs, SW Norway. Finally, the thermodynamics of eclogite-facies metamorphic reactions will be discussed together with two additional deformation experiments on almost pure amphibole samples.

"Auch die Pause gehört zur Musik."
- *Stefan Zweig*

II METHODOLOGY

2.1 SAMPLES, SAMPLE PREPARATION & CHARACTERIZATION OF THE STARTING MATERIALS

Field observations reveal pseudotachylites in various high-pressure rocks regardless of their chemical composition and water content. Therefore, to better understand the underlying mechanism/s on the formation of intermediate-depth earthquakes, different rock types have to be investigated.

Within this thesis in total five different rock samples were investigated during either hydrostatic or deformation experiments. Three blueschists from Alpine Corsica, France, Tianshan, China, as well as from Syros, Greece, plus one mafic granulite from the Bergen Arcs, Norway, and a tremolite sample, Balmat, NY, USA, served as sample materials. The blueschist samples from Corsica and Syros as well as the tremolite sample were provided by colleagues. Granulite samples from the Bergen Arcs, Norway, and additionally a lawsonite-eclogite sample from Corsica, France, were collected during two field studies, respectively. The samples, their preparation and the resulting starting materials are presented in the following.

2.1.1 Blueschists

The Corsican blueschist

A lawsonite-blueschist (Lws-Bs) from Alpine Corsica served as sample material for the experiments. This sample was provided by Prof. Christian Chopin. Having experienced peak metamorphic conditions of approximately 520 ± 20 °C and 2.3 ± 0.1 GPa (Vitale Brovarone et al., 2011), it mostly consists of glaucophane (Gln, mineral abbreviations follow Whitney and Evans, 2010) and lawsonite (Lws) (Figure 12), where Lws often appears as lenses. The Gln:Lws ratio of approximately 3:2 is estimated from optical analyses of several thin sections. The minor phases, actinolite (Act), garnet (Grt), phengite (Ph), titanite (Ttn), and omphacite (Omp1), with $X_{jd} \approx 0.4$ and $X_{di} \approx 0.6$, represent less than 15 % of the rock's volume. Apatite (Ap), and albite (Ab) are also found in limited amounts. The mineral phases Gln, Omp1, and Act were chemically investigated (Table 3) and the analyses are in good agreement with those previously reported (Vitale Brovarone et al., 2011).

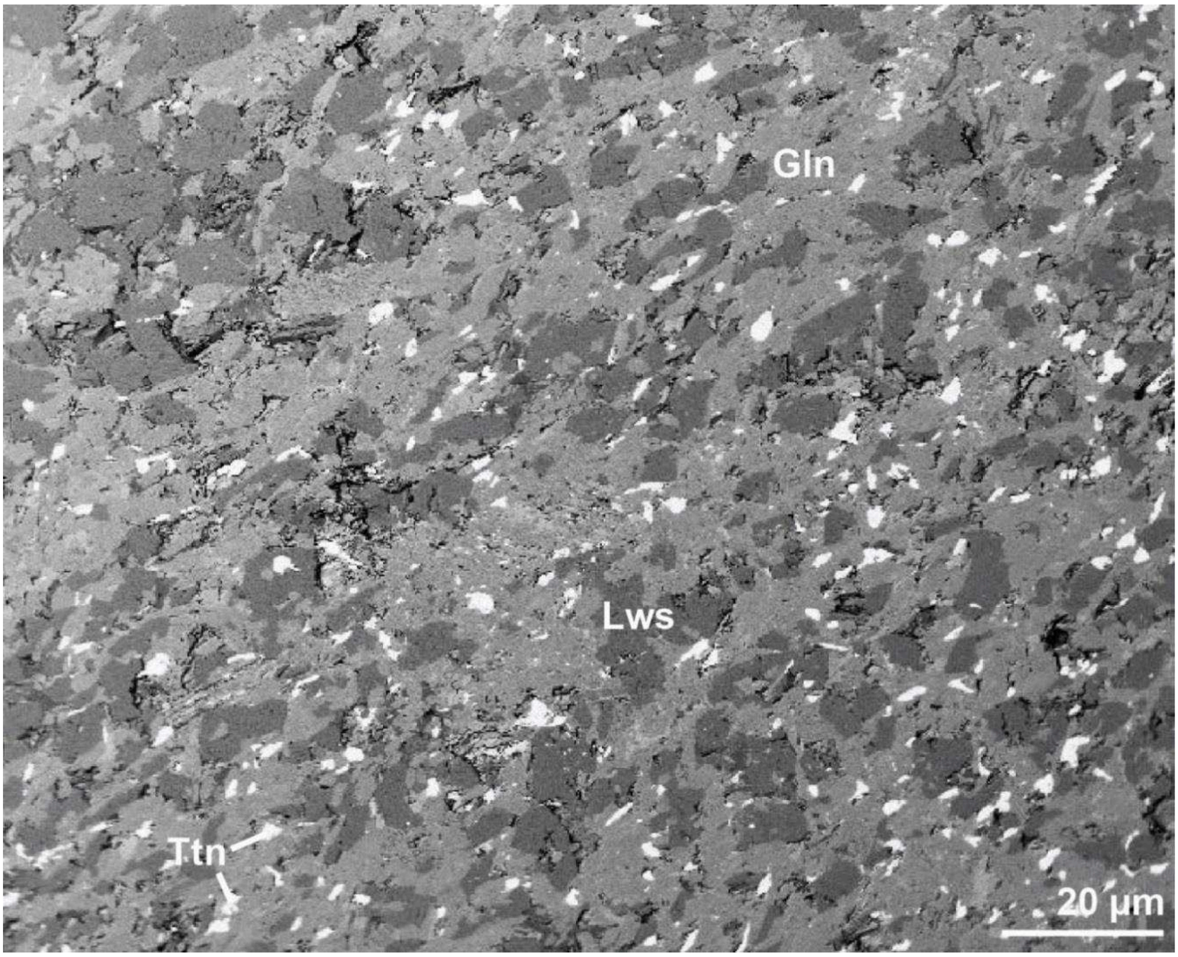

Figure 12: BSE image of the natural Corsican blueschist sample. Gln= glaucophane; Lws= lawsonite; Ttn= titanite.

Table 3: Chemical analyses of the natural Corsican blueschist major phases.

Oxide	Gln	Lws	Act	Omp1
SiO_2	58.42	38.34	58.36	56.07
TiO_2	-	0.04	0.07	0.08
Al_2O_3	10.81	32.56	0.75	8.79
Cr_2O_3	0.03	0.02	-	-
MgO	9.69	-	18.08	8.01
FeO	11.27	0.34	9.37	7.13
MnO	0.11	-	0.49	0.22
CaO	0.61	17.39	11.93	13.59
Na_2O	7.39	-	0.58	6.70
K_2O	0.03	-	0.06	0.04
Total	98.36	88.70	97.71	100.64

During a field trip to Alpine Corsica additional samples were collected around the area of the Mte San Petrone. The sample COSI-16_05, the only one presented in this thesis, was found at the summit of Mte San Petrone (Figure 13). The area around Mte San Petrone is dominated by metabasalts that underwent lawsonite-eclogite-facies conditions (Vitale Brovarone et al., 2013). The collected sample is microcrystalline and mostly consists of bluish crystals (Figure 14A). Lenses of garnet crystals seem to be aligned along the foliation of the sample. The edge of the specimen reveals a green surface (Figure 14) with elongated greenish crystals on its surface (Figure 14B). Several of these greenish bands, oriented parallel to each other, can be found within the specimen and all these bands cut through the sample foliation (Figure 14A). For the geological and petrographic background of this area, the interested reader is referred to Healy et al. (2009), Ravna et al. (2010), Vitale Brovarone et al. (2011), and Vitale Brovarone et al. (2013).

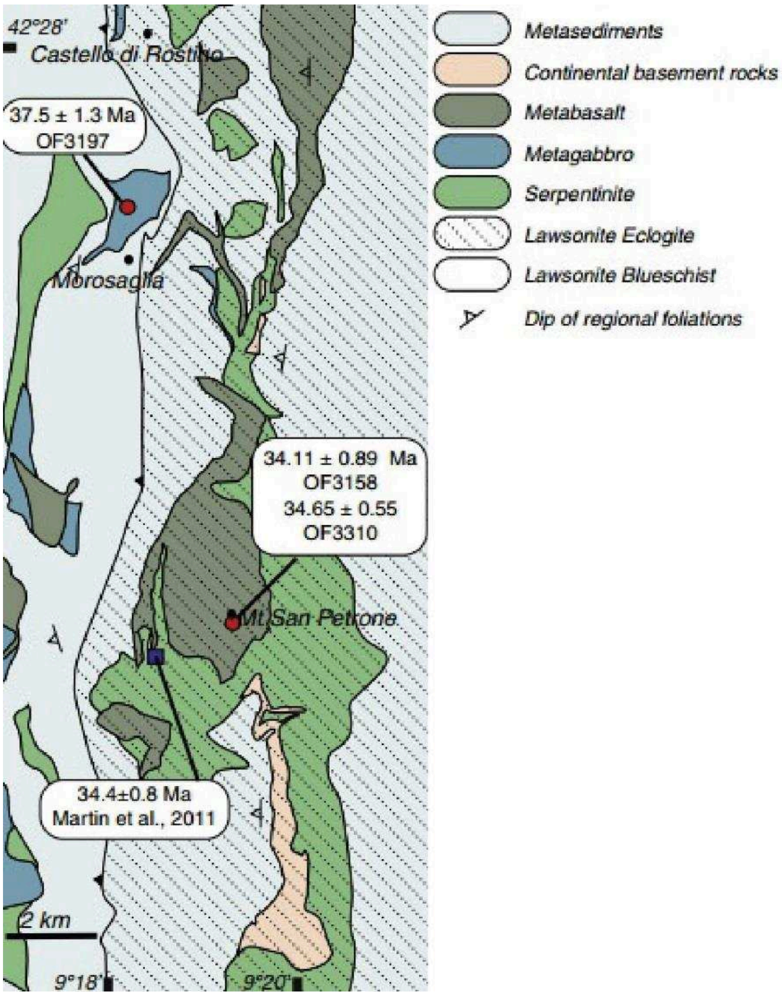

Figure 13: Modified after Vitale Brovarone et al. (2011). Geological map showing the location of the sample COSI-16_05, collected on the summit of the Mt San Petrone.

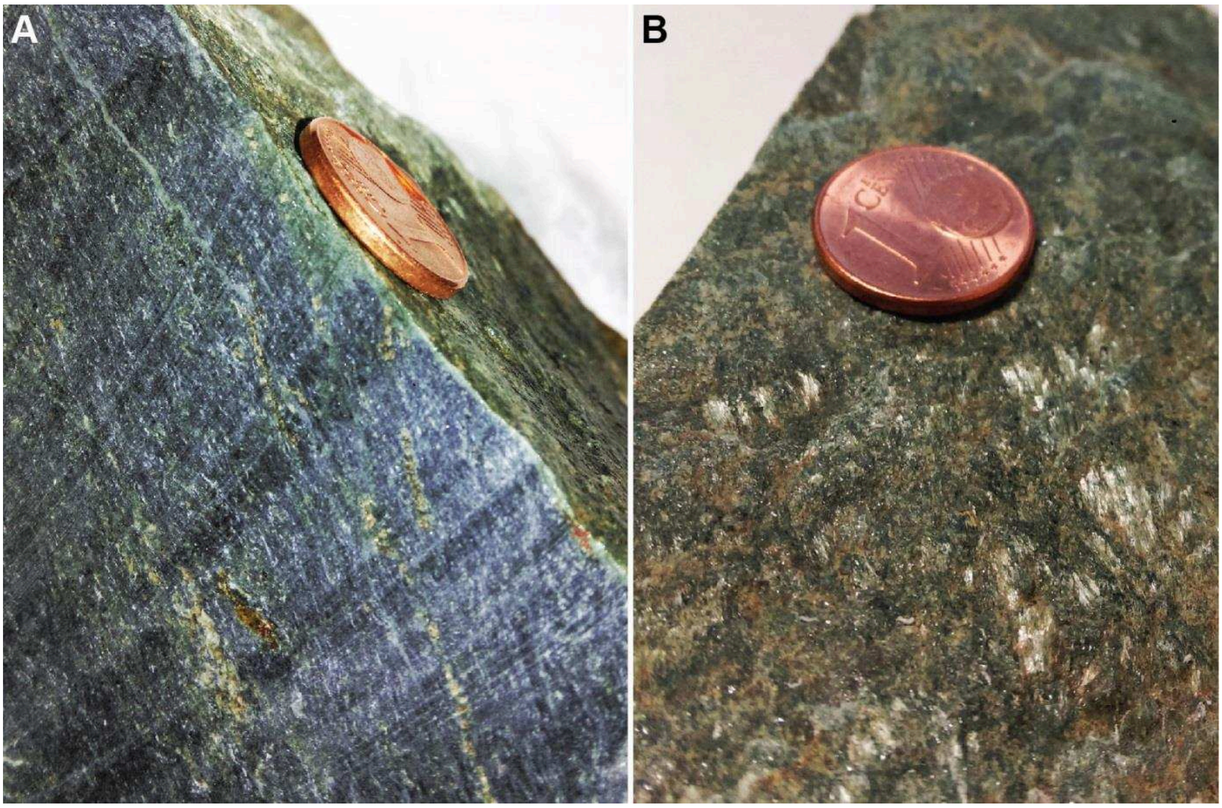

Figure 14: Sample COSI-16_05 exhibiting mostly glaucophane (blue) and omphacite (green) as matrix phases. Garnet crystals (reddish) form smaller lenses or bands (A). Parallel bands of greenish crystals cross-*cut the sample's foliation. An edge of the sample exposes a greenish b*and demonstrating sheared crystals (B).

Tianshan blueschist

The Tianshan blueschist sample (Figure 15) was provided by Prof Timm John and Léa Bayet. The estimated peak-metamorphic condition this sample experienced are $P \approx 1.5$-2.3 GPa and $T \approx 603$-853 K (Klemd et al., 2011). Only a limited blue domain, identified as blueschist, was used for this thesis. The blueschist is sandwiched between a brownish and a white layer rich in calcite and quartz, respectively. The greenish part of this handspecimen is mostly composed of epidote group mineral reflecting greenschist-facies conditions. A representative glaucophane analysis from the Tianshan blueschist is shown below in Table 4.

Table 4: Representative chemical analysis of a glaucophane crystal from the Tianshan blueschist sample.

Oxide	Gln
SiO_2	59.07
TiO_2	-
Al_2O_3	10.74
MgO	11.22
FeO	9.78
MnO	0.01
CaO	0.82
Na_2O	6.34
K_2O	0.02
Total	98.59

Figure 15: Handspecimen provided by Prof. Timm John. Only a small part from the blue layer, identified as blueschist, was taken for the production of the starting material.

2.1.2 Granulite

Natural samples from the island Holsnøy, Norway, were collected to serve for the deformation experiments. Both, rock fragments and drill core samples, were collected in an area in the North of Ådnefjell (Figure 16). Rock fragments were used to obtain the starting material for the deformation experiments. From the drill cores thin sections were produced for the later microstructural and chemical comparison between lab and field.

In total seven drill cores were taken in different regions that show pseudotachylite main faults or structures interpreted as injection veins. This thesis only presents two representative drill cores, HA-14-02 and HA-14-03, from a pseudotachylite network (highlighted in red in Figure 17) from Ådnefjell (North). In the case of HA-14-02 the core was drilled in an injection-vein with a thickness of around 2.5 cm, oriented perpendicular to a thinner pseudotachylite fault-vein (Figure 17). HA-14-03 was drilled on a pseudotachylite fault-vein with a thickness of around 0.5 cm (Figure 17).

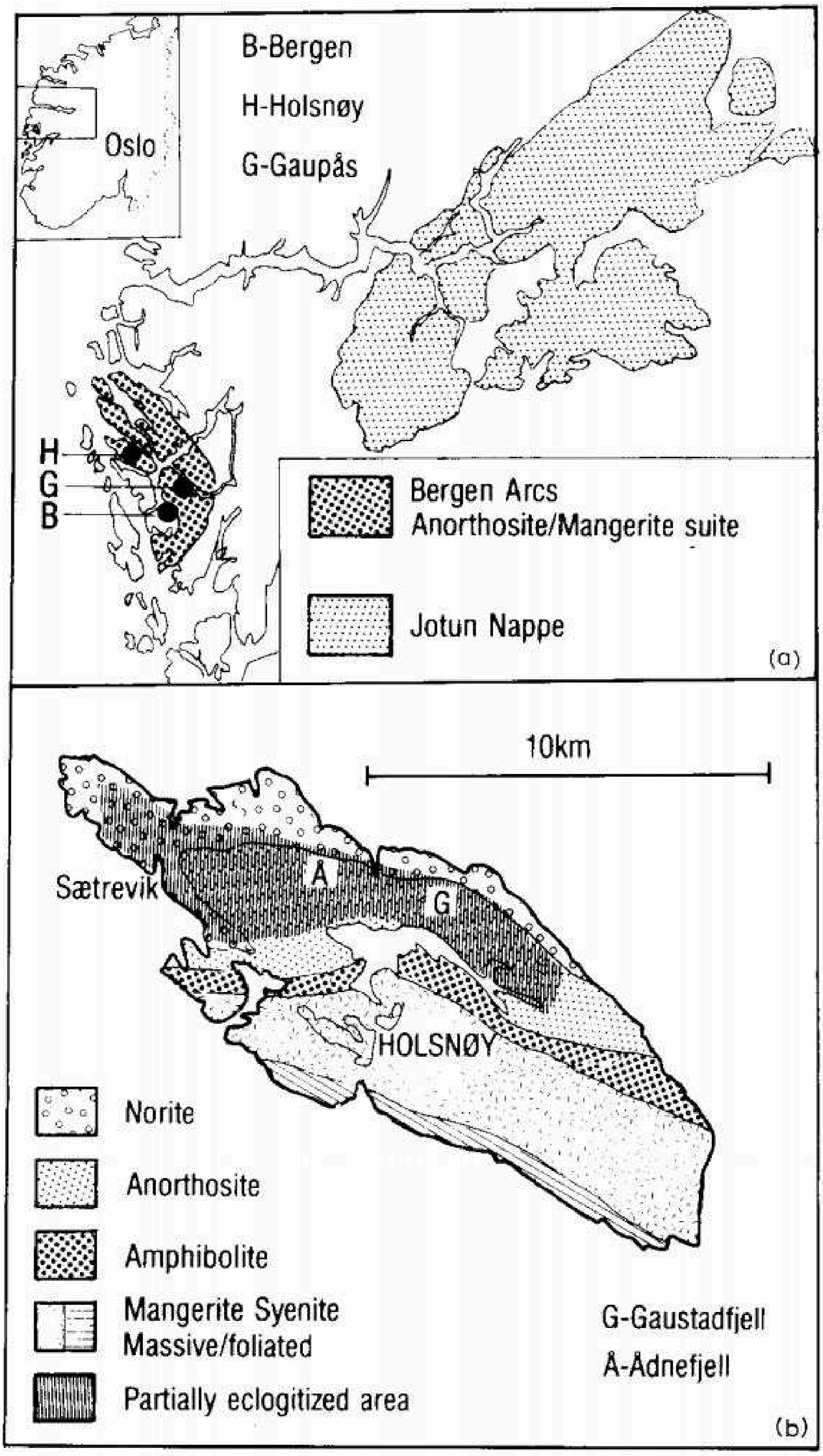

Figure 16: From Austrheim (1987). The maps show the location of the Bergen Arcs in SW-Norway (a). (b) Geological map of the island Holsnøy demonstrating the sampling position Ådnefjell.

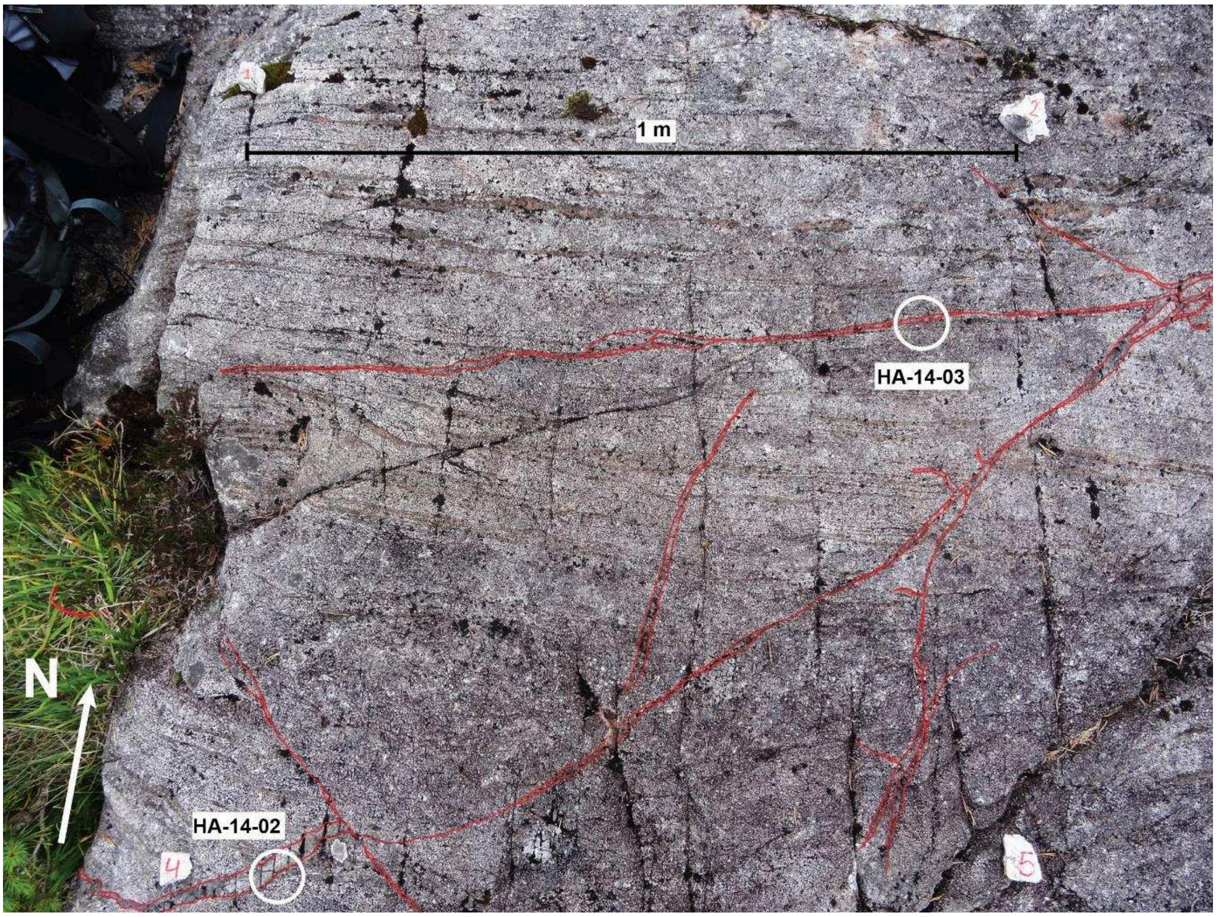

Figure 17: Pseudotachylite network (highlighted in red) in granulite host rock from Ådnefjell (North) showing the sample locations of the two drill cores, HA-14-02 and HA-14-03, presented in this thesis.

The pseudotachylite fault and injection veins are rather easy to identify, because their dark color contrast with the whitish granulite (Figure 18B, D). The fault and the injection vein exhibit sometimes larger fragments in their fine grained matrix. Next to the pseudotachylite fault a greenish zone locally appears within the granulite (Figure 18D).

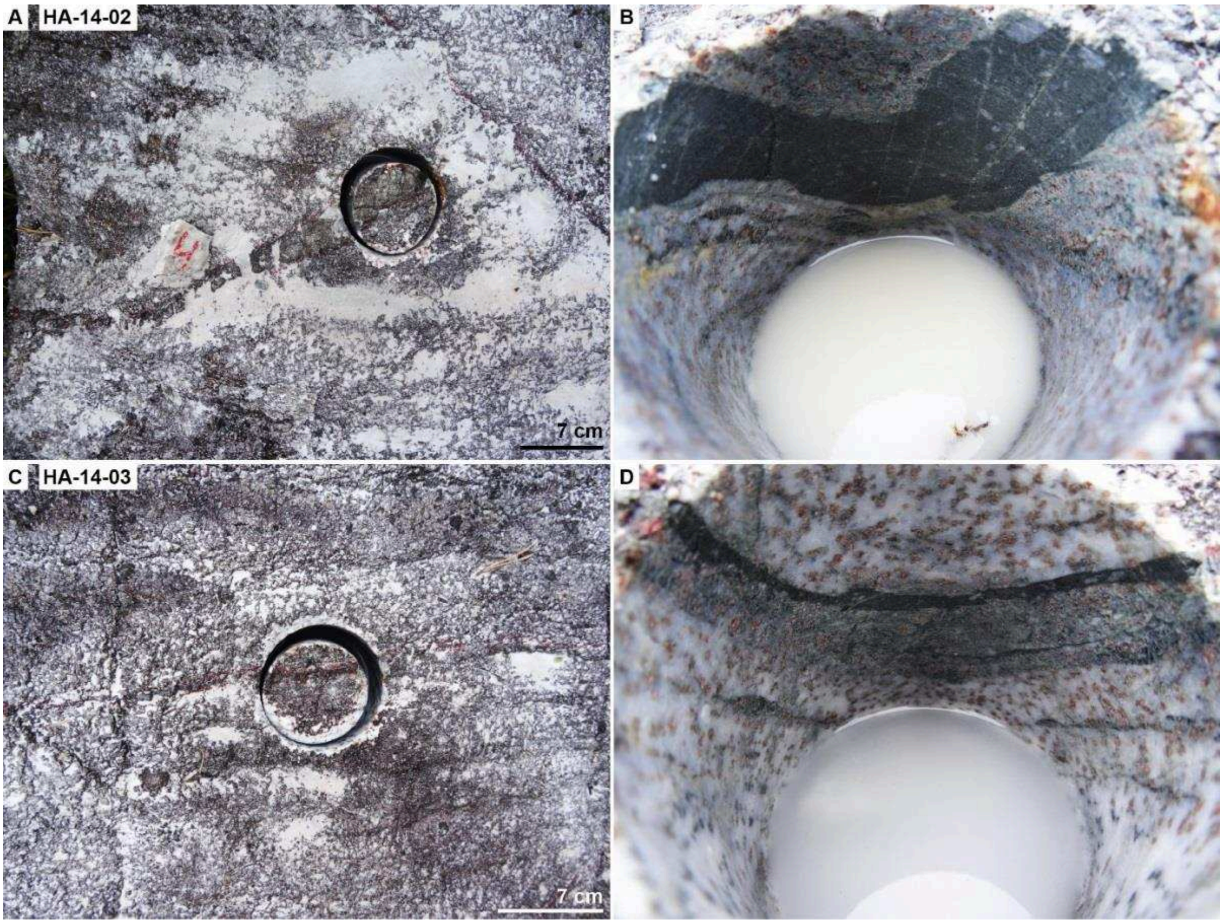

Figure 18: A and C) Close-ups of the two drill core locations presented in Figure 17. Pseudotachylite main fault (D) and injection vein (B) appear much darker than the bright granulite.

Chemical composition of plagioclase, representing the main phase, and clinopyroxene as minor phase of this mafic granulite are shown in Table 5 (Jamtveit et al., 1990). Plagioclase shows intermediate composition with $An_{0.45}Ab_{0.53}Or_{0.02}$. The clinopyroxenes are Ca-rich with $Di_{0.51}CaTs_{0.19}En_{0.29}$ (Cpx nomenclature after Morimoto et al., 1988).

Table 5: From Jamtveit et al. (1990). Chemical composition of plagiclase and clinopyroxene of the mafic granulite form Holsnøy.

Oxide	Plg	Cpx
SiO_2	57.82	48.92
TiO_2	-	0.15
Al_2O_3	26.87	11.63
MgO	-	11.15
FeO	-	4.76
MnO	-	-
CaO	9.12	21.30
Na_2O	5.94	1.75
K_2O	0.28	-
Total	100	99.6

2.1.3 Amphiboles

Tremolitite

The sample for the tremolite deformation experiment was provided by Prof. Pamela Burnley (Figure 19). The sample location is Balmat County, New York, USA and it is almost exclusively composed of tremolite (Kirby, 1987). A representative chemical analysis is shown in the table below. The analysis of tremolite (Table 6) reveals with $Na_{0.1}Ca_{1.9}Mg_5Si_8O_{22}(OH)_2$ almost end-member composition ($Ca_2Mg_5Si_8O_{22}(OH)_2$).

Table 6: Representative chemical analysis of tremolite.

Oxide	Tr
SiO_2	59.86
TiO_2	-
Al_2O_3	0.10
MgO	24.87
FeO	0.02
MnO	0.36
CaO	12.97
Na_2O	0.20
K_2O	0.13
Total	98.51

Figure 19: The tremolitite sample used for the experiments was provided by Prof. Pamela Burnley. The sample consists almost purely of tremolite (Kirby, 1987).

Blueschist from Syros, Greece

This blueschist sample from the island Syros, Greece, was provided by Prof. Loic Labrousse (Figure 20). It is mostly composed of glaucophane (blue parts in Figure 20) with only very few accessory phases, e.g. chlorite (green areas in Figure 20), epidote, and titanite.

Figure 20: Blueschist sample from Syros, Greece. This sample was provided L. Labrousse The bluish parts of the hand specimen are made of glaucophane. The greenish areas mostly consists of chlorite.

2.2 SAMPLE PREPARATION

A fragment of the Lws-Bs, selected for its homogeneous distribution of Gln and Lws content, was crushed, ground and sieved to a grain size fraction < 38 µm. A Frantz isodynamic magnetic separator was used to segregate Gln and Lws. Three different powders with different Gln:Lws ratios were produced to investigate the possible impact of the chemistry of the starting material on the experimental results.

The sample preparation of the other samples, Tianshan blueschist, tremolite, Syros blueschist, and granulite, were less elaborate, because only bulk rock powders were used for the experiments. Therefore a selected volume of each sample was crushed and sieved to a grain-size of < 38 µm.

Powders were used rather than the intact rock, because of i) the heterogeneity and anisotropy in mineralogy (e.g. due to Lws lenses) and texture (schistosity), which would considerably hamper the sample-to-sample comparison and ii) the need of a small grain-size (< 38 µm) for the in-situ X-ray powder diffraction (XRD) during the D-DIA deformation experiments of the samples.

2.3 CHARACTERIZATION OF THE STARTING MATERIALS

For the characterization of the starting materials the rock powders were embedded in epoxy and then chemically analyzed using a SEM. Selected element distribution maps were merged using the software ImageJ (Abramoff et al., 2004) leading to composite images. These images highlight the chemical difference between the phases within the starting material. This makes it possible to calculate the exposed surface of each phase. Based on these values phase proportions and ratios can be estimated assuming a isotropic phase distribution within the starting material.

2.3.1 Blueschists

Corsican blueschist

Na and Ca element distribution maps can be directly transformed to different Gln:Lws ratios (Figure 21). The bulk-rock, Gln-rich, and Lws-rich powders show Gln:Lws ratios of approximately 1:1, 2:1, and 1:3, respectively. As in the natural rock, minor and accessory phases comprise around 15 % of the powder volume.

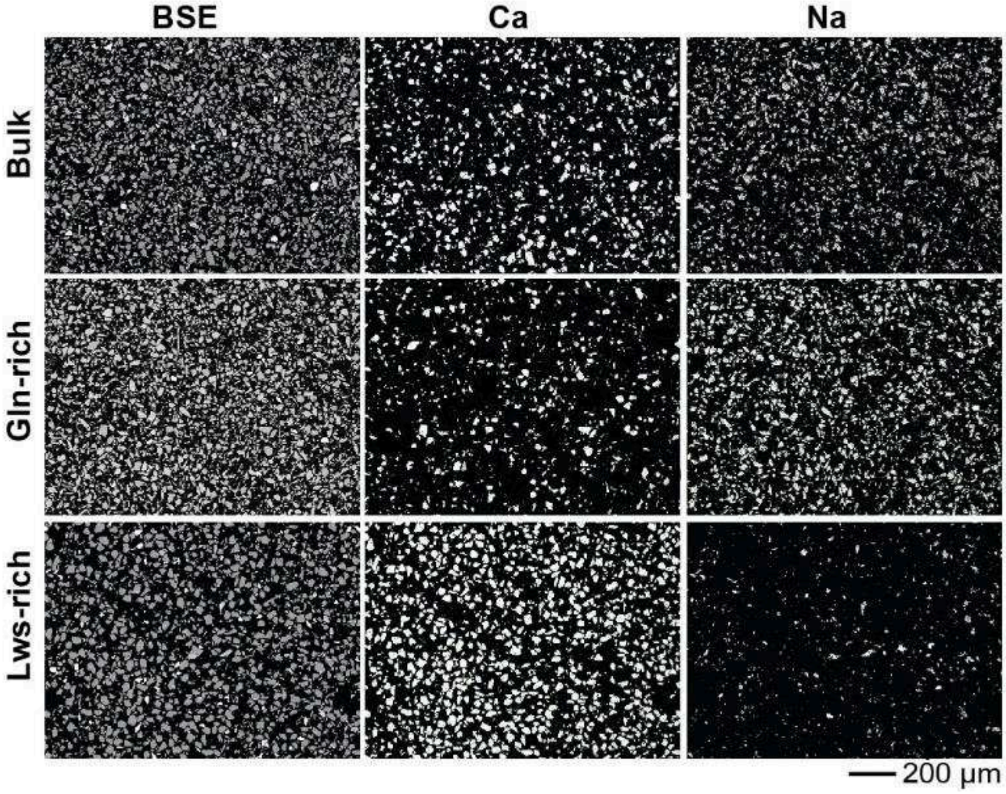

Figure 21: Element distribution maps of the three different powders, bulk rock, Gln-rich, and Lws-rich, used for the experiments. The Gln:Lws ratio of the powders can be directly transferred from the presented Ca- and Na-distribution maps.

Additionally, three drill cores of the Corsican blueschist were investigated to compare the results of the powder experiments with intact samples. The cylindrical drill cores with a size of approximately 3.5 mm diameter and 7.3 mm height were drilled very close one to another to avoid textural and chemical differences. The drill cores were exclusively used for the Griggs deformation experiments.

The microstructure of the hot-pressed sample reveals thin rims around glaucophane crystals appearing brighter in BSE mode (Figure 22). Thicker areas of these coronas were identified as omphacite. These rims are absent in the natural Corsican blueschist and therefore the hot-pressed rock used for the experimental run BSh_3_973 initially contains more omphacite relative to the other runs where powders were used as starting material.

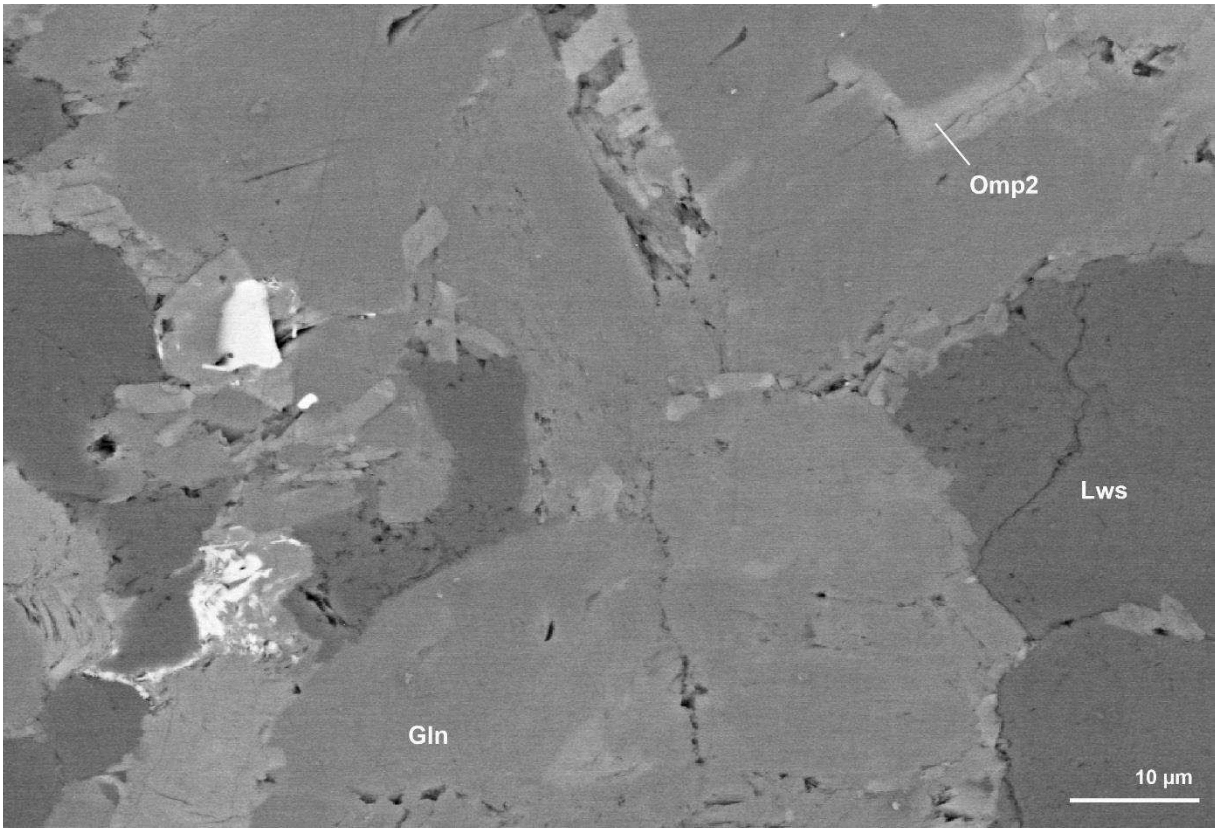

Figure 22: BSE images of the hydrostatic run BSh_3_923. Glaucophane crystals show omphacite rims.

Tianshan blueschist

Chemical analyses using the scanning electron microscope (SEM) and electron microprobe analyses (EMPA) on the Tianshan blueschist starting material demonstrate, that this blueschist is mostly composed of glaucophane and quartz in a ratio of approximately 1:1. Minor phases are titanite, calcite, and epidote group minerals.

2.3.2 Granulite

As with the blueschist samples, a part of a granulite sample was crushed and pieces appearing to contain mostly plagioclase were selected and sieved to a grain size < 38 µm. A part of this powder was embedded in epoxy and chemically analyzed using the SEM. Analysis on the starting material reveal that it is composed of around 90 % plagioclase, 5 % clinopyroxene, and the remaining 5 % composed of accessory phases, e.g. quartz, phlogopite, garnet and spinel.

2.3.3 Amphiboles

The tremolitite sample contains 99.x vol. % tremolite and <1 vol. % accessory phases. Based on a Na-Mg-Si composite image of the blueschist sample from Syros, Greece, and the additional information from the Ca and the K distribution maps the phase proportions of this rock powder is determined to be > 95 % glaucophane (turquoise phase in Figure 23). The remaining phases, which make up < 5 % are chlorite (green phase in Figure 23), albite (dark blue in Figure 23), epidote, quartz (red in Figure 23), apatite, actinolite, phengite (K-distribution map in Figure 23), titanite, and calcite (Ca-distribution map in Figure 23).

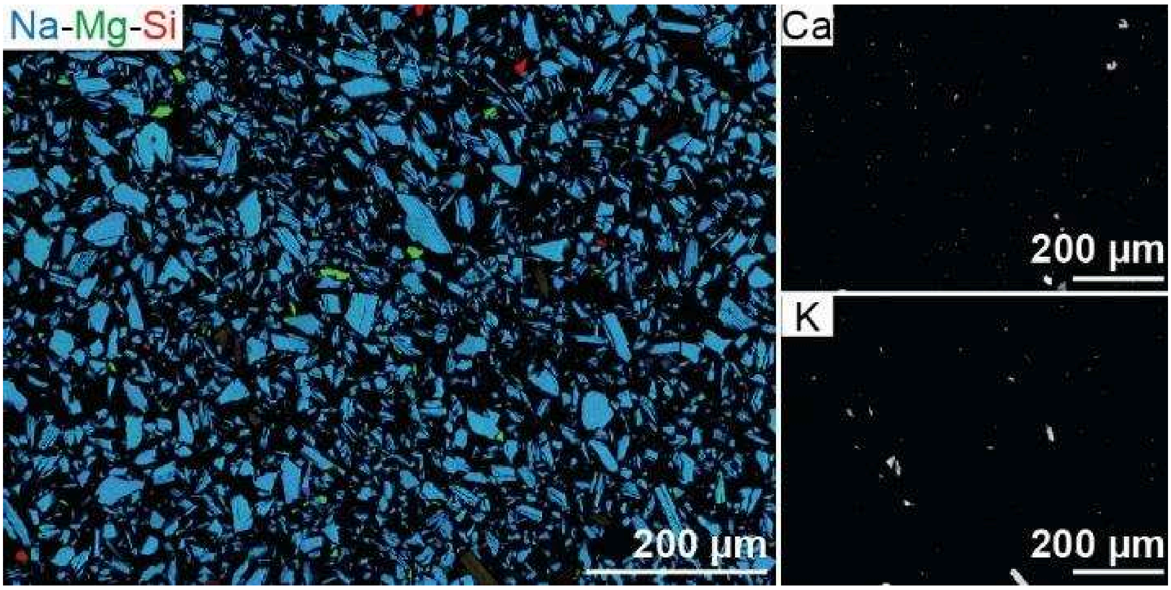

Figure 23: Composite image showing the Na, Mg, and Si distribution of the glaucophane starting material (left side; turquoise= glaucophane, green= chlorite, dark blue= albite, red= quartz). The element distribution maps of Ca and K on the right hand side demonstrate the presence of either titanite, calcite, epidote, and apatite or phengite

2.4 EXPERIMENTAL & ANALYTICAL METHODS

Different deformation apparatus as well as a hydrostatic press were used to obtain the experimental results. The main motivation to perform deformation and additional hydrostatic experiments was to compare the microstructures of the deformation experiments with those of their static counterparts. Highlighting the impact of deformation on the structural and chemical evolution of the samples is of particular interest, because most of the experimental work on metamorphic or metasomatic reactions was performed under hydrostatic conditions. Only little is known on how an anisotropic stress field affects metamorphic reactions and most of the experimental work investigating this problem was performed on monophasic samples (Kirby, 1987; Richter et al., 2016). Various samples and starting materials were used for deformation and hydrostatic experiments performed for this thesis (Table 7).

Table 7: Compilation of all experiments conducted using the D-DIA, the Griggs, and the piston cylinder press.

Sample	Abbreviations used	Starting material	Press type		
			Piston cylinder	Griggs	D-DIA
Corsican blueschist	BSh, BS, GLN, LWS	rock powder	X	X	X
	BSd	drill core		X	
	BS	hot-pressed powder			X
Tianshan blueschist	TS-BS	rock powder	X	X	
Norwegian granulite	NG	rock powder		X	X
Tremolitite	TR	rock powder	X		X
Syros blueschist	GLS	rock powder			X

2.4.1 HYDROSTATIC PISTON CYLINDER EXPERIMENTS

The hydrostatic experiments were conducted using a piston cylinder press at Ruhr-Universität Bochum. Hydrostatic piston-cylinder experiments were conducted using rock powders of the Corsican blueschist, the Tianshan blueschist and tremolitite, respectively.

Experimental setup & sample assembly

For the piston cylinder experiments, the rock powders were filled into gold capsules and mechanically sealed. Two different salt sample holders were machined to either host three or four samples for each experimental run. The samples in the three hole sample holder have an outer diameter of approximately 4 mm and the samples of the four hole sample holder around 3 mm outer diameter. The height of the samples is always around 10 mm. The sample holder is sandwiched between a top and a bottom salt cylinder and all three salt cylinders are surrounded by a graphite furnace (Figure 24). The furnace is in contact with an upper and a lower graphite disk. An outer salt cylinder encloses the graphite furnace and the three inner salt cylinders. The Ni-Cr/Ni thermocouple is oriented parallel towards the samples and it is stabilized with a pyrophyllite tube placed within the upper metal sleeve and the inner salt cylinder at the bottom. A pyrophyllite gasket surrounds the two metal sleeves at the bottom of the sample assembly.

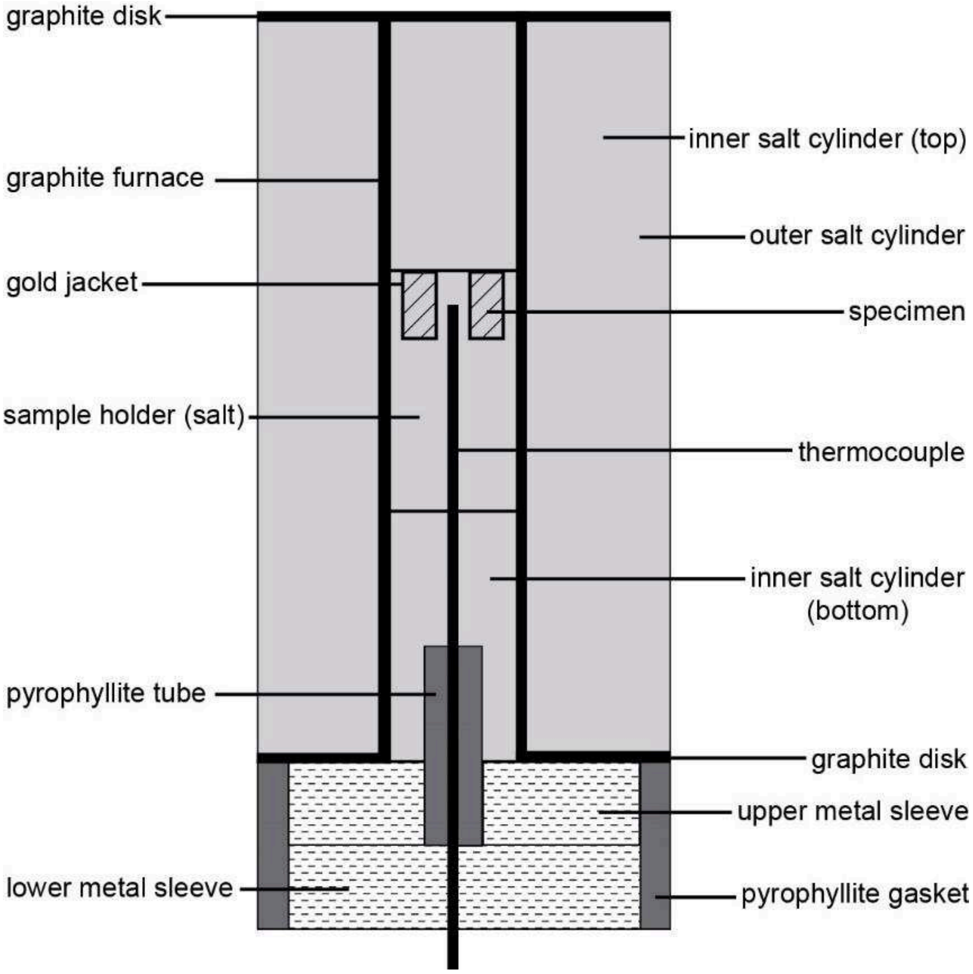

Figure 24: Schematic drawing of the sample assembly used for the hydrostatic piston cylinder experiments (not to scale).

Experimental procedure

To compare the static with the deformed microstructures the Corsican blueschist powder samples was kept at 3 GPa and 823, 923, and 1023 K, respectively, for around 12 h (Table 8). In the case of the Tianshan powder sample the hydrostatic experiment was conducted at 2 GPa and 823 K (Table 8). The tremolite powder was hot-pressed at around 2 GPa and 823 K. First, compression was launched with a compression rate of around 2 MPa/min. After a few MPa were reached heating was started with a heating rate of 10 K/min. The decompression rate was set to 0.5 MPa/min to avoid decompression cracks. The confining pressure was calculated in the same way as for the deformation experiments by multiplying a constant representing the cross-sectional surface ratio of the confining pressure piston and the sample assembly with the oil pressure in the hydraulic ram. The sample abbreviations follows the same principle as used for the deformation experiments, but for the hydrostatic piston cylinder experiments an “h” was added after the powder type.

Table 8: Experimental conditions of the hydrostatic piston cylinder experiments.

Sample	Starting material	Pc [Gpa]	T range [K]	Duration [h]
BSh_3_823	Corsican blueschist bulk rock	3	823	≈ 12
BSh_3_923	Corsican blueschist bulk rock	3	923	≈ 12
BSh_3_1023	Corsican blueschist bulk rock	3	1023	≈ 12
TS-BSh_2_823	Tianshan blueschist bulk rock	2	823	≈ 12
TRh_2_823	Tremolite power	2	823	≈ 12

2.4.2 GRIGGS DEFORMATION EXPERIMENTS

All Griggs experiments presented in this thesis were performed at Ruhr-Universität Bochum Table 9.

Table 9: Griggs experiments on different starting material performed at Ruhr-Universität Bochum.

Sample	Starting material	P_c [GPa]	T range [K]	Strain rate [s^{-1}]	Maximum axial strain [%]
BSd_3_823	drill core CB	3	823	≈ $2\cdot10^{-5}$	≈ 5
BSd_3_923	drill core CB	3	923	≈ $2\cdot10^{-5}$	≈ 5
BSd_3_1023	drill core CB	3	1023	≈ $2\cdot10^{-5}$	≈ 6
BS_2_1023	Bulk rock powder CB	2	823-1023	≈ $2\cdot10^{-5}$	≈ 14
GLN_2_823a	Gln-rich powder CB	2	823	≈ $2\cdot10^{-5}$	≈ 49
GLN_2_823b	Gln-rich powder CB	2	823	≈ $2\cdot10^{-5}$	≈ 21
TS-BS_2_823a	Bulk rock powder TS-BS	2	823	≈ $2\cdot10^{-5}$	≈ 27
TS-BS_2_823b	Bulk rock powder TS-BS	2	823	≈ $2\cdot10^{-5}$	≈ 11

Griggs apparatus at Ruhr-Universität Bochum

Deformation experiments on the Griggs apparatus were conducted at Ruhr-Universität Bochum (Figure 25). Five deformation experiments were performed on either powders of a lawsonite-bearing blueschist from Corsica, France, or on a blueschist from Tianshan, China. Additionally, three deformation experiments on intact drill cores of the Corsican blueschist were conducted at varying temperature conditions but constant pressure conditions. The aim of those deformation experiments was to investigate the rheological behavior of different blueschists, but also to compare the results between intact and powder samples. Another objective was the comparison of the mechanical and microstructural results obtained with a Griggs rig with those using a D-DIA apparatus.

Figure 25: Griggs apparatus at Ruhr-Universität Bochum.

Experimental setup & sample assembly

The solid-medium Griggs apparatus is mainly designed based on the original drawings after Griggs (1960s). The Griggs rig is very similar to a piston cylinder press with the difference that an additional deformation piston can be moved independently to create an anisotropic stress field in the sample (Figure 26). First, both pistons, the confining pressure and the deformation piston, are moved together until the prescribed load is reached. Confining pressure on the sample is generated due to the progression of both pistons, the confining and the deformation piston. During advancement the confining pressure piston crushes a weak solid pressure medium, in most cases salt, surrounding the sample. Then the deformation of the sample can be initialized by further moving the deformation piston to compress the sample.

The cylindrical sample assembly contains several pieces performing both sealing and minimizing of friction (Figures 27; 28). The sample is put in a gold capsule that exhibits one open end, and covered on this side by a 0.25 mm thick gold foil. On top and on the bottom of the sample, nonporous Al_2O_3 pistons are placed. An inner cylinder composed of a phyrophyllite tube, the graphite furnace, and an inner salt cylinder with an inconel sleeve surrounds the sample. Two holes with different lengths were drilled into the pyrophyllite cylinder for the thermocouples. The pyrophyllite cylinder, together with the thermocouples, stabilizes the sample assembly mechanically and also shields the graphite furnace from the outer and inner salt cylinder. Both Ni-CrNi thermocouples are oriented parallel to the sample and placed either on the lower or the upper end of the sample. The lower thermocouple is controlling the automatic temperature system. An inconel sleeve is used to reduce the axial temperature gradient in the sample (Nelson, 1977). The graphite furnace, the graphite disk on top and the metal sleeves provide the electrical connection to allow heating of the sample. The outer and the inner salt cylinders act as solid pressure-medium. Additionally, a layer of loose salt with a thickness of around 2 mm is put on top of the sample to improve the pressure-medium coverage around the sample. Depending on the chemical composition of the salt, its flow behavior can change and influence the precision of the stress determination. It has been shown that the differential stress resolution can be lowered to a few MPa by using specific salt mixtures (Green & Borch 1989, 1990; Gleason & Tullis, 1993; Tingle at al., 1993). A pyrophyllite gasket on the bottom shields the metal sleeves from the pressure vessel. For a homogeneous force distribution, induced by the confining pressure piston, a metal plug composed of an outer Al-tube and an inner Sn-ring is placed on top of a thin Fe-disk. This disk prevents the metal to flow into the furnace to cause sample damage. An upper Al-ring together with the small and the large mitre rings are used to seal the sample assembly. For further details on the apparatus and the sample assembly used, the interested reader is referred to Rybacki et al. 1998.

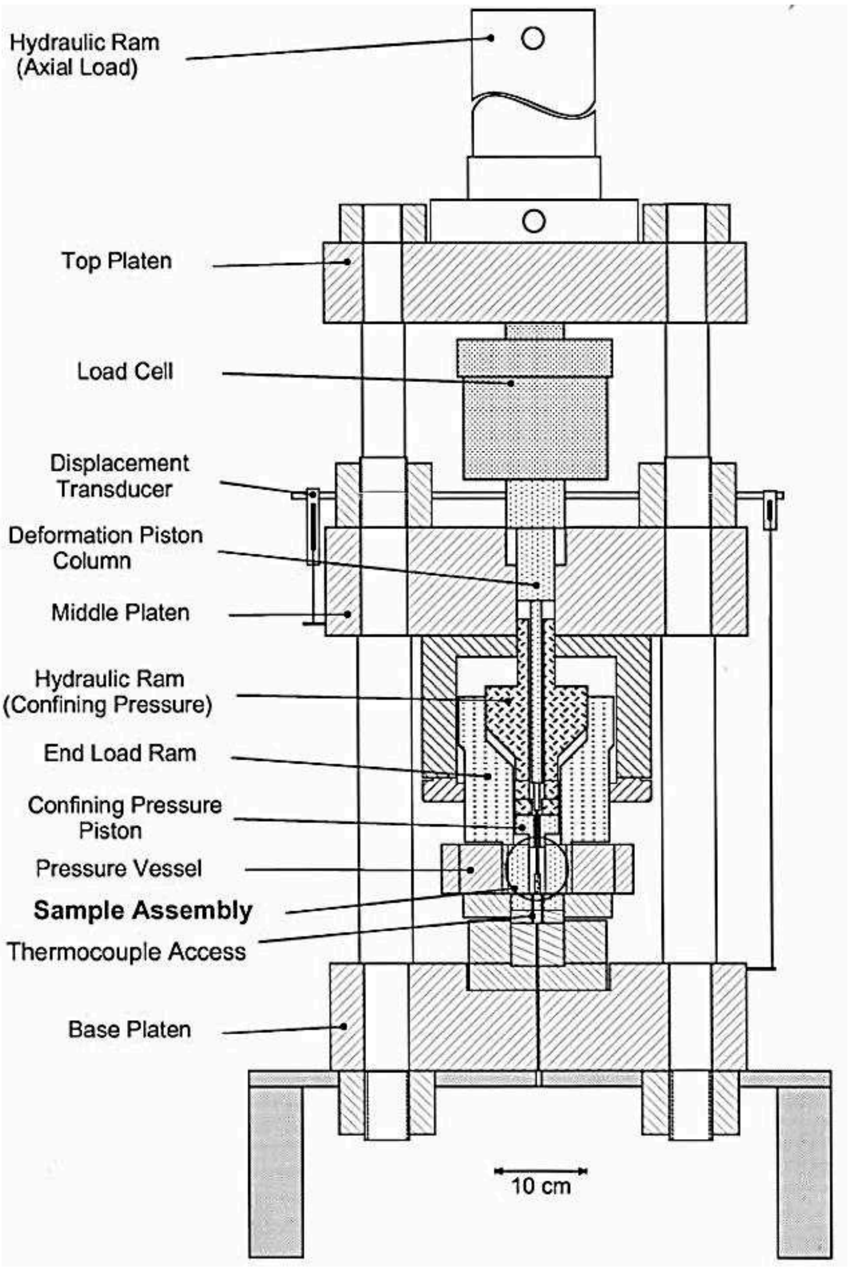

Figure 26: From Rybacki et al. (1998). Schematic drawing of the Griggs apparatus at Ruhr-Universität Bochum

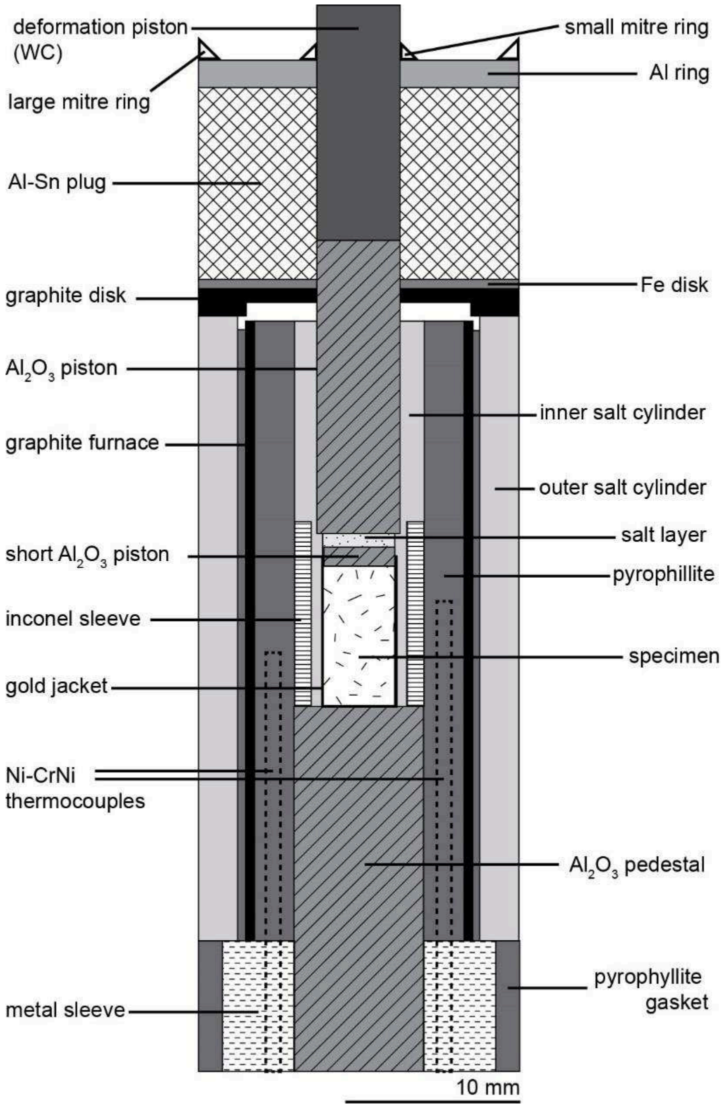

Figure 27: Modified after Rybacki et al. (1998). Drawing of the sample assembly used for the deformation experiments on the Griggs rig.

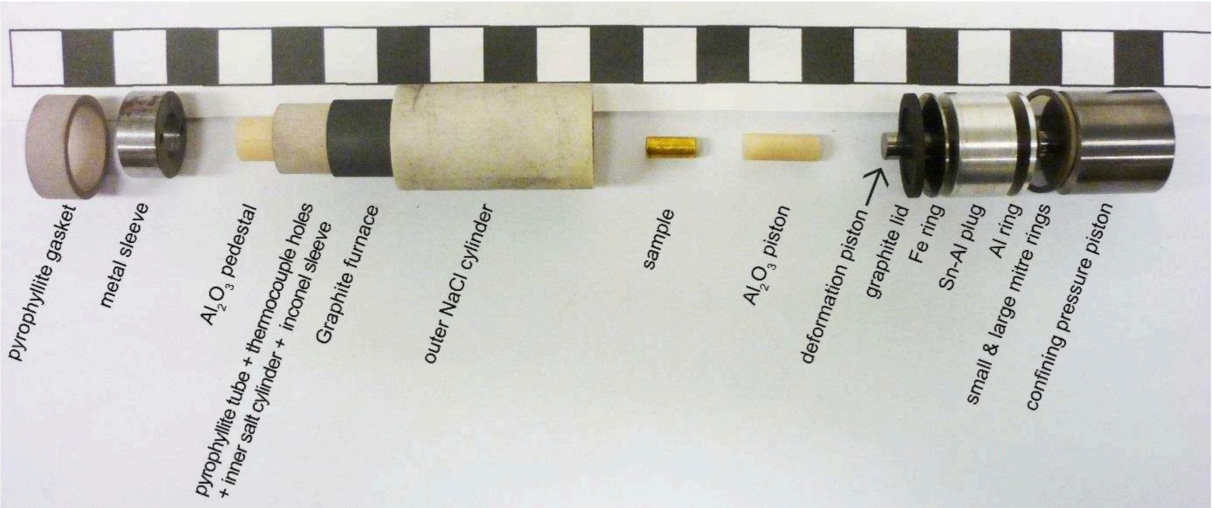

Figure 28: Image of the sample assembly where a combined deformation piston was used for the experiments. The Al_2O_3 was left out for powder experiments conducted under 823 K.

Experimental procedure

In the case of the powder deformation experiments the loose rock powder was filled into a gold capsule and manually pressed for several seconds. The sample height after this cold-pressing was around 9 mm. The sample diameter was with approximately 3.5 mm for all Griggs samples the same. Drill cores were not re-machined and just placed into the capsules. Every deformation experiment was conducted at a constant strain rate of around $2 \cdot 10^{-5}$ s^{-1}.

The compression rate for the runs GLN_2_823a and TS-BS_2_823a was set to 1 MPa/min. Other runs were conducted with a compression rate of 2 MPa/min. After several MPa were reached the heating was launched with a heating rate of 10 K/min to 823 K. The hydraulic ramp for the confining pressure was either stopped at around 62.9 MPa oil pressure which corresponds to a confining pressure of approximately 2 GPa (powder experiments) or at around 94.5 MPa oil pressure corresponding to approximately 3 GPa (drill core experiments). After one hour of hot-pressing deformation was started by applying a constant piston advancement of 1 mm/h. After deformation, the deformation piston was retracted with a constant rate of 1 mm/h to avoid a second hit point of the sample with the deformation piston during decompression. The decompression rate was first set to 1 MPa/min and later increased to 2 MPa/min. Cooling started after deformation was stopped with a rate of 10 K/min. For the run BS_2_1023 a second heating ramp from 823 to 1023 K was programmed with the same rate of 10 K/min. The second syndeformational heating ramp was launched after the yield point of the sample was reached.

For the drill core experiment BSd_3_923, a longer Al_2O_3 piston (Al_2O_3 + WC piston = 16 mm) was used than for the two other drill core runs where a short Al_2O_3 piston was chosen for deformation. The cold powder deformation experiments ($T \leq 823$ K) were all performed using a solid WC piston (16 mm length) instead of a combined Al_2O_3 + WC deformation piston. For the powder deformation experiment BS_2_1023 a combined piston (Al_2O_3 + WC piston = 16 mm length) was chosen again.

Data acquisition & Data treatment

Data acquisition was performed by a program adapted to the system that directly receives the data from the load cell, the pressure cell, the displacement transducers and the thermocouples. This is necessary to detect the hit-point while deforming the sample. For the calculation of the confining pressure and the deviatoric stress on the sample it was assumed, that the sample remains a regular cylinder with constant volume during inelastic deformation. Confining pressure was calculated by multiplying the cross-sectional surface ratio between sample assembly and confining plus deformation pistons with the oil pressure in the hydraulic rams. The axial stress data was measured suing an external load cell. To convert the axial load given in kN to GPa a constant derived from the surface ratio of the deformation piston and the sample was multiplied by the load data. Temperature was recorded directly from the signals of both thermocouples. Axial shortening of the sample was calculated using the data from the displacement transducers. The resolution of the confining pressure and the axial stress from the transducers is around 0.2 MPa and for the axial displacement approximately 0.08 µm. The radial temperature gradient is assumed to lie between 10 and 30 K and the microstructure of the samples after deformation do not show any evidence for a pronounced temperature gradient neither. After the Griggs deformation experiments the data was corrected for the stiffness of the machine and for dynamic friction, the friction between the parts acting parallel to the shortening direction. For the stiffness correction a stiffness test on a dummy Al_2O_3 sample was performed. From that the true displacement or the true deformation of the sample was calculated as

true displacement= measured displacement – stiffness · actual load

with stiffness= length/force.

Dynamic friction can be corrected by first determining the hit-point - the point of first contact between the deformation piston and sample. Then the regression line before the hit-point will be used to correct for dynamic friction by subtracting the displacement-dependent increase in load due to friction from the current load.

2.4.3 D-DIA APPARATUS

Deformation experiments were performed using a deformation multi-anvil (D-DIA) apparatus (Figure 29). This press is located at the GSECARS synchrotron beamline 13-BM-D at the Advanced Photon Source, Argonne National Laboratory, Chicago.

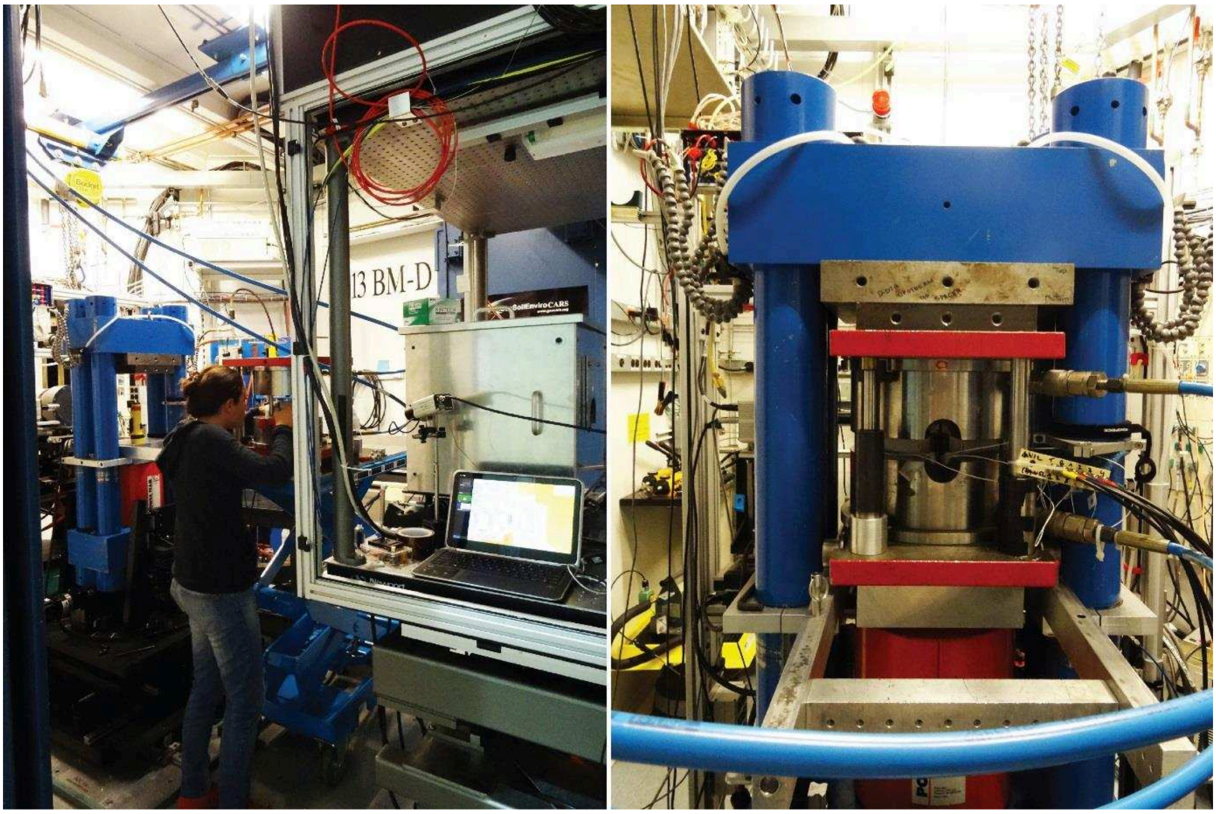

Figure 29: D-DIA apparatus at the Advanced Photon Source (APS) Chicago.

Experimental Setup & sample assembly

During nominal isotropic pressurization, a main ram controls the advancement of four horizontal and two vertical anvils that compress the sample assembly until a prescribed load is reached. Differential rams, which move the vertical anvils independently, create a deviatoric stress field in the sample assembly (Wang et al., 2003). Anvils are made of tungsten carbide (WC), except for two horizontal anvils composed of sintered diamond that are translucent to X-rays. The use of synchrotron X-rays allows for in-situ monitoring of strain, using radiographs of the sample, but also for recording powder diffraction patterns from which phase changes and stress state are deduced (Figure 30). Temperature is inferred from temperature-output power calibrations with an uncertainty below 10 %. Raterron et al. 2013 demonstrated the existence of non-negligible axial temperature gradients of about 155 K/mm with the sample's center colder than the edges.

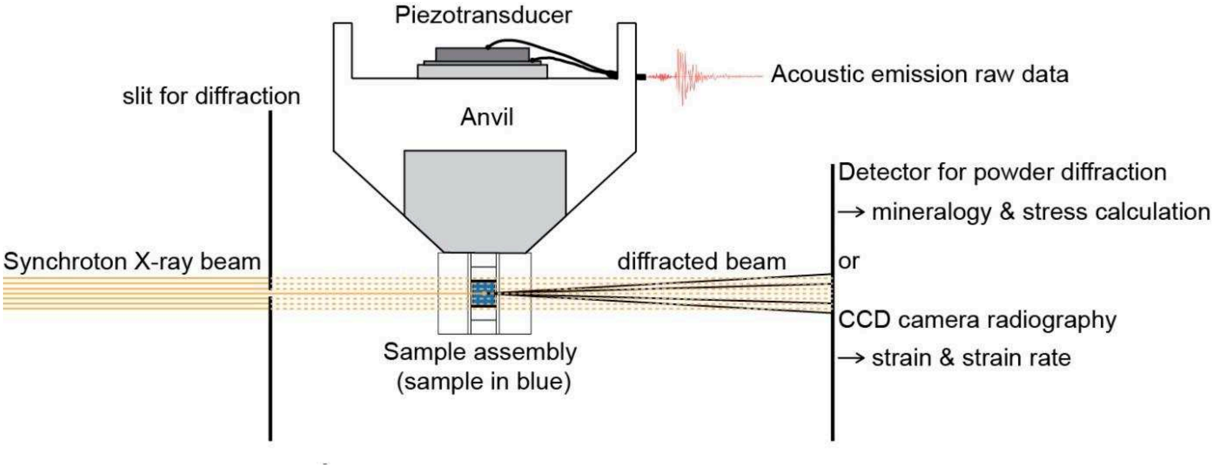

Figure 30: Schematic drawing of the experimental setup for the D-DIA experiments. For the sake of clarity only the upper vertical anvil is shown.

The powder was placed in a cylindrical BN sleeve surrounded by the graphite furnace and placed into 9 x 9 x 8 mm amorphous Boron-epoxy cuboids. The sample is sandwiched between two gold foils and two alumina pistons (Figure 31). The initial size of the powder charge is approximately 2.1 mm in diameter by 3 mm in height. The Corsican blueschist powders were hot-isostatically pressed before triaxial deformation at temperatures of about 583 to 653 K for approximately 1 h. Sample BS_3_1073 was hot-pressed in a piston-cylinder apparatus at 3 GPa and 923 K for 1 day, then machined and loaded in the deformation cell assembly. This sample was kept at isostatic conditions at 583 K in the D-DIA for only 30 min. The granulite bulk rock powder was isostatically hot-pressed at around 994 K also for 1 h prior to deformation. The amphibole powders, tremolite and glaucophane, were also isostatically hot-pressed at either 740 K or 656 K, respectively, for 1 h.

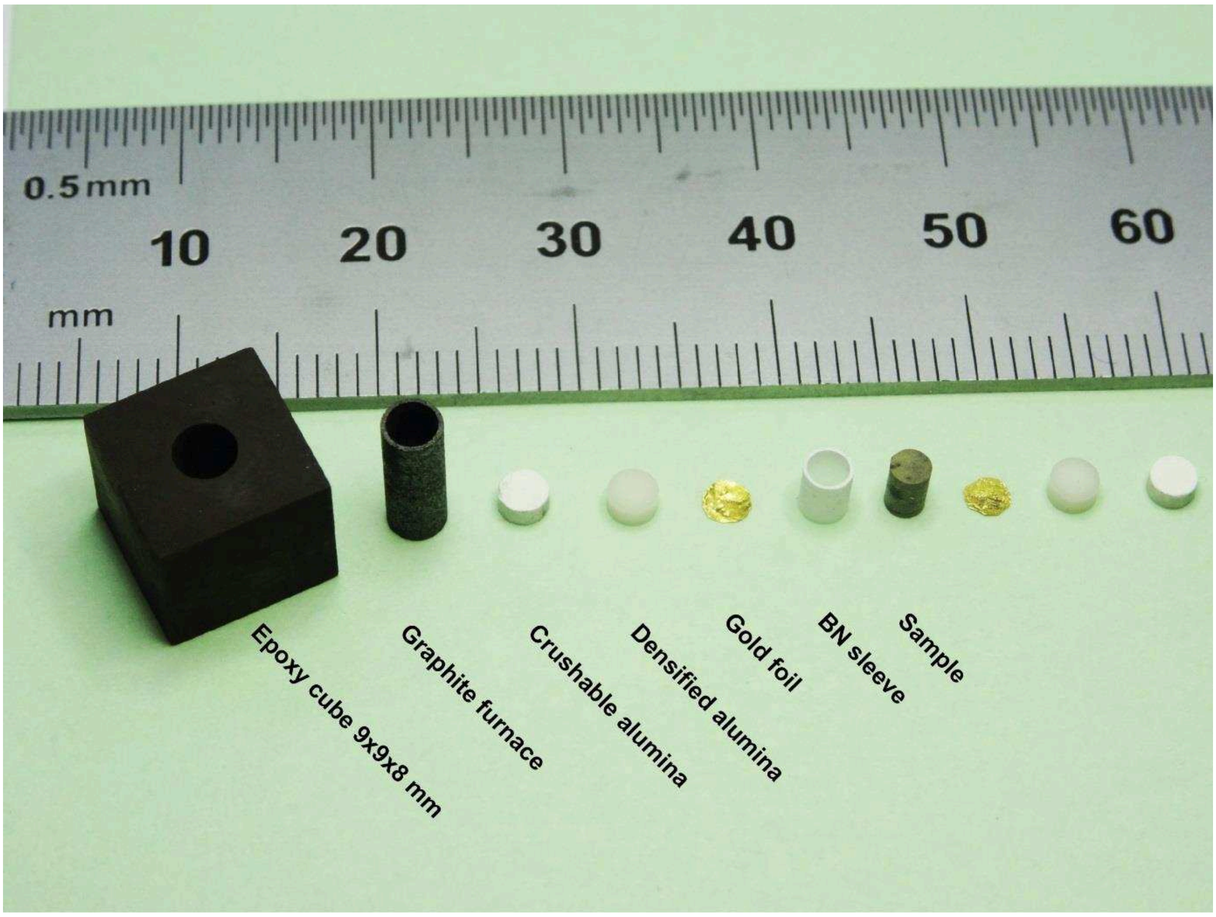

Figure 31: Sample assembly for theD-DIA defomration experiments.

Experimental procedure

Corsican blueschist

After the hot-pressing, deformation with a strain rate of about 10^{-5} s^{-1} was started. Syndeformational heating was performed by increasing the power in steps of 10 W corresponding to a temperature increase of approximately 50 K. The heating steps were initiated at 10, 15, 20, 25, 30, and 35 % strain for the Gln-enriched and the Lws-enriched samples, at 10, 20, 30, and 40 % strain for the run BS_1.5_1121, and at 5, 12, 18, 20, 25, 30, and 35 % strain for the run BS_3_1073.

Granulite

As for the deformation experiments on the different blueschist powders, the granulite bulk rock powder was isostatically hot-pressed at either 2 GPa (NG_2_1225) or at 3 GPa (NG_3_1225) under around 720 K prior to deformation. Heating steps for the run NG_2_1225 were performed at 14 % axial strain from 720 to 1123 K and at 21, and 32 % axial strain in steps of around 50 K. The sample was quenched at a finite axial strain of around 34 % at approximately 1225 K. Sample NG_3_1225 was heated from 720 K at around 14 % axial strain to 1173 K and at 31 % axial strain to 1225 K. The sample was quenched at around 39 % axial strain and 1225 K.

Amphiboles

For both experimental runs either the tremolite or glaucophane powder as starting material was loaded and hot-isostatically pressed for around one h before starting the deformation. The glaucophane powder was hot-pressed at approximately 3 GPa and 656 K and the tremolite powder at around 2 GPa and 740 K. Syndeformational heating for the glaucophane deformation experiment (GLS_3.3_1043) was performed by increasing the temperature from the annealing temperature by around 50 K at 6, 10, 17, 22, and 32 % axial strain. The sample was quenched at approximately 1043 K at a finite strain of about 39 %. The first heating step for the tremolite experiment (TR_2_838) occurred at around 2 % strain from 740 to 750 K and the following steps at 23 % to 790 and at 35 % to 840 K at which it was quenched at about 42 % finite strain.

In situ data acquisition setup, stress and strain computations

The X-ray transmission images and diffraction patterns of the samples were acquired using a monochromatic synchrotron X-ray beam at 13-BMD ($\lambda = 0.2431$ Å, approximately 51 keV) during the course of deformation runs (Figure 32). The typical acquisition time for images was 2 s and for the diffraction pattern 300 s. In image mode, the beam is typically 2 mm x 3 mm, i.e., comparable to initial sample size, and the CCD camera is positioned to capture the radiograph. In diffraction mode, the CCD camera is moved out of the diffraction path and slits reduce the beam size to typically 200 x 200 microns. Therefore, only a limited volume in the center of the sample is probed. The detector tilt and rotation relative to the incident beam were calibrated using the diffraction pattern of a CeO_2 standard and the software Fit2D (Hammersley et al., 1996).

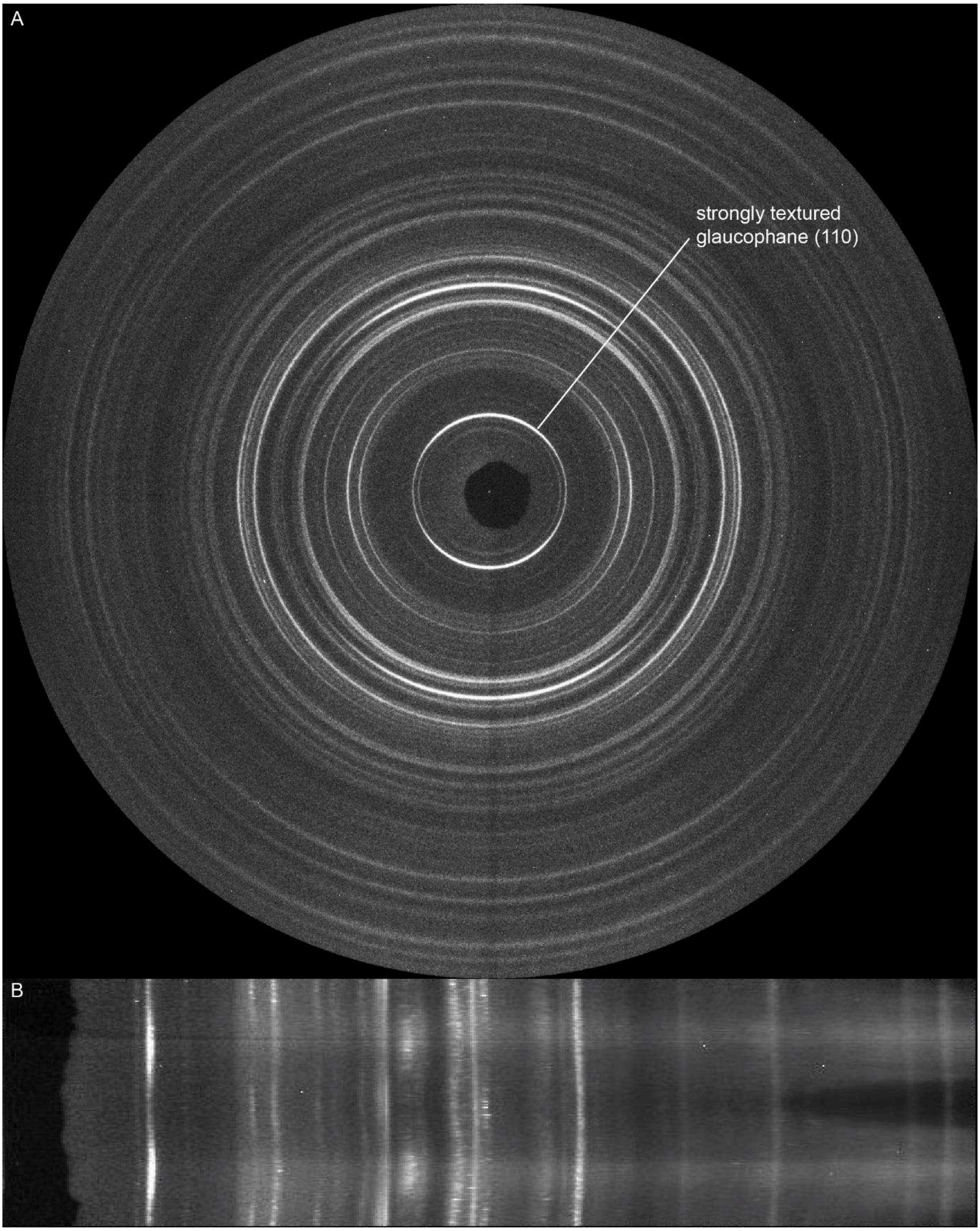

Figure 32: Powder-diffraction pattern of a lawsonite-blueschist powder. A) Debye rings showing strongly textured glaucophane (110). B) Unrolled powder-diffraction pattern.

The d-spacing of a crystal is sensitive to the orientation of the diffracting plane with respect to an anisotropic stress field. For instance, the d-spacing of lattice planes oriented perpendicular to the direction of the maximum principal stress σ_1 decreases and thus the diffraction line shifts to higher 2θ

angles. Therefore, in a powder with random crystal orientations, the different responses of lattice planes to anisotropic stress result in a distortion or pseudo-ellipticity of the Debye rings that are initially circular under hydrostatic conditions. This distortion is called lattice strain and can be used as a proxy for the differential stress effectively acting on the polycrystalline aggregate (Uchida et al., 1996, Singh et al., 1998). The deviation of the diffracting plane normal from the maximum compression axis is characterized by an angle ψ related to the diffraction angle θ according to:

$$\cos\psi = \cos\theta\cos\delta \tag{9}$$

where δ represents the projection of ψ on the detector plane. Calculation of differential stress was performed using Fit2D (Hammersley et al., 1996) and the multifit-polydefix software (Merkel and Hilairet, 2015). The relation between the d-spacing $d_{(hkl)}$ (for a lattice plane with indices hkl) and the lattice strain $Q_{(hkl)}$ reads:

$$\frac{d_{(hkl)}(\psi) - d_{P,(hkl)}(\psi)}{d_{P,(hkl)}(\psi)} = Q_{(hkl)}\left(1 - 3\cos^2\psi\right) \tag{10}$$

(Uchida et al., 1996; Singh et al., 1998) where $d_{P,(hkl)}$ denotes the d-spacing at “hydrostatic” or isotropic stress (used for mean stress calculation) and $d_{(hkl)}(\psi)$ corresponds to the d-spacing of the plane hkl with angle ψ to the maximum principal stress. For each experiment, the d-spacings were extracted from the diffraction pattern and fitted in a $d_{(hkl)}$ over ψ plot.

For the experiments performed on the Corsican blueschist powders the refinement of the lattice strain relied on the $d_{P,(hkl)}$ of up to five crystallographic planes. The planes (110), (-111), and (151) of glaucophane were always used but sometimes also the (-202) and the (240) planes for the processing of experiments on the bulk-rock or the Gln-rich powders. For tests on the Lws-rich powder, the three crystallographic planes (002), (201), and (202) of lawsonite sufficed to refine the unit cell volume. We employed the second-order equation of state for Gln and Lws (Comodi et al., 1991; Mao et al., 2007) and constraints on their thermal expansion (Holland et al., 1996; Jenkins and Corona, 2006). The refinement of the lattice strains of the experimental run performed on the almost pure glaucophane powder obtained from the Syros blueschist relied on the five crystallographic planes (110), (040), (131), (151), and (-202) of Gln. As for the runs performed on the Corsican blueschist powder the same second-order equation of state and the same thermal expansion coefficient for Gln were applied for the calculation. The lattice strain of the tremolite experiments was refined using four different crystallographic planes (020), (110), (-111), and (151) and we employed the second-order equation of state (Comodi et al., 1991) as well as its thermal expansion (Jenkins et al., 1991). For the experimental runs on the granulite bulk rock powder the refinement was conducted using four crystallographic planes

(-201), (111), (-130), (002) of Plg. The second-order equation of state (Angel et al., 2004) and the thermal expansion coefficient (Tribaudino et al., 2010) of albite were employed to obtain the lattice strain values.

Mean stress σ_m is calculated as:

$$\sigma_m = \frac{\sigma_1 + \sigma_2 + \sigma_3}{3} \tag{11}$$

where σ_1 denotes the maximum principal stress, and σ_2 and σ_3 are considered identical to the confining pressure P_c . The confining pressure is determined based on the shift in peak position before and after compression and heating. Differential stress $t_{(hkl)}$ was calculated for a specific plane using the lattice strain $Q_{(hkl)}$ according to (2) and the effective moduli $G_{(hkl)}$:

$$t_{(hkl)} = 6\, Q_{(hkl)} G_{(hkl)}. \tag{12}$$

effective moduli $G_{(hkl)}$ derive from the elastic compliances S_{ij} (inverted from the stiffness matrix C_{ij}) for Gln (Bezacier et al., 2010) and Lws (Mao et al., 2007) for the Corsican blueschist and Syros blueschist experiments. For the tremolite experiment elastic constants of hornblende (Aleksandrov & Ryzhova, 1961) were used because no data on the elasticity of tremolite was found in the literature and since both minerals belong to the calcic-amphibole group. For the granulite experiments the elastic constants of low albite (Brown et al., 2006) were used for the calculation of $t_{(hkl)}$. The differential stress is obtained by averaging the $t_{(hkl)}$ values observed for the two most intense diffraction peaks. For the Corsican blueschist and Syros blueschist runs, these corresponded to the (110) and (151) planes of glaucophane, which were also used to average the differential stress on tremolite, and to the (002) and (201) planes of lawsonite for the Lws-rich experiment. The differential stress on Plg of the granulite experiments was averaged using the (-130) and the (002) crystallographic planes.

The calculated differential stresses do not represent absolute values (see Hilairet et al., 2012, for a detailed discussion). Due to difficulties in calculating the effective moduli for low-symmetry phases like Gln and Plg, the calculation relied on orthorhombic instead of monoclinic symmetry except for the experimental run GLS_3_1043 performed on the almost pure glaucophane powder from the Syros blueschist. The refinement of the lattice strain of this experiments lead to reasonable differential stress values even by applying monoclinic symmetry. For a single experiment (BS_3_1073), it was possible to simultaneously calculate the differential stresses from Gln and Lws crystals. While the calculated differential stresses lie in the same order for the two phases, Lws appears to support more differential stress than Gln, in agreement with previous experimental studies on blueschist rheology (Kim et al., 2013).

Bulk axial strain was determined using the radiographs of the samples. The gold foils on top and below a sample act as strain markers due to their high X-ray absorption contrast compared to the sample and the ceramic pistons. The current length of the sample was determined by measuring the distance between the shadows of the gold foils and strain ε was calculated by comparing the change in sample length, ΔL, with the initial length L before the deformation was started, i.e.:

$$\varepsilon = \frac{\Delta L}{L} \tag{13}$$

Strain rate was calculated by relating the strain to the time increments between radiographs.

Monitoring of mineral reactions using powder-diffraction pattern

The powder-diffraction patterns were also used to continuously monitor the phase assemblage, using diffraction peak heights for individual phases integrated over the 360° of the Debye rings (Figure 32). To plot the diffraction pattern and to estimate the peak height the program Dioptas was used (Prescher et al., 2015). This is a crude estimate and does not take into account the effects of evolution in preferred orientations. To monitor the evolution of the diffraction-pattern during deformation, crystallographic data files (jcpds files) were loaded into the program. Most of these files represent the properties of end-member phases. Though, most of the phases present in the starting materials are solid solutions. The chemical deviation will change the position of the diffraction peaks and will therefore complicate a distinct correlation. Another difficulty that arises is the low crystal symmetry, e.g. amphibole (monoclinic) in blueschist and plagioclase (triclinic) in granulite samples, of most phases present in the powders. Low-symmetry crystals show many diffraction peaks (Figures 33-38) and together with the peaks of the minor and accessory phases this results in many peak overlaps in the powder-diffraction pattern. Increasing temperature will widen the diffraction peaks so that previously distinct peaks may form a peak envelope. Consequentially, the monitoring of peak growth or disappearance is hindered.

The breakdown of lawsonite, triggered at the end of the two lawsonite-blueschist experiments, can easily be observed, because of the two lawsonite diffraction peaks, (002) and (110), do not interfere with intense peaks of other phases (Figure 33).

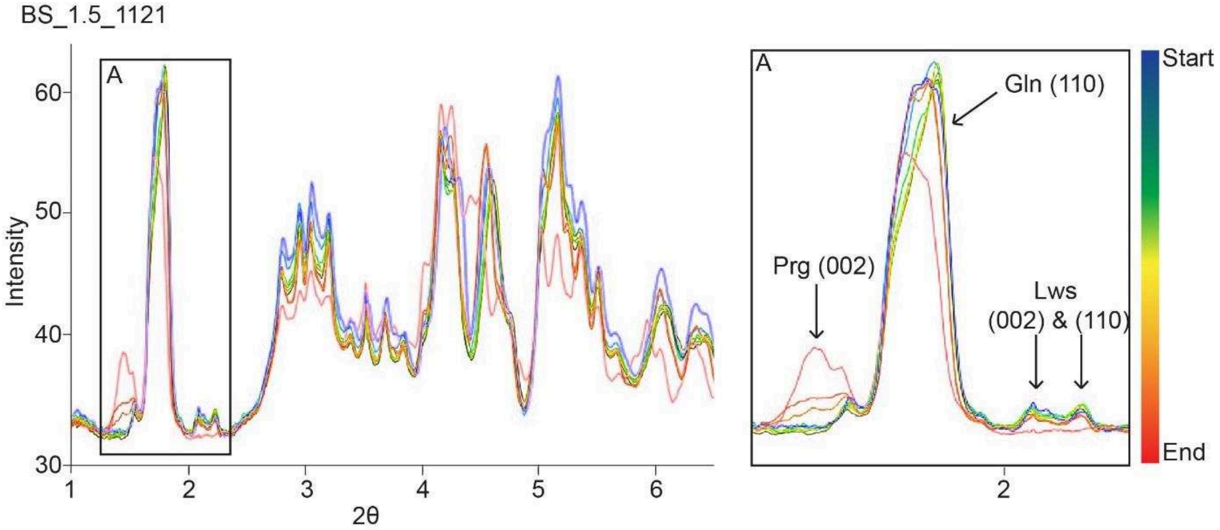

Figure 33: Integrated powder-diffraction pattern of a Lws-blueschist powder (BS_1.5_1121) showing the disappearance of lawsonite.

The eclogitization progress in the blueschist samples and in the almost pure glaucophane sample was followed based on the evolution of the most intense omphacite peak (-221) (Figures 34; 35). However, this peak lies in the vicinity of the glaucophane peaks (310) and (221). This makes it difficult to unequivocally track the evolution of the omphacite (-221) peak. An interesting observation from these diffraction-pattern is the apparent peak shift of the (310) in all the blueschist samples and the glaucophane sample during deformation. All other glaucophane peaks only change their height during the experiment, due to texture evolution or all shift together due to the increase in stress (Figures 34; 35). The (310) peak however shifts towards the position that corresponds to the location of the most intense diffraction peak of omphacite (-221). The same observation can be made on the (240) of glaucophane. This peak lies directly next to a diffraction peak (220) of omphacite (Figures 34; 35). This diffraction peak is less intense and the observable peak shift is also less pronounced relative to that of Gln (310) to Omp (-221).

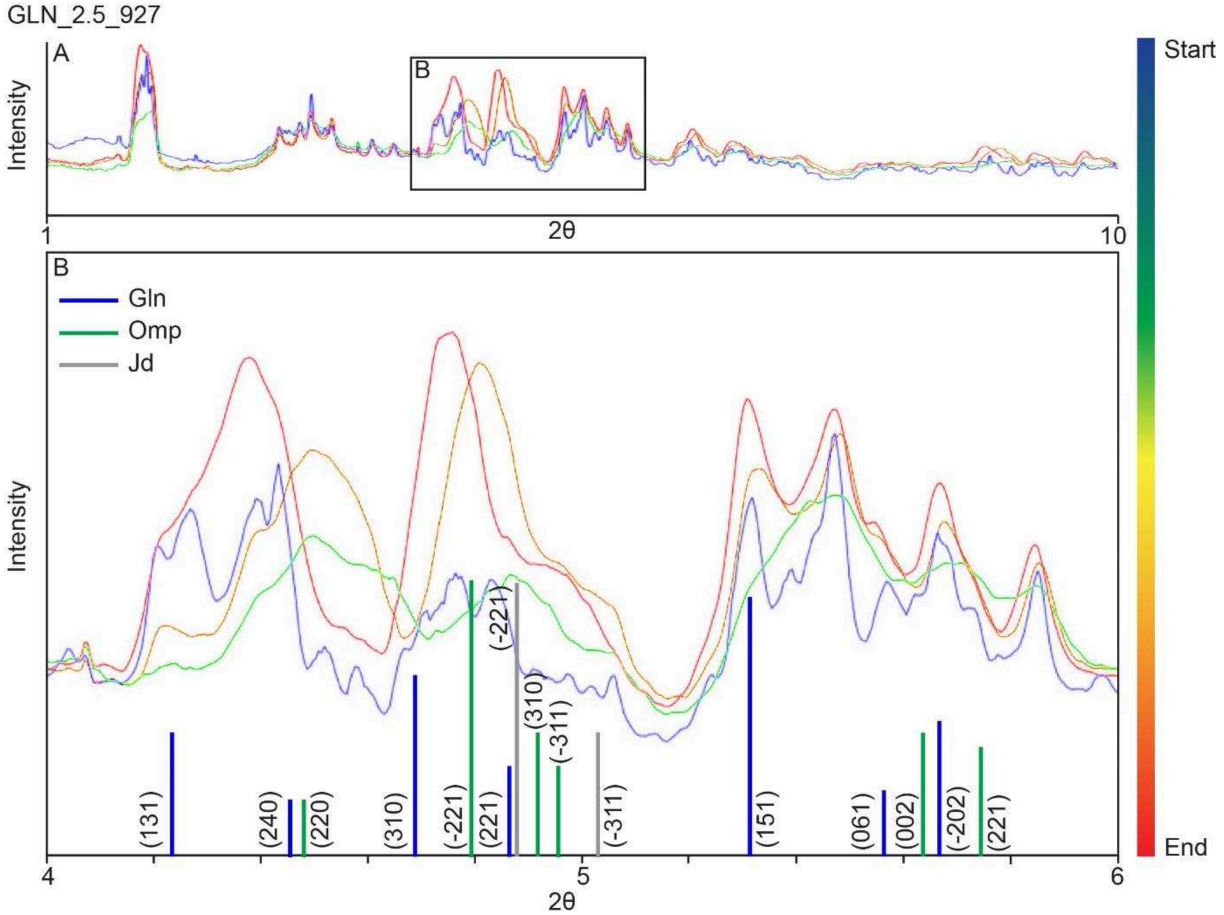

Figure 34: Integrated powder-diffraction pattern of a glaucophane enriched powder (GLN_2.5_927).

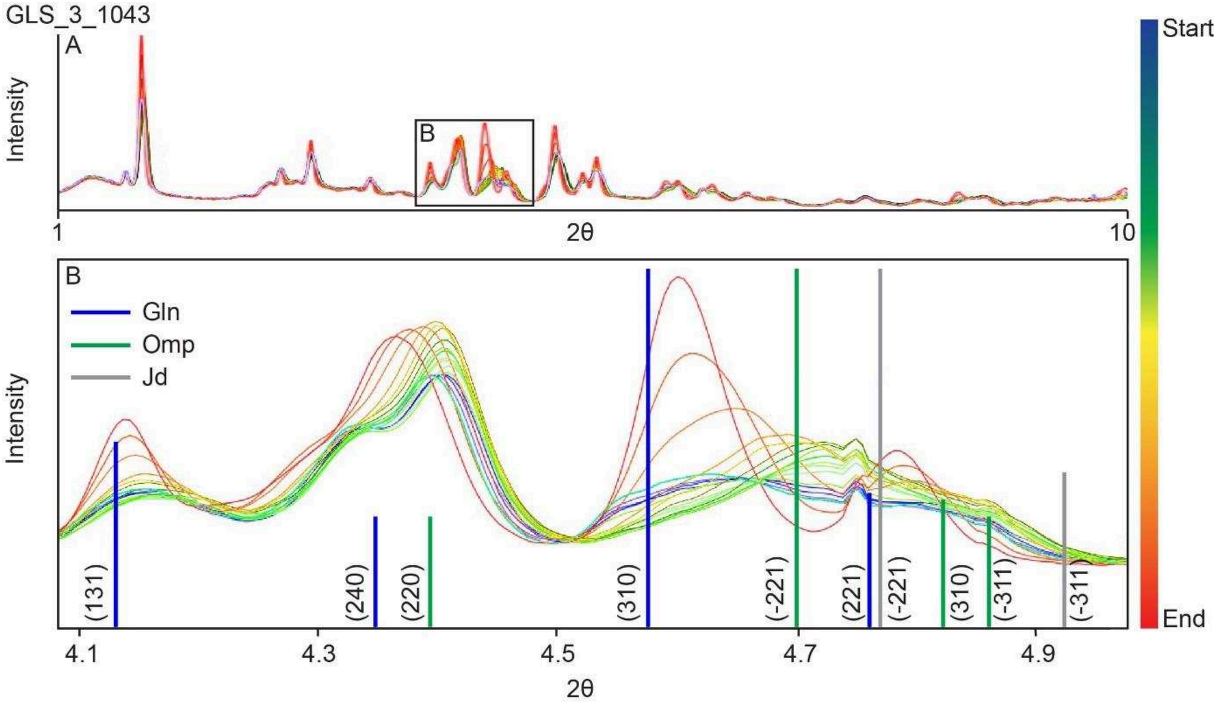

Figure 35: Integrated powder-diffraction pattern of the experiment GLS_3_1043.

For the granulite deformation it was even more difficult to observe peak growth or disappearance, because almost all phases, that are useful for monitoring the eclogitization process, coincide with plagioclase peaks (Figures 36; 37). Although the tremolite sample consists almost exclusively of tremolite the diffraction patterns are very “noisy” which makes it hard to determine the mineralogical evolution during deformation (Figure 38).

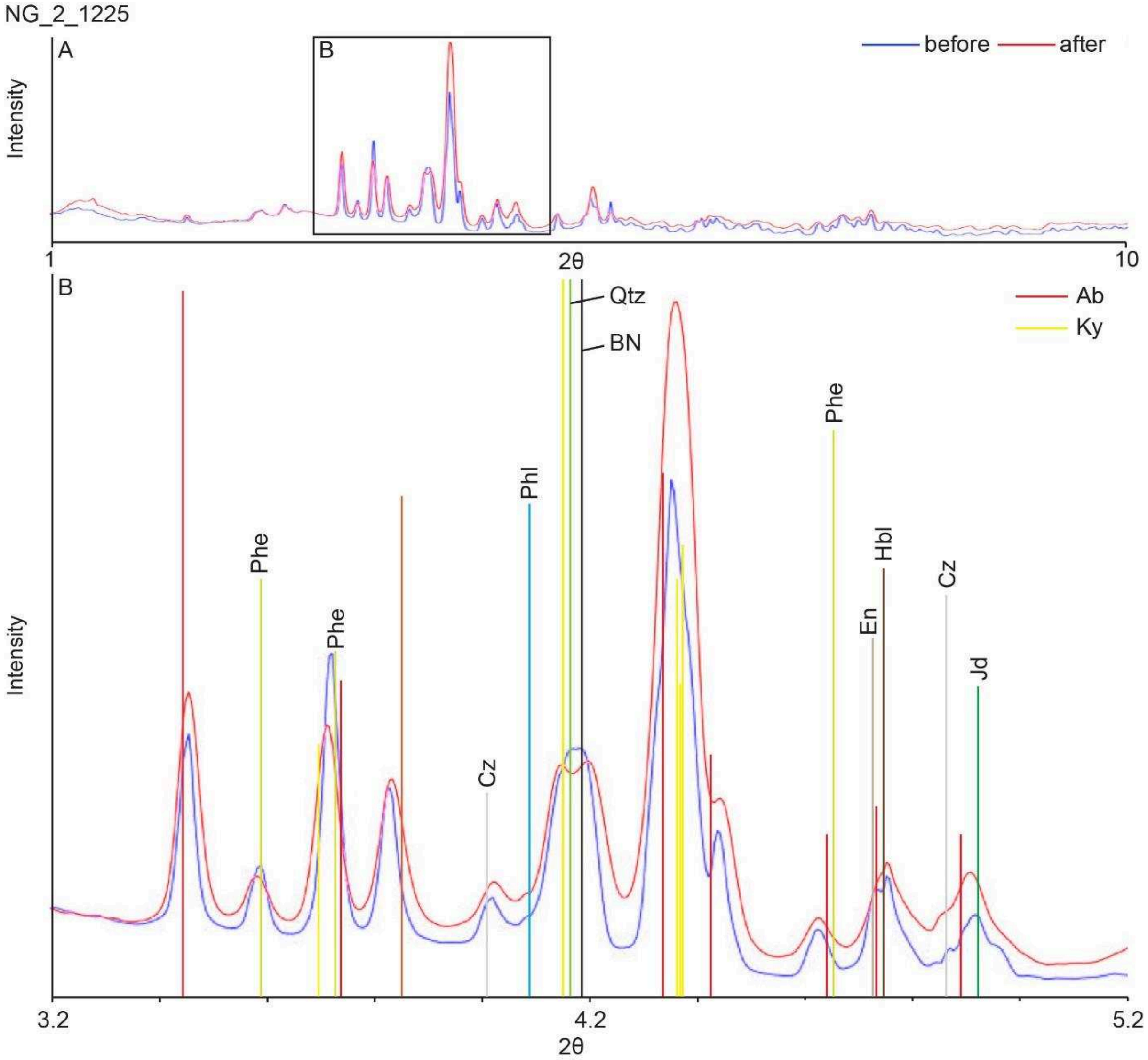

Figure 36: Integrated powder-diffraction pattern of the experiment NG_2_1225 on granulite powder deformed under 2 GPa confining pressure.

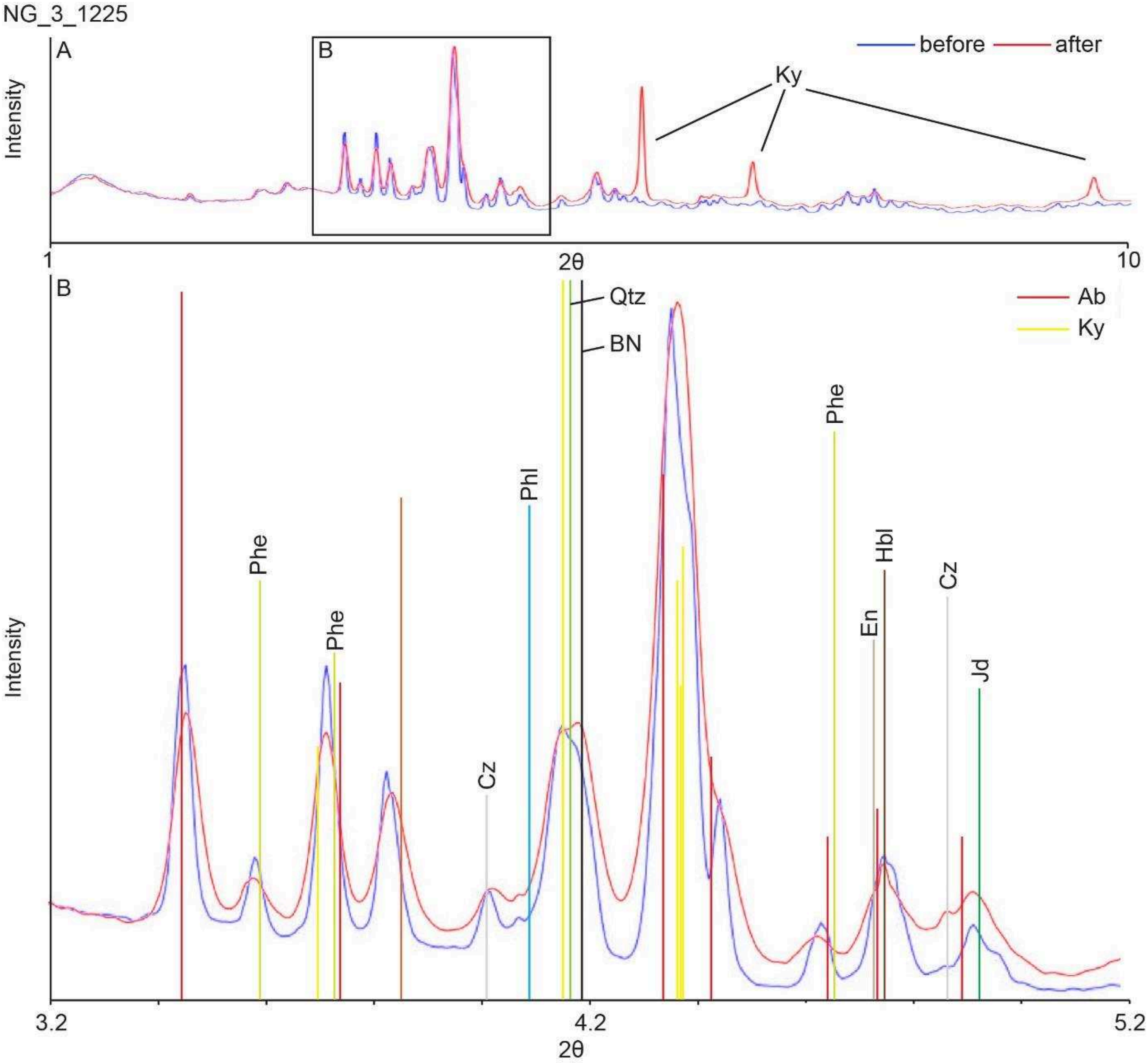

Figure 37: Integrated powder-diffraction pattern of the experiment NG_2_1225 on granulite powder deformed under 2 GPa confining pressure.

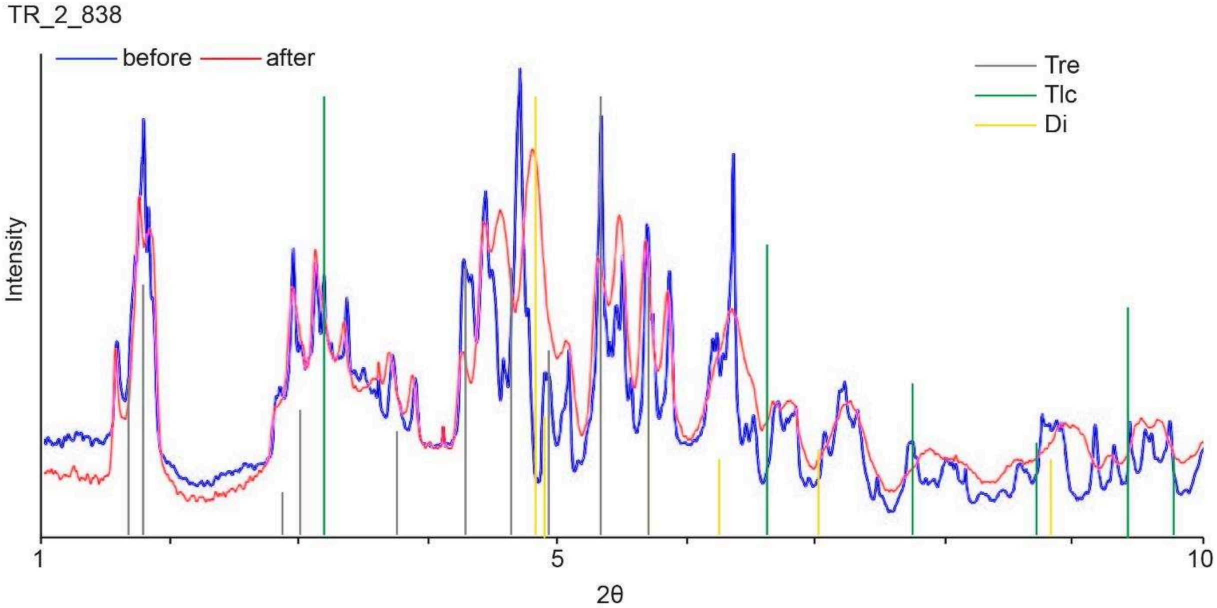

Figure 38: Integrated powder-diffraction pattern of the tremolitite deformation experiment.

Although the in-situ monitoring of the mineralogical evolution based on powder-diffrcation patterns is a very strong and useful tool, this tecnique represents the least reliable method used in this thesis. Therefore, the observations on the powder-diffraction patterns are only useful in conjuction with microstructural observations of the samples before and after the deformation experiments.

Acoustic emission setup and localization technique

Piezoceramic lead-zirconate transducers with a thickness of 0.5 mm, a diameter of 10 mm, and a resonance frequency of 2-4 MHz (see also Schubnel et al., 2013, for details of the setup) were placed behind each of the six anvils (Figures 30; 39). Acoustic emission (AE) waveforms were acquired simultaneously from all six transducers using a multi-channel oscilloscope. Emissions were recorded over the entire duration of each experiment, including cold compression, hydrostatic heating, deformation, and syndeformational heating sequence, then quenching and decompression. In fact, during the first stage of compression many AEs were recorded, which are attributed to powder compaction. From ca. 1 GPa to the final confining pressure (Table 10), no further AEs were recorded demonstrating that the AEs subsequently recorded during triaxial deformation are not caused by the compaction. Furthermore, previous deformation experiments with the same acoustic setup and the same sample assembly (Gasc et al., 2011) demonstrated that except for the porous alumina, deformation of the cell materials does not result in AEs, thus excluding the assembly as a cause for the AEs recorded in the present study.

Figure 39: Custom-made acoustic emission sensor used for the deformation experiments at the APS Chicago.

Locations of AEs were determined using a constant P-wave velocity of 8000 m/s determined by previous experiments with the same experimental setup (Schubnel et al., 2013). It is assumed that the travel time within each anvil remains constant over the course of an experiment. The travel time in the sintered diamond anvils was calculated to be 0.78 µs lower than in the WC anvils. Picking of the first arrivals was performed manually as the total number of AEs recorded during deformation was limited. The travel time was first corrected for anvil type, then the difference in arrival times between each pair of facing anvils was interpreted as a difference in travel-time within the sample assembly. The precision of the location of AEs along each of the three axis between the 3 anvil pairs lies within the sensor thickness of around 0.5 mm. The exact localization of each hypocenter in the sample would require a more sophisticated AE data analysis which lies beyond the scope of the presented thesis. Event localization together with the polarization of the event made it also possible to determine the source mechanism by using the software InSite. In this thesis these data are presented in so called k-T plots where T stands for the isotropic and k for the deviatoric component of the recorded event. The experimental conditions of all D-DIA experiments performed are listed below in Table 10.

Table 10: Experimental conditions of the all D-DIA experiments.

Sample	Experiment #	Starting material	P_c [GPa]	T range [K]	Strain rate [s^{-1}]	Maximum strain [%]
BS_3_1073	D1616	BS-bulk	3	583-1073	$4\cdot10^{-5}$	40
BS_1.5_1121	D1661	BS-bulk	1.5	649-1121	$7\cdot10^{-5}$	42
GLN_3.5_948	D1655	Gln-rich	3.5	659-948	$1\cdot10^{-5}$	42
GLN_2.5_927	D1618	Gln-rich	2.5	654-927	$2\cdot10^{-5}$	43
GLN_2.5_762	D1807	Gln-rich	2.5	656-762	$4\cdot10^{-5}$	37
LWS_2.5_925	D1667	Lws-rich	2.5	656-925	$3\cdot10^{-5}$	40
NG_2_1225	D1810	NG-bulk	2	994-1225	$6\cdot10^{-5}$	34
NG_3_1225	D1811	NG-bulk	3	994-1225	$5\cdot10^{-5}$	36
TR_2_838	D1621	Tr-powder	2	740-838	$5\cdot10^{-5}$	42
GLS_3_1043	D1815	Gln-powder	3	656-1043	$3\cdot10^{-5}$	39

2.5 ANALYTICAL METHODS

For the microstructural analyses the samples were cut, polished and carbon coated. For the Raman spectroscopy this coating was removed.

2.5.1 Scanning electron microscopy

Qualitative chemical analysis and most of the microstructural analysis were performed on a Zeiss Sigma field-emission scanning electron microscope (FE-SEM) at Ecole Normale Supérieure Paris. The applied accelerating voltage was set to 15 kV. To resolve small structures with the granulite samples the accelerating voltage was lowered to 10 kV for the element distribution maps. Every presented image was taken in backscattered electron (BSE) mode.

2.5.2 Electron microprobe analysis

The quantitative chemical and microstructural analysis were conducted using a Jeol JXA 8200 Superprobe at the Geocampus in Berlin, Germany, and a Cameca SX 100 at the Institut des Sciences de la Terre at Université Pierre et Marie Curie Paris, France. For the electron microprobe analysis (EMPA) an acceleration voltage of 15 kV was set, which corresponds to a current of around 20 nA on the sample surface.

2.5.3 Transmission electron microscopy

To investigate the nanostructure of selected samples thin Focused Ion Beam (FIB) sections were cut in the TEM:FIB laboratory at the GeoForschungsZentrum Potsdam, Germany, and using a FEI Strata

DB 235 at IEMN at the University of Lille, France. The TEM analyses were performed on a JEM 2011 at the Laboratoire de réactivité de surface at Université Pierre et Marie Curie Paris, France. Every image presented in this study was taken in bright field (BF) mode with an acceleration voltage of 200 kV.

2.5.4 Raman spectroscopy

Raman spectroscopy was performed on a Renishaw inVia Raman Microscope at Ecole Normale Supérieure Paris. The analyses were conducted by using a Cobalt 514 nm laser.

> "Man kann auf seinem Standpunkt stehen,
> aber man sollte nicht darauf sitzen."
> - *Erich Kästner*

III ECLOGITIZATION OF BLUESCHIST

The motivation behind the study on blueschist samples, forming this chapter, was to experimentally investigate if and how metamorphic reactions during eclogitization of blueschist have an influence on the formation of intermediate-depth seismicity in subduction zones. These experiments are of particular interest to test the hypothesis of dehydration embrittlement as viable mechanism to trigger earthquakes in the oceanic crust. A recently published study demonstrated that the dehydration of almost pure lawsonite samples under deviatoric stress can cause faulting under high pressure accompanied by acoustic emissions (Okazaki & Hirth, 2016). However, there is no natural rock equivalent that exclusively contains lawsonite. Therefore, this chapter presents deformation experiments on different blueschist samples with varying amounts of hydrous phases in order to decipher the influence of the liberation of water on faulting under high-pressure conditions.

3.1 EXPERIMENTAL RESULTS

3.1.1 Hydrostatic piston cylinder experiments

Microstructural & chemical analysis

The microstructure of the experiment conducted at 3 GPa and 823 K reveals that much more omphacite is present in the sample compared to the starting material (Figures 40; 41a-c). Omphacite can be found as rims around glaucophane grains and as patches at glaucophane grain junctions (Figure 41b; c). After 3 GPa and 923 K the sample shows even more omphacite forming coronas around glaucophane (Figure 41d-f). The sample microstructure after 1023 K shows a completely different phase assemblage compared to the starting material (Figure 41g-i). There is no lawsonite left and most of the glaucophane was consumed during omphacite growth. Larger garnet crystals clearly show a brighter core and a darker rim (Figure 41h, i). The BSE contrast of the garnet coronas correlates very well with the contrast of smaller and sometimes idiomorphically shaped garnet crystals implying a similar chemical composition (Figure 41h, i). Kyanite and quartz can also be found in the sample, which were absent in the starting material. Relative to the two other experiments performed under 823 and 923 K, respectively, the sample also shows many more pores between the crystals.

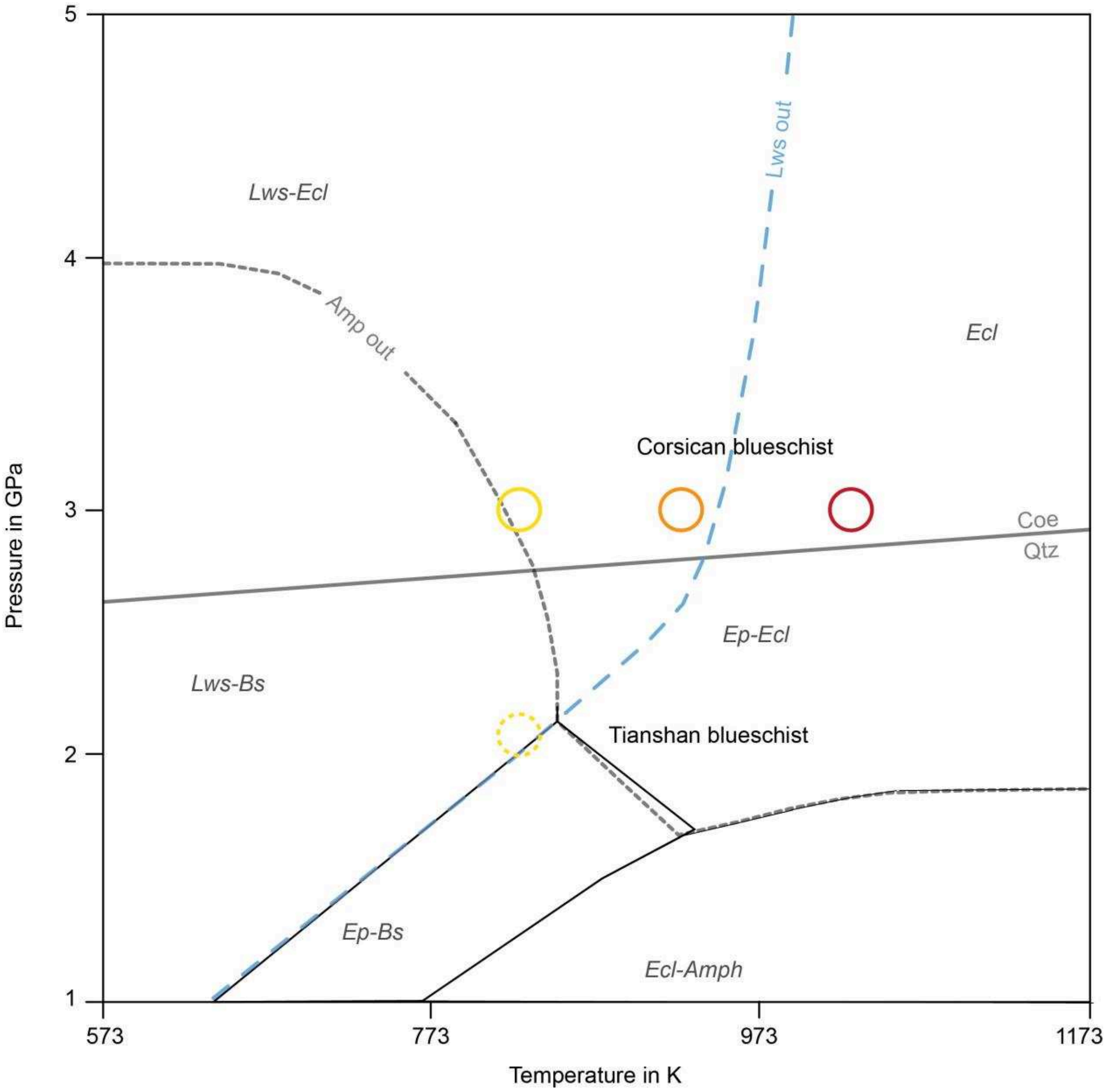

Figure 40: Experimental conditions of the hydrostatic piston cylinder experiment performed using the Corsican blueschist and the Tianshan powders.

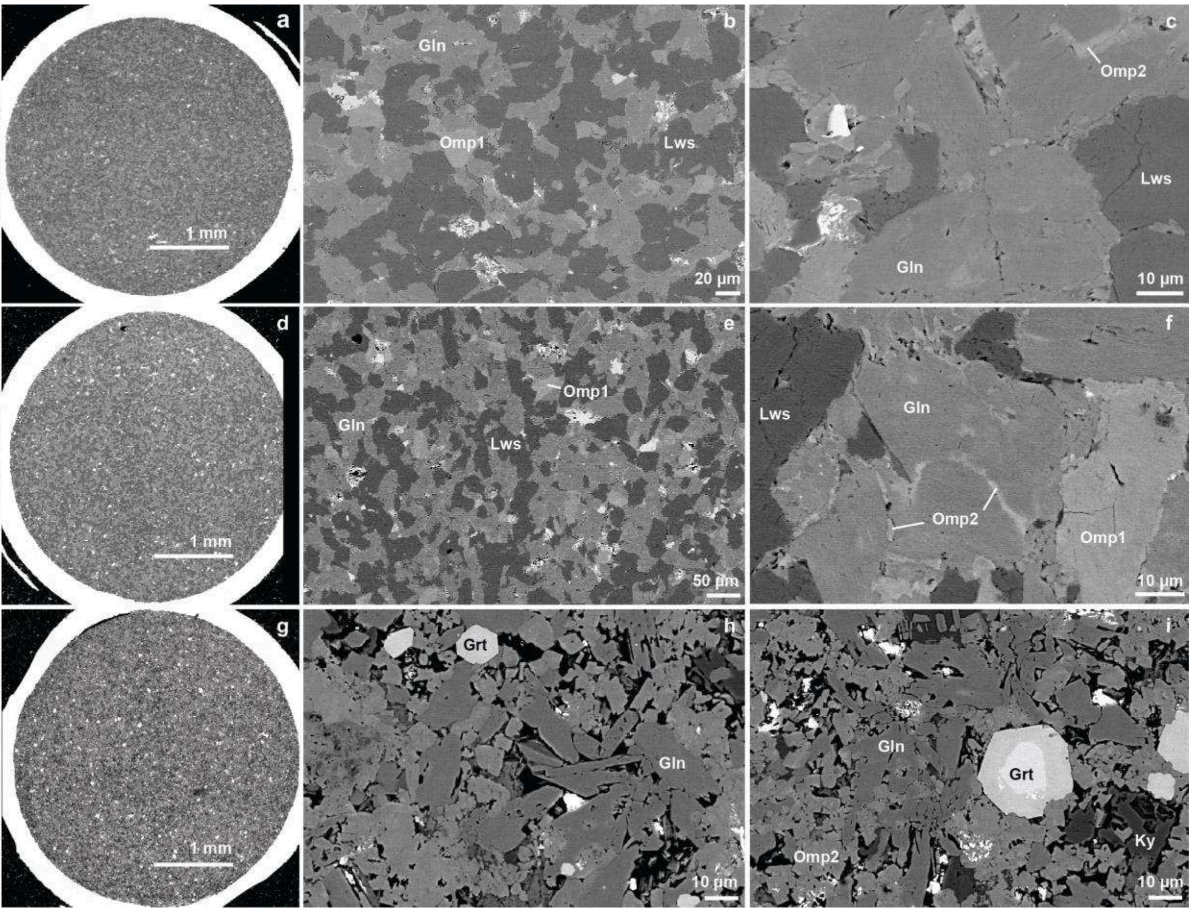

Figure 41: Three different piston-cylinder experiments, performed at 3 GPa and 823 K, 923 K, and 1023 K respectively. The bulk-rock powder of the natural Lws-blueschist was used as a starting material. The BSE images of the samples clearly demonstrate the proceeding eclogitization of the Lws-blueschist with increase in temperature. The powder, hot-pressed at 823 K (a-c) shows only few newly grown omphacite rims around Gln grains. In the run at 923 K the growth of Omp as coronas around Gln is even more advanced. In both runs lawsonite was still stable. The experimental run at 1023 K (g-i) shows no more lawsonite, but the eclogite-facies mineral assemblage omphacite and garnet. The porosity increase due to the denser mineral assemblage of eclogite is also visible (g-i). No evidence for an amorphous material was found in any sample.

After the experiment the microstructure of the sample conducted using the Tianshan powder shows no microscopic difference relative to the starting material. All phases were stable under the applied experimental conditions (Figure 42).

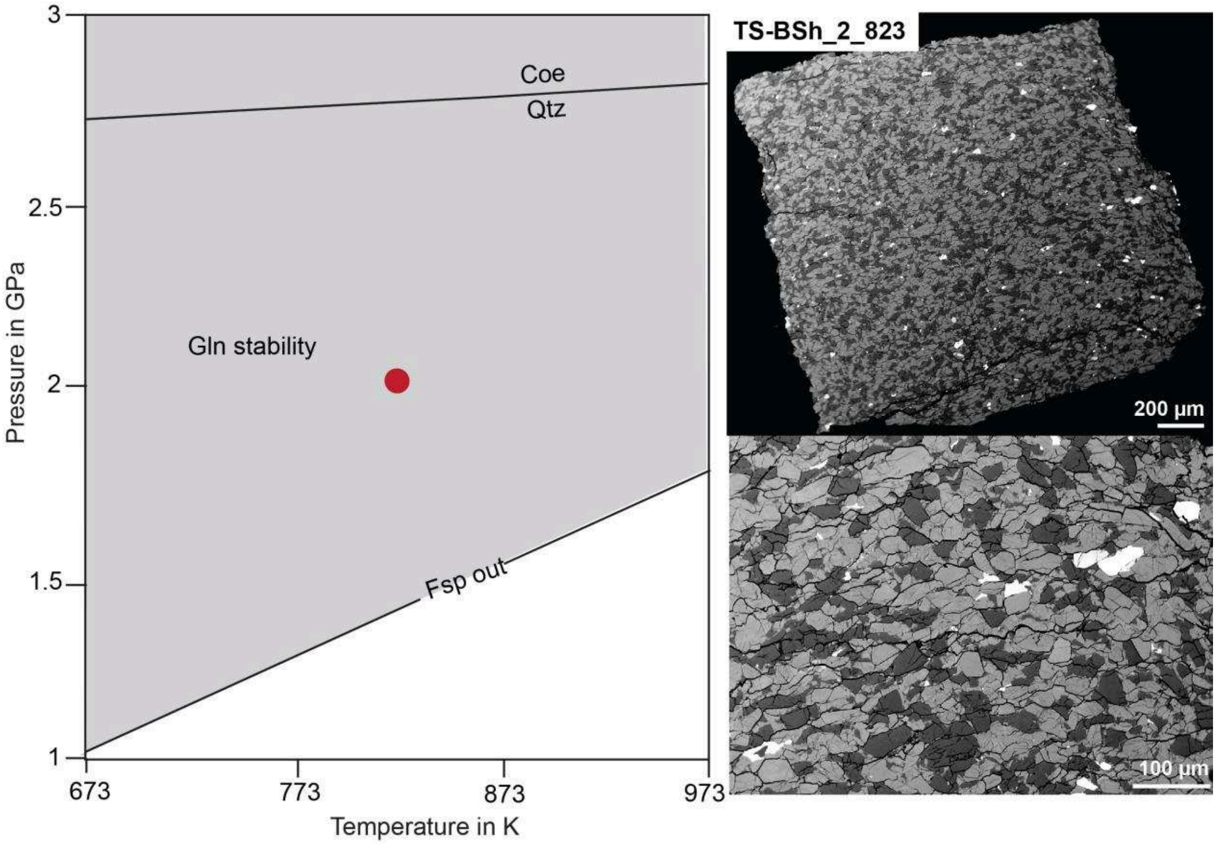

Figure 42: P-T pseudotsection of the bulk rock blueschist from Tianshan (bulk rock chemistry from KLemd et al., 2015) and microstructures of the Tianshan bulk rock powder after a piston cylinder experiment performed under 2 GPa and 823 K for around 12 h.

3.1.2 DEFORMATION EXPERIMENTS

Griggs deformation experiments

Mechanical data

All Griggs deformation experiments using a powder as starting material were conducted at a confining pressure of around 2 GPa and the runs on the drill cores at 3 GPa. The experimental conditions of each experiment are listed below in Table 11.

Table 11: Sample, starting material and experimental conditions of the Griggs deformation experiments. CB= Corsican blueschist; BSd= drill core sample; GLN= glaucophane enriched powder; BS= bulk rock powder; TS-BS= Tianshan blueschist

Sample	Starting material	P_c [GPa]	T range [K]	Strain rate [s^{-1}]	Maximum axial strain [%]
BSd_3_823	drill core CB	3	823	$2 \cdot 10^{-5}$	≈ 5
BSd_3_923	drill core CB	3	923	$2 \cdot 10^{-5}$	≈ 5
BSd_3_1023	drill core CB	3	1023	$2 \cdot 10^{-5}$	≈ 6
BS_2_1023	Bulk rock powder CB	2	823-1023	$2 \cdot 10^{-5}$	≈ 14
GLN_2_823a	Gln-rich powder CB	2	823	$2 \cdot 10^{-5}$	≈ 49
GLN_2_823b	Gln-rich powder CB	2	823	$2 \cdot 10^{-5}$	≈ 21
TS-BS_2_823a	Bulk rock powder TS-BS	2	823	$2 \cdot 10^{-5}$	≈ 27
TS-BS_2_823b	Bulk rock powder TS-BS	2	823	$2 \cdot 10^{-5}$	≈ 11

Based on the stress-strain curves some of the samples show evidence of brittle failure (Figure 43). The curves of the experiments on the intact drill core samples BSd_3_823, BSd_3_923, and BSd_3_1023, which are all performed under P_c= 3 GPa and different temperatures only exhibit elastic loading (Figure 43). Almost all powder experiments (GLN_2_823a, GLN_2_823b, BS_2_1023, and TS-BS_2_823a), performed under a confining pressure of 2 GPa, show strain softening but TS-BS_2_823b. Here the axial load limit of around 80 kN was reached at approximately 11 % strain (Figure 43). A little bump in the stress-strain curves may derive from the compaction of the salt layer on top of the sample (black arrow in Figure 43). Run BS_2_1023 was not kept under a constant temperature during deformation but heated up to 1023 K as the yield point was reached at around 4 % axial strain (grey arrow in Figure 43).

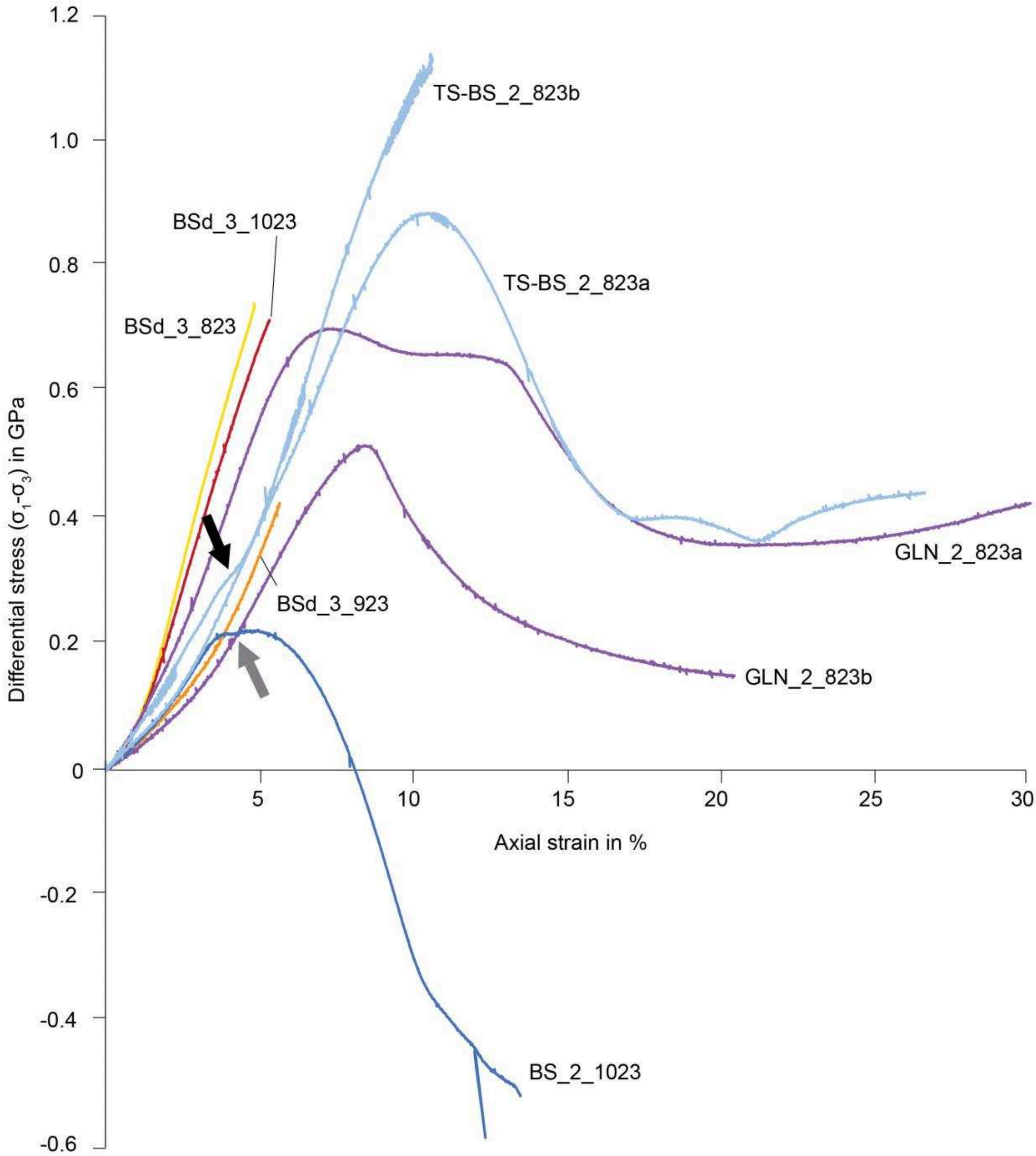

Figure 43: Differential stress over axial strain curves for the Griggs experiments. Different colors of the curves reflect different starting material. Violet: experiments performed on glaucophane enriched Corsican blueschist powder; dark blue: experiments on bulk rock powder of the Corsican blueschist; light blue: experiments conducted on bulk rock powders of the Tianshan blueschist, Yellow, orange, and red: experiments on intact drill core samples of the Corsican blueschist (yellow= 823 K, orange= 923 K, red= 1023 K). Black and grey arrows: see text for explanation

Microstructural and chemical analysis

Drill core experiments under 3 GPa

In the following, the direction of axial load is always oriented perpendicular to the top and bottom edges of each image. Under an optical microscope the drill core samples BSd_3_823 and BSd_3_923 exhibit structures similar to fractures cutting diagonal through the samples (Figure 44A, B). In the sample BSd_3_823 they appear whitish and in the sample BSd_3_923 darker compared to the host rock. The drill core sample deformed under the highest temperature of 1023 K shows no such structures but a band composed of reddish and green minerals (Figure 44C). Back-scattered electron images from the SEM demonstrate, that the whitish structures in BSd_3_823 are fractures cutting through the sample (Figure 45A). The overview image of the sample BSd_3_923 reveals no clear microscopic strain localization (Figure 45F). Horizontal cracks due to decompression are cutting through the sample BSd_3_1023 (Figure 45K). White rectangles indicate the location of different higher magnification micrographs (Figure 45) which allow closer view of the samples' microstructures.

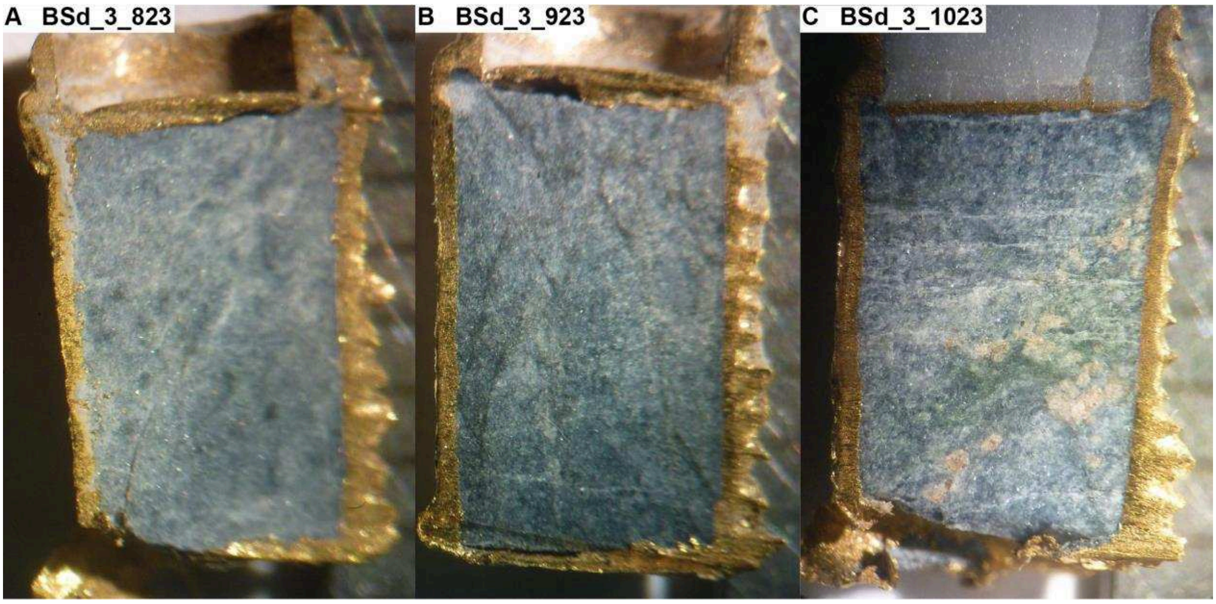

Figure 44: Optical microscopy images of the drill core samples after deformation. A) P_c= 3 GPa, T= 823 K; B) P_c= 3 GPa, T= 923 K; C) P_c= 3 GPa, T= 1023 K. The strain rate was constant during each experimental run with around $2 \cdot 10^{-5}$ s^{-1}.

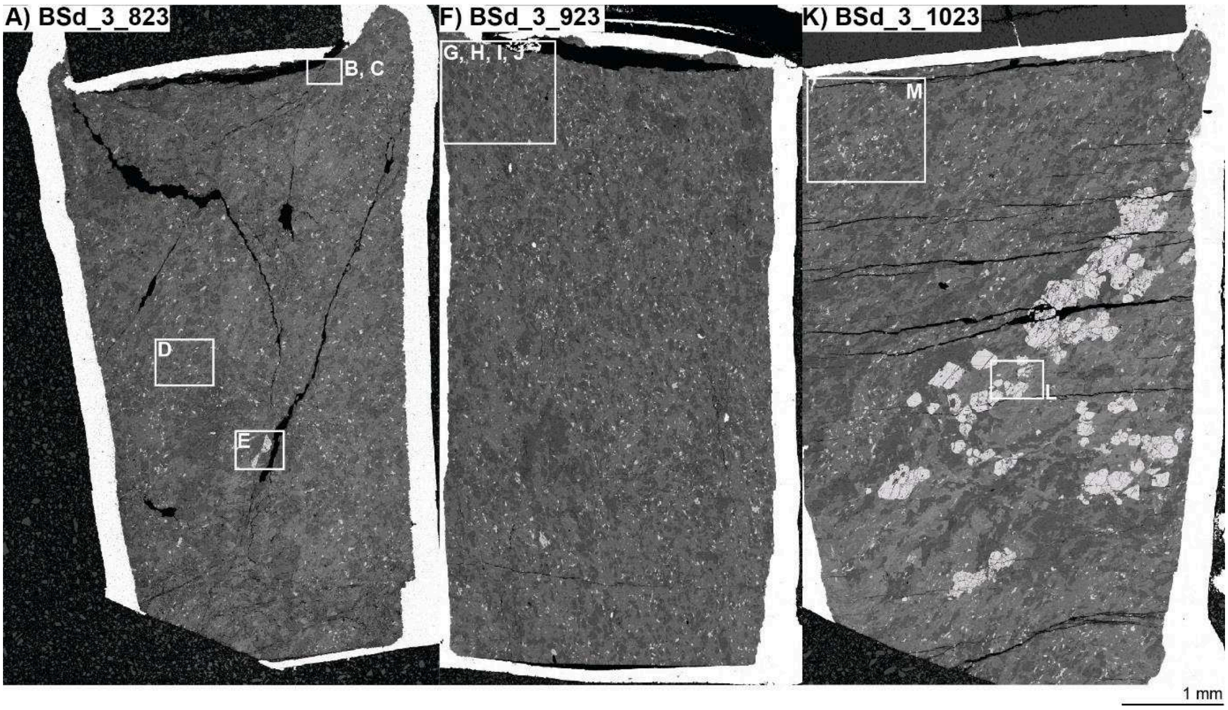

Figure 45: BSE images taken at the SEM showing the drill core samples in the same order as in Fig. The white rectangles exhibit the locations selecetd for higher magnification micrographs. Sample BSd_3_823 has fractures cross-cutting the entire sample. These structures are absent in the samples deformed under higher temperatures of 923 and 1023 K. Sample BSd_3_923 does not show microstructural evidence for strain localization under this magnification. BSd_3_1023 exhibits several horizontal cracks due to decompression and a wide band formed by brighter crystals.

Four BSE images show the microstructure of the sample BSd_3_823 (Figure 46). This experiment was conducted within the lawsonite stability field, but outside the calculated amphibole stability field (yellow circles Figure 47). The microstructure shows no evidence for the breakdown of lawsonite, which confirms that lawsonite stayed stable during deformation. Glaucophane grains also do not show microscopic evidence for decomposition during deformation. In Figure 46B, C, and E different magnification of fractures are shown demonstrating flow-like structures of the minerals at their borders. Compared to areas, which are not cross-cut by fractures (Figure 46C) the amount of omphacite is much higher in the vicinity of the fractures and can often be found directly along the fractures (Figure 46C, E). Figure 46E exhibits a narrow fault that dissects and displaces a garnet crystal. This narrow fault is oriented parallel to a larger fracture, cross-cutting the entire sample.

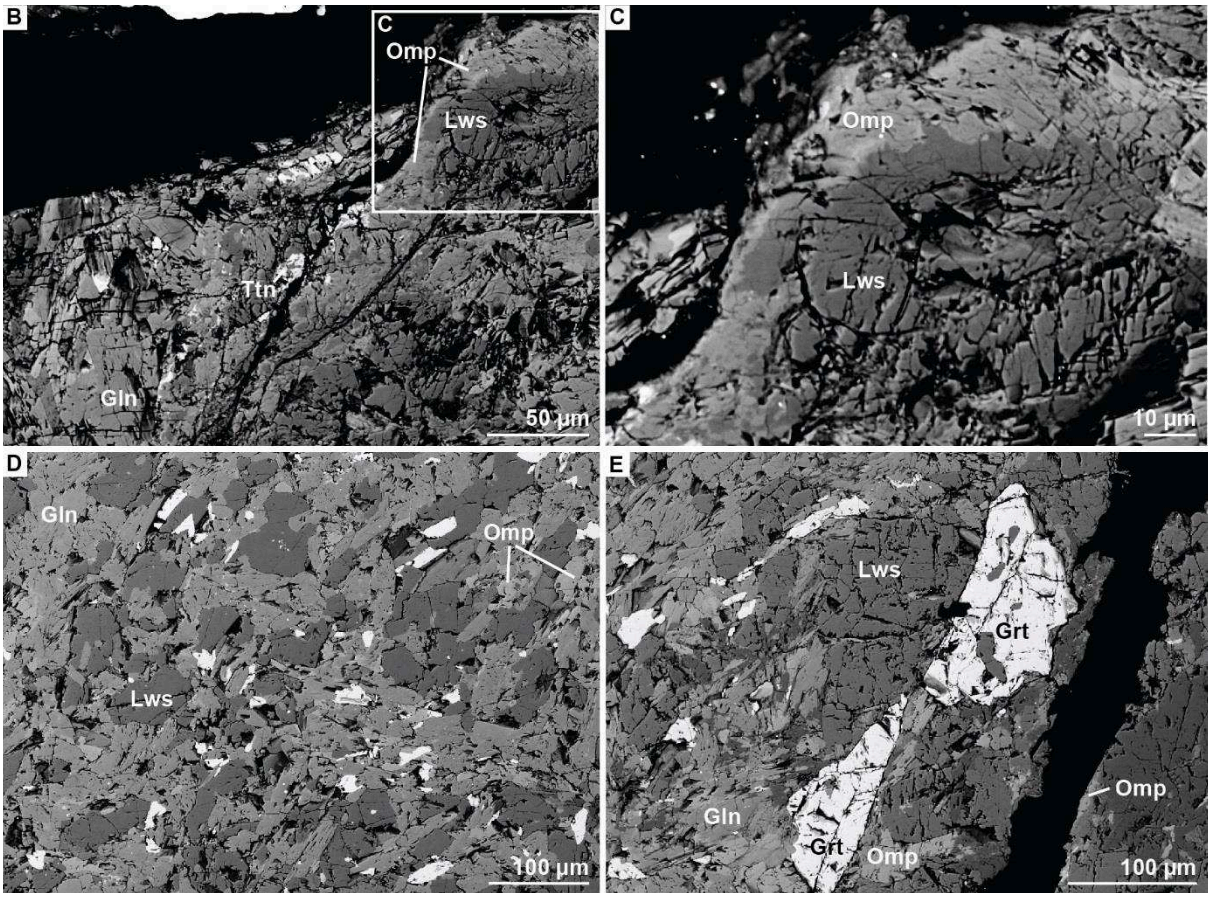

Figure 46: Four different BSE images showing higher magnification images of sample BSd_3_823. B) Corner of the sample exhibits fractures with omphacite (Omp) along its borders. C) Closer magnification of an area marked in B). D) Region in the sample unaffecetd by fracturing. Much less Omp can be found in these areas compared to the vicinity of fractures. E) Dissected and displaced garnet crystal along a narrow fault.

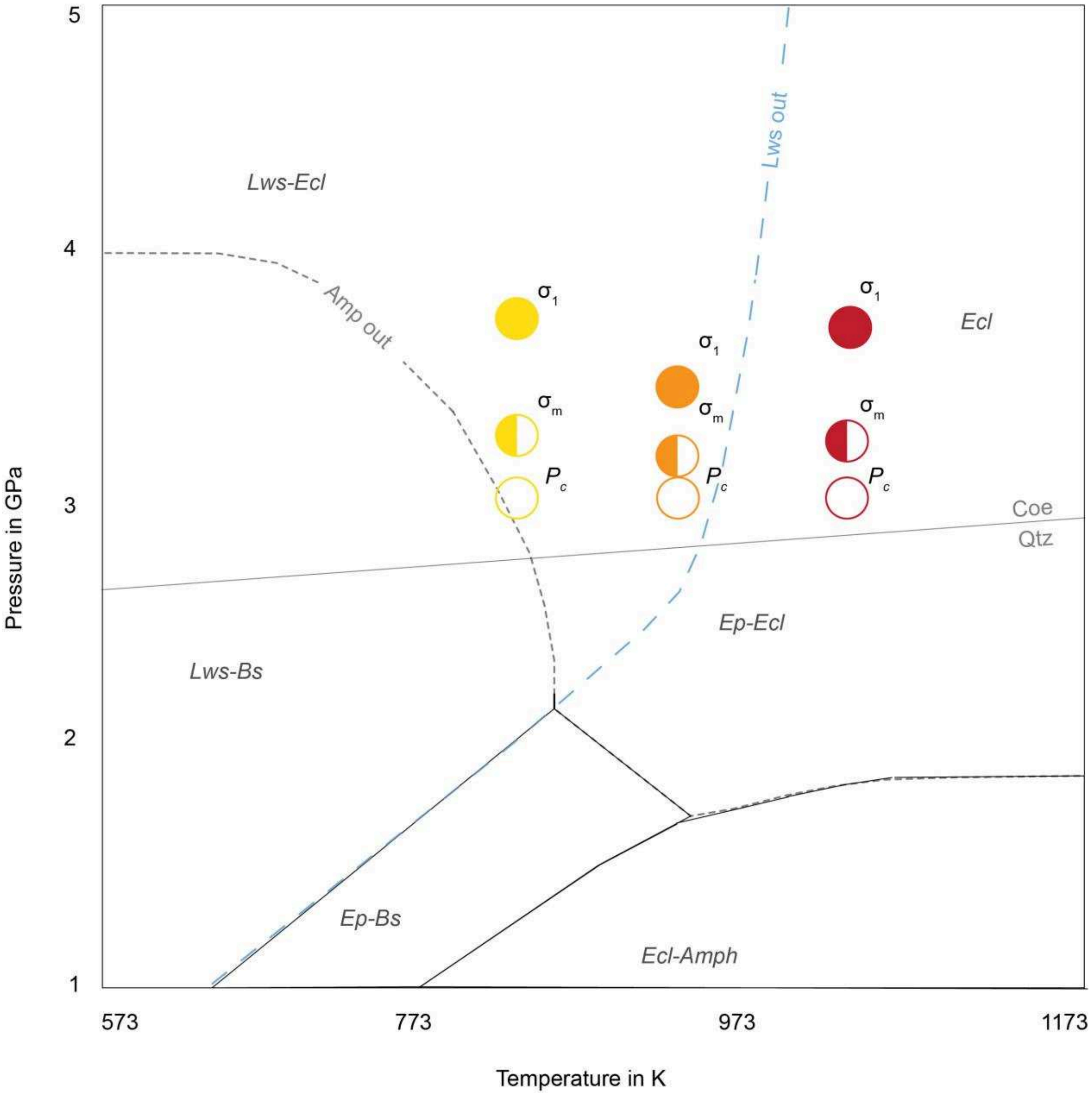

Figure 47: P-T pseudosection with superimposed P_c, σ_m, *and* σ_1 for the deformation experiments performed on the intact Corsican blueschist drill cores. Yellow colored circles represent the experiment conducted at 823 K, orange circles at 923 K, and red circles at 1023 K.

The microstructure of the sample BSd_3_923 (Figure 48) demonstrates very fine bands of sheared crystals (white and black arrows in Figure 48H). Most of these conjugated shear bands are found in the upper third of the sample. These narrow shear bands are mainly bordered by lawsonite and a brighter phase interpreted as secondary omphacite (black arrow in Figure 48H). The mineral determination is only based on qualitative chemical analyses, showing omphacite-like composition, and BSE contrast between the brighter phase and omphacite from the starting material. Based on the thermodynamically modelled P-T pseudosection, the sample was deformed outside the amphibole stability field and under conditions where lawsonite is about to break down, but the overall microstructure shows no evidence that lawsonite was unstable due to the higher temperature (orange circles Figure 47). Compared to the initial phase composition of the Corsican blueschist and to areas showing no or homogeneous strain distribution within the sample much more omphacite is present in regions where shear bands are found and is spatially related to glaucophane crystals (Figure 48I, J).

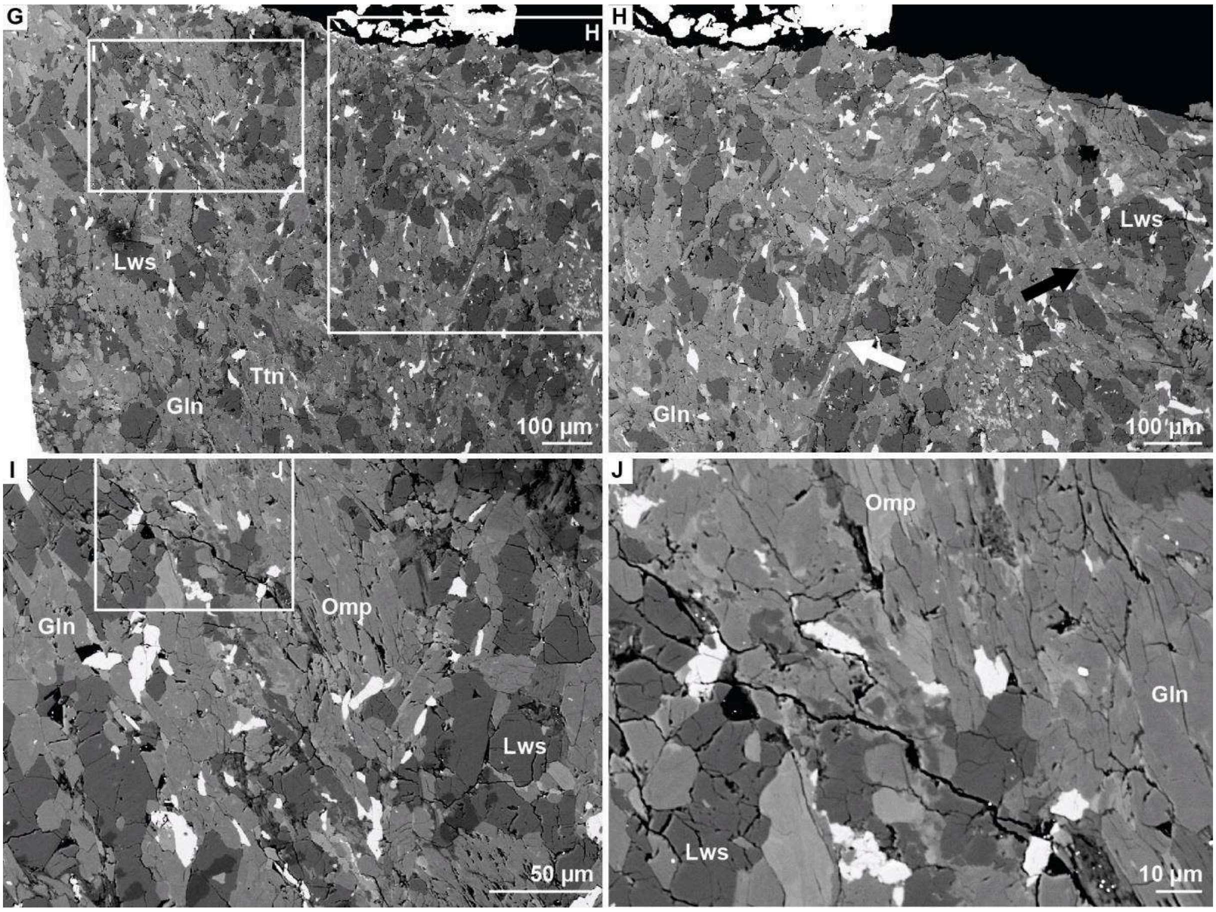

Figure 48: BSE images of sample BSd_3_923. G) White rectangles show the positions chosen for high magnification images. H) Black and white arrows mark the narrow shear bands, that can be found in the microstructure. The shear band highlighted by the black arrow is almost exculsively formed by omphacite. I) Closer view on a shear band and location of the high magnification image shown in J). J) Much more omphacite, always spatially associated to glaucophane, can be found in the vicinity of the shear bands.

Based on the calculated P-T pseudosection it is expected that both, lawsonite and glaucophane, are unstable during deformation of sample BSd_3_1023 (red circles Figure 47). The microstructure reveals no fractures, but narrow shear bands in the sample (Figure 49L), which are similar to those of the run BSd_3_923 (Figure 48). These bands are mostly formed by sheared glaucophane, lawsonite and omphacite (Figure 49L). Another structure present in this sample can be seen in the optical micrograph (Figure 44); a wide band composed of mainly omphacite and garnet. This band consisting of eclogite-facies minerals starts in the upper right corner of the sample and can be followed through the entire sample to the lower left corner. There are two types of garnet crystals distinguishable by their size. One group is rather large with around > 100 µm and the second group is much smaller with an average grain size of approximately < 30 µm (Figure 49M). These small garnet crystals are often found in fractures dissecting and displacing larger garnet crystals (Figure 49M). A thin layer of fine grained (< 30 µm) garnet crystals can be found along the fault separating two larger garnet crystals (Figure 49M).

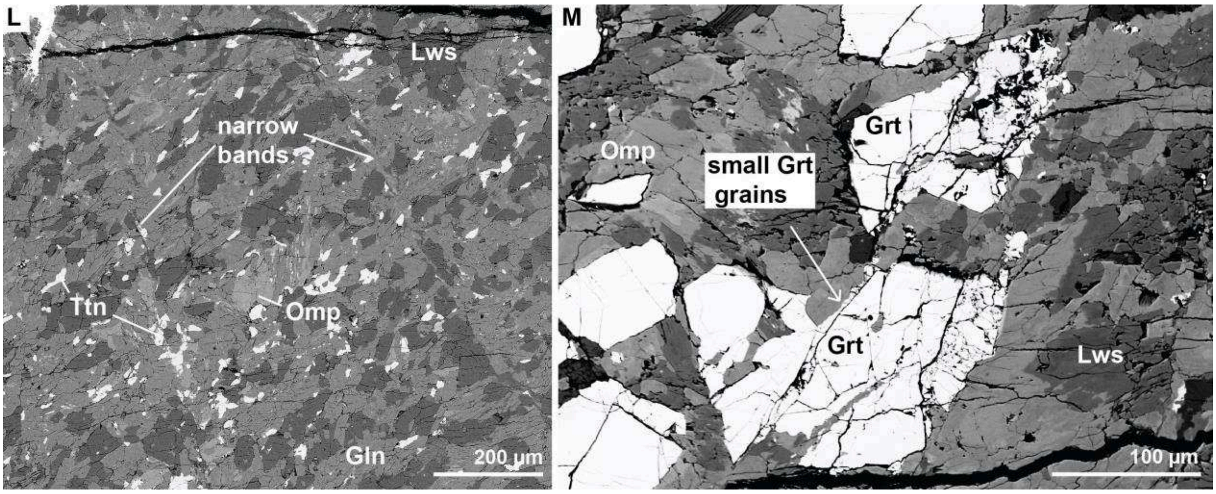

Figure 49: L) The microstructure of the sample BSd_3_1023 reveals dissect and offset garnet crystals and M) conjugated shear bands as already observed in the microstructures of the other two samples.

Powder experiments under 2 GPa

Both runs GLN_2_823a (violet circles in Figure 50) and GLN_2_823b (yellow circles in Figure 50), performed using the Gln-enriched powder of the Corsican lawsonite-blueschist, show very similar microstructures. Therefore only the experiment GLN_2_823a will be presented and discussed. In both cases the samples were deformed within the lawsonite field. The microstructure of run GLN_2_823a shows conjugated faults cutting through the entire sample (Figure 51A). At higher magification, one can see that the main fault is accompanied by several very narrow faults oriented parallel or sub-parallel to the main fracture (Figure 51B, C). Crystals in this zone are dissected and displaced several times along narrow fractures (Figure 51C). Glaucophane grains show very thin rims composed of a brighter material too small to be unambiguously identified, but the chemical composition as well as the BSE contrast both point to omphacite.

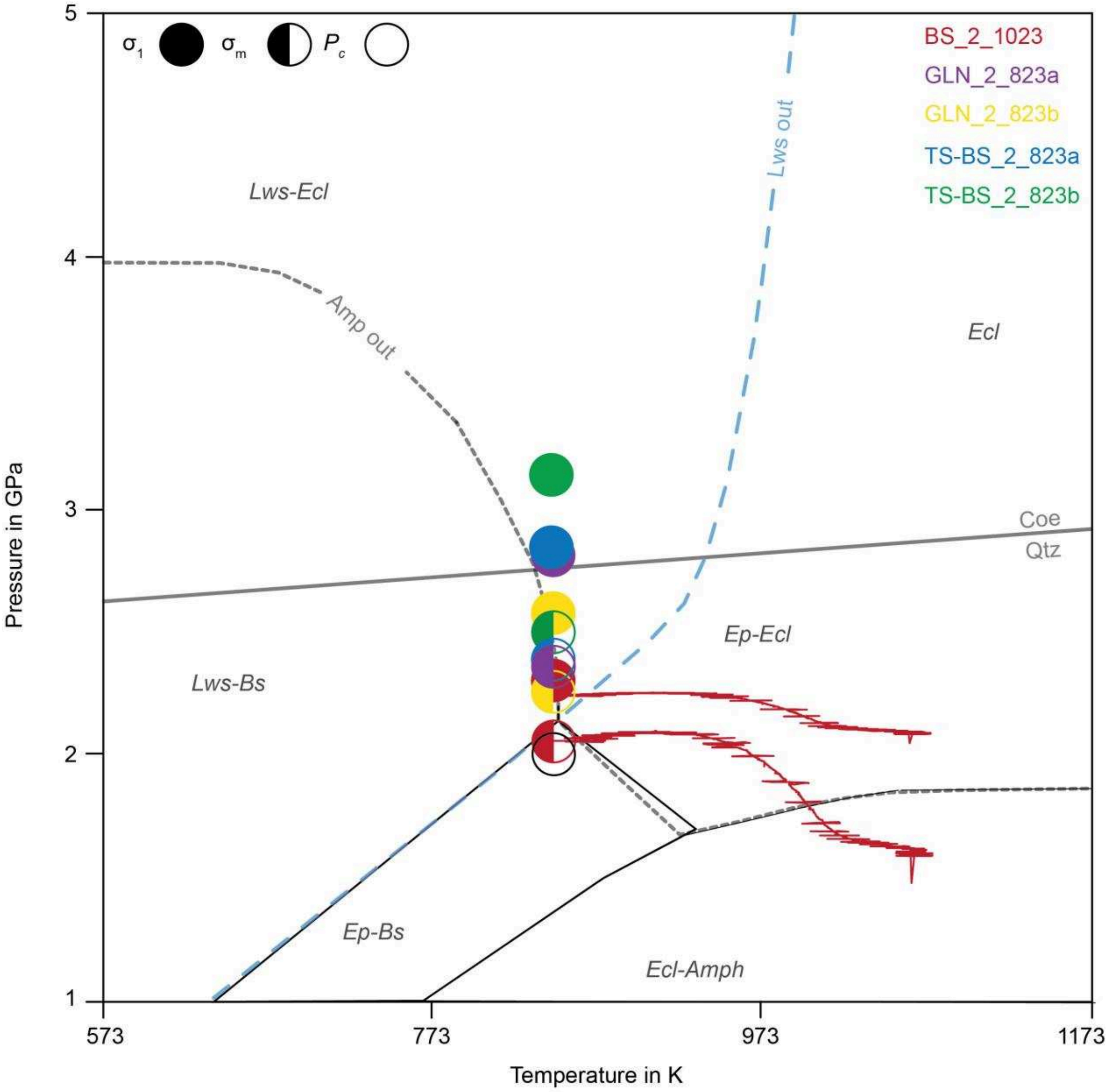

Figure 50: The powder deformation experiments were conducted under isothermal conditions except the run BS_2_1023 (red circles and curves), which was heated from 823 to 1023 K. Filled circles show the respective σ_1 (based on axial load data) and half-filled circles the calculated σ_m for each run.

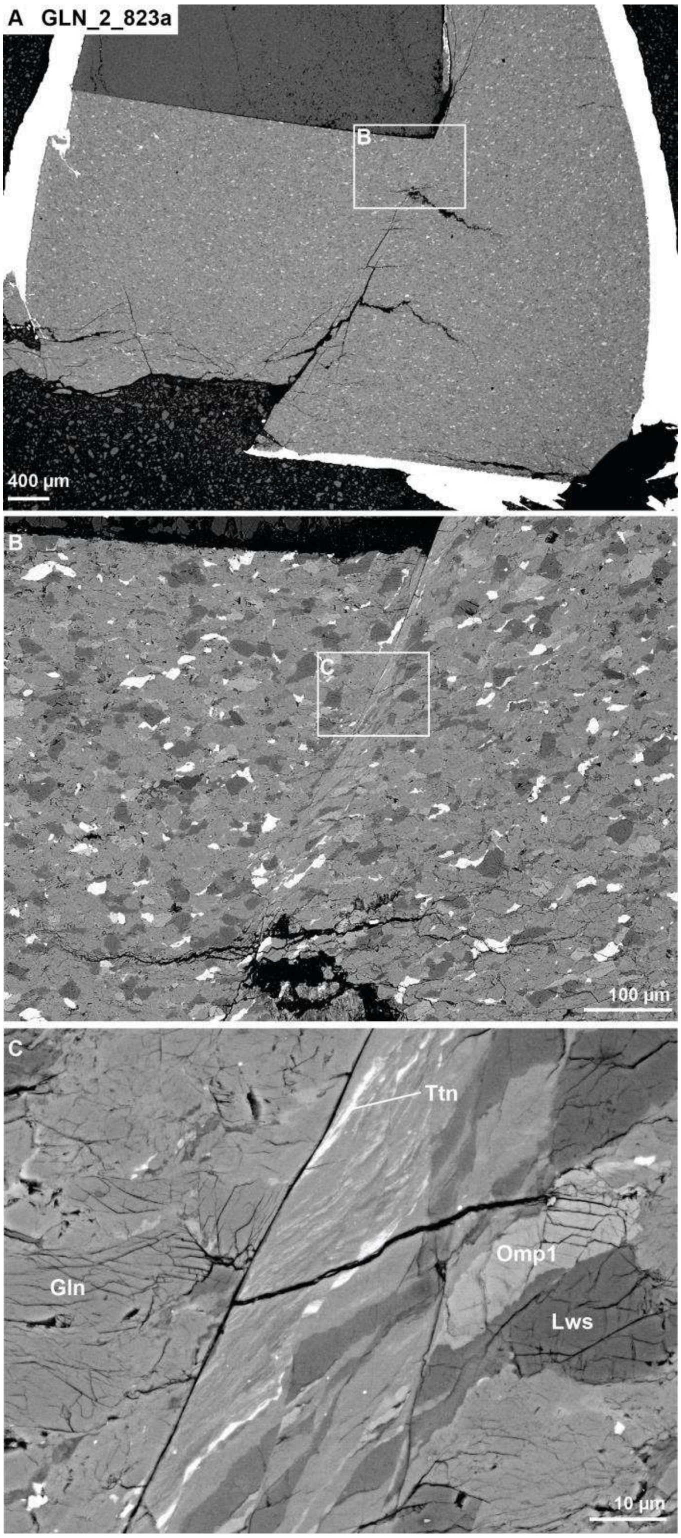

Figure 51: BSE images showing three different magnifications of the microstructure of run GLN_2_823a. A) The overview of the sample after deformation shows conjugated fractures cutting through the entire sample. White rectangles show the locations of two different magifications presented in B and C. B) Magnification of the main fracture, which cuts through the sample. The zone along the fracture appears to be highly deformed. C) A set of narrow fractures form a fault zone within which crystals are dissect and displaced along narrow faults oriented parallel or sub-parallel to the main fracture.

Sample BS_2_1023 (red circles and curves in Figure 50) was conducted on the Corsican lawsonite-blueschist bulk rock powder. After reaching the yield point the sample was heated up to 1023 K (red curves in Figure 50) to trigger the breakdown of lawsonite. Lawsonite pseudomorphs can be found in the entire sample and are composed of epidote needles indicating that lawsonite became unstable due to syndeformational heating (Figure 52B, C). Glaucophane grains exhibit rims identified as omphacite (Figure 52C). A fracture appears in the sample, starting in the upper right corner and propagated several hundred µm towards the sample's center (Figure 52B). This fracture is not very sharp and seems to be overprinted by the newly formed dehydration products derived from the lawsonite breakdown (Figure 52C).

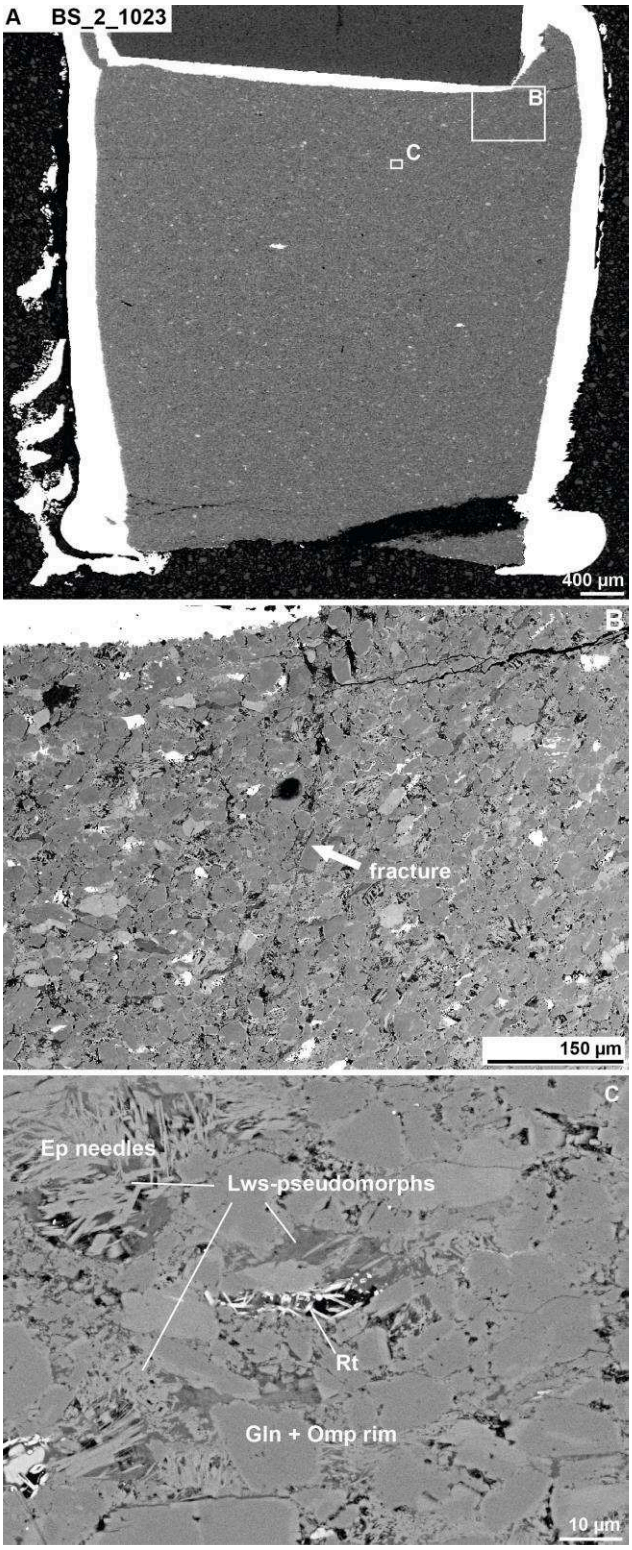

Figure 52: Different high magnification images of sample BS_2_1023 demonstrate the microstruture after deformation and heating up to 1023 K. A) The overview image shows no microstructural evidence for strain localization. B) At higher magnification a narrow fracture is visible, that seems to be overprinted by dehydration products formed due to the breakdown of lawsonite triggered while heating. C) Lawsonite-pseudomorphs are found in the entire sample. These structures are filled by an epidote group mineral. Glaucophane crystals show omphacite rims. Under the conducted experimental conditions titanite was no longer stable and decomposed to rutile (Rt).

The experiments TS-BS_2_823a (blue circles in Figure 50) and TS-BS_2_823b (green circles in Figure 50) were both performed using the bulk rock blueschist powder from the Tianshan blueschist sample. Both samples were deformed within the amphibole stability field (Figures 53, 54). The microstructure of run TS-BS_2_823a (Figure 53) shows fractures starting in the bottom corners of the sample and narrow faults, which dissected and displaced titanite and quartz grains (Figure 53A). Under the SEM areas showing strain localization do not differ in their mineralogy compared to the starting material or regions unaffected by fractures. In the microstructure of TS-BS_2_823b the strain seems to be homogeneously distributed within the whole sample (Figure 54A).

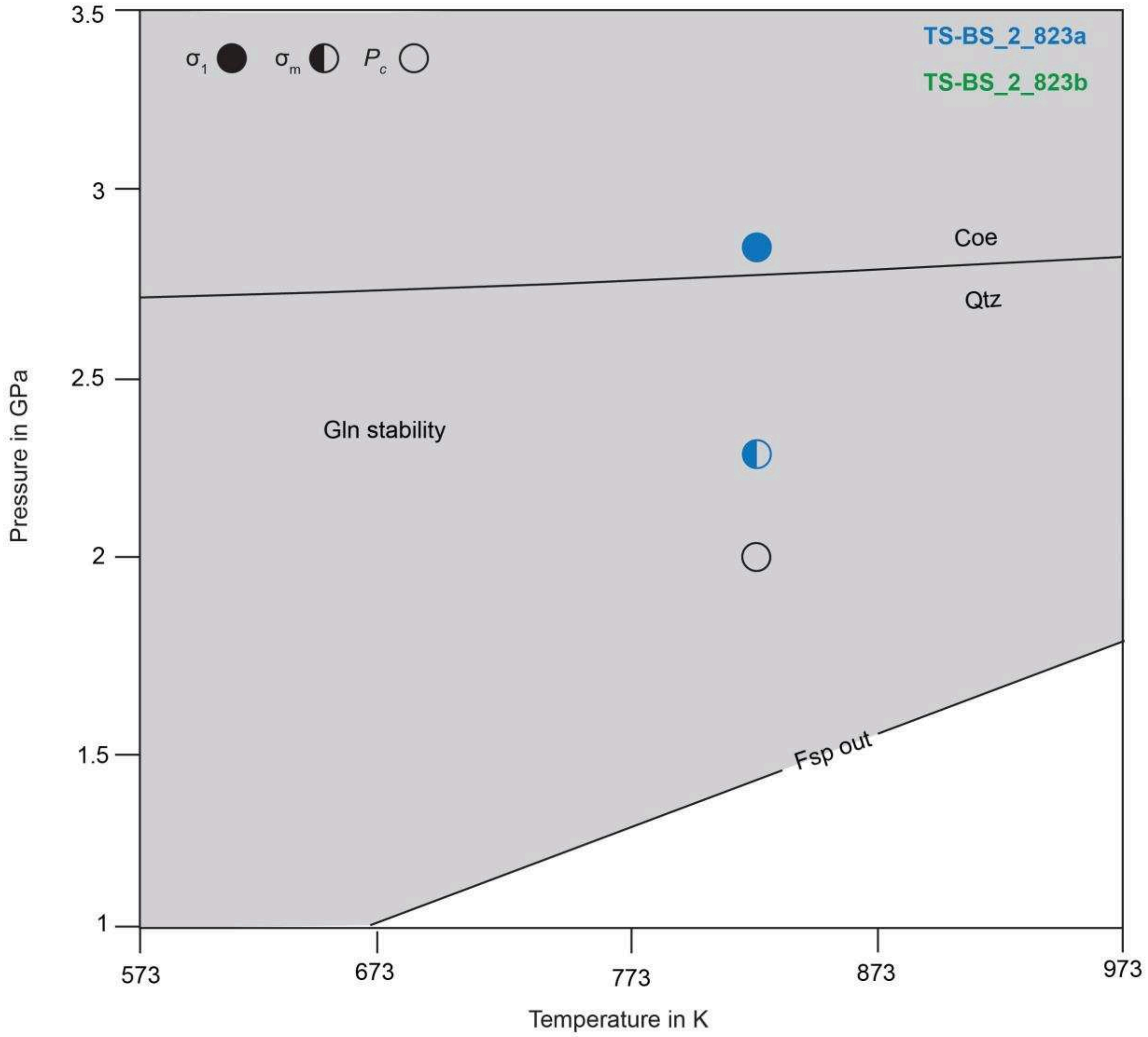

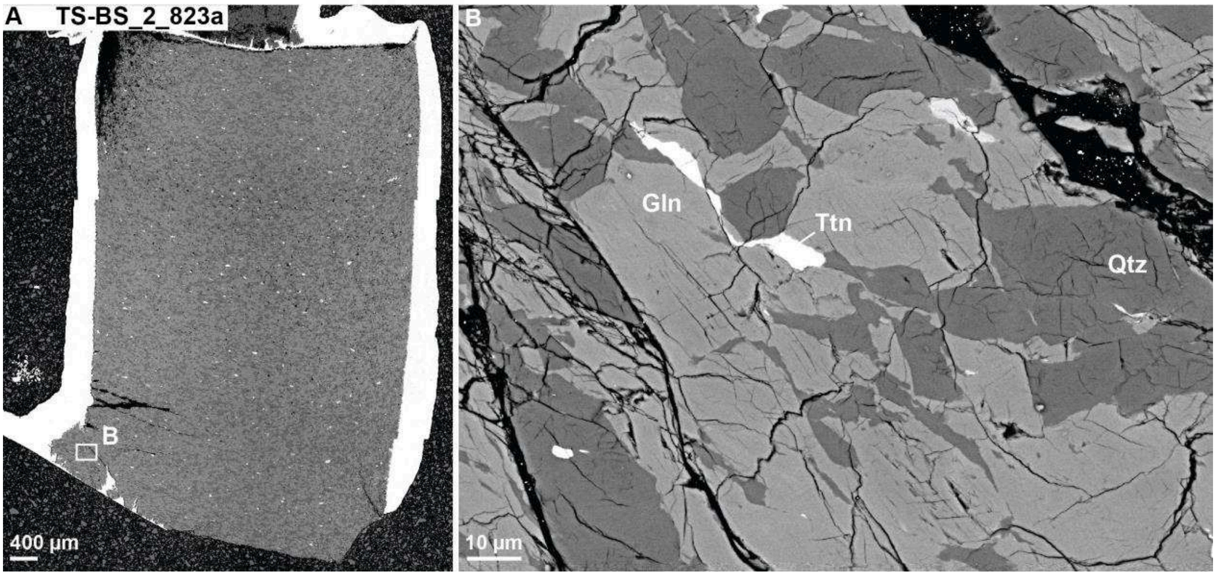

Figure 53: Microstructure of the sample TS-BS_2_823a. Fractures evolved in the corners of the sample showing dissceted and displaced crystals.

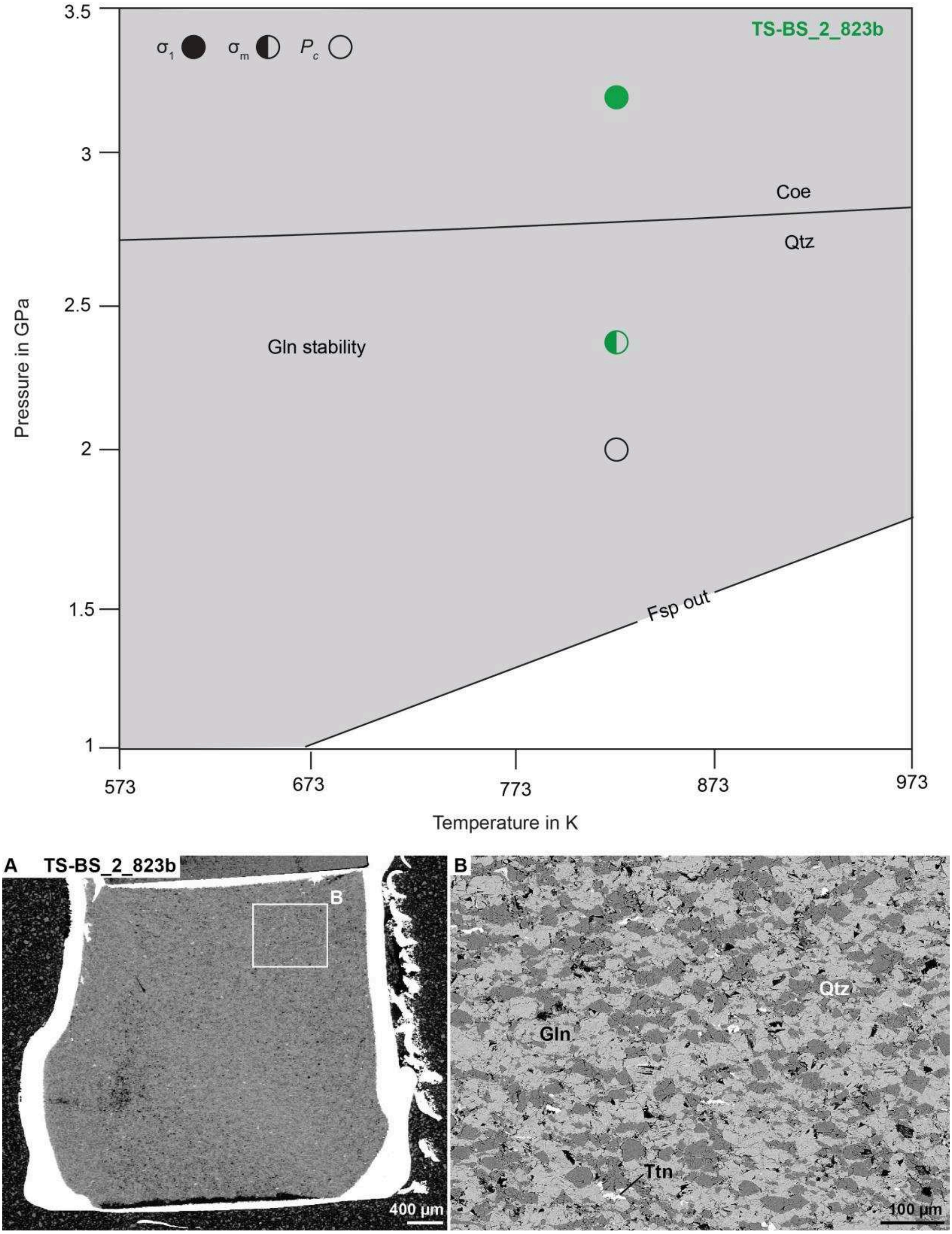

Figure 54: The microstructure of the sample TS-BS_2_823b shows no evidence for macro- or microscopic strain localization.

D-DIA deformation experiments

Paper

LABORATORY EARTHQUAKES TRIGGERED DURING ECLOGITIZATION OF LAWSONITE-BEARING BLUESCHIST

by

Sarah Incel, Nadège Hilairet, Loïc Labrousse, Timm John, Damien Deldicque, Thomas Ferrand,
Yanbin Wang, Jörg Renner, Luiz Morales, Alexandre Schubnel

Earth and Planetary Science Letters, 459 (2017), 320-331

ABSTRACT

The origin of intermediate-depth seismicity has been debated for decades. A substantial fraction of these events occurs within the upper plane of Wadati-Benioff double seismic zones believed to represent subducting oceanic crust. We deformed natural lawsonite-rich blueschist samples under eclogite-facies conditions ($1.5 < P < 3.5$ GPa; $583 K < T < 1121 K$), using a D-DIA apparatus installed at a synchrotron beamline continuously monitoring stress, strain, phase changes, and acoustic emissions (AEs). Two distinct paths were investigated: i) heating during deformation at pressures > 2.5 GPa to maximum temperatures ranging from 762-1073 K, during which lawsonite and glaucophane became gradually unstable while entering the stability field of lawsonite-eclogite and the breakdown reaction of lawsonite was only crossed in case of the highest final temperature; ii) heating while deforming at a pressure < 2 GPa to a maximum temperature of 1121 K associated with crossing the breakdown reaction of lawsonite and successively entering the stability fields of epidote-blueschist and eclogite-amphibolite but not of lawsonite-eclogite. Upon entering the Lws-Ecl stability field samples exhibited brittle failure, accompanied by the radiation of AEs. In-situ X-ray diffraction and microstructural analysis demonstrate that fractures are topologically related to the formation of omphacite. Amorphous material was detected along the fractures by transmission-electron microscopy without evidence for free-water. Since the newly formed omphacite crystals are small compared to the initial grains, we interpret the observed mechanical instability as a transformation-induced runaway under stress triggered during the transition from lawsonite-blueschist to lawsonite-eclogite. In contrast, we find no microstructural evidence that the breakdown of lawsonite, and hence the liberation of water leads to the fracturing in samples that experienced the highest quench temperatures of 1073 and 1121 K, although some AEs were detected during an experiment performed at 1.5 GPa. Our experimental results challenge the concept of "dehydration embrittlement", which ascribes the genesis of intermediate-depth earthquakes to the breakdown of hydrous phases in the subducting oceanic plate. Instead we suggest that grain-size reduction (transformational faulting) during the transition from lawsonite-blueschist to lawsonite-eclogite leads to brittle failure of the deviatorically loaded samples.

1. INTRODUCTION

Intermediate-depth earthquakes occur between approximately 50 to 300 km (Gutenberg and Richter, 1945; Hacker et al., 2003). Almost all intermediate-depth earthquakes occur in subduction zones and follow two distinct planes – the so-called upper and lower Wadati-Benioff planes of seismicity (Frohlich, 1989; Brudzinski et al., 2007). The upper plane is believed to correspond to earthquakes generated within the subducting oceanic crust while the lower plane is ascribed to earthquakes located in the subjacent mantle (Hacker et al., 2003).

For several decades, scientists have been puzzled by the occurrence of earthquakes at intermediate-depths at which rocks are expected to deform plastically under the prevailing pressures and temperatures (Raleigh and Paterson, 1965; Green and Burnley, 1989). A multitude of theoretical, experimental, and field studies addressed this problem (e.g., Kirby, 1987; Green and Burnley, 1989; Hirth and Tullis, 1994; Dobson et al., 2002; Austrheim and Andersen, 2004 ; Jung et al., 2004; Hacker et al., 2003; John and Schenk, 2006; Kelemen and Hirth, 2007; John et al., 2009; Gasc et al., 2011; Schubnel et al., 2013; Deseta et al., 2014; Thielmann et al., 2015). From these, three main hypotheses for the mechanisms of intermediate-depth earthquakes emerged: i) thermal runaway or shear heating (Hobbs and Ord, 1988; John et al., 2009; Prieto et al., 2013), ii) dehydration embrittlement (Green and Houston, 1995; Hacker et al., 2003; Jung et al., 2004), and iii) transformational faulting (Kirby, 1987; Green and Burnley, 1989; Schubnel et al., 2013). The term thermal runaway describes the feedback between shear heating and the temperature-dependent rock rheology. The dehydration embrittlement model postulates a change from ductile to brittle behavior due to an increase in pore-fluid pressure and hence a decrease in effective stress during the breakdown of hydrous phases in the rock. Finally, transformational faulting refers to mechanical weakening of the rock caused by volume and/or enthalpy changes but also by grain-size reduction during transformation.

So far, most experimental work testing these hypotheses focused on serpentine- dehydration experiments in the pressure-temperature range of intermediate-depth seismicity. Investigating metamorphic reactions within metabasalts of the descending oceanic crust has been almost completely disregarded (except for Okazaki and Hirth, 2016), although the distribution of hypocenters within the subducting oceanic crust correlates very well with the thermodynamically expected stability fields of different paragenesis for basaltic rock compositions at elevated pressures and temperatures (Peacock and Wang, 1999; Hacker et al., 2003; Kita et al., 2006). Indeed, hypocenter locations in cold subducting oceanic crust such as below northern Japan (Kita et al., 2006) coincide with the predicted stability field of lawsonite-eclogite (Lws-Ecl), i.e. an intermediate facies between lawsonite blueschists (Lws-Bs), comprising glaucophane and lawsonite as hydrous phases, and eclogites (Ecl) whose paragenesis of garnet + omphacite is nominally dry. The lack of seismicity once entering the stability field of eclogite is striking (Kita et al., 2006) and this seismic boundary suggests that metamorphic reactions during the transition from Lws-Bs to Ecl transiently change the rheology of the rock and enable brittle failure.

The key objective of the present contribution is to distinguish the mechanical impacts of glaucophane and lawsonite breakdown and their potential link with brittle failure. We performed deformation experiments with in-situ monitoring of phase content and acoustic emissions on lawsonite-bearing blueschist samples. The discussion focuses on the influence of metamorphic reactions during deformation on the micro- and nanostructures as well as on the record of acoustic emissions. Finally, we present a plausible mechanism for brittle failure of the samples during their transformation to eclogite.

2. THE CORSICAN BLUESCHIST

2.1 SAMPLE DESCRIPTION

A lawsonite-blueschist (Lws-Bs) from Alpine Corsica served as sample material. Having experienced peak metamorphic conditions of approximately 520 ± 20 °C and 2.3 ± 0.1 GPa (Vitale Brovarone et al., 2011) it mostly consists of glaucophane (Gln, mineral abbreviations follow Whitney and Evans, 2010) and lawsonite (Lws), where Lws often appears as lenses. The Gln:Lws ratio of approximately 3:2 is estimated from optical analyses of several thin sections. The minor phases actinolite (Act), garnet (Grt), phengite (Ph), titanite (Ttn), and omphacite (Omp1), with $X_{jd} \approx 0.4$ and $X_{di} \approx 0.6$, comprise less than 15 % of the rock's volume. Apatite (Ap), and albite (Ab) are also found in limited amounts (Vitale Brovarone et al., 2011). The mineral phases Gln, Omp1, and Act were chemically investigated (Figure 1) and our analyses are in good agreement with those previously reported (Vitale Brovarone et al., 2011).

2.2 SAMPLE PREPARATION

A fragment of the Lws-Bs, selected for its homogeneous distribution of Gln and Lws content, was crushed, ground and sieved to a grain size fraction < 38 µm. A Frantz isodynamic magnetic separator was used to segregate Gln and Lws. Three different powders with different Gln:Lws ratios were produced: i) bulk-rock, ii) glaucophane-rich (Gln-rich), and iii) lawsonite-rich (Lws-rich) (Figure 1). Powders were used rather than the intact rock, because of i) the heterogeneity in mineralogy (e.g. due to Lws lenses) and texture (schistosity), which would considerably hamper the sample-to-sample comparison and ii) the need of a small grain-size (< 38 µm) for the in-situ X-ray powder diffraction (XRD) during the deformation of the samples (more details in 3.4).

2.3 CHARACTERIZATION OF THE STARTING MATERIAL

Powders were embedded in epoxy and afterwards characterized by element mapping of Ca and Na using a scanning electron microscope (SEM). Element ratios were calculated using the software ImageJ (Abramoff et al., 2004) and can be directly transformed to different Gln:Lws ratios (Figure 1). The bulk-rock, Gln-rich, and Lws-rich powders show Gln:Lws ratios of approximately 1:1, 2:1, and 1:3, respectively. As in the natural rock, minor and accessory phases comprise around 15 % of the powder volume. For these three different powders, three different P-T pseudosections were calculated in the NCFMASH system using the thermodynamic modeling software Theriak-Domino (De Capitani and Petrakakis, 2010). As expected for a divariant reaction, the position of the Gln-out reaction depends on the system's stoichiometry, hence on the Gln:Lws ratio (Figure 1). The slightly lower stability of amphibole (Amp) or rather Gln at HP/ LT of the Gln-rich powder relative to the bulk-rock powder (Figure 2) is related to an increase of Fe and Mg content with increasing Gln in the system stabilizing the almandine component of Grt. The univariant Lws-breakdown curve (Lws = Ep) shifts with bulk chemistry due to the Ca balance between garnet (grossular component) and lawsonite. The calculated stability fields of the different metabasalts and the positions of the different Gln- and Lws-out curves for the three powders (Figure 2) are in agreement with previous findings (Vitale Brovarone et al., 2011).

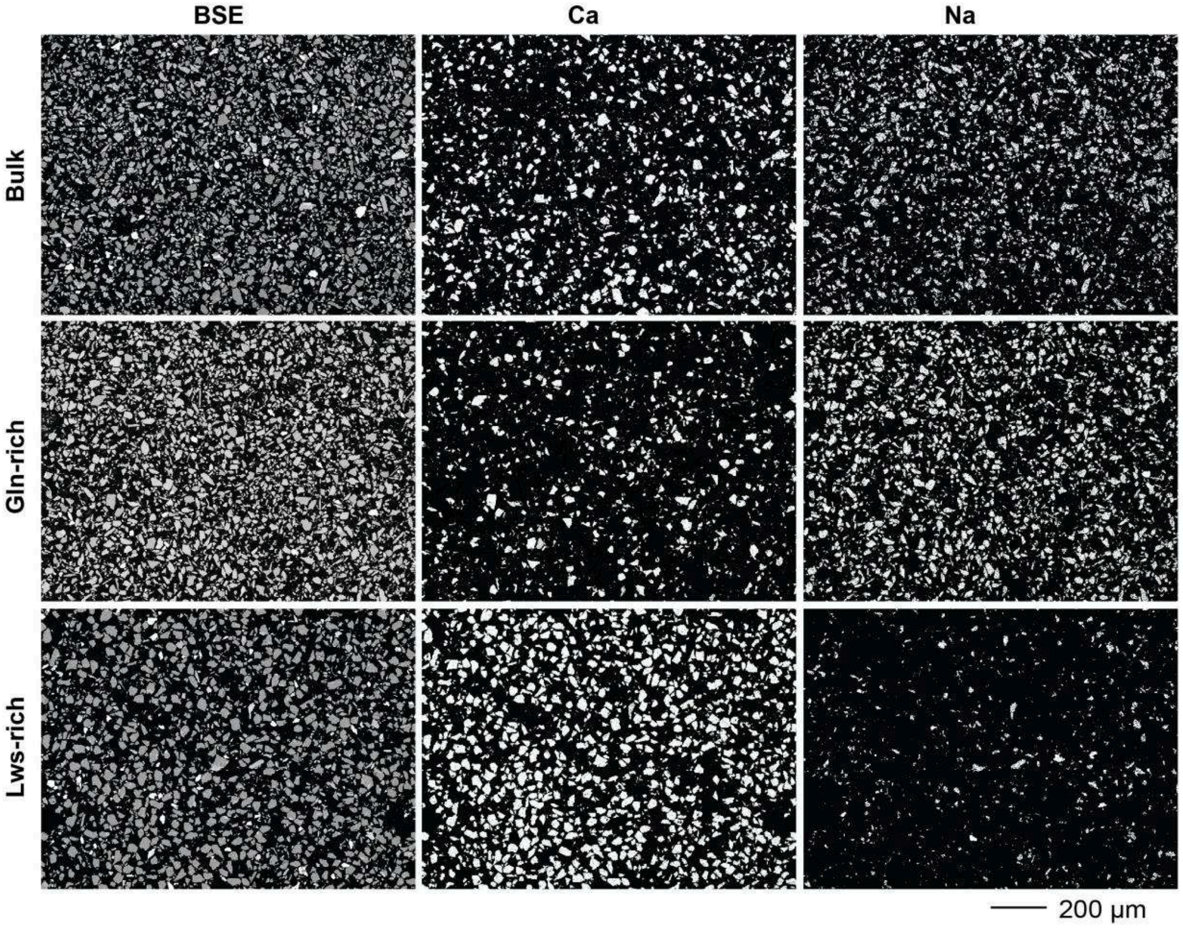

Oxides	Gln	Lws	Act	Omp1
SiO_2	58.42	38.34	58.36	56.07
Al_2O_3	10.81	32.56	0.75	8.79
CaO	0.61	17.39	11.93	13.59
Na_2O	7.39	0.00	0.58	6.70
FeO	11.27	0.34	9.37	7.13
MgO	9.69	0.00	18.08	8.01
K_2O	0.03	0.002	0.06	0.04
MnO	0.11	0.00	0.49	0.22
TiO_2	0.00	0.04	0.07	0.08
Cr_2O_3	0.03	0.02	0.00	0.00
Total	98.36	88.70	97.71	100.64

	Ca [%]	Na [%]
Bulk Gln/ Lws ≈ 1 :1	46	54
Gln-rich Gln/ Lws ≈ 2 :1	33	67
Lws-rich Gln/ Lws ≈ 1 :3	71	29

Figure 1: Characterization of the three different powders and their Ca:Na ratios and chemical analyses of major phases of the Corsican blueschist.

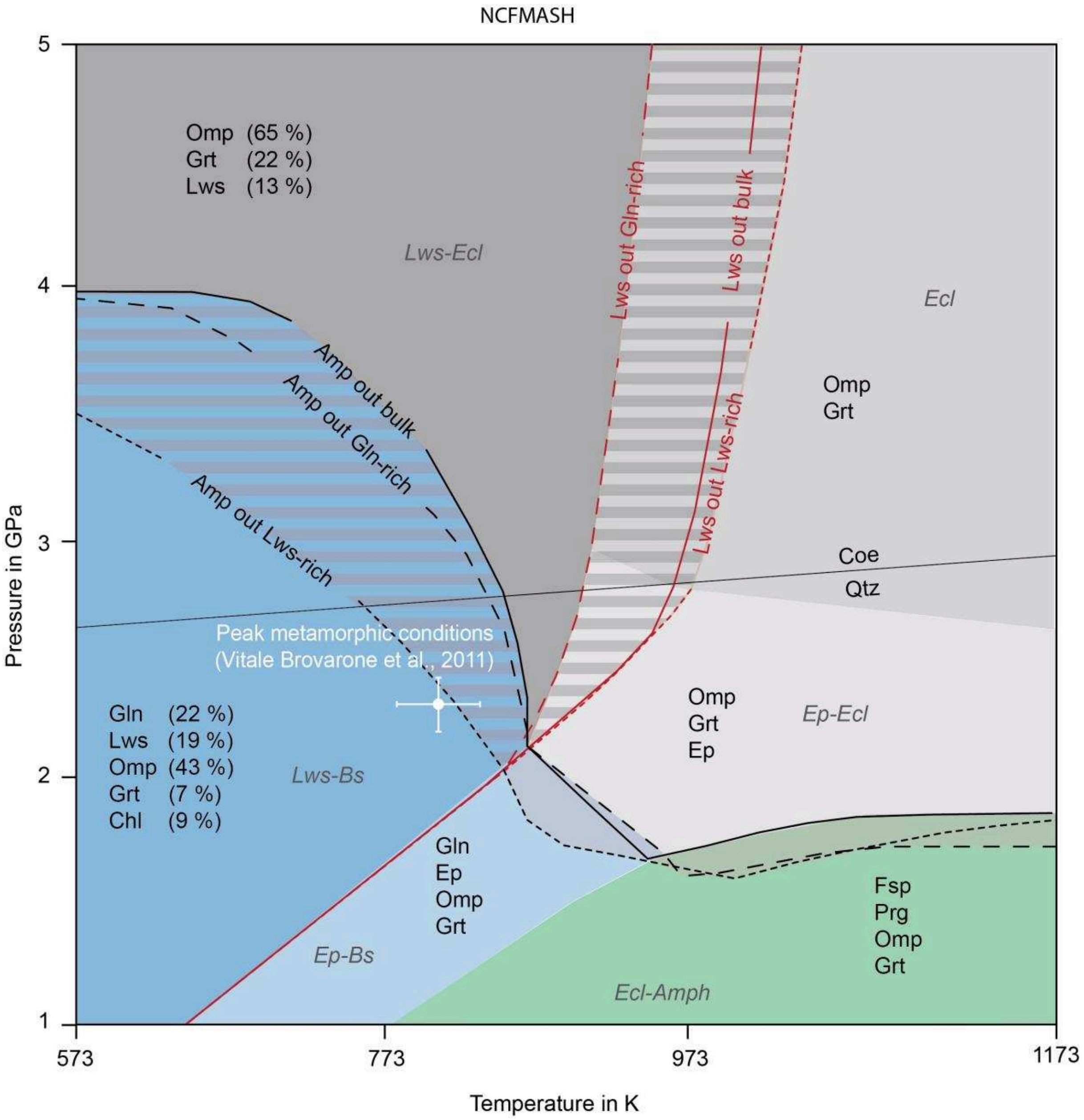

Figure 2: Summarized P-T pseudosection showing the Amp- and the Lws-out curves for the three different powders (Lws-Ecl: lawsonite-eclogite, Lws-Bs: lawsonite-blueschist, Ep-Bs: epidote-blueschist, Ecl-Amph: eclogite-amphibolite, Ep-Ecl: epidote-eclogite, Ecl: eclogite).

3. EXPERIMENTAL METHODS

3.1 EXPERIMENTAL SETUP

Deformation experiments were performed using a deformation diamond-anvil (D-DIA) apparatus, attached to the GSECARS synchrotron beamline 13-BM-D at the Advanced Photon Source Chicago. During nominal isotropic pressurization, a main ram controls the advancement of four horizontal and two vertical anvils that compress the sample assembly until a prescribed load is reached. Differential rams, which move the vertical anvils independently, create a deviatoric stress field in the sample assembly (Wang et al., 2003). Anvils are made of tungsten carbide (WC), except for two horizontal anvils composed of sintered diamond, translucent to X-rays. The use of synchrotron X-rays allows for in-situ monitoring of strain, using radiographs of the sample, but also for recording powder diffraction patterns from which phase changes and stress state are deduced. Temperature is inferred from temperature-output power calibrations with an uncertainty below 10 %. Raterron et al. 2013 demonstrated the existence of non-negligible axial temperature gradients of about 155 K/mm with the sample's center colder than the edges.

3.2 SAMPLE ASSEMBLY

The powder was placed in a cylindrical BN sleeve surrounded by the graphite furnace and placed into 9 x 9 x 8 mm amorphous Boron-epoxy cuboids. The sample is sandwiched between two gold foils and two alumina pistons (Figure 3). The initial size of the powder charge is approximately 2.1 mm in diameter by 3 mm in height. All powders were hot-isostatically pressed before triaxial deformation at temperatures of about 583 to 653 K for approximately 1 h. Sample BS_3_1073 was hot-pressed in a piston-cylinder apparatus at 3 GPa and 923 K for 1 day, then machined and loaded in the deformation cell assembly. This sample was kept at isostatic conditions at 583 K in the D-DIA for only 30 min.

3.3 EXPERIMENTAL PROCEDURE

After the hot-pressing, deformation with a strain rate of about 10^{-5} s^{-1} was started. Syndeformational heating was performed by increasing the power in steps of 10 W corresponding to a temperature increase of approximately 50 K. The heating steps were initiated at 10, 15, 20, 25, 30, and 35 % strain for the Gln-enriched and the Lws-enriched samples, at 10, 20, 30, and 40 % strain for the run BS_1.5_1121, and at 5, 12, 18, 20, 25, 30, and 35 % strain for the run BS_3_1073.

3.4 IN SITU DATA ACQUISITION SETUP, STRESS AND STRAIN COMPUTATIONS

The X-ray transmission images and diffraction patterns of the samples were acquired using a monochromatic synchrotron X-ray beam at 13-BMD (λ = 0.2431 Å, approximately 51 keV) during the course of deformation runs (Figure 3). The typical acquisition time for images was 2 s and for the diffraction patterns 300 s. In image mode, the beam is typically 2 mm x 3 mm, i.e., comparable to initial sample size, and the CCD camera is positioned to capture the radiograph. In diffraction mode, the CCD camera is moved out of the diffraction path and slits reduce the beam size to typically 200 x 200 microns. Therefore, only a limited volume in the center of the sample is probed. The detector tilt and rotation relative to the incident beam were calibrated using the diffraction pattern of a CeO_2 standard and the software Fit2D (Hammersley et al., 1996).

The d-spacing of a crystal is sensitive to the orientation of the diffracting plane with respect to an anisotropic stress field. For instance, the d-spacing of lattice planes oriented perpendicular to the direction of the maximum principal stress σ_1 decreases and thus the diffraction line shifts to higher 2θ angles. Therefore, in a powder with random crystal orientations, the different responses of lattice planes to anisotropic stress result in a distortion or pseudo-ellipticity of the Debye rings that are initially circular under hydrostatic conditions. This distortion is called lattice strain and can be used as a proxy for the differential stress effectively acting on the polycrystalline aggregate (Uchida et al., 1996, Singh et al., 1998). The deviation of the diffracting plane from the normal to the maximum compression axis is characterized by an angle ψ related to the diffraction angle θ according to:

$$\cos\psi = \cos\theta\cos\delta \tag{1}$$

where δ represents the projection of ψ on the detector plane. Calculation of differential stress was performed using Fit2D (Hammersley et al., 1996) and the multifit-polydefix software (Merkel and Hilairet, 2015). The relation between the d-spacing $d_{(hkl)}$ (for a lattice plane with indices hkl) and the lattice strain $Q_{(hkl)}$ reads:

$$\frac{d_{(hkl)}(\psi) - d_{P,(hkl)}(\psi)}{d_{P,(hkl)}(\psi)} = Q_{(hkl)}\left(1 - 3\cos^2\psi\right) \tag{2}$$

(Uchida et al., 1996; Singh et al., 1998) where $d_{P,(hkl)}$ denotes the d-spacing at “hydrostatic” or isotropic stress and $d_{(hkl)}(\psi)$ corresponds to the d-spacing of the plane hkl with angle ψ to the maximum principal stress. For each experiment, the d-spacings were extracted from the diffraction patterns and fitted in a $d_{(hkl)}$ over ψ plot.

The refinement of the lattice strain relied on the $d_{P,(hkl)}$ of up to 5 crystallographic planes. The planes (110), (-111), and (151) of glaucophane were always used but sometimes also the (-202) and the (240) planes for the processing of experiments on the bulk-rock or the Gln-rich powders. For tests on the Lws-rich powder, the 3 crystallographic planes (002), (201), and (202) of lawsonite sufficed to refine the unit cell volume. We employed the second-order equation of state for Gln and Lws (Comodi et al., 1991; Mao et al., 2007) and constraints on their thermal expansion (Holland et al., 1996; Jenkins and Corona, 2006).

Mean stress σ_m calculates as:

$$\sigma_m = \frac{\sigma_1 + \sigma_2 + \sigma_3}{3} \tag{3}$$

where σ_1 denotes the maximum principal stress, and σ_2 and σ_3 are considered identical to the confining pressure P_c determined based on the shift in peak position before and after compression and heating. Differential stress $t_{(hkl)}$ was calculated for a specific plane using the lattice strain $Q_{(hkl)}$ according to (2) and the effective moduli $G_{(hkl)}$:

$$t_{(hkl)} = 6\, Q_{(hkl)} G_{(hkl)}. \tag{4}$$

The effective moduli $G_{(hkl)}$ derive from the elastic compliances S_{ij} (inverted from the stiffness matrix C_{ij}) for Gln (Bezacier et al., 2010) and Lws (Mao et al., 2007). In the following, the differential stress is obtained by averaging the $t_{(hkl)}$ values observed for the two most intense diffraction peaks. For the bulk-rock and the Gln-rich experiments, these corresponded to the (110) and (151) planes of glaucophane and to the (002) and (201) planes of lawsonite for the Lws-rich experiment.

The calculated differential stresses do not represent absolute values (see Hilairet et al., 2012, for a detailed discussion). Due to difficulties in calculating the effective moduli for low-symmetry phases like Gln, the calculation relied on orthorhombic instead of monoclinic symmetry. For a single experiment, it was possible to simultaneously calculate the differential stresses from Gln and Lws crystals. While the calculated differential stresses lie in the same order for the two phases, Lws appears to support more differential stress than Gln (Figure 5c), in agreement with previous experimental studies on blueschist rheology (Kim et al., 2013).

The powder-diffraction patterns were also used to continuously monitor the phase assemblage, using diffraction peak heights for individual phases integrated over the 360° of the Debye rings. While this is a crude estimate and does not take into account the effects of evolution in preferred orientations, the changes in intensities observed here are consistent with the microstructural observations and with the calculated pseudosections.

Bulk axial strain was determined using the radiographs of the samples. The gold foils on top and below a sample act as strain markers due to their high X-ray absorption contrast compared to the sample and the ceramic pistons. The current length of the sample was determined by measuring the distance between the shadows of the gold foils and strain ε was calculated by comparing the change in sample length, ΔL, the initial length L before the deformation was started, i.e.:

$$\varepsilon = \frac{\Delta \mathrm{L}}{\mathrm{L}} \tag{5}$$

Strain rate was calculated by relating the strain to the time increments between radiographs.

3.5 ACOUSTIC EMISSION SETUP AND LOCALIZATION TECHNIQUE

Piezoceramic lead-zirconate transducers with a thickness of 0.5 mm, a diameter of 10 mm, and a resonance frequency of 2-4 MHz (see also Schubnel et al., 2013, for details of the setup) were placed behind each of the six anvils (Figure 3). Acoustic emission (AE) waveforms were acquired simultaneously from all six transducers by a multi-channel oscilloscope. Emissions were recorded over the entire duration of each experiment, including cold compression, hydrostatic heating, deformation, and syndeformational heating sequence, then quenching and decompression. In fact, during the first stage of compression many AEs were recorded, which are attributed to powder compaction. From ca. 1 GPa to the final confining pressure (Table 1), no further AEs were recorded demonstrating that the AEs subsequently recorded during triaxial deformation are not caused by the compaction. Furthermore, previous deformation experiments with the same acoustic setup and the same sample assembly (Gasc et al., 2011) demonstrated that except for the porous alumina, deformation of the cell materials does not result in AEs, thus excluding the assembly as a cause for the AEs recorded in the present study.

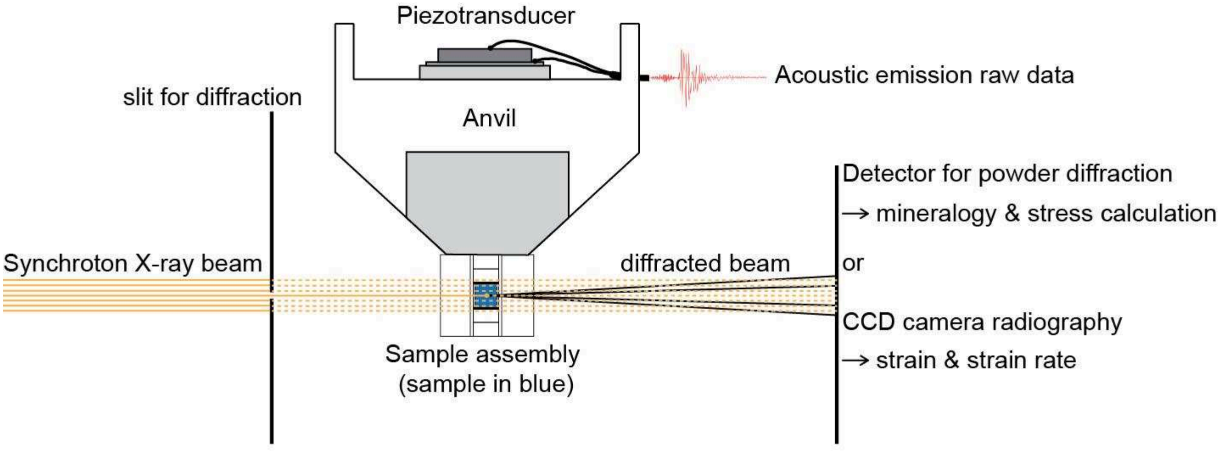

Figure 3: Schematic drawing of the experimental setup for the D-DIA experiments. For the sake of clarity only the upper vertical anvil is shown.

Locations of AEs were determined using a constant P-wave velocity of 8000 m/s determined by previous experiments with the same experimental setup (Schubnel et al., 2013). It is assumed that the travel time within each anvil remains constant over the course of an experiment. The travel time in the sintered diamond anvils was calculated to be 0.78 µs lower than in the WC anvils. Picking of the first arrivals was performed manually as the total number of AEs recorded during deformation was limited. The travel time was first corrected for anvil type, then the difference in arrival times between each pair of facing anvils was interpreted as a difference in travel-time within the sample assembly. The precision of the location of AEs along each of the three axis between the 3 anvil pairs lies within the sensor thickness of around 0.5 mm. The exact localization of each hypocenter in the sample would require a more sophisticated AE data analysis which lies beyond the scope of the present study.

Table 1: Experimental conditions of the six D-DIA experiments.

Sample	Experiment #	Starting material	P_c [GPa]	T range [K]	Strain rate [s^{-1}]	Maximum strain [%]
BS_3_1073	D1616	BS-bulk	3	583-1073	$4 \cdot 10^{-5}$	40
BS_1.5_1121	D1661	BS-bulk	1.5	649-1121	$7 \cdot 10^{-5}$	42
GLN_3.5_948	D1655	Gln-rich	3.5	659-948	$1 \cdot 10^{-5}$	42
GLN_2.5_927	D1618	Gln-rich	2.5	654-927	$2 \cdot 10^{-5}$	43
GLN_2.5_762	D1807	Gln-rich	2.5	656-762	$4 \cdot 10^{-5}$	37
LWS_2.5_925	D1667	Lws-rich	2.5	656-925	$3 \cdot 10^{-5}$	40

4. RESULTS

Our study comprises six deformation experiments using the three powders at the experimental conditions shown in Table 1. The sample nomenclature uses letters to represent the powder type, i.e. BS for blueschist bulk-rock, GLN for Gln-rich, and LWS for the Lws-rich powder, and numbers to give confining pressure in GPa and the quench temperature in K on the second and third position, respectively.

4.1 MECHANICAL DATA, IN-SITU XRD ANALYSIS, AND AE RECORDS

Differential stress decreased during syndeformational heating in all tests, i.e., independent of sample composition (Figure 4a-f). The recorded diffraction patterns reveal that the intensity of the Omp (-221) peak, the most intense peak of Omp, first increases above approximately 573 K but decreases above 700 K all the way to the end of the deformation (Figure 4g- i). The sample, which was hot-pressed in a piston-cylinder, initially shows more Omp, but follows the same Omp (-221) intensity evolution as the other samples hot-pressed in the D-DIA (Figure 4i). The Lws (002) peak completely disappears in bulk-rock samples (BS_1.5_1121, BS_3_1073) passing 734 and 1020 K, respectively (Figure 4d, j, f, l). The intensity of this peak decreases but does not vanish for samples enriched with either Lws (LWS_2.5_925) or Gln (GLN_2.5_927) quenched at around 830 K. The intensity remains constant in the lowest temperature experiment, quenched at 762 K well before the breakdown of Lws (GLN_2.5_762, Figure 4e, k).

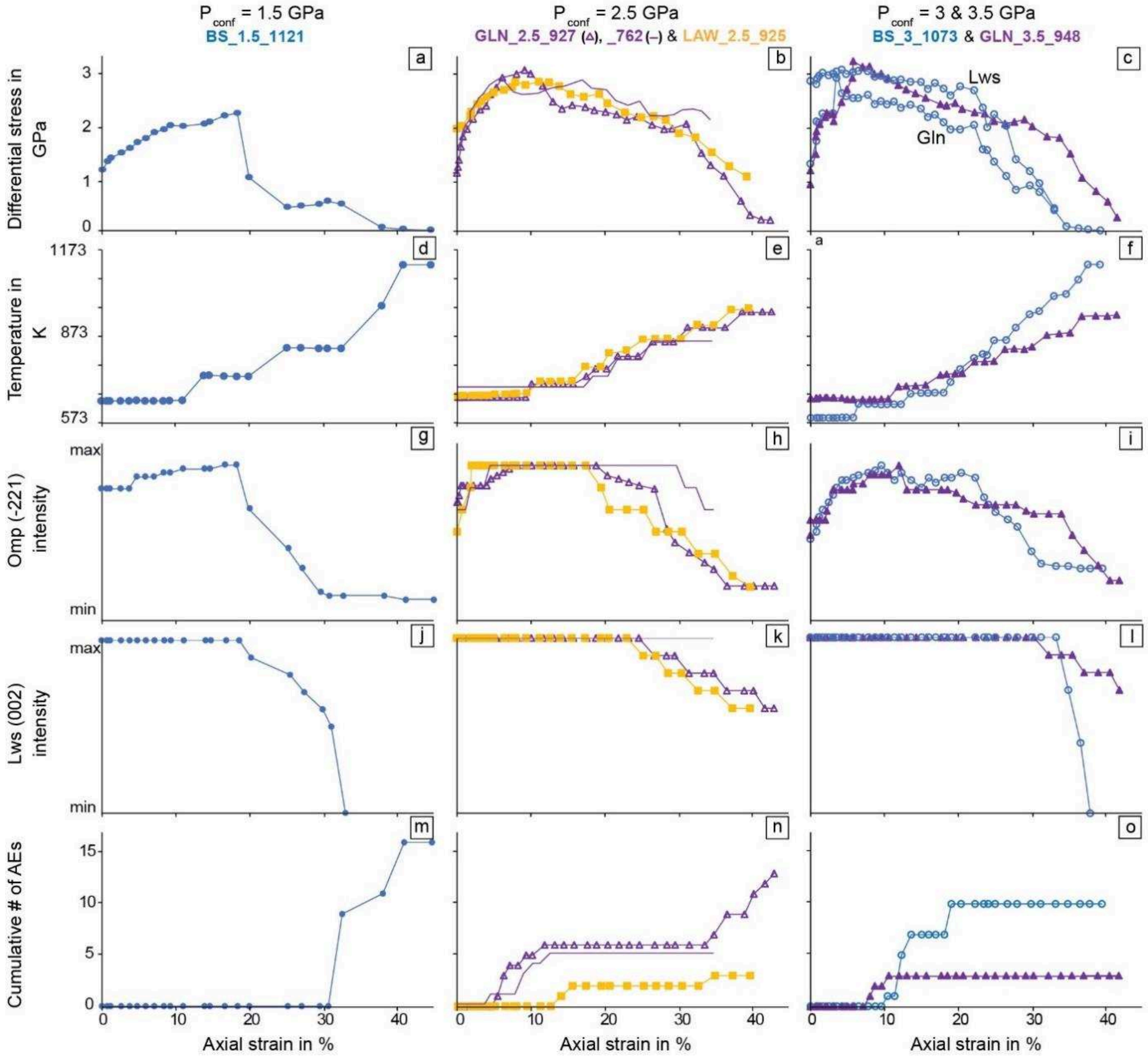

Figure 4: Mechanical data and peak intensities (proxy for phase proportion) from in-situ XRD, and record of AEs. The columns represent the low pressure (1.5 GPa), the intermediate pressure (2.5 GPa), and the high pressure (3 - 3.5 GPa) experiments (from left to right). Color code: bulk-rock in blue, Gln-rich powder in violet, Lws-rich powder in yellow. For the run BS_3_1073 it was possible to calculate the differential stress on Gln and Lws.

Acoustic emissions tend to occur in two clusters – one at low temperatures (around 640 to 700 K) and one at higher temperatures (approximately 830 to 1121 K) (Figure 4m-o), but not every experiment actually yield both clusters. For example, the experiment on a sample with bulk-rock composition (BS_1.5_1121) conducted at the lowest confining pressure of 1.5 GPa exhibits only the high-temperature cluster (Figure 4m), while a sample with the same composition deformed at a confining pressure of approximately 3 GPa only shows the low-temperature cluster (Figure 4o).

4.2 MICROSTRUCTURAL ANALYSES – SEM AND EMPA

Observed microstructures are similar for the suite of experiments. Only the bulk-rock sample deformed at the lowest confining pressure of 1.5 GPa (BS_1.5_1121) exhibits no fracture related to deformation (Figure 5g). We focus here on presenting four representative experiments, one representing each powder composition and additionally the low-pressure bulk-rock experiment (BS_1.5_1121), which shows no macroscopic strain localization. The microstructure of the sample quenched at the lowest temperature (GLN_2.5_762) is shown in the supplementary material in Figure S1. The Gln-enriched sample (GLN_2.5_927) and the Lws-enriched sample (LWS_2.5_925) were both deformed at a confining pressure of approximately 2.5 GPa (Table 1) and quenched before the complete breakdown of Lws expected from the computed pseudosection (Figure 2). The tests on the bulk-rock powder (BS_1.5_1121, BS_3_1073) were performed at 1.5 and 3 GPa, respectively, and quenched after the breakdown of Lws.

4.2.1 Microstructural and chemical analysis of the Gln-enriched sample

The Gln-enriched sample (GLN_2.5_927) exhibits two fractures starting in the lower corners of the sample extending diagonally towards the sample center (Figure 5a). Several narrow fractures, oriented parallel to the main fractures, dissect and offset grains of Lws and Omp1 (Figure 5b). The horizontal fracture is a typical decompression feature.

A narrow fracture parallel to a main fracture shows slightly brighter than average edges in backscattered electron (BSE) mode, indicating a change in chemistry (Figure 5c). Profiles across such a fracture show Ca enrichment in the brighter zones at the fracture edges (Figure 6b, d) related to the formation of a second generation of omphacite. In comparison to Omp1 of the starting material, this secondary omphacite, called Omp2 in the following, has a higher jadeite component of $X_{jd} \approx 0.7$. Mineral chemical data (wavelength-dispersive (WDX) and energy-dispersive X-ray spectrometry (EDX)) of Omp2 of all samples after deformation was plotted in a Ca-Al-Na ternary plot to demonstrate chemical variations of Omp2 (open circles in Figure 6c) and for the main phases Gln, Omp1, and Act of the natural blueschist (solid circles in Figure 6c). Strikingly, the composition of Omp2 plots between the Gln and Omp1 composition of the natural Lws-Bs (Figure 6c). These microstructural observations match well with the growth of the Omp (-221) peak during the first stage of the deformation (Figure 4g, h, i). The incipient breakdown of Lws is evidenced by its association with small epidote (Ep) needles - its dehydration product at low-pressure/high-temperature (LP/HT) conditions (Figure 5b).

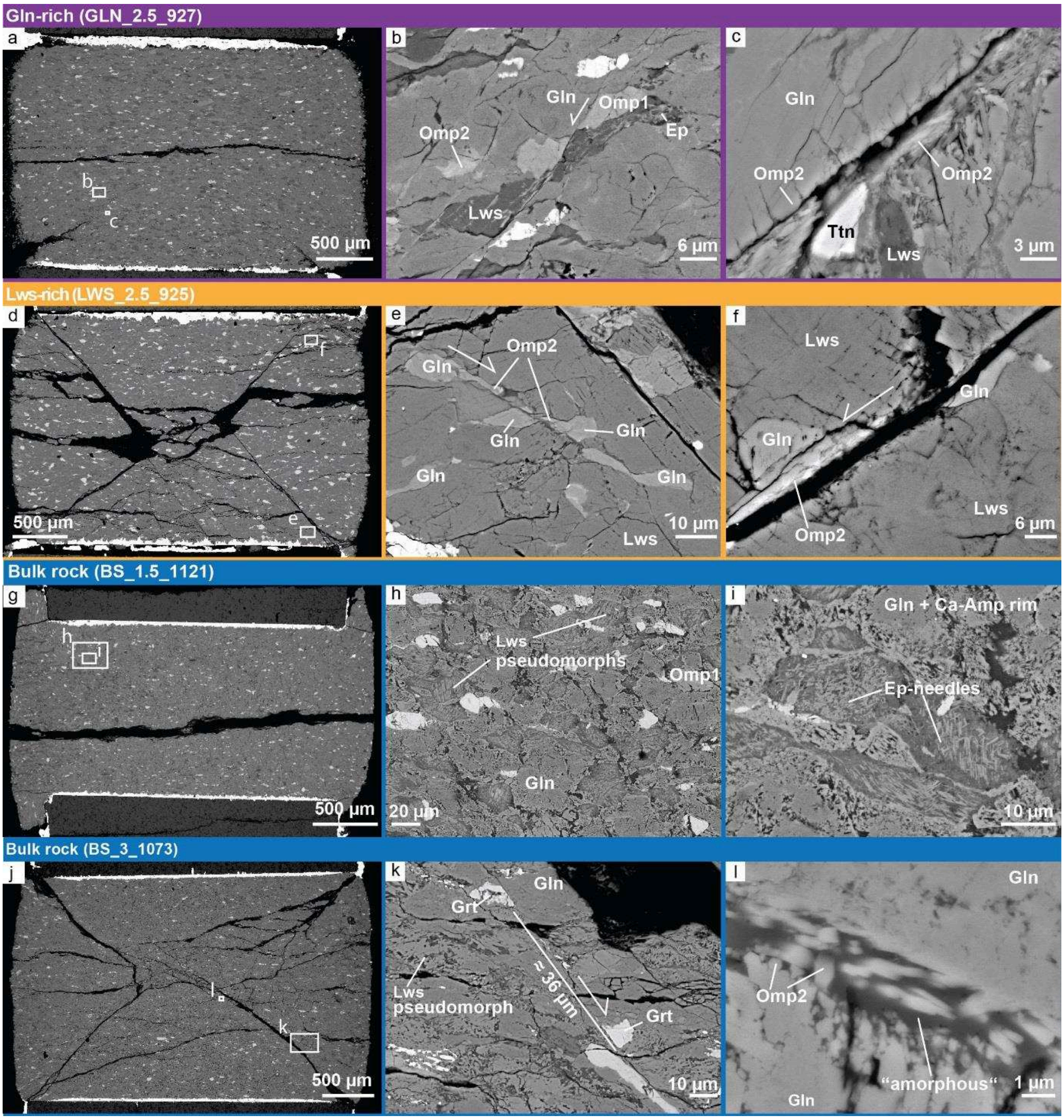

Figure 5: BSE images taken at the SEM using an acceleration voltage of 15 kV. The four rows represent the microstructure of the runs GLN_2.5_927 (a, b, c), LWS_2.5_925 (d, e, f), BS_1.5_1121 (g, h, i), and BS_3_1073 (j, k, l). The color represents the starting material used for the experiment (violet: Gln-rich, yellow: Lws-rich, and blue: bulk-rock). The BSE images a, d, g, and j are overview images of the samples GLN_2.5_927, LWS_2.5_925, BS_1.5_1121, and BS_3_1073, respectively, after deformation. The maximum compression direction σ_1 is oriented vertically on the images (parallel to the short edge).

4.2.2 Microstructure and mineral chemical analysis of the Lws-enriched sample

The Lws-enriched sample is cross-cut by two main fractures (Figure 5d). Several narrow fractures are oriented parallel or sub-parallel to these main fractures. Along one of these narrow fractures, Gln grains are observed that are dissected and offset (Figure 5e). The fracture edges exhibit a brighter than average contrast, resulting from Omp2 (Figure 5f). Most of the Omp2 crystals are located along fractures as was found for the Gln-enriched sample (GLN_2.5_927), too.

In most places, the fracture-filling material was lost during preparation of the samples, but some fractures are still filled by a material appearing dark in BSE mode (Figure 5e) implying that its average atomic number is smaller than the adjacent Lws and Gln crystals (Figure 5e). These zones are so narrow that EDX or WDX measurements give mixed analysis of filling material and rock matrix. After the interaction with the electron beam, this dark material always shows holes implying a poor crystallinity.

4.2.3 Microstructure and chemical analysis of the bulk-rock samples

The samples prepared from bulk-rock powder (BS_1.5_1121, BS_3_1073) were performed at two different confining pressures, 1.5 GPa and 3 GPa, and quenched after the breakdown of Lws. Pseudomorphs after Lws appear as patches filled with Ep needles (Figure 5i, k). Their occurrence is in good agreement with the thermodynamically expected stability of Lws (Figure 2). After deformation, the lowest pressure experiment (BS_1.5_1121) only shows a horizontal decompression crack, but no macroscopic strain localization (Figure 5g). Rims of Ca-Amp formed around Gln grains (Figure 5i). The high-pressure sample (BS_3_1073) is completely cross-cut by sample-size fractures (Figure 5j). Brighter zones along fractures, pores, and rims around Gln crystals were identified as Omp2 (Figure 5k, l). This sample also shows crystals offset along shear fractures (Figure 5k). Garnet grains exhibit growth zonation with Ca enrichment in the rim relative to its core (Figure 6a). A filled fracture between two Gln crystals shows tiny crystals “floating” within a dark material filling the fracture (Figure 5l) of which the larger ones, with an idiomorphic crystal shape, were classified as Omp2. Holes left after EDX and WDX measurements within this zone suggest that this dark material is poorly crystalline or amorphous. Observations on samples prepared in a piston-cylinder apparatus (as the hot-pressed sample BS_3_1073, see 1.3.6) show no evidence that this amorphous material represents a remnant of an incomplete reaction (Figure S2 in the supplementary material).

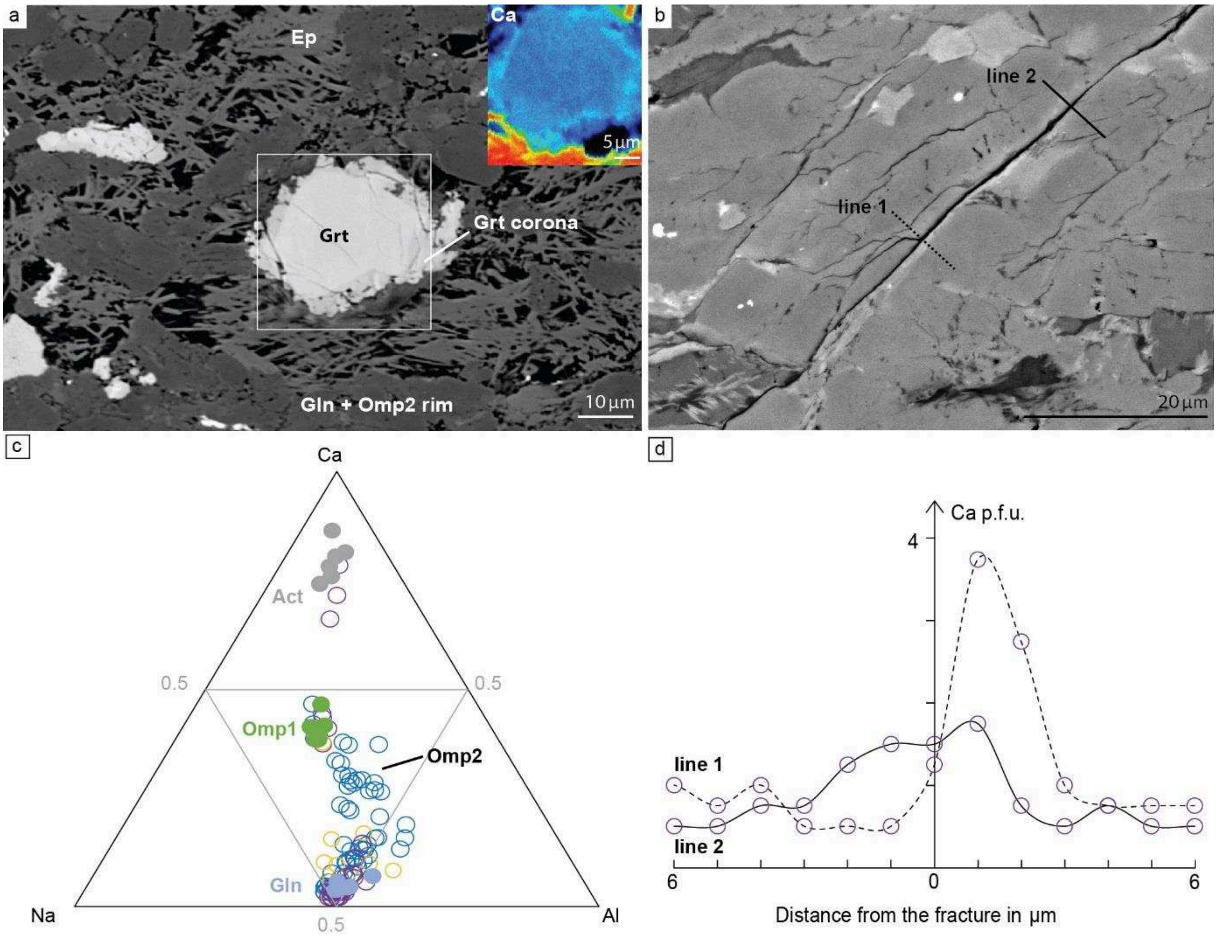

Figure 6: a) BSE image showing a brighter Grt core and a darker newly grown Grt corona. The white rectangle marks the position selected for an element distribution map, which is shown for Ca in the upper right corner. b) BSE image with the position of two line measurements, which correspond to the two profiles in the Ca p.f.u. over distance plot in d). c) Ca-Na-Al (a.p.f.u.) ternary plot for individual mineral compositions. Solid circles represent WDX analyses of Act (grey), Omp1 (green), and Gln (purple) from the natural Corsican blueschist. The open circles represent all WDX and EDX analyses on the deformed samples (blue: bulk-rock, violet: Gln –rich, yellow: Lws –rich). d) Two profiles *corresponding to the two lines in b) showing Ca enrichment of the region on the fracture's wall.*

4.3 NANOSTRUCTURAL ANALYSIS – TRANSMISSION ELECTRON MICROSCOPY (TEM)

The focused ion beam (FIB) sections for the Gln-enriched sample (GLN_2.5_927) were cut across a fracture with edges indicating Omp2 and Ca-Amp. The TEM images taken in bright field (BF) mode document the structure of the fracture at different scales (Figure 7). The sealed fracture appears brighter in the TEM images relative to the surrounding material indicating that this area is either thinner, poor in heavy atoms or less crystalline than the surrounding phases. The adjacent grains were identified as Ca-Amp and Omp2 (Figure 7b). The contact between the fracture filling-material and Omp2 and the absence of spots in the diffraction pattern reveal that the material filling out the fracture is amorphous (Figure 7c). Grains next to the fracture exhibit 120° triple junctions (Figure 7c).

The FIB section in the sample prepared from the bulk-rock sample (BS_3_1073) was cut across a narrow, sealed fracture along which a pair of displaced garnet crystal was found. The TEM images were also taken in BF mode. The most striking observation is the occurrence of a bright, according to diffraction analyses amorphous material appearing as bubbles (Figure 8a, d) or pockets in the matrix sometimes “trapped” within nests of Ep-needles (Figure 8e). These bubbles and pockets are completely absent in the Gln-enriched sample (GLN_2.5_927) quenched before the Lws-breakdown. The fracture, across which this FIB section was cut, appears to be filled by idiomorphic shaped garnet crystals varying in size (Figure 8f), surrounded by a bright, amorphous groundmass (Figure 8c, f, g). Amorphous material thus occurs at two structurally different sites, bubbles and pockets in the matrix or filling material in fractures. The grains next to the fracture were in most cases found to be Omp2 (Figure 8c, d). Unfortunately, it was not possible to obtain precise chemical analysis of the amorphous material in either FIB section.

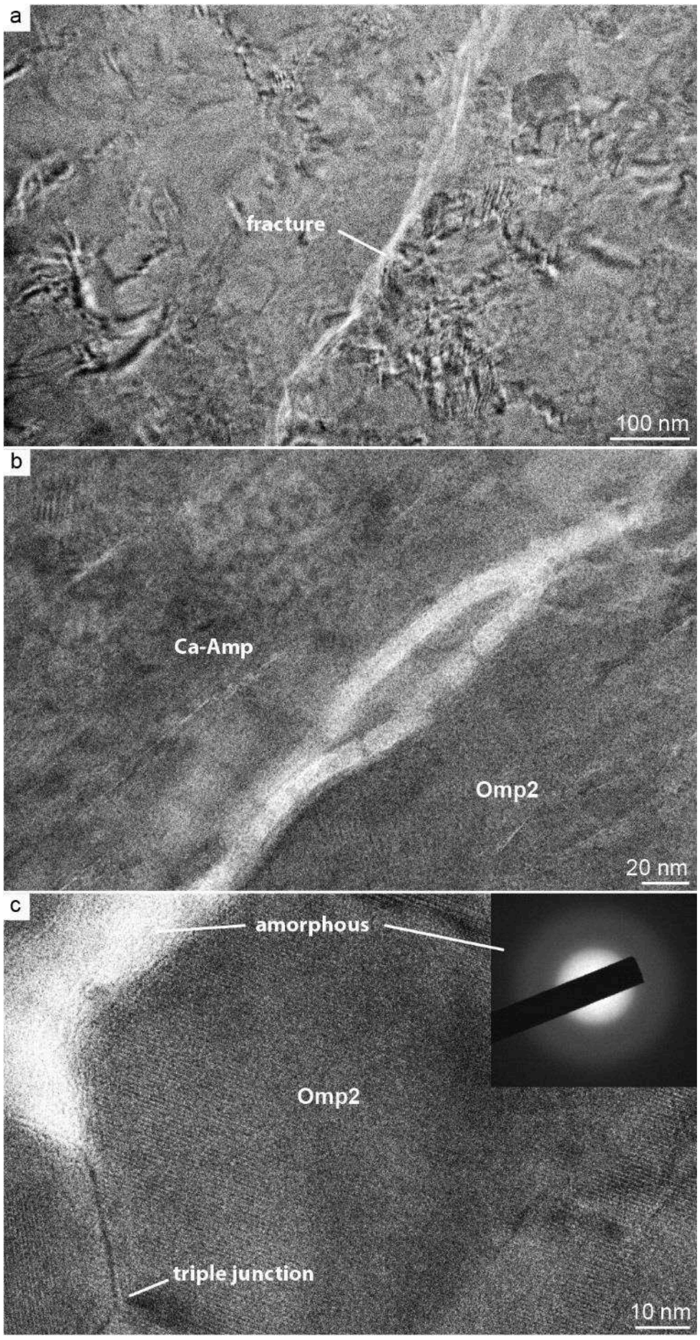

Figure 7: TEM images (BF mode) of the experiment GLN_2.5_927. a) The fracture appears brighter. b) High magnification image of the fracture. On the upper left side of the fracture a Ca-Amp was found, which shows a chemical composition close to actinolite. On the lower right side of the fracture Omp2 was detected. c) Triple junction between three grains identified as Omp2. The diffraction image in the upper right corner demonstrates that the material filling out the fracture is amorphous.

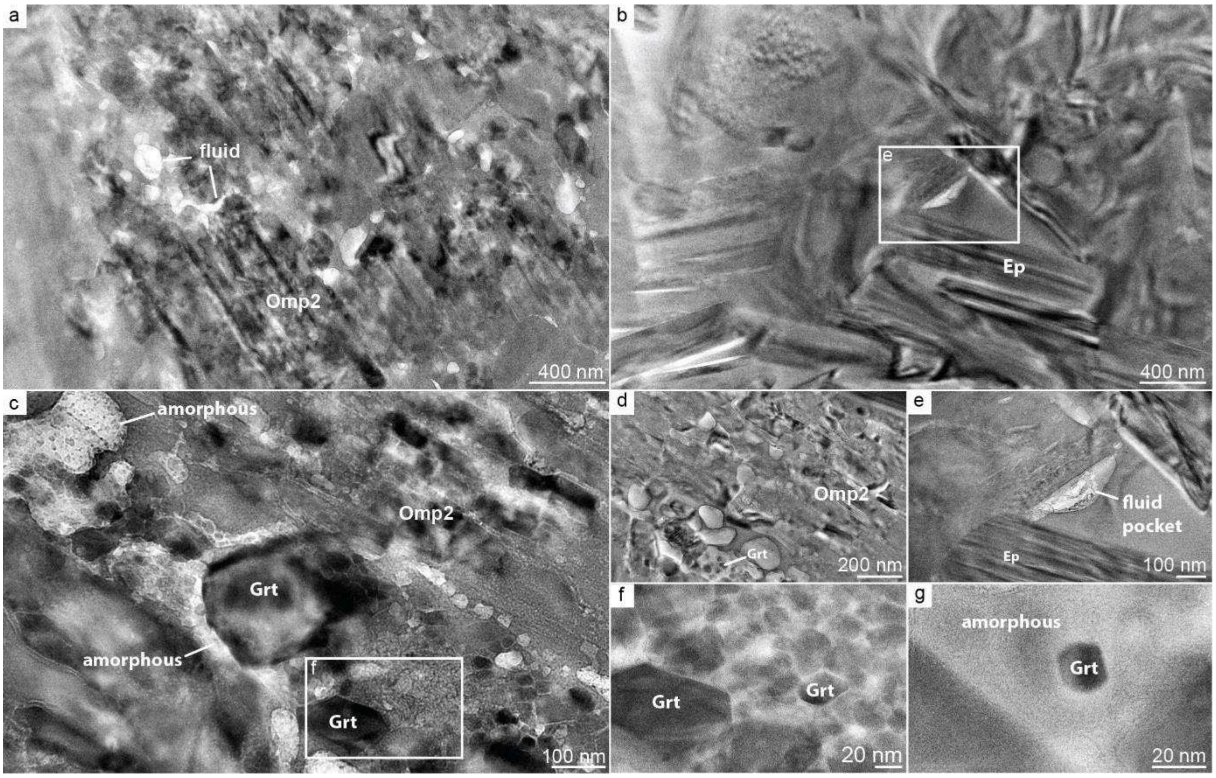

Figure 8: TEM images (BF mode) showing the nanostructure of the sample BS_3_1073. a) Omp2 crystal surrounded by fluid. b) Epidote needles, the dehydration product of Lws, trapping a fluid. The white rectangle shows the position of image e. c) High magnification image of the shear fracture across which the FIB section was cut. The fracture appears brighter and shows many idiomorphic Grt crystals *"floating" within an amorphous material. In the upper right corner just next to the fracture, small* idiomorphic crystals appear which were identified as Omp2. The white rectangle marks the position of the high magnification image shown in f. d) High magnification image of an Omp2 crystal. In the lower left corner of this image a brighter bubble-like structure appears, which incorporates darker small crystals. The bright material is amorphous and the tiny crystals are garnets. e) High magnification image of the fluid pocket of image b. f) High magnification image of the area marked with the white rectangle in c. A brighter material surrounds idiomorphic garnet crystals. A mixture of this bright, amorphous material and this idiomorphic Grt grains fills out the whole shear fracture. g) High magnification image of an *idiomorphic Grt crystal "floating" within amorphous material.*

5. DISCUSSION

5.1 COMPARISON BETWEEN EXPERIMENTS QUENCHED BEFORE AND AFTER LWS BREAKDOWN

The P-T path experienced by a sample during deformation controls its microstructure, phase assemblage and the occurrence of AEs (Figure 9). At high P_c (> 3 GPa), experiments only show an early low-temperature AE cluster at around 638–701 K. Experiments at intermediate P_c (around 2.5 GPa) exhibit two successive clusters, one at low temperatures of 638–701 K and one at high temperatures of around 831 – 927 K. Finally, the experiment at low P_c (< 1.5 GPa) only exhibits a high-temperature AE cluster beginning at around 873 K and not ceasing until the end of the experiment at 1121 K. Thus, the pattern of AE occurrence during syndeformational heating strongly depends on confining pressure, regardless of the powder type used for the experiment (Figure 4m, n, o).

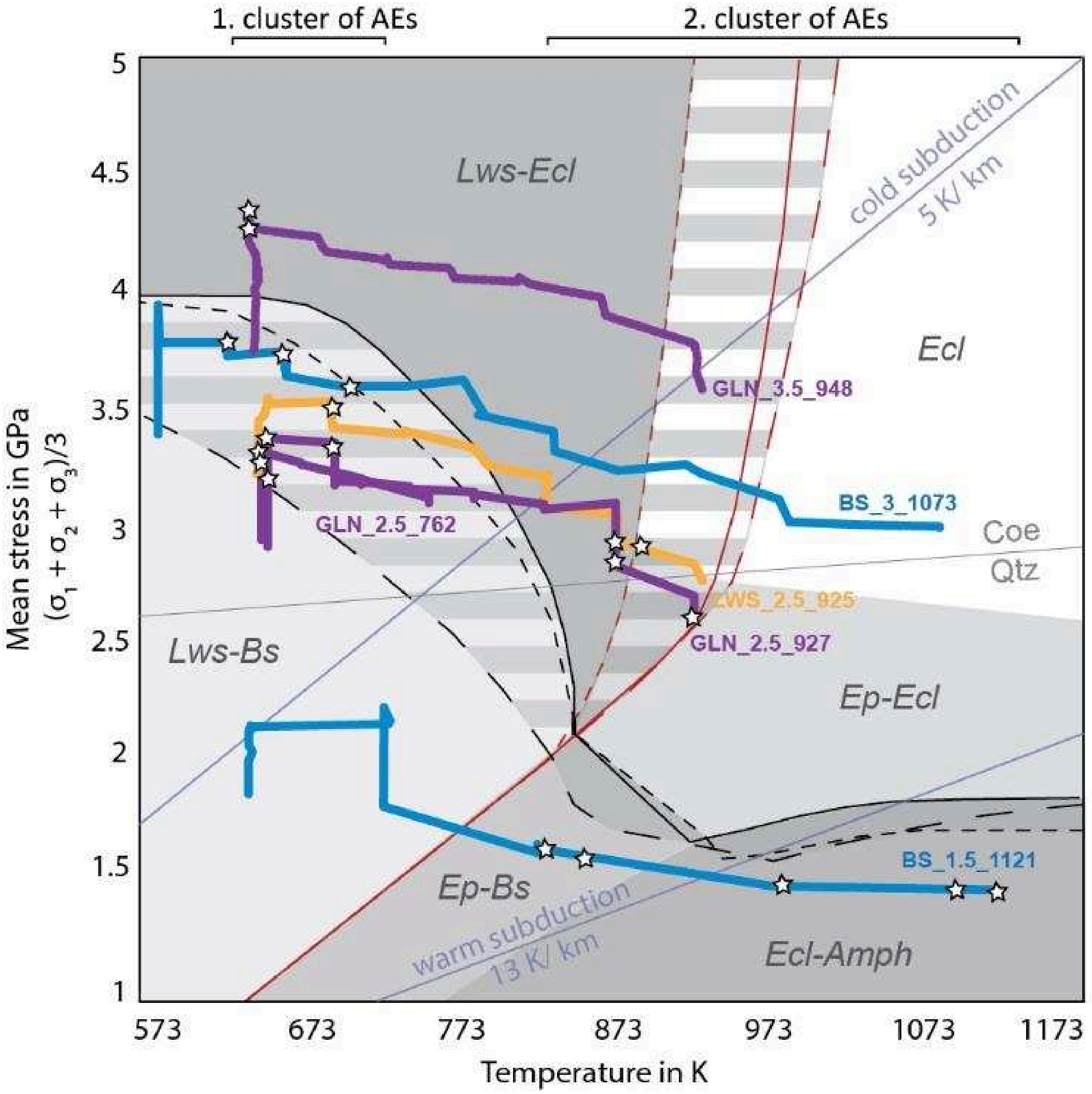

Figure 9: Mean stress versus temperature paths of all experiments superimposed to the same P-T pseudosection as in Figure 2. Acoustic emissions recorded during the deformation are represented as stars and often correlate with stress drops in the experimental mean stress versus T curves. Most of the low-temperature AEs occurred prior to stress drops. The high-temperature AEs were often recorded while heating and are not accompanied by bigger stress drops. Two clusters of AEs are observed – the first at low-temperature, and the second at high-temperature. The Amp- and the Lws-out reactions are indicated as in Figure 2. The low-temperature cluster of AEs plots within the transition area between Lws-Bs and Lws-Ecl. The second high-temperature cluster of AEs correlates with the breakdown of Lws.

The samples quenched after the Lws breakdown (BS_1.5_1121, BS_3_1073) differ from those quenched before (GLN_2.5_927, LWS_2.5_925) by the occurrence of pseudomorphs after Lws and bubbles composed of amorphous material interpreted as a quenched Lws-breakdown derived fluid. The appearance of Ep in the high pressure experiment (BS_3_1073) suggests either that the experiment was quenched at lower pressure than calculated, that Ep stability extends to higher pressures than thermodynamically predicted, or that it survives metastably (Figure 9). Except for the bubbles which are absent in the nanostructure of the Gln-enriched sample (GLN_2.5_927) micro- and nanostructures are similar for the Lws-enriched sample (LWS_2.5_925), the high-pressure bulk-rock sample (BS_3_1073) and the Gln-enriched sample (GLN_2.5_927). All three samples exhibit amorphous material filling fractures with adjacent Omp2 crystals (Figure 7c, 8c, d).

5.2 TRANSITION FROM LWS-BS TO LWS-ECL

Mean stress is used as a measure of thermodynamic pressure assuming that the change in slope of the equilibrium curves under non-hydrostatic conditions can be neglected (MacDonald, 1957; Kirby, 1987). During the first stage of deformation the calculated mean stress and the confining pressure differ by 0.7-1 GPa (Figure 9; Table 1). The difference decreases towards the end of the experiments due to the decrease in differential stress with increasing temperature (Figure 4a- f). The uncertainty regarding the relevant thermodynamic state variable does not affect the prognosis from the calculated P-T pseudosections that the experiments performed at $P_c > 2.5$ GPa enter the Lws-Ecl stability field except of the experiment performed at $P_c < 2$ GPa (Figures 2, 9).

The occurrence of the low-temperature AE cluster (shown as stars in Figure 9) matches the expected transition conditions for Lws-Bs to Lws-Ecl and the growth of the (-221) peak of omphacite (Figure 4). The powder diffraction pattern were taken from a small volume of the sample center and therefore do not quantify spatial stress heterogeneities in the samples, e.g., stress concentrations at the edges, that might lead to local variations in phase stability. Combined with the observation that Omp2 occurs along shear fractures, the correlation of formation of Omp2 with the low-temperature AE records suggests that its appearance at HP/LT triggered the brittle failure of the sample. The formation of Omp2 is related to the breakdown of Gln and the liberation of Ca derived from the successive disappearance of Lws at HP (Lws-Bs ≈ 19% Lws to Lws-Ecl ≈ 13% Lws, Figure 2).

The amorphous material filling the fractures suggests that slip along the fracture generated a melt (likely due to frictional heating) out of which idiomorphic crystals grew (Figures 8f, 7c). The absence of bubbles and pockets acts as evidence that the reaction initiating the brittle failure of the sample released no or only minor amounts of fluid in the Gln-enriched sample (GLN_2.5_927) quenched before the breakdown of Lws at HT (Figure 7). Therefore, we suppose that the grain-size reduction during the formation of Omp2 at HP/LT may have acted as weakening mechanism (Spray, 1995) and that nanocrystalline Omp2 at the edges of the fracture may represent remnants of the nucleation zones for failure (Figure 5c, f). Due to the small grain size the Omp2 crystals could only be distinguished in FIB sections at the TEM and therefore a significant quantification of the grain-size distribution was not possible. The notion of a rapid transformation to Omp2 is supported by the chemical and structural similarity between Omp2 and Gln and the recognition that Ca diffusion, derived from

Lws, is fast and possibly even enhanced by a high grain-boundary density during the reaction (Putnis, 2014).

Our observations of a high Jd content of Omp2 ($X_{jd} \approx 0.7$ %) texturally linked to Gln is in accord with the breakdown reaction for glaucophane, Gln → 2 Jd + Tlc, quoted by Carman and Gilbert, 1983. This exothermic reaction with an enthalpy of reaction of about -8.9 kJ (Holland, 1988) may facilitate the generation of a melt. However, HP talc (Tlc) was neither found in the XRD nor in any of the samples after deformation in contrast to its occurrence in MORB (Wei and Clarke, 2011). The absence of Tlc in our samples may result from (partial) melting of the reaction products during fast shear. The amorphous material should show a chemistry close to talc stoichiometry, but within this study it was not possible to precisely analyze the amorphous material.

The sample prepared with bulk-rock composition (BS_3_1073), which entered the Lws-Ecl stability field at HP/LT, showing only the low-temperature cluster of AEs is the only one which exhibits newly grown Ca-rich Grt coronas (Figure 6a) and idiomorphically shaped Grt crystals are "floating" within the amorphous fracture-filling materials (Figure 8). These newly formed Grt crystals can be linked to the metamorphic reaction 4 Gln + 3 Lws → 8 Jd + 3 Di + 3 Prp + 7 Qtz + 7 H_2O (Evans, 1990). The absence of Grt in all other samples might be related to a combination of its high nucleation barrier and the lack of initial Grt grains in the starting material acting as nucleation sites (Rubie, 1998). In samples where Grt is absent, the amorphous material filling the fractures might represent the sink for Fe and Mg liberated from Gln.

5.3 BREAKDOWN OF LAWSONITE

The P-T domain in which the high-temperature AEs were recorded matches with the thermodynamically expected breakdown of Lws (Figure 9). Therefore, we suppose that these AEs were triggered by the associated dehydration reaction. The microstructure of the sample deformed under the lowest confining pressure (BS_1.5_1121), that did not enter the stability field of Lws-Ecl (Figure 9), reveals the absence of macroscopic strain localization (Figure 5g). The recorded AEs are therefore either linked to fractures that are overprinted by ongoing plastic deformation or to other processes during dehydration, e.g. the formation of pseudomorphs after lawsonite or the growth of Ca-Amp rims around Gln (Figure 5h, i). The observation that most of the high-temperature AEs do not coincide with bigger stress drops and were mostly recorded while heating additionally strengthens the interpretation that these AEs were not caused by the brittle failure of the samples (Figure 9). In contrast to our observations, a recently published experimental study reported that dehydration of Lws leads to brittle fracturing accompanied by AEs (Okazaki and Hirth, 2016). Okazaki and Hirth 2016 used almost pure lawsonite samples and this difference in chemical composition of the starting material could explain the contrasting observations.

5.4 LINK TO NATURAL OBSERVATIONS

The relocalization of seismic events below Hokkaido, NE Japan, shows that they occur where the expected position of the subducting oceanic crust coincides with the upper Wadati-Benioff plane (Kita et al., 2006). Additional information from thermodynamic modeling implies a link between metamorphic reactions during the eclogitization of Lws-Bs and seismicity (Hacker et al., 2003; Kita et al., 2006). The involvement of the breakdown of hydrous phases (lawsonite and amphibole) during eclogitization leads to the proposition of dehydration embrittlement as possible mechanism for intermediate-depth seismicity (Hacker et al., 2003; Jung et al., 2004; Okazaki and Hirth, 2016). Yet, a recent study on source-parameter modelling and the energy budget of intermediate-depth earthquakes of the Bucaramanga Nest, Columbia (Prieto et al., 2013), concluded that the combination of narrow shear zones (less than 3 cm), rapid stress drops, and localized temperature increase is best explained by shear heating. A geochemical, petrological, and micro-textural study investigating the formation of pseudotachylites (PST) in metagabbros from Alpine Corsica comes to a similar conclusion (Deseta et al., 2014). The analyzed PSTs show different water contents ranging from 0–4 wt. % and the authors therefore suggest that the dehydration of hydrous phases is unlikely to trigger the formation of PST at high pressure. The authors explain the generation of melt due to fusion of the wall rock minerals. The amount of water present in the PST will therefore only depend on the availability of hydrous minerals in the fracture zone and their fusion during fast shear. Since PSTs are also be found in anhydrous rocks like lower crustal gabbros (Andersen et al., 1990; John et al., 2009) the instability related to Lws breakdown may well result from strain localization due to aspects of the reaction other than the dehydration, e.g. density change, grain-size reduction, and liberation of heat during reaction. Numerical simulations show that grain-size reduction and shear heating are the most likely causes for the formation of HP-pseudotachylites (John et al., 2009; Thielmann et al., 2015).

6. CONCLUSIONS

We experimentally reproduced the transition from lawsonite-blueschist to lawsonite-eclogite, the expected metamorphic evolution of a lawsonite-bearing blueschist during cold subduction. We did not find any evidence for a straightforward link between the breakdown of Lws and the failure of the samples that would support a mechanism akin to dehydration embrittlement. Instead we showed that metamorphic reactions during the transition from lawsonite-blueschist to lawsonite-eclogite can cause fracturing accompanied by AEs matching observations from seismicity locations in cold subduction zones, numerical simulations, and field observations. Shear fractures are decorated with newly grown omphacite grains, enriched in Jd content and texturally linked to Gln, which suggests that the breakdown reaction for glaucophane, Gln $\rightarrow$ 2 Jd + Tlc may have played a role in triggering shear instabilities. We argue that grain-size reduction due to the formation of nanocrystalline secondary omphacite grains and latent heat release by the reaction act in conjunction as weakening mechanism triggering the brittle failure of the samples. Shear heating fuses the wall rock next to the fracture surface and the melt is later quenched as amorphous material filling the fractures – a possible laboratory equivalent to natural pseudotachylites.

ACKNOWLEDGEMENT

The authors would like to thank Christian Chopin for providing the blueschist sample for this study. The research leading to these results has received funding from the People Program (Marie Curie Actions) of the European Union's Seventh Framework Program FP7/2017-2013/ under REA grant agreement n° 604713 and from the Agence Nationale pour la Recherche (project "DELF" ANR-12-JS06–0003). Portions of this work were performed at GeoSoilEnviroCARS (The University of Chicago, Sector 13), Advanced Photon Source (APS), Argonne National Laboratory. GeoSoilEnviroCARS is supported by the National Science Foundation - Earth Sciences (EAR-1128799) and Department of Energy- GeoSciences (DE-FG02-94ER14466). This research used resources of the Advanced Photon Source, a U.S. Department of Energy (DOE) Office of Science User Facility operated for the DOE Office of Science by Argonne National Laboratory under Contract No. DE-AC02-06CH11357.

Abramoff, M.D., Magalhaes, P.J., Ram, S.J., 2004. Image Processing with ImageJ. Biophotonics International, 11, 7, 36-42

Andersen, T., Austrheim, H., Burke, E.A.J., 1990. Fluid inclusions in granulites and eclogites from the Bergen Arcs, Caledonides of W. Norway. Mineral. Mag. 54, 145–158.

Austrheim, H., Andersen, T.B., 2004. Pseudotachylytes from Corsica: Fossil earthquakes from a subduction complex. Terra Nov. 16, 193–197. doi:10.1111/j.1365-3121.2004.00551.x

Bezacier, L., Reynard, B., Bass, J.D., Wang, J., Mainprice, D., 2010. Elasticity of glaucophane, seismic velocities and anisotropy of the subducted oceanic crust. Tectonophysics 494, 201–210. doi:10.1016/j.tecto.2010.09.011

Brudzinski, M.R., Thurber, C.H., Hacker, B.R., Engdahl, E.R., 2007. Global Prevalence of Double Benioff Zones. Science (80-.). 316, 1472–1474. doi:10.1126/science.1139204

Carman, J.H., Gilbert, M.C., 1983. Experimental studies on glaucophane stability. Am. J. Sci., 283-A, 414-437,

Comodi, P., Mellini, M., Ungaretti, L., Zanazzi, P.F., 1991. Compressibility and high pressure structure refinement of tremolite, pargasite and glaucophane. Eur. J. Mineral. 3, 485–499.

De Capitani, C., Petrakakis, K., 2010. The computation of equilibrium assemblage diagrams with Theriak/Domino software. Am. Mineral. 95, 1006–1016. doi:10.2138/am.2010.3354

Deseta, N., Ashwal, L.D., Andersen, T.B., 2014. Initiating intermediate-depth earthquakes: Insights from a HP-LT ophiolite from Corsica. Lithos 206-207, 127–146. doi:10.1016/j.lithos.2014.07.022

Dobson, D.P., Meredith, P.G., Boon, S. a., 2002. Simulation of subduction zone seismicity by dehydration of serpentine. Science 298, 1407–1410. doi:10.1126/science.1075390

Evans, B.W., 1990. Phase relations of epidote-blueschists. Lithos 25, 3–23. doi:10.1016/0024-4937(90)90003-J

Frohlich, C., 1989. The nature of deep-focus earthquakes. Ann. Rev. Earth Planet. Sci. 17, 227–254.

Gasc, J., Schubnel, A., Brunet, F., Guillon, S., Mueller, H.J., Lathe, C., 2011. Simultaneous acoustic emissions monitoring and synchrotron X-ray diffraction at high pressure and temperature: Calibration and application to serpentinite dehydration. Phys. Earth Planet. Inter. 189, 121–133. doi:10.1016/j.pepi.2011.08.003

Green, H. and Houston, H., 1995. the Mechanics Earthquakes 169–213.

Green, H.W., Burnley, P., 1989. A new self-organizing mechanism for deep-focus earthquakes. Nature

341, 733–737. doi:10.1038/341733a0

Gutenberg, B., Richter, C.F., 1945. Seismicity of the earth. Bull. Geol. Soc. Am. 56, 603–667. doi:10.1130/0016-7606(1945)56[603:SOTE]2.0.CO;2

Hacker, B.R., Peacock, S.M., Abers, G.A., Holloway, S.D., 2003. Subduction factory 2. Are intermediate-depth earthquakes in subducting slabs linked to metamorphic dehydration reactions? J. Geophys. Res. 108, 2030. doi:10.1029/2001JB001129

Hammersley, A.P., Svensson, S.O., Hanfland, M., Fitch, A.N., Hausermann, D., 1996. Two-dimensional detector software: From real detector to idealised image or two-theta scan. High Press. Res. 14, 235–248. doi:10.1080/08957959608201408

Hilairet, N., Wang, Y., Sanehira, T., Merkel, S., Mei, S., 2012. Deformation of olivine under mantle conditions: An in situ high-pressure, high-temperature study using monochromatic synchrotron radiation. J. Geophys. Res. Solid Earth 117. doi:10.1029/2011JB008498

Hirth, G., Tullis, J., 1994. The brittle-plastic transition in experimentally deformed quartz aggregates. J. Geophys. Res. 99, 11731–11747. doi:10.1029/93JB02873

Hobbs, B.E., Ord, A., 1988. Plastic instabilities: Implications for the origin of intermediate and deep focus earthquakes. J. Geophys. Res. Solid Earth 93, 10521–10540. doi:10.1029/JB093iB09p10521

Holland, T.J.B., 1988. New Heat Capacity and Thermodynamic Data. Cell 134–142.

Holland, T.J.B., Redfern, S.A.T., Pawley, A.R., 1996. Volume behavior of hydrous minerals at high pressure and temperature: II. Compressibilities of lawsonite, zoisite, clinozoisite, and epidote. Am. Mineral. 81, 341–348.

Jenkins, D.M., Corona, J.C., 2006. Molar volume and thermal expansion of glaucophane. Phys. Chem. Miner. 33, 356–362. doi:10.1007/s00269-006-0083-0

John, T., Medvedev, S., Rüpke, L.H., Andersen, T.B., Podladchikov, Y.Y., Austrheim, H., 2009. Generation of intermediate-depth earthquakes by self-localizing thermal runaway. Nat. Geosci. 2, 137–140. doi:10.1038/ngeo419

John, T., Schenk, V., 2006. Interrelations between intermediate-depth earthquakes and fluid flow within subducting oceanic plates: Constraints from eclogite facies pseudotachylytes. Geology 34, 557–560. doi:10.1130/G22411.1

Jung, H., Green II, H.W., Dobrzhinetskaya, L.F., 2004. Intermediate-depth earthquake faulting by dehydration embrittlement with negative volume change. Nature 428, 545–549. doi:10.1038/nature02412

Kelemen, P.B., Hirth, G., 2007. A periodic shear-heating mechanism for intermediate-depth earthquakes in the mantle. Nature 446, 787–790. doi:10.1038/nature05717

Kim, D., Katayama, I., Michibayashi, K., Tsujimori, T., 2013. Rheological contrast between glaucophane and lawsonite in naturally deformed blueschist from Diablo Range, California. Isl. Arc 22, 63–73. doi:10.1111/iar.12003

Kirby, S.H., 1987. Localized polymorphic phase transformations in high-pressure faults and applications to the physical mechanism of deep earthquakes. J. Geophys. Res. 92, 13789. doi:10.1029/JB092iB13p13789

Kita, S., Okada, T., Nakajima, J., Matsuzawa, T., Hasegawa, A., 2006. Existence of a seismic belt in the upper plane of the double seismic zone extending in the along-arc direction at depths of 70-100 km beneath NE Japan. Geophys. Res. Lett. 33, 1–5. doi:10.1029/2006GL028239

MacDonald, G.J.F., 1957. Thermodynamics of solids under non-hydrostatic stress with geologic applications. Am. J. Sci. doi:10.2475/ajs.255.4.266

Mao, Z., Jiang, F., Duffy, T.S., 2007. Single-crystal elasticity of zoisite Ca2Al3Si3O12 (OH) by Brillouin scattering. Am. Mineral. 92, 570–576. doi:10.2138/am.2007.2329

Merkel, S., Hilairet, N., 2015. Multifit / Polydefix : a framework for the analysis of polycrystal deformation using X-rays. J. Appl. Crystallogr. 48, 1307–1313. doi:10.1107/S1600576715010390

Okazaki, K., Hirth, G., 2016. Dehydration of lawsonite could directly trigger earthquakes in subducting oceanic crust. Nature 530, 81–4. doi:10.1038/nature16501

Peacock, S.M.S., Wang, K., 1999. Seismic consequences of warm versus cool subduction metamorphism: examples from southwest and northeast japan. Science 286, 937–9. doi:10.1126/science.286.5441.937

Prieto, G.A., Florez, M., Barrett, S.A., Beroza, G.C., Pedraza, P., Blanco, J.F., Poveda, E., 2013. Seismic evidence for thermal runaway during intermediate-depth earthquake rupture. Geophys. Res. Lett. 40, 6064–6068. doi:10.1002/2013GL058109

Putnis, a., 2014. Why Mineral Interfaces Matter. Science (80-.). 343, 1441–1442. doi:10.1126/science.1250884

Raleigh, C.B., Paterson, M.S., 1965. Experimental deformation of serpentinite and its tectonic implications. J. Geophys. Res. 70, 3965. doi:10.1029/JZ070i016p03965

Raterron, P., Merkel, S., Holyoke, C.W., 2013. Axial temperature gradient and stress measurements in the deformation-DIA cell using alumina pistons. Rev. Sci. Instrum. 84. doi:10.1063/1.4801956

Rubie, D.C., 1998. Disequilibrium during metamorphism: the role of nucleation kinetics. What Drives Metamorph. Metamorph. React. Spec. Publ. 138 138, 199–214. doi:10.1144/GSL.SP.1996.138.01.12

Schubnel, A., Brunet, F., Hilairet, N., Gasc, J., Wang, Y., Green, H.W., 2013. Deep-focus earthquake analogs recorded at high pressure and temperature in the laboratory. Science 341, 1377–80. doi:10.1126/science.1240206

Singh, A.K., Balasingh, C., Mao, H., Hemley, R.J., Shu, J., 1998. Analysis of lattice strains measured under nonhydrostatic pressure. J. Appl. Phys. 83, 7567. doi:10.1063/1.367872

Spray, J.G., 1995. Pseudotachylyte controversy: fact or friction? Geology. doi:10.1130/0091-7613(1995)023<1119:PCFOF>2.3.CO

Thielmann, M., Rozel, A., Kaus, B.J.P., Ricard, Y., 2015. Intermediate-depth earthquake generation and shear zone formation caused by grain size reduction and shear heating. Geology 43, 791–794. doi:10.1130/G36864.1

Uchida, T., Funamori, N., Yagi, T., 1996. Lattice strains in crystals under uniaxial stress field. J. Appl. Phys. 80, 739–746. doi:10.1063/1.362920

Vitale Brovarone, A., Groppo, C., Hetényi, G., Compagnoni, R., Malavieille, J., 2011. Coexistence of lawsonite-bearing eclogite and blueschist: Phase equilibria modelling of Alpine Corsica metabasalts and petrological evolution of subducting slabs. J. Metamorph. Geol. 29, 583–600. doi:10.1111/j.1525-1314.2011.00931.x

Wang, Y., Durham, W.B., Getting, I.C., Weidner, D.J., 2003. The deformation-DIA: A new apparatus for high temperature triaxial deformation to pressures up to 15 GPa. Rev. Sci. Instrum. 74, 3002–3011. doi:10.1063/1.1570948

Wei, C.J., Clarke, G.L., 2011. Calculated phase equilibria for MORB compositions: A reappraisal of the metamorphic evolution of lawsonite eclogite. J. Metamorph. Geol. 29, 939–952. doi:10.1111/j.1525-1314.2011.00948.x

Whitney, D.L., Evans, B.W., 2010. Abbreviations for names of rock-forming minerals. Am. Mineral. 95, 185–187. doi:10.2138/am.2010.3371

SUPPLEMENTARY MATERIAL

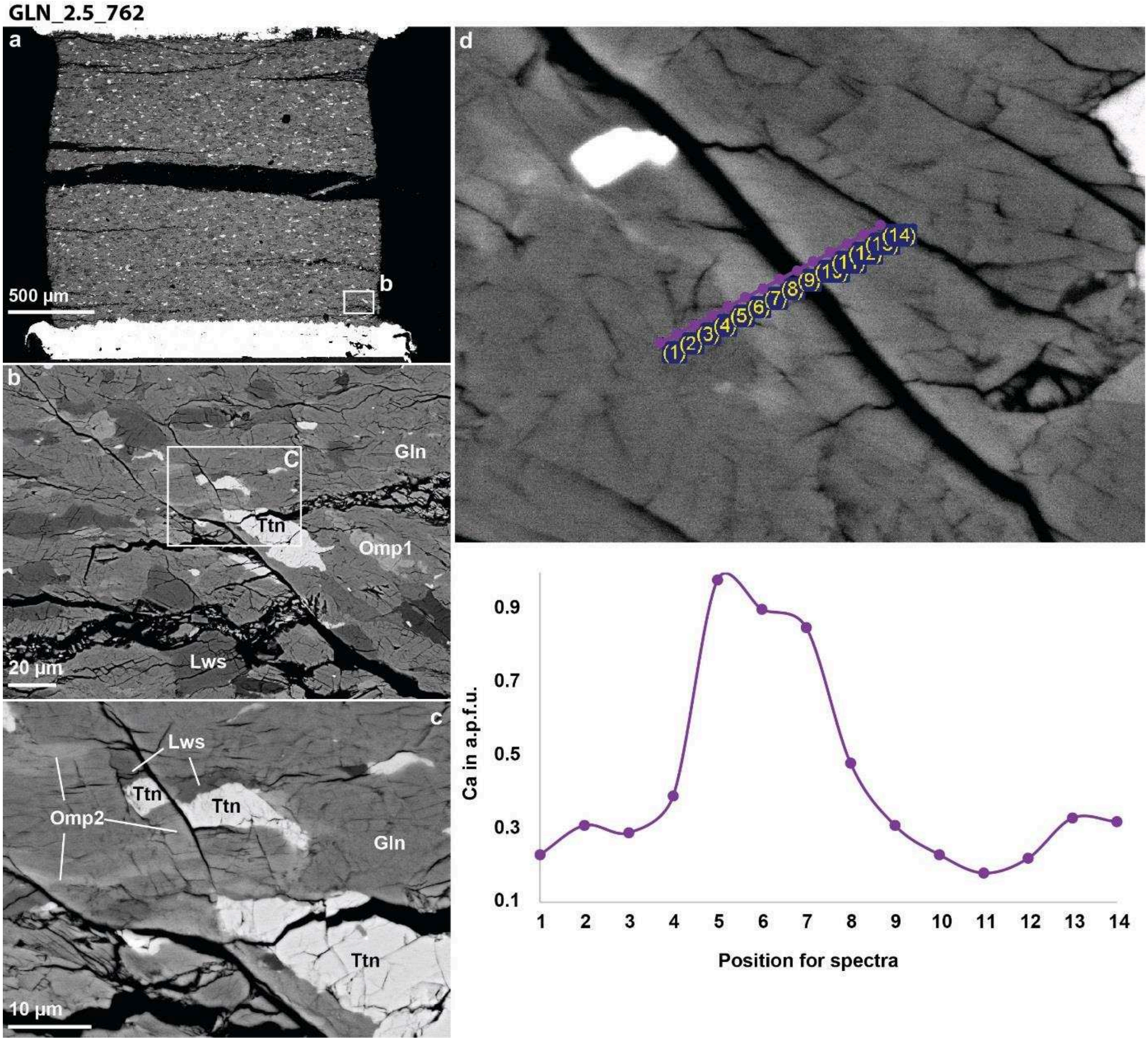

Figure S1: Microstructure and chemical analyses of the sample GLN_2.5_762. All images were taken in BSE mode at the SEM. a) Overview of the sample after deformation and the position of image b. b) Showing a fracture from the sample corner towards its center. c) Showing a high magnification image of the area marked in image b and dispalced Ttn grains along the fracture. d) The borders of the fracture appear brighter in BSE mode and the corresponding line measurement below demonstrates, that one side of the fracture is clearly enriched in Ca.

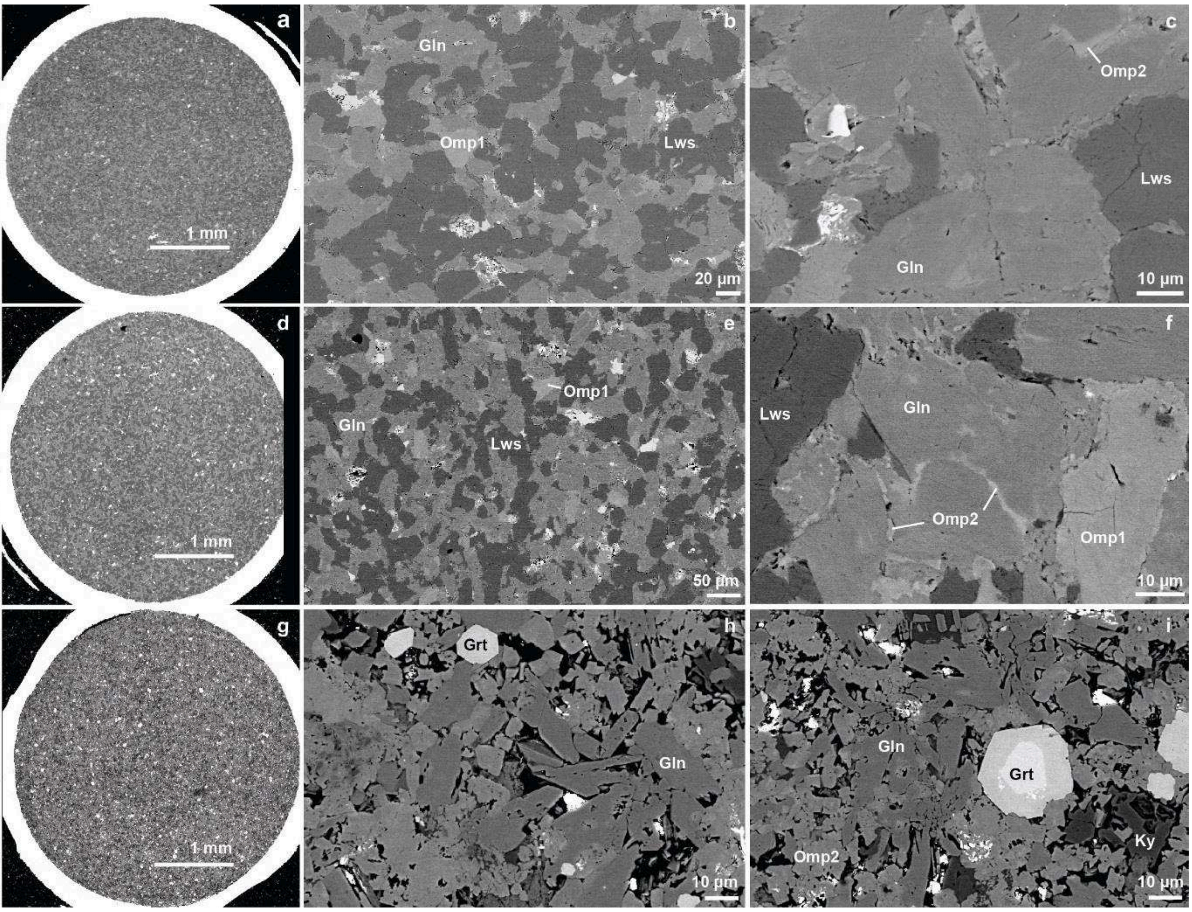

Figure S2: Three different piston-cylinder experiments, performed at 3 GPa and 550 °C, 650 °C, and 750 °C respectively. The bulk-rock powder of the natural Lws-blueschist was taken as starting material. The BSE images of the samples clearly demonstrate the proceeding eclogitization of the Lws-blueschist with increase in temperature. The powder, hot-pressed at 550 °C (a-c) shows only few newly grown omphacite rims around Gln grains. In the run at 650 °C the growth of Omp as coronas around Gln is even more advanced. In both runs lawsonite was still stable. The experimental run at 750 °C (g-i) shows no more lawsonite, but the eclogite-facies mineral assemblage omphacite and garnet. The porosity increase due to the denser mineral assemblage of eclogite is also visible (g-i). No evidence for an amorphous material was found in any sample.

3.2 Discussion of all experimental results

3.2.1 Incomplete or frictional melting?

The hydrostatic experiments on the Corsican blueschist demonstrate the progressive eclogitization of a lawsonite-bearing blueschist with increasing temperature (Figure 41), but show no evidence for incomplete melting that could explain the appearance of amorphous material filling out the fractures of two investigated D-DIA samples (Figures 7; 8 in paper). Therefore the material that can be found in the nanostructures of the samples GLN_2.5_927 and BS_3_1043 has to derive from frictional melting of the wall rock due to fast slip. The static experiments on the Tianshan powder show no evidence that any mineral reaction occurred under the prevailing experimental conditions (Figure 42).

3.2.2 High-pressure faulting of lawsonite-bearing blueschist

All samples, regardless of the starting material (powder or drill core) and the press type (D-DIA or Griggs) used for the deformation experiments, reveal brittle failure if the sample entered the lawsonite-eclogite stability field during deformation (Figure 9 paper). These samples consistently demonstrate a higher amount of (nanocrystalline) omphacite along the shear fractures (Figures 5; 6; 7; 8) compared to regions showing no localized strain (Figures 5g). In the D-DIA experiments the transition from lawsonite-blueschist to lawsonite-eclogite at HP/LT conditions was accompanied by AEs. Therefore it was concluded, that the growth of omphacite, demonstrating the transition from Lws-Bs to Lws-Ecl, enabled fast brittle failure due to grain-size reduction in conjunction with densification during eclogitization. Since the Griggs experiments on larger samples using the same powders, but also on intact drill core sample BSd_3_823, reveal similar microstructural observation (Figures 46; 51), it can be concluded that failure also occurred due to densification and grain-size reduction during eclogitization of Lws-Bs within the stability field of lawsonite (Figure 55).

3.2.3 Lawsonite breakdown – dehydration of the samples

Microstructures of the samples that either did not enter the stability field of Lws-Ecl (BS_1.5_1121) or where the dehydration was triggered right after the sample entered the Lws-Ecl stability field, show either no evidence (BS_1.5_1121) for strain localization or the onset of brittle failure that is overprinted by the dehydration products (Figures 5g, 52b). This implies that the breakdown of lawsonite softens rather than embrittles the samples.

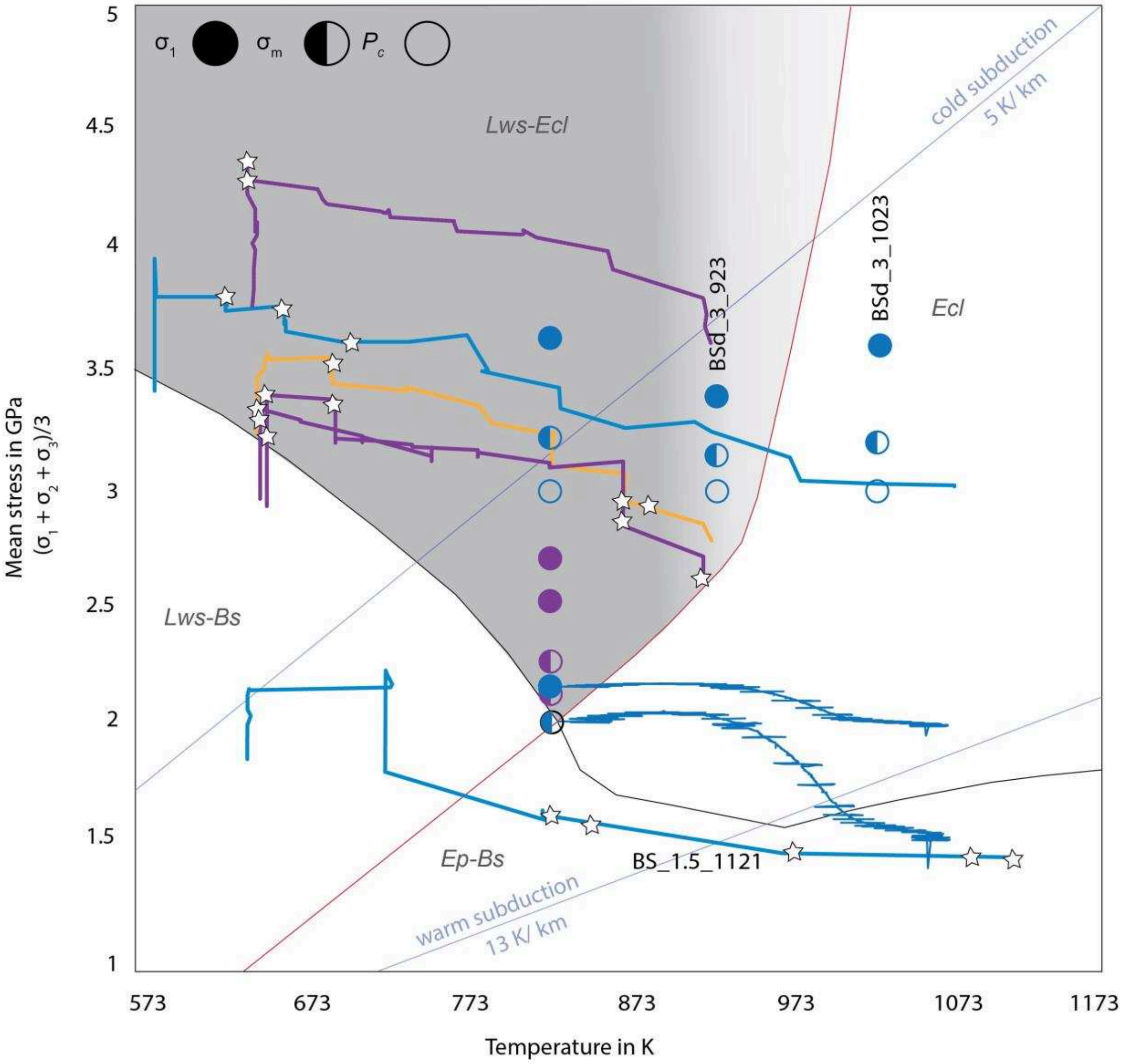

Figure 55: All deformation experiments on the lawsonite-bearing blueschist superimposed on the P-T pseudosection. The grey shaded area shows the region of brittle failure in the stability field of Lws-Ecl. Drill core samples BSd_3_923, BSd_3_1023 and the D-DIA sample BS_1.5_1121 reveal no microstructural evidence for high-pressure faulting. Sample BSd_3_923 was deformed in the stability field of Lws-Ecl, but the temperature under which the experiment was conducted was probably too high to favor ductile instead of brittle deformation.

3.2.4 Brittle/ductile behavior of lawsonite-blueschist drill-core samples

Microstructural observations of all three drill core samples reveal no evidence that lawsonite became unstable during deformation, although the sample BSd_3_1023 was deformed outside the stability field of lawsonite (Figure 55). This could be due to the larger grain-size and a resulting decrease in reacting surface of the lawsonite crystals relative to those of the Lws-blueschist powders. Why some drill core samples show shear fractures (BSd_3_823 in Figure 46E) and others shear bands (BSd_3_923 in Figure 48, BSd_3_1023 in Figure 49L) may be explained by the differences in temperature. The drill core sample BSd_3_823 deformed in the Griggs rig under the lowest temperature of 823 K, within the stability field of lawsonite, exhibits fractures cutting through the sample. In this HP/LT deformation experiments the fractures are systematically decorated with omphacite grains (Figures 46c). The drill core sample deformed under temperatures > 823 K show shear bands. In the experiment BSd_3_1023, performed under the highest temperatures, dissected and displaced garnet crystals can be found along these shear bands (Figure 49M). This implies that the crystals forming these bands, mostly glaucophane, lawsonite and omphacite, show ductile, and garnet crystals brittle deformation under the prevailing experimental conditions.

3.2.5 Influence of mineralogy

Compared to the lawsonite-bearing blueschist samples from Corsica, the Tianshan blueschist deformation experiments reveal no unequivocal evidence for brittle failure under high-pressure. Both experiments were performed under the same experimental conditions, but reveal different mechanical as well as microstructural results (Figures 43; 53; 54). The sample height, the piston used and the salt layer thickness were all very similar. The microstructure of the sample TS-BS_2_823a shows fractures (Figure 53) and the run TS-BS_2_823b reveals no fracturing (Figure 54). A possible reason for this discrepancy between both runs could be the alignment of the sample. The BSE images of both samples after deformation show that sample TS-BS_2_823a slightly turned during deformation (Figure 53). This misalignment of the sample could produce higher stresses in some regions. In these regions stress could have been locally high enough so that the sample crosses the breakdown reaction of glaucophane that could have triggered faulting. Although no microstructural evidence for metamorphic reaction assisted faulting could be found in this sample. The reason why sample TS-BS_2_823b shows no fractures related to deformation could be that it did not cross any expected phase boundary (Figure 56).This would strengthen the theory of glaucophane breakdown as a cause for brittle failure in blueschists under high-pressure conditions.

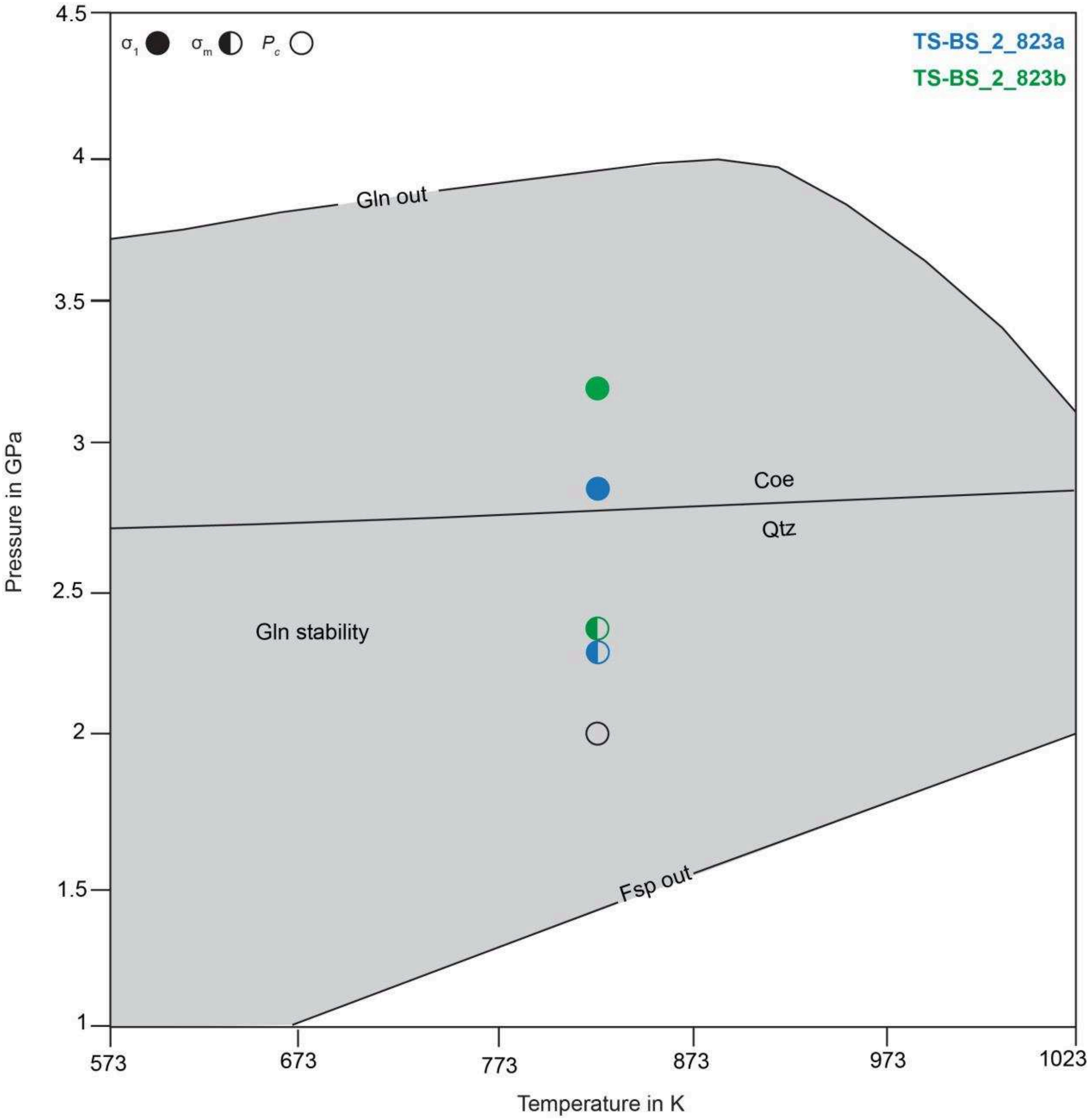

Figure 56: Griggs experiments on Tianshan blueschist powders (TS-BS_2_823a in blue and TS-BS-2_823b in green) superimposed on the P-T pseudosection of the bulk rock chemistry of the Tianshan blueschist (Klemd et al., 2015) calculated using Theriak Domino.

3.3 LINK TO NATURE

3.3.1 Geophysical observations

The combination of the experimental results with geophysical observations shows that there is a very good correlation between the P-T range in which seismic events are recorded in nature in cold subduction zones, e.g. NE Japan (circles in Figure 57), and the recorded AEs during the transition from Lws-blueschist to Lws-eclogite in the laboratory (blue stars in Figure 57). Okazaki & Hirth, 2016 state that their experimental results on almost pure lawsonite samples point towards dehydration embrittlement as a viable weakening mechanism to explain intermediate-depth seismicity in cold subduction zones. However, the authors note that seismic events at intermediate-depth are also recorded in the oceanic crust in warm subduction zones where lawsonite is absent. Under these conditions the prograde metamorphism path will cross the epidote-blueschist field (Peacock and Wang, 1999). The experimental observations of this thesis point towards densification and grain-size reduction during eclogitization as possible weakening mechanism to trigger intermediate-depth earthquakes in subduction zones. These processes are independent of the hydration state of the blueschist and therefore represent a viable mechanism to explain intermediate-depth seismicity in both types of subduction zones.

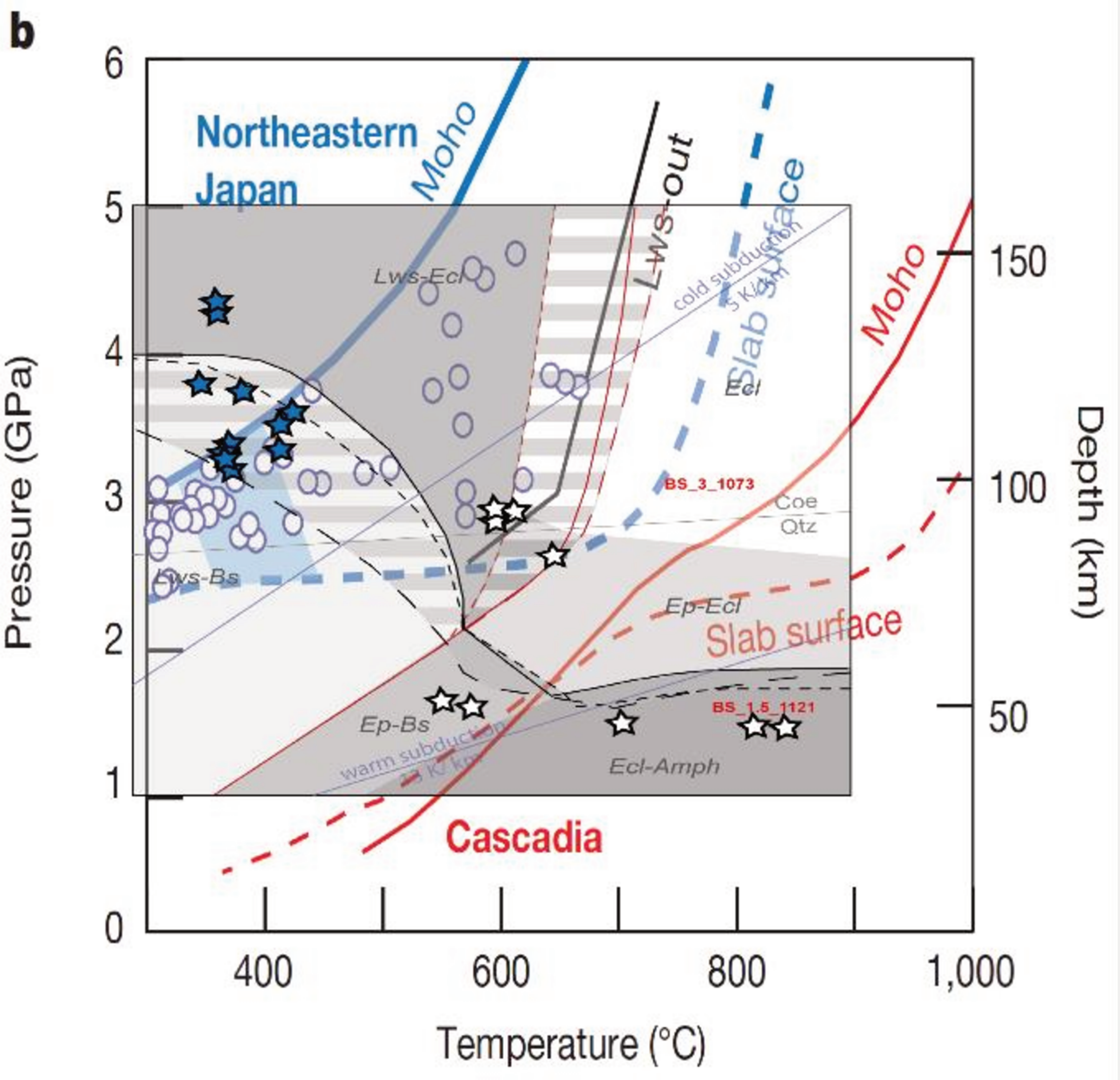

Figure 57: Modified from Okazaki & Hirth (2016) and combined with Fig. from Incel et al. (2017). Blue circles represent seismic events in nature and the stars show the AEs recorded during deformation of the Lws-blueschist samples in the D-DIA apparatus.

3.3.2 Field observations

A preliminary field trip to the Alpine part of Corsica was made in order to document the expression of syn-eclogitization strain localization under natural conditions. For the geological and petrographic background of this area the interested reader is referred to Healy et al., 2009, Ravna et al., 2010, Vitale Brovarone et al., 2011, and Vitale Brovarone et al., 2013.

Electron images taken in BSE mode at the SEM and qualitative EDX analyses of the sample COSI-16_05 reveal that the matrix is mainly composed of glaucophane, lawsonite, and omphacite. Minor phases are titanite and garnet. The occurrence of omphacite in the matrix together with glaucophane and lawsonite as main matrix phases points to lawsonite-blueschist that underwent higher pressure conditions and partially transformed to lawsonite-eclogite. Lenses composed of garnet and omphacite follow the foliation of the sample, highlighted by aligned titanite (Figure 58). Black holes within these bands are interpreted as holes from garnet crystals that popped out during sample preparation (Figure 58). Measurements of a structure that cross-cuts the sample’s foliation (white rectangle in Figure 58) reveal it is mainly composed of two phases identified as lawsonite and Ca-amphibole (Figure 59). Due to the strong crystal orientation of idiomorphically shaped lawsonite crystals in this zone they seem to flow within a matrix of Ca-amphiboles (Figure 59). Inside this band at least one larger fracture appears, which first cross-cuts but later turns into the foliation of the sample (Figures 58, 59). The idiomorphic lawsonite crystals appear to have the same orientation (in this two-dimensional view) as the fractures (Figure 59).

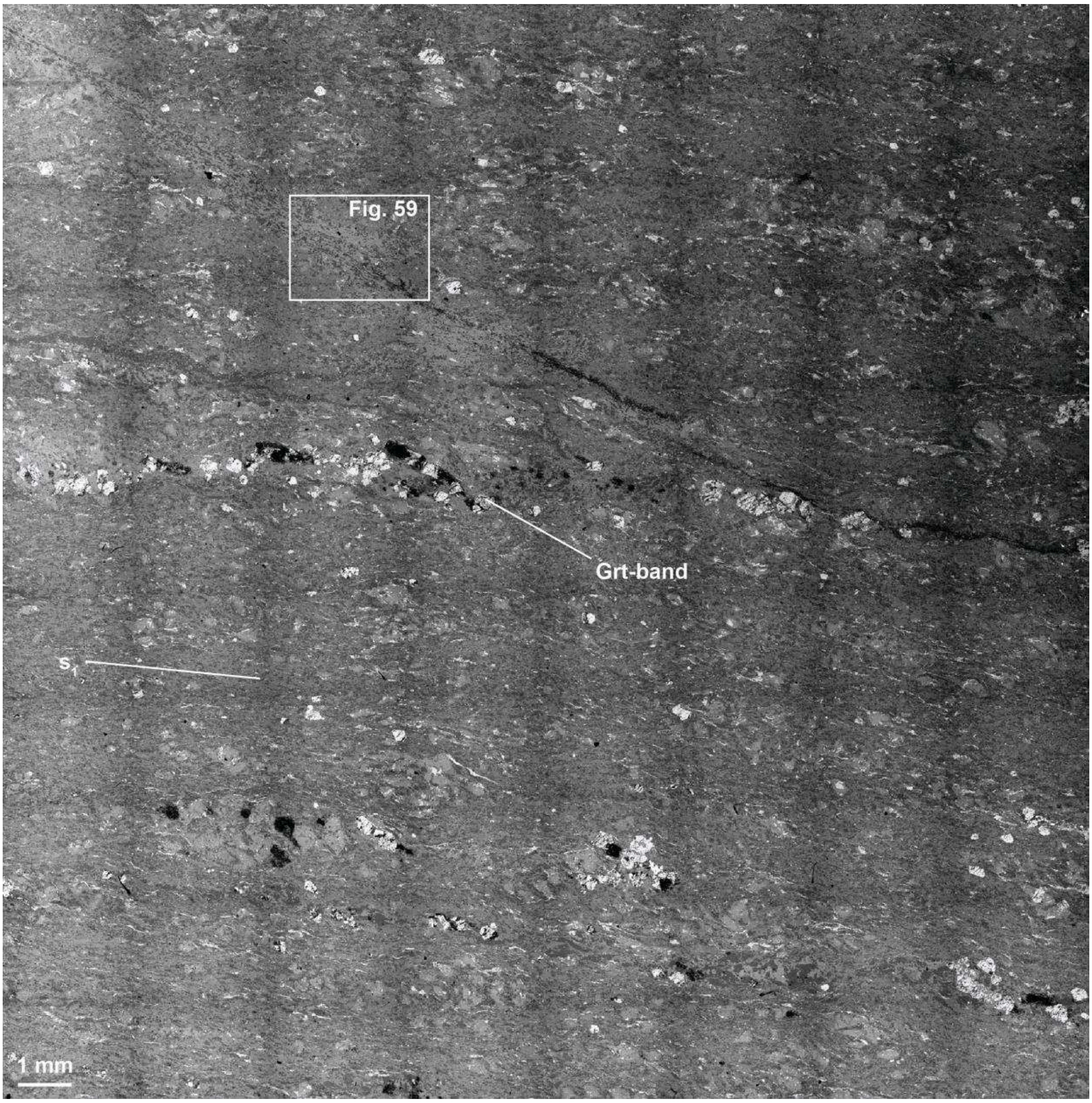

Figure 58: BSE image showing the microstructure of the sample COSI 16_05 and the position of Figure 59.

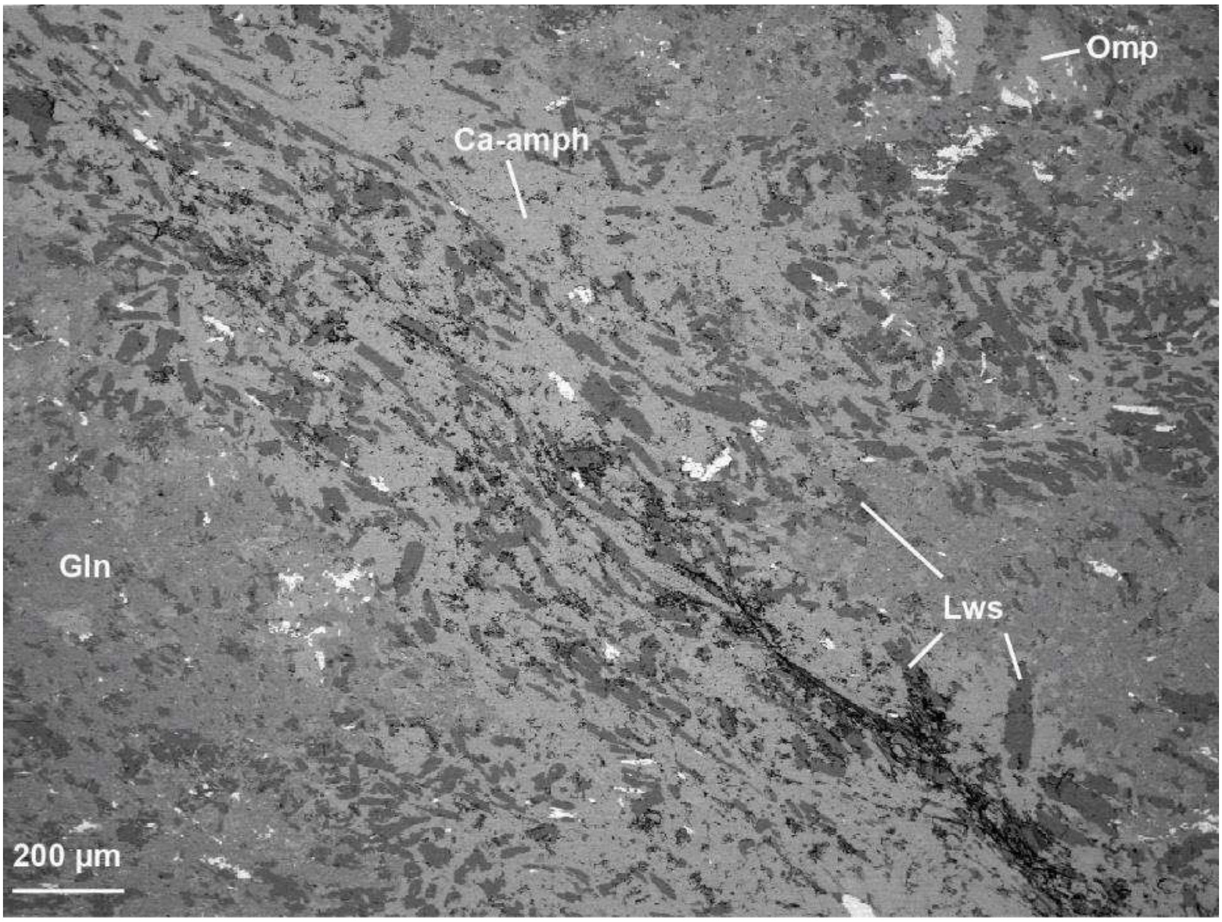

Figure 59: Closer view of the microstructure shown in Figure 58. The band, which appeared green in the hand specimen is mainly composed of lawsonite and Ca-amphibole. Lawsonite crystals are strongly oriented and are idiomorphically shaped within this band.

Based on thermodynamic models Ca-amphiboles are expected to be stable at lower pressures than glaucophane (Figure 2 paper). Therefore the occurrence of larger amounts of Ca-amphibole in these bands points towards lower pressure conditions relative to the matrix of the sample, dominated by the high-pressure minerals glaucophane, lawsonite, omphacite, and garnet. The occurrence of larger amounts of omphacite and garnet reveals that the sample underwent eclogitization. This process is accompanied by dehydration as well as densification of the rock. The growth of the hydrous phases, lawsonite and Ca-amphibole, forming bands implies, that this zone underwent hydration rather than dehydration relative to the surrounding bulk rock. Another interesting observation is the spatial relation of these bands to fractures cross-cutting the sample's foliation. Putting all observations in a context and linking them with observations from the deformation experiments, the P-T history of this sample can be interpreted in the following way:

Peak metamorphic conditions were reached at around 2.3 GPa and 793 K (Vitale Brovarone et al., 2011). Based on the experimental results, fracturing of this natural sample may have occurred under HP/LT conditions during the transition from lawsonite-blueschist to lawsonite-eclogite. This process will create pathways for fluids. Stress drop due to faulting and injection of an external fluid into the rock may have triggered the growth of a lower pressure amphibole, Ca-amphibole, and lawsonite along the fault at a later stage. The strong crystal orientation of the idiomorphically shaped lawsonite crystals implies a slow growth process during motion. Due to the formation of these phases the initial fracture and the phases (e.g. omphacite, found in the microstructures along the fractures after the deformation) that were associated with this process may have been overprinted. Imagining, that the experimental samples were exposed to an external fluid and would have enough time to react, they might look similar to this natural sample. However, this interpretation is only based on preliminary microstructural results and analysis and is therefore highly speculative. It also does not take into account chemical differences between these bands and the host rock. More time has to be spent to better investigate the sample's microstructure and of other collected hand specimens in order to better compare the natural microstructures with those of the deformation experiments from the laboratory.

3.4 CONCLUSION

The experimental results presented in this thesis reveal no evidence for a link between the breakdown of lawsonite as trigger for intermediate-depth seismicity in cold subduction zones. Instead all deformed samples demonstrate that brittle failure occurred during the transition from lawsonite-blueschist to lawsonite-eclogite, expressed by the growth of omphacite. This observation is strengthened by the good correlation between the P-T range in which natural seismic events occur in cold subduction zones and the recorded AEs in the lab. After deformation, omphacite can be found along the fractures in each sample that underwent brittle failure. The observation that all lawsonite-blueschist samples, the natural drill cores as well, seem to behave in the same way regardless of their phase ratio, grain-size, and initial texture makes it possible to better correlate the laboratory results with natural observations. Based on the experimental results densification during eclogitization in conjunction with grain-size reduction is proposed as viable mechanisms to explain the formation of intermediate-depth seismicity in the oceanic crust in cold subduction zones. These mechanisms would also explain the formation of intermediate-depth seismicity in less hydrous rocks, e.g. epidote-blueschists, in warm subduction zones. Linking our laboratory microstructures to natural microstructures is tricky, because the laboratory samples were quenched under conditions comparable to peak pressure conditions during prograde metamorphism. Natural rocks in the field reveal their whole P-T history and often show structure that were overprinted and reworked during retrograde metamorphism.

“Was ich nicht erlernt habe, das habe ich erwandert.”

- Johann Wolfgang von Goethe

IV ECLOGITIZATION OF GRANULITE

The role of fluids in rock metamorphism is crucial, because, even if they do not actively take part in some mineral reactions, they act as a catalyst to trigger and support reaction progress. Therefore in completely dry rocks mineral reactions are kinetically hampered because of the lack of fluid as a transport medium to carry chemical components from dissolution to precipitation sites. The previous chapter treated the eclogitization of oceanic crust, so the transition of hydrous blueschist to eclogite accompanied by the liberation of fluids during dehydration reactions. In this case the metamorphic reactions will produce a fluid phase to run the eclogitization process. However eclogitization is also observed in the lower oceanic crust, as well as lower continental crust, which are composed of less hydrated lithologies (gabbros to anorthosites and granodiorites for instance). Field observations in the Bergen Arcs, but also within the Kråkenes gabbro in Western Norway (Lund & Austrheim, 2003) reveal eclogite-facies pseudotachylites as structural evidence for ancient seismic events in nominally anhydrous rock of the lower continental crust. In these dry rocks eclogitization is accompanied by the hydration of the rock, believed to be caused by the influx of an external fluid (Jamtveit et al., 1990). Geophysical observations coupled with thermodynamic models also suggest that regions of the rather dry lower continental crust reveals intermediate-depth seismicity in areas that are expected to be partially eclogitized (Tibet-Himalaya collision zone; Hétenyi et al., 2007; Liang et al., 2011). The motivation behind the experiments presented in this chapter, was to investigate if and how eclogite-facies metamorphic reactions in nominally anhydrous granulites could cause mechanical instabilities leading to brittle failure under high-pressure/high-temperature conditions.

4.1 EXPERIMENTAL RESULTS

Two deformation experiments on granulite were performed using the D-DIA apparatus. Runs were performed at different confining pressures of approximately 2 GPa and 3 GPa, respectively (Table 12). Deformation started in either run at around 994 K and the samples were quenched at about 1225 K (grey curves in Figures 60; 61).

Table 12: Experimental conditions of the D-DIA deformation experiments on granulite.

Sample	Experiment #	Starting material	P_c [GPa]	T range [K]	Strain rate [s^{-1}]	Maximum strain [%]
NG_2_1225	D1810	NG-bulk	2	994-1225	$6 \cdot 10^{-5}$	34
NG_3_1225	D1811	NG-bulk	3	994-1225	$5 \cdot 10^{-5}$	36

4.1.1 Evolution of stress

Although deformed under different confining pressures, the evolution of both stress-strain curves are very similar. The first part of the differential stress over strain curves are shown as dashed line, because of unreliable differential stress values due to a poor peak fit. In the following only the stress evolutions represented by the black solid curves will be discussed (Figures 60; 61). During the first stage of deformation, under constant temperature of around 720 K, the differential stress increases to approximately 1.8 GPa for NG_2_1225 and 2.2 GPa for NG_3_1225 at around 12 % axial strain. Then stress drops in both runs to around 1.7 and 1.4 GPa, respectively. During the first temperature increase, stress continuously decreases to approximately 1 GPa in both runs. In both experiments the stress drop does not coincide with this first increase in temperature. Afterwards the differential stress remains rather constant for the run NG_2_1225 until the samples were quenched at around 35 % axial strain. In the stress-strain curve of NG_3_1225, differential stress slightly increases to around 1.4 GPa at 27 % axial strain and then decreases again until the end of deformation. The sample NG_3_1225 was also quenched at approximately 35 % axial strain.

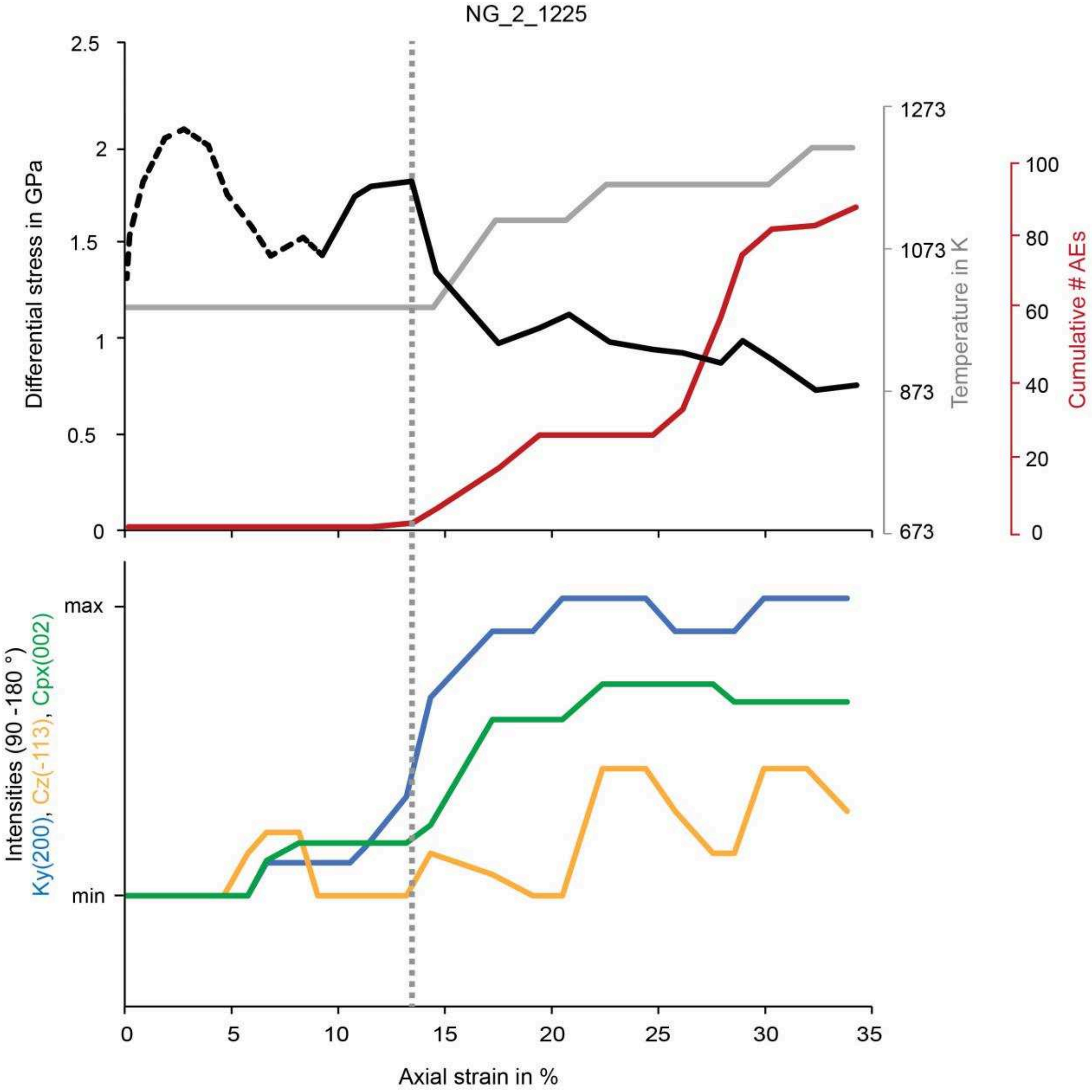

Figure 60: Mechanical data and XRD observation during deformation of the sample NG_2_1225. Differential stress (black), temperature (grey), and cumulative number of AEs (red) over axial strain in %. The lower plot shows the textural evolution of the intensities of Ky (200), Cz (-113), and Cpx (002). The stress drop at around 12 % axial strain coincides with the onset of AEs.

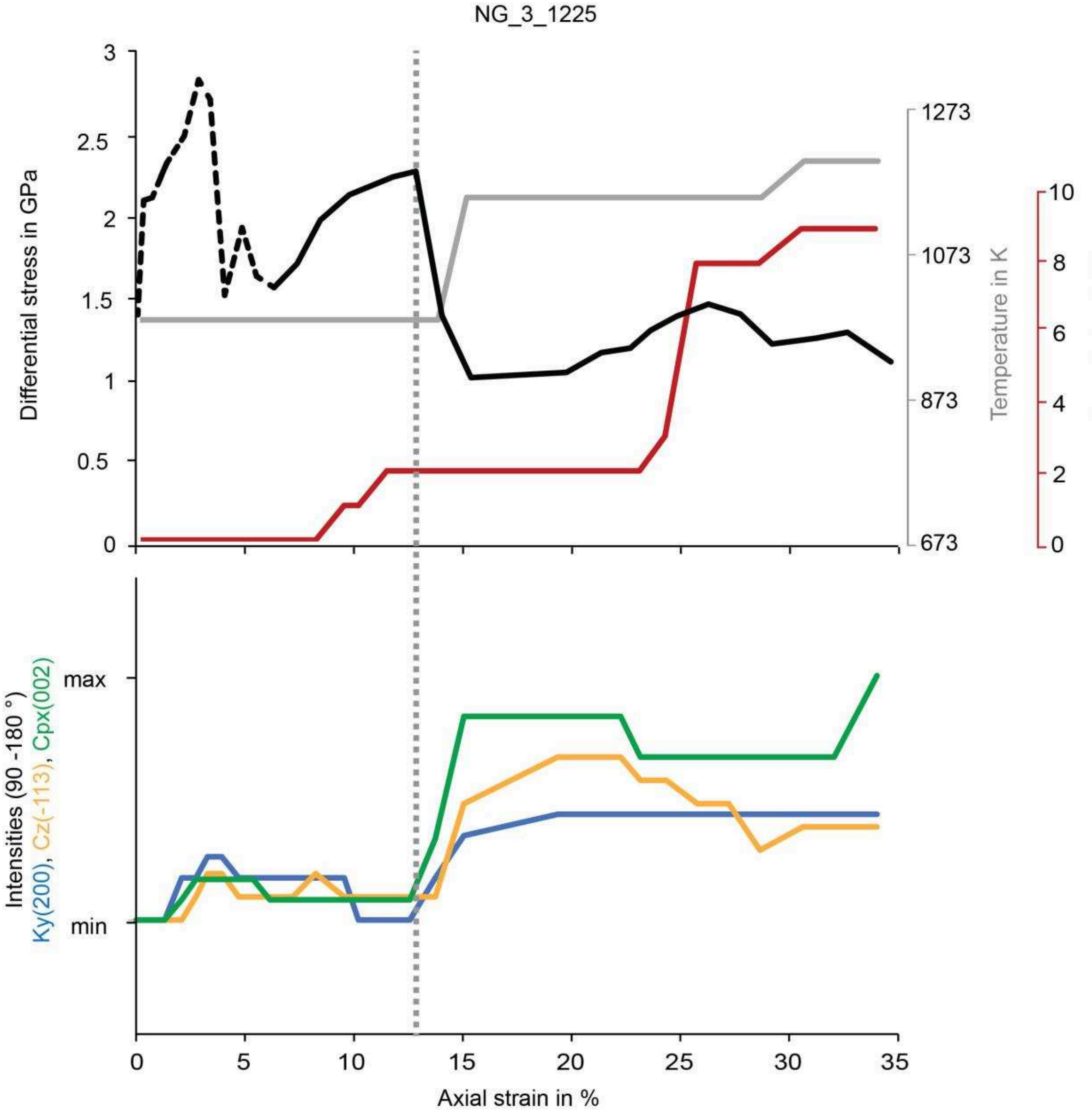

Figure 61: Mechanical data and XRD observation during deformation of the sample NG_3_1225. Differential stress (black), temperature (grey), and cumulative number of AEs (red) over axial strain in %. The lower plot shows the textural evolution of the intensities of Ky (200), Cz (-113), and Cpx (002). In this run the onset of AEs does not correlate with the stress drop at 12 % axial strain.

4.1.2 Acoustic activity during deformation

In the lower pressure experiment NG_2_1225 87, and in the higher pressure run NG_3_1225, 9 AEs were recorded during deformation. Acoustic emissions occur in two different bursts. During deformation of NG_2_1225 the first burst of AEs starts at around 12 % to approximately 20 % axial strain. The onset of AEs correlates very well with the drop in differential stress (red curves in Figures 60; 61). The second burst was recorded from around 25 % until the end of deformation at approximately

35 % axial strain. Both bursts of AEs are slightly shifted for the run NG_3_1225. The first burst of AEs was recorded from around 8 to 12 % axial strain and the second from 26 % to the end of deformation.

4.1.3 Textural evolution

Due to many peak overlaps in the powder-diffraction patterns, integrated over 360°, it was not possible to monitor the eclogitization process during deformation (see 2.4 for further explanations). However by only looking at a slice integrated from 90 to 180° three diffraction peaks of important eclogite-facies phases appear in the powder-diffraction pattern. The use of these 90° degree slices does not give evidence about the growth or disappearance of certain minerals, but information on the textural evolution during deformation. Three diffraction peaks of (002) clinopyroxene, (-113) of clinozoisite, and (200) of kyanite were monitored, respectively, to track the textural evolution of these plagioclase decomposition products (Figures 60; 61; details on plagioclase stability are discussed under 1.4.3). At lower strains these three diffraction peaks increase in height either implying that those phases start to grow along a preferred orientation or that they were already present and re-orientate due to deformation (Figures 60; 61). In run NG_2_1225 the intensities increase at around 5 % and in NG_3_1225 earlier at approximately 2 % axial strain (Figure 60). These intensities remain rather constant until the stress drops at 12 % axial strain. During the decrease in differential stress all three peak intensities increase remarkably in both samples. Afterwards they stay more or less constant until the end of the experiment (Figures 60, 61).

4.1.4 Microstructural and chemical analysis

NG_2_1225

A low magnification image of the D-DIA sample NG_2_1225, deformed under 2 GPa confining pressure, is shown in Figure 62A. A fracture appears in the upper left corner of the sample (Figure 62A, B). By zooming into this area, marked by the white rectangle in Figure 62A, the microstructure in the vicinity of this fracture reveals a zone of higher porosity (area enclosed by the dashed lines in Figure 62B).

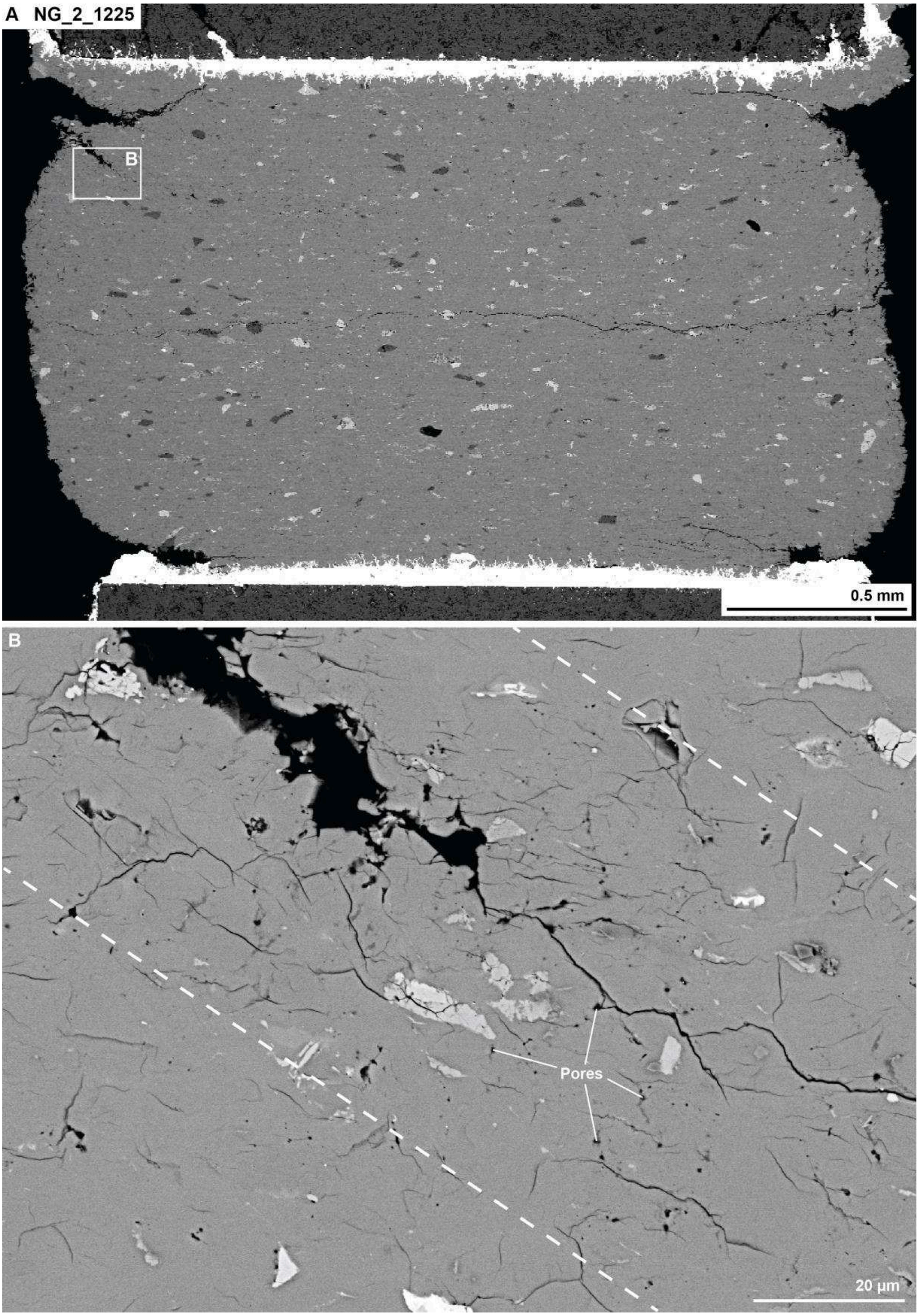

Figure 62: BSE images of the D-DIA sample NG_2_1225. A) Overview image demonstrating the location of the higher magnification image shown in B. B) Zone with higher porosity within the vicinity of a small fracture.

The entire sample exhibits larger areas with increased porosity. Within these regions “patches” of, in BSE mode, darker material relative to the surrounding plagioclase can be found in the sample (Figure 63B, C, F). This material appears to be poorly crystalline, because holes are found after interaction with the electron beam at the SEM. These patches are almost always associated with nanometer-sized plagioclase crystals (Figure 63C, D). Dissected and displaced crystals can also be found in the microstructure of NG_2_1225 (Figure 63E, F). By zooming into the region, highlighted by the white rectangle in Figure 63E, elongated clinozoisite crystals can be found within the fractures (Figure 63F). The fractures borders are decorated by small plagioclase crystals (Figure 63F). Another important observation is the lack of pyroxene grains from the starting material. Instead crystals showing intergrown pyroxene, amphibole, and kyanite crystals can be found randomly distributed in the sample (Figure 63B). These “pockets” contain varying phase amounts. Some are dominated by amphibole intergrown with kyanite and only minor pyroxene and others are almost exclusively composed of pyroxene with many kyanite needles.

Some of these patches, found in the microstructure, are filled by poorly crystalline material that surrounds idiomorphic crystals (Figures 64A). Around the idiomorphically shaped quartz crystals many vesicles appear in the dark material (Figures 64A). White arrows in Figures 64A highlight areas where nanocrystalline plagioclase grains appear in the presented area. These nanocrystals are not randomly oriented, but often aligned along two different directions with an angle of approximately 45° from σ_1 (long edge of the images) (Figures 64). Very similar structures can be found throughout the entire sample at different scales (Figures 64B, C). The dark, poorly crystalline material can be found around plagioclase rectangles that show crystal edges oriented approximately 45° from σ_1.

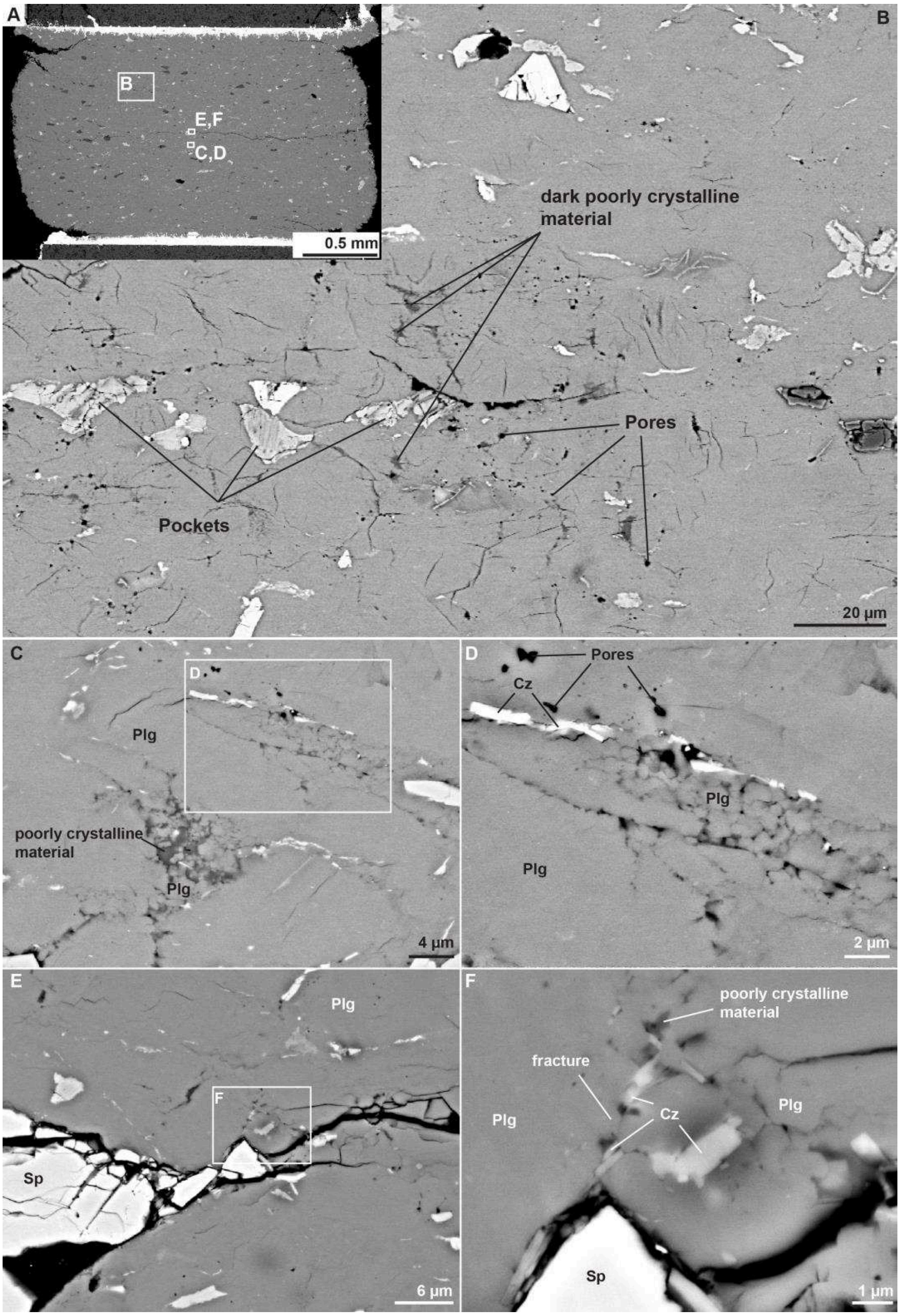

Figure 63: Different BSE images presenting the microstructure of the sample NG_2_1225. A) Overview image for the higher magnification images presented in B-F. B) Area showing higher porosity and pockets mainly composed of pyroxene and kyanite needles. Often a dark (relative to Plg in BSE mode) poorly crystalline material is associated with the appearance of pores. C) Region showing a closer view *of a “patch” filled by poorly crystalline material surrounded by small (< 1* µm) plagioclase crystals. D) Higher magnification reveals small plagioclase grains associated with clinozoisite and porosity. E) Dissected and displaced spinel crystal showing F) elongated clinozoisite crystals within the narrow fracture.

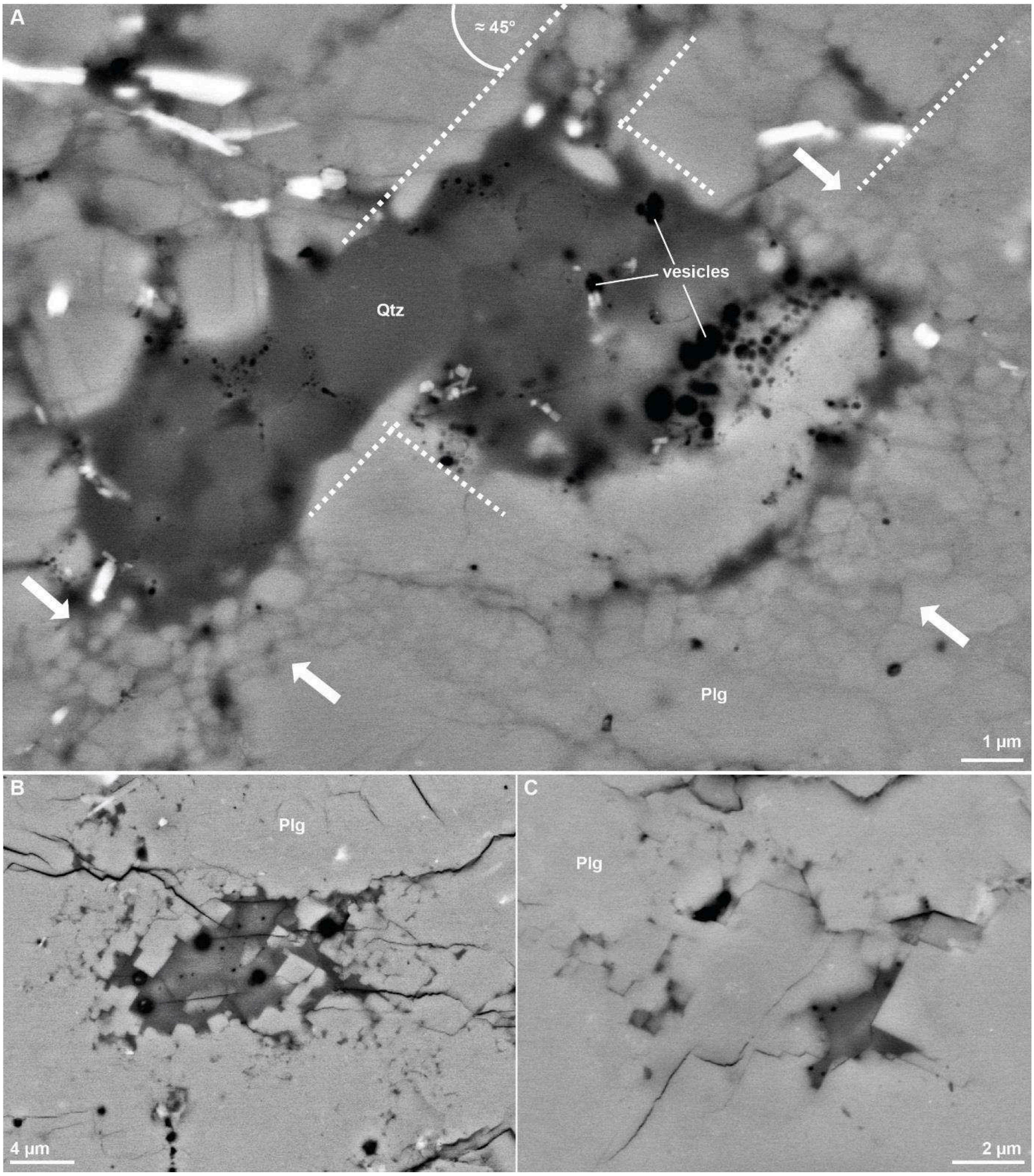

Figure 64: A common feature are patches filled with dark poorly crystalline material. A) Patch with idiomorphic quartz crystals floating within the dark material exhibiting many vesicles. The patch shows edges oriented around 45° towards σ_1. White arrows highlight the appearance of nanocrystalline plagioclase. B) Another patch shows also the dark material with large vesicles and small plagioclase grains at the borders of this structure demonstrating crystal edges around 45° towards σ_1. C) Very small patches within plagioclase showing the same characteristics as in B.

NG_3_1225

The sample NG_3_1225 shows no fractures that can be related to deformation (Figure 65A). At higher magnification, many very narrow bright bands appear in the sample's microstructure with mainly two orientations (Figure 65B).

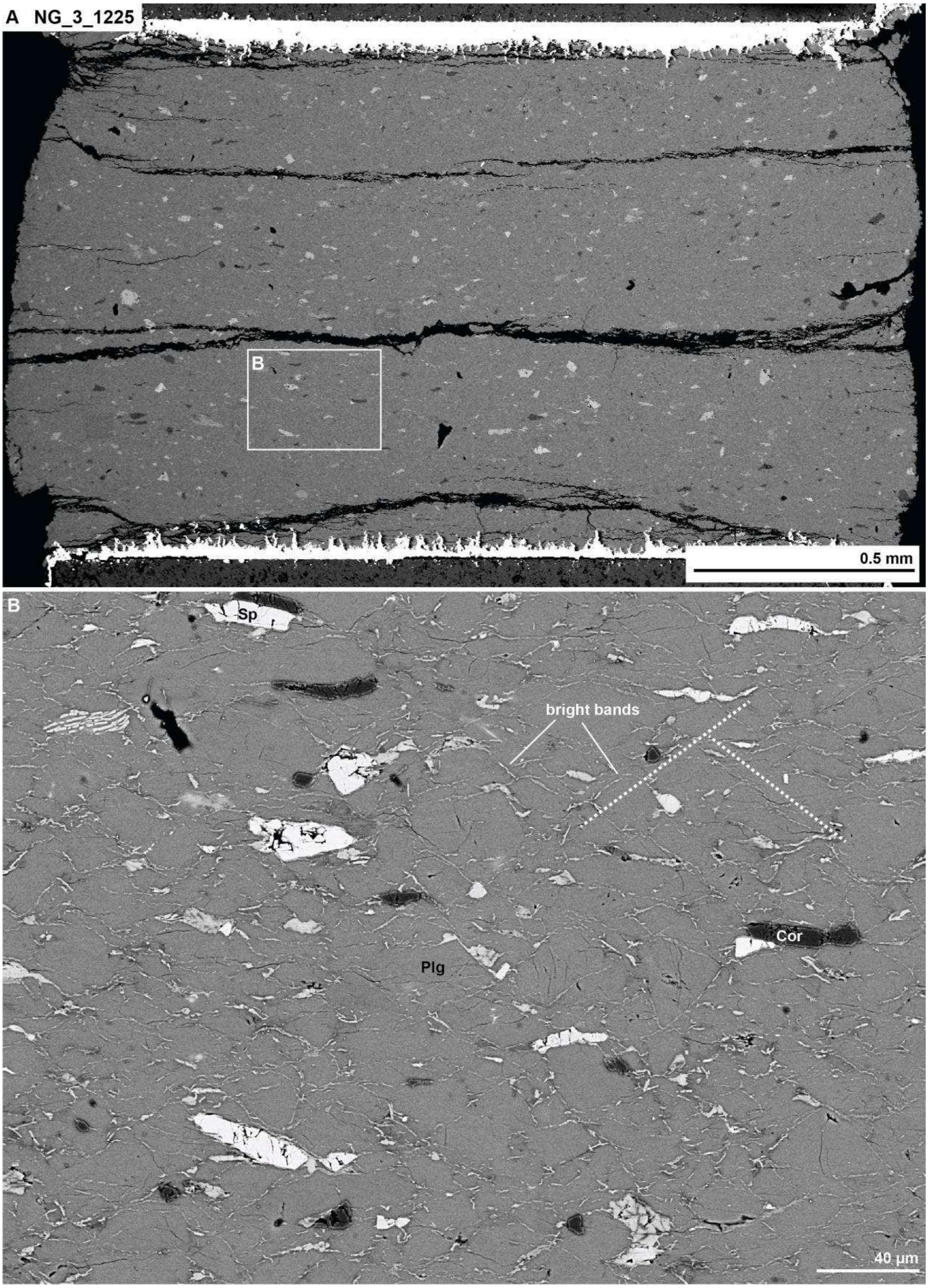

Figure 65: Sample NG_3_1225 after deformation. A) Many decompression cracks cut horizontally through the sample. B) The microstructure of this sample reveals two group of bands mostly composed of clinozoisite crystals. The bands of each group are all oriented more or less parallel to each other.

The orientation of these two sets was measured within a selected area (BSE image in Figure 66) using ImageJ (Abramoff et al., 2004) and the measurements reveal that both groups of bands are oriented either around 45° or - 45° from σ_1 (solid line Figure 66). The dashed line demonstrates the total of all measured structures in the presented area including cracks.

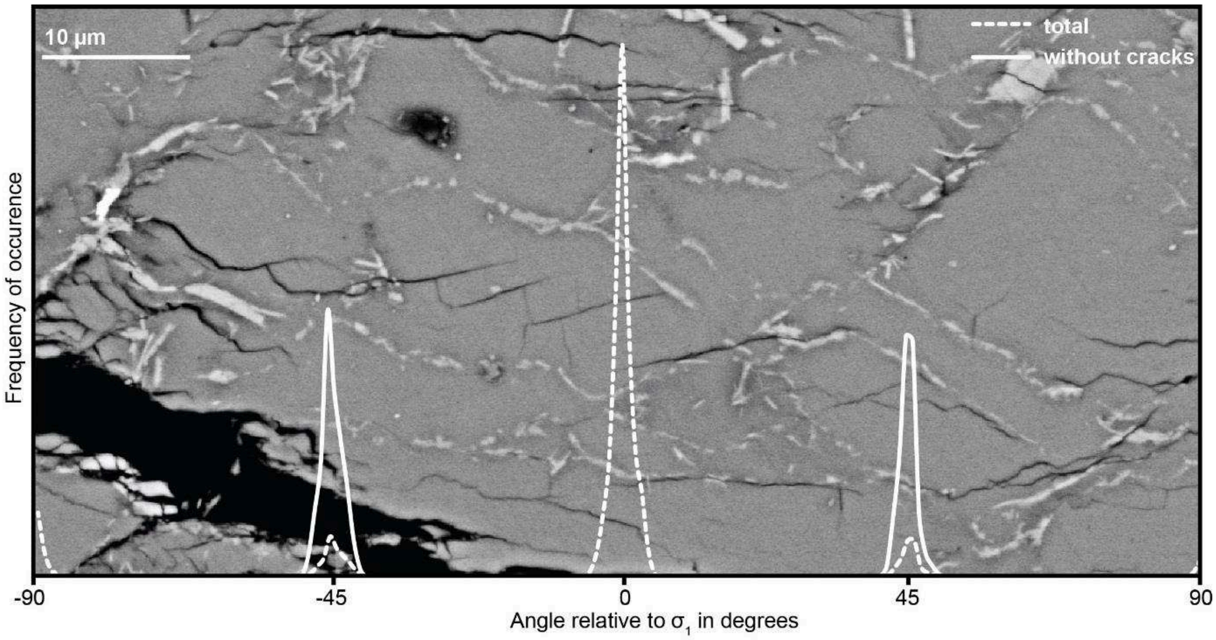

Figure 66: BSE image of the sample NG_3_1225 shows an area selected for a structure distribution plot using the software ImageJ. Both groups of Cz-bands are oriented either 45 or -45° towards σ_1. The dashed line shows the measurement of all detected structures, cracks included, and the solid white line only the distribution of the Cz-bands with respect to σ_1.

Chemical analyses and a composite image, a superposition of different element distribution maps (calculated using ImageJ), of an area shown in Figure 67A exhibit that these bands are mostly composed of clinozoisite (brownish grains in Figure 67B). Other minerals that are also forming these bands are quartz (yellow) and kyanite. Regions appearing turquoise in the plagioclase, adjacent to these bands, are enriched in Na and Si (Figure 67B). In some places dissect and displaced spinel crystals are found along a band filled with mostly elongated clinozoisite grains (Figure 67C). As in the previously discussed sample, no pyroxene grains from the starting material can be found in the microstructure of NG_3_1225. But instead pockets of intergrown phases that are randomly distributed in the entire sample. Most pockets demonstrate a complex intergrown polyphase assemblage with areas composed of phlogopite together with idiomorphic garnet crystals and sometimes quench textures (Figure 67D). A larger pocket was chosen for an element distribution map (Figure 68A, B). The composite image, calculated using the software INCA, reveals a phase assemblage of amphibole, omphacite, kyanite, garnet, and phlogopite over a very small area (Figure 69C; Table 13). Amphibole shows a chemical composition close to pargasite (after Leake et al., 1997). All garnet crystals found in these structures are very small (< 1 µm). Therefore precise chemical analyses are not possible and will give mixed analysis, e.g. the untypical high amount of K measured in the garnet derives from an adjacent phlogopite (Table 13; Figures 67D; 68B, C).

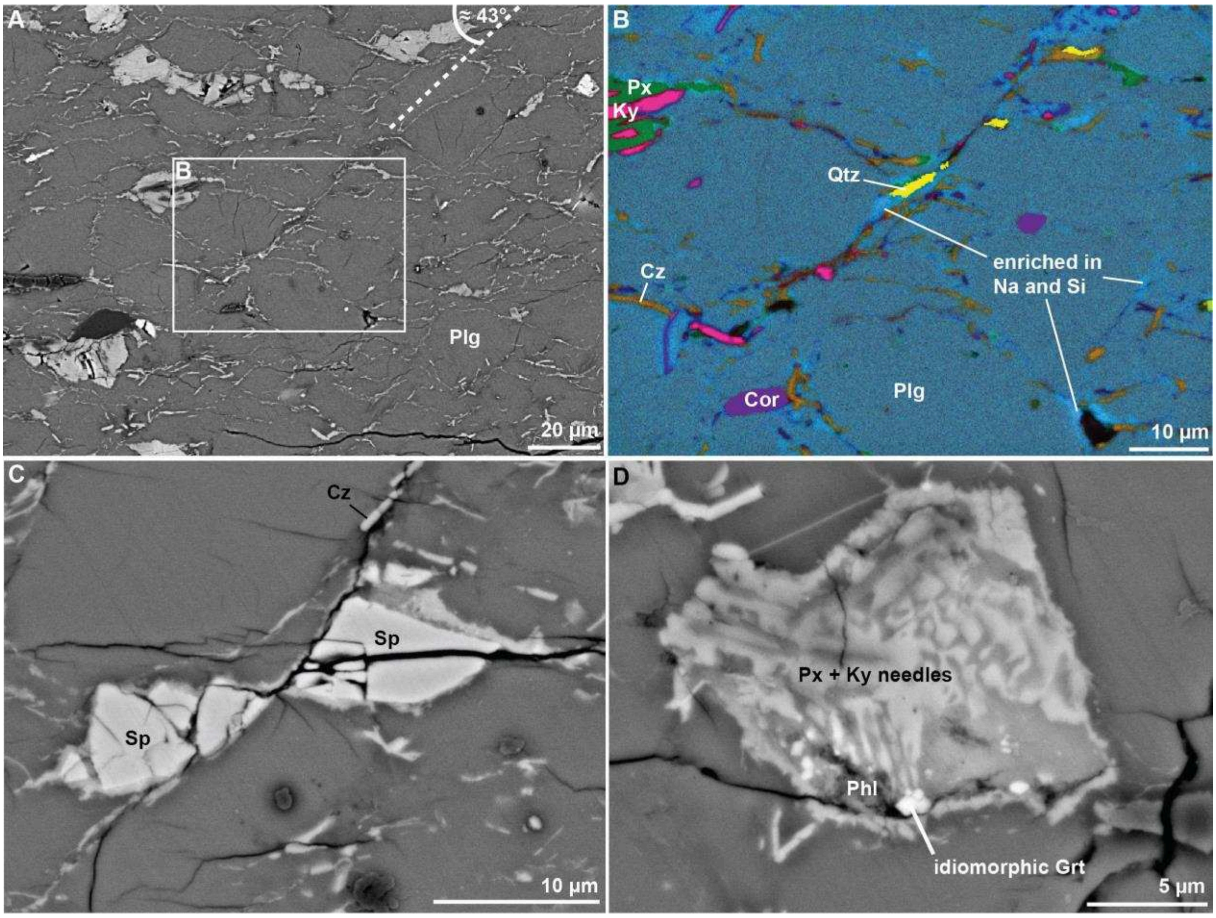

Figure 67: A) BSE image showing many Cz-bands. The white rectangle B exhibits the zone selected for an element distribution map. B) A composite image created by merging element maps using the software ImageJ. This image demonstrates that the bands are mostly composed of Cz (brownish color), minor Qtz (yellow) and Ky (pink). The turquoise areas along these bands are enriched in Si and Na. C) Dissected and displaced Spinel crystal along one of these bands. D) Pocket composed of many Px and Ky needles showing quench texture. In the lower area of this structure phlogopite incorporating idiomorphically shaped garnet crystals appear.

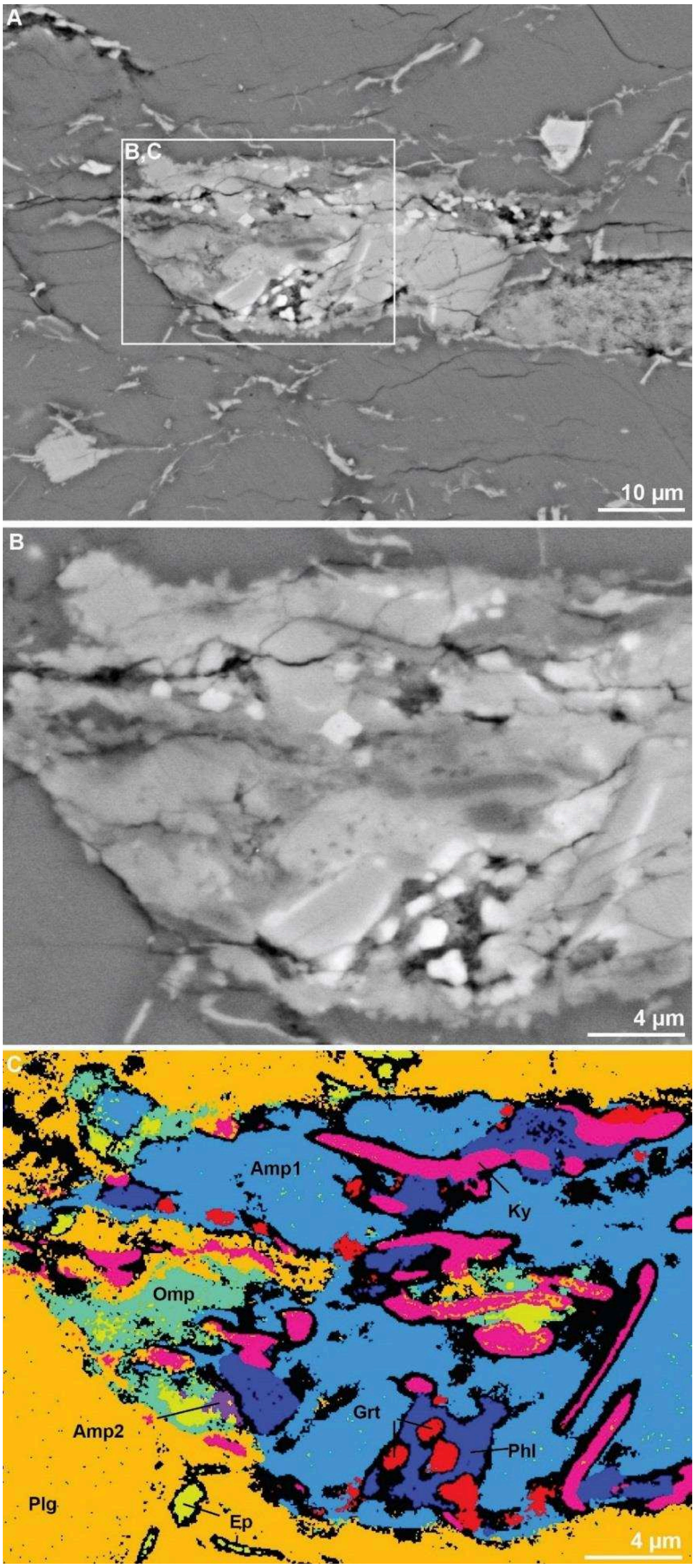

Figure 68: A) Overview of a pocket chosen for a detailed chemical analysis. B) Idiomorphic garnet crystals appear in this pocket. C) A composite image calculated using INCA demonstrates that this pocket contains many different phases, e.g. Amp, Omp, Grt, Phl, and Ky needles.

Table 13: Chemical analyses of different pocket phases.

Oxide [wt.%]	Amp	Omp	Ky	Phl	Grt
SiO_2	41.96	51.47	36.58	37.47	34.27
TiO_2	0.03	0.02	0.03	0.78	-
Al_2O_3	18.29	14.02	62.99	18.10	29.98
FeO	9.77	4.72	0.62	7.89	19.40
MnO	0.02	-	-	-	0.30
MgO	12.40	8.79	0.09	18.73	9.71
CaO	11.77	17.02	0.35	0.23	4.14
Na_2O	1.56	4.02	0.05	0.23	0.65
K_2O	1.81	0.06	-	9.84	0.46
Total	97.62	100.11	100.71	93.28	98.91

Although most of the areas of this samples are covered with these bright clinozoisite-bands, there are some regions that are lacking these structures. A striking observation is the increase in porosity within the regions that show no clinozoisite-bearing bands (Figure 69). This observation that areas of higher porosity show no or much less of these bands is consistent over the entire sample. At the sample's border a wider zone showing higher porosity seems to be oriented in the same way as the fracture zone, which also exhibits higher porosity in sample NG_2_1225 (Figure 62).

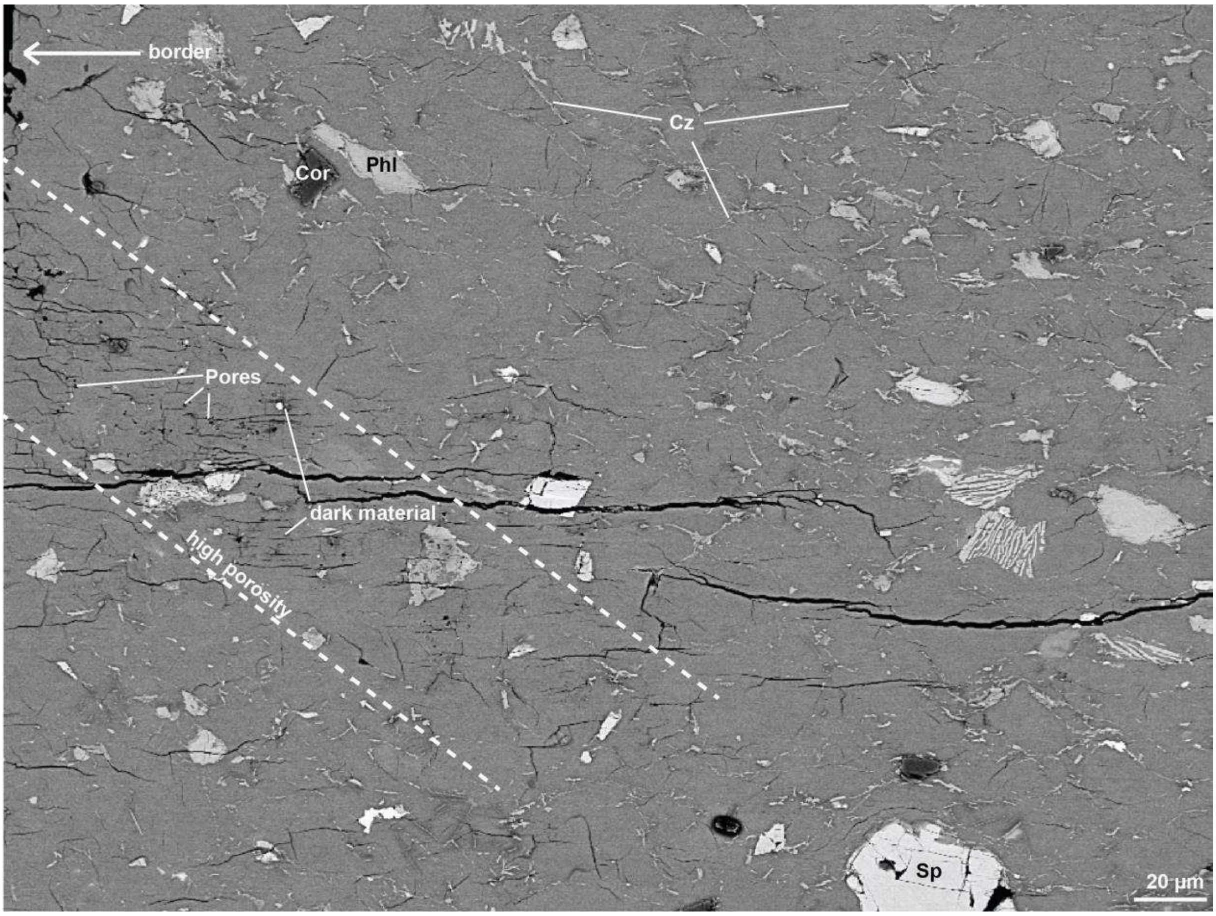

Figure 69: The sample NG_3_1225 is almost entirely covered by these bright Cz-bands, but some in which these bands are missing show an increase in porosity. This zone forms a band in an angle of about 45° towards σ_1

In these areas of increased porosity (Figure 70 B, C), small patches of dark material, which are darker in BSE mode relative to plagioclase, appear within these zones (Figure 70D). Compared to the previous sample these patches are rather small and less abundant.

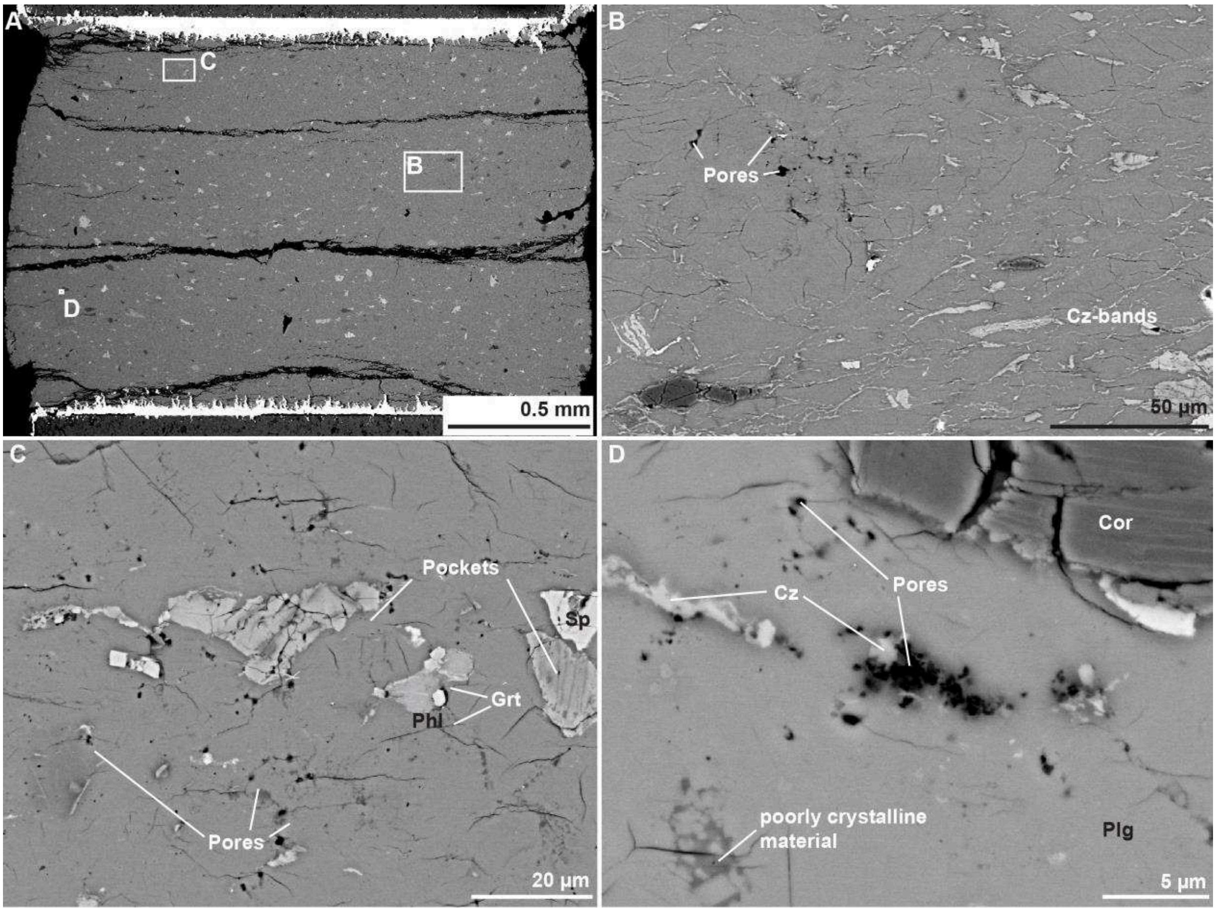

Figure 70: BSE images of the sample NG_3_1225 exhibiting areas of high porosity in which Cz-bands are absent (A). B) Many pores appear together with dark (relative to plagioclase in BSE mode) patches. C) Compared to Plg grains from the starting material, very small Plg crystals can be found within dark patches of poorly crystalline material. D) Idiomorphically shaped Grt crystal floating within a poorly crystalline material.

4.1.5 Nanostructural analysis

For nanostructural analyses, one FIB section of the sample NG_3_1225 was cut over an clinozoisite band (Figure 71). Different images, all taken in BF mode, show different areas and magnifications of this band (Figure 72).

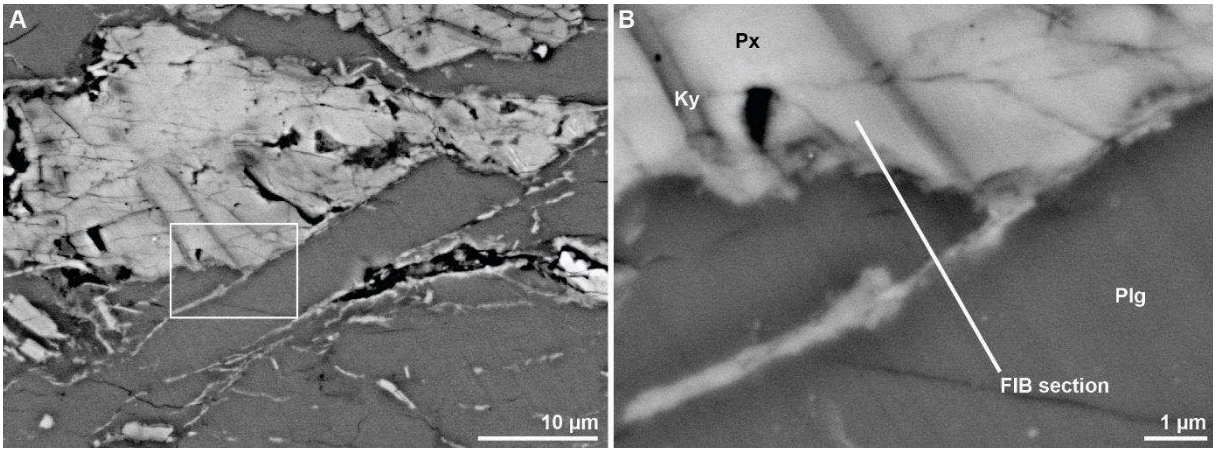

Figure 71: BSE images showing the location chosen for the FIB section cut in the sample NG_3_1225.

In this cross-sectional view around 200 nm large elongated crystals, identified as clinozoisite, can be found in the upper zone of this band (Figure 72A, B). Further down the grain size reduces dramatically (Figure 72C, D). The material forming this band reveals no clear crystal shapes anymore (Figure 72D). Within this area tiny crystals seem to float into a brighter poorly crystalline material (Figure 72E). At the bottom of this FIB section clinozoisite grains appear and are elongated along the direction of the band (Figure 72F). The borders of the band are formed by small, around 10 nm large crystals, which are too small for an unambiguous chemical analysis.

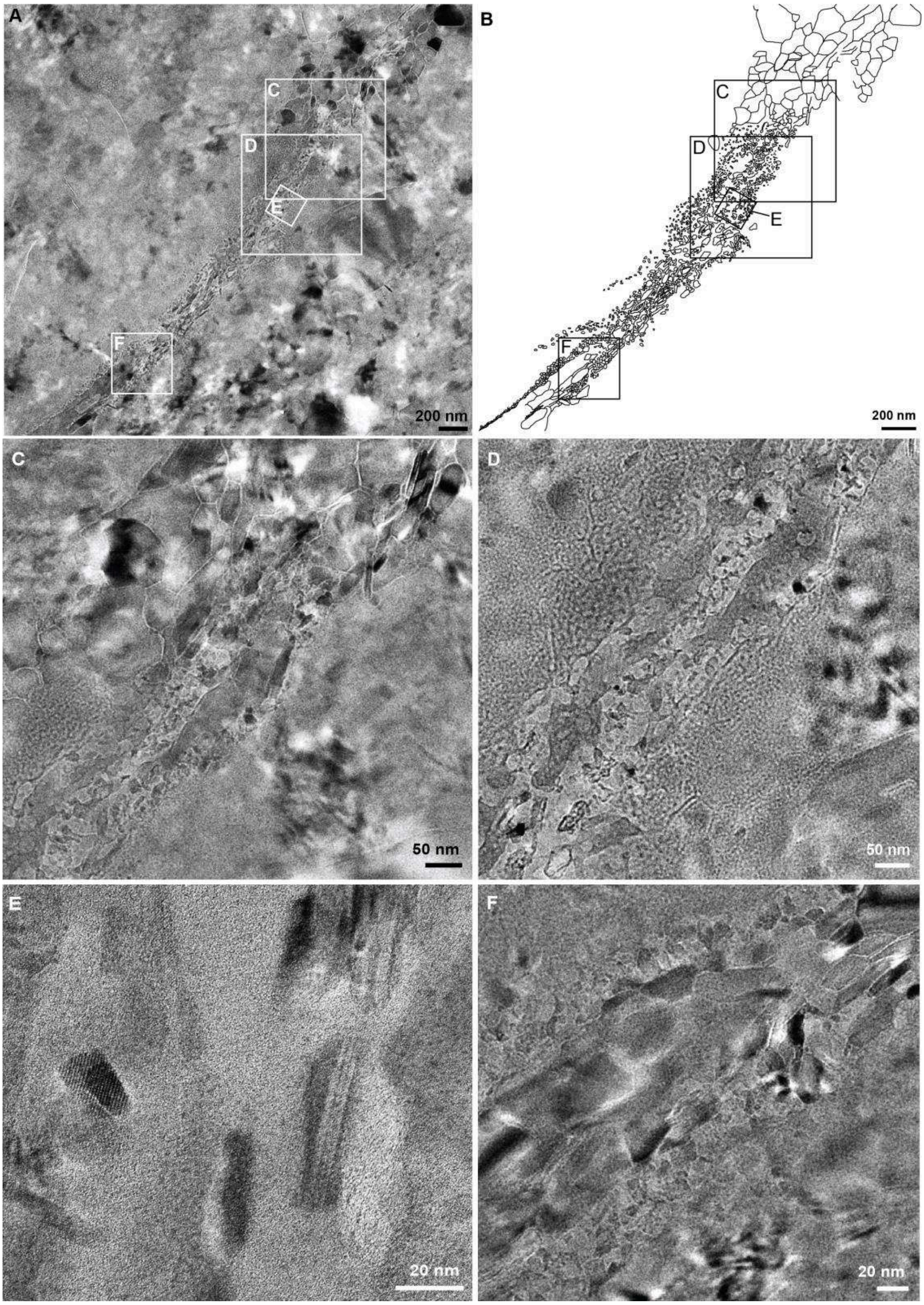

Figure 72: TEM images exhibiting a cross-sectional overview of the Cz-band across which the FIB section was cut and different magnifications of this band. A) Rectangles mark the positions chosen for higher magnification images presented in C-F. B) Schematic drawing of the band C) The upper part of this band is dominated by larger Cz-grains. D) Further down no more crystals can be distinguished. E) Smaller crystals seem to float within a brighter material showing no crystal lattice planes. F) The lower part of this band reveals elongated clinozoisite crystals. The borders of this band show small crystals.

Diffraction images across the zone shown in Figure 72D prove that the crystallinity decreases towards the center of the band (Figure 73). Some small crystals cause the diffraction spots within these images, but most of the material is amorphous (Figure 73).

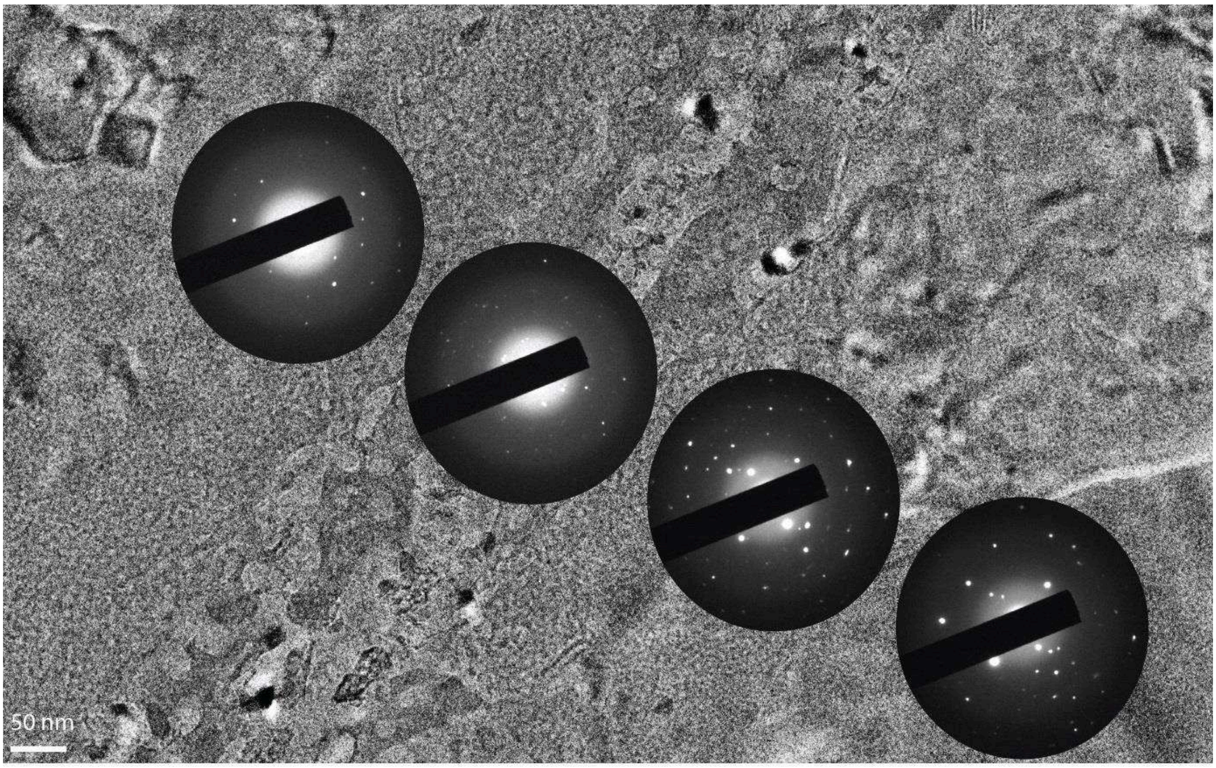

Figure 73: TEM image taken in BF mode showing the decrease in crystallinity over the investigated Cz-band.

4.2 DISCUSSION

4.2.1 Similarities & differences

The two granulite samples reveal many common microstructures, but also some striking differences after deformation. Both runs were conducted within the same temperature range (Table 12) and the differential stress evolutions during deformation are very similar (Figures 60; 61). In both samples the plagioclase breakdown products Cz, Ky, and Cpx seem to grow or to re-orientate in distinct directions (Figures 60; 61). This process is enhanced during the stress drop at around 12 % axial strain, observed in both curves. One important microstructural observation is the absence of pyroxene grains from the starting material in both samples after deformation. Instead both samples show pockets composed of many different phases that sometimes show quench textures (Figures 63B; 67D; 68). Another interesting observation is the occurrence of zones exhibiting high porosity (Figures 62; 63; 69; 70) always accompanied by the appearance of patches filled by poorly crystalline material (Figures 64; 70D). Almost all of these patches are associated with small plagioclase crystals (< 1 µm) surrounding the poorly crystalline material (Figure 64). In both microstructures dissected and displaced crystals can be found along fractures, filled with clinozoisite needles (Figures 63F, 67C, 72). During the deformation of both runs, AEs were recorded in two different bursts; the first at lower strains/temperatures and the second at higher strains/temperatures (Figures 60; 61). However one difference between both experiments is the recorded number of AEs during deformation, with 87 for the lower pressure experiment NG_2_1225 and 9 for the higher-pressure run NG_3_1225. The onset of AEs is also shifted between both runs. Acoustic emissions were recorded earlier in the high-pressure run NG_3_1225 than in the lower-pressure run NG_2_1225 (Figures 60; 61). This shift seems to correlate with the first appearance or the re-orientation of the plagioclase breakdown products Cz, Ky, and Cpx (Figures 60; 61). Another striking difference is the appearance of these bright bands mostly formed of clinozoisite in the high-pressure sample NG_3_1225, which are much less pronounced or absent in sample NG_2_1225, deformed under lower confining pressure (Figures 62; 63; 65D; 67A).

Table 14: Compilation of similarities and differences between both granulite deformation experiments.

	Similarity	Difference
Confining pressure		X
Temperature range	X	
Stress evolution	X	
Onset of growth/re-orientation (Cz, Ky, Cpx)		X
Growth/re-orientation (Cz, Ky, Cpx)	X	
Onset of AEs		X
Bursts of AEs	X	
Total # AEs		X
No Px from starting material	X	
Porosity	X	
Patches	X	
Pockets	X	
Cz-bands		X

Both samples show microstructural evidence for brittle failure and AEs were recorded during deformation of both runs (Figures 63E; 67C). The microstructures reveal that different processes occurred during deformation. The following discussion tries to decipher which of these processes lead to faulting accompanied by AEs under high-pressure/high-temperature conditions.

4.2.2 Eclogitization of granulite

Although the eclogitization of granulite is mainly expressed by the breakdown of plagioclase, both processes will be discussed separately. As already mentioned in the short introduction of this chapter, metamorphic reactions only occur in the presence of a fluid phase as catalyst or transport medium. Eclogitization of the deformation samples is expressed by the growth of the plagioclase decomposition phases Cz, Ky, Cpx (Jd), and Qtz according An + fluid ↔ Cz + Ky + Qtz (+ fluid) and Ab ↔ Jd + Qtz. After deformation the high-pressure experiment NG_3_1225 shows a much higher amount of the three anorthite breakdown products relative to the lower pressure run NG_2_1225. Due to the small grain-size (large surface area) of the granulite powder, used as starting material, it is expected that water from air humidity was adsorbed onto the charged crystal surfaces. This could have hydrated the sample and initiated the anorthite decomposition. The anorthite breakdown products form bands along which dissected and displaced crystals can be found in the microstructure of the high-pressure run NG_3_1225 (Figure 67B). NG_2_1225 also exhibits dissected and displaced crystals along faults in which clinozoisite crystals can be found, but to a much lower extent (Figure 63E, F). This implies that the high-pressure experiment NG_3_1225 underwent more intense eclogitization during deformation relative to NG_2_1225. Interestingly, in most areas, showing the onset of eclogitization of the samples, only the anorthite breakdown product can be found and mostly along bands or within fractures (Figure 67B). This could be explained by the stability of the two plagioclase components anorthite and albite. Both breakdown reactions involve a negative volume change of approximately -14 and – 17 %, respectively (Table 2). Therefore pressure changes will highly affect the stability of both phases. Anorthite relative to albite is less stable under higher pressure (Figure 74). Consequentially, it is expected that first the anorthite component will decompose and later if pressure increases also albite. Hence, the remaining plagioclase will be continuously enriched in Na during the breakdown of anorthite. Thus correlates well with the microstructures observed in NG_3_1225. Plagioclase is enriched in Na along the bands formed by Ky, Cz, and Qtz (Figure 67B).

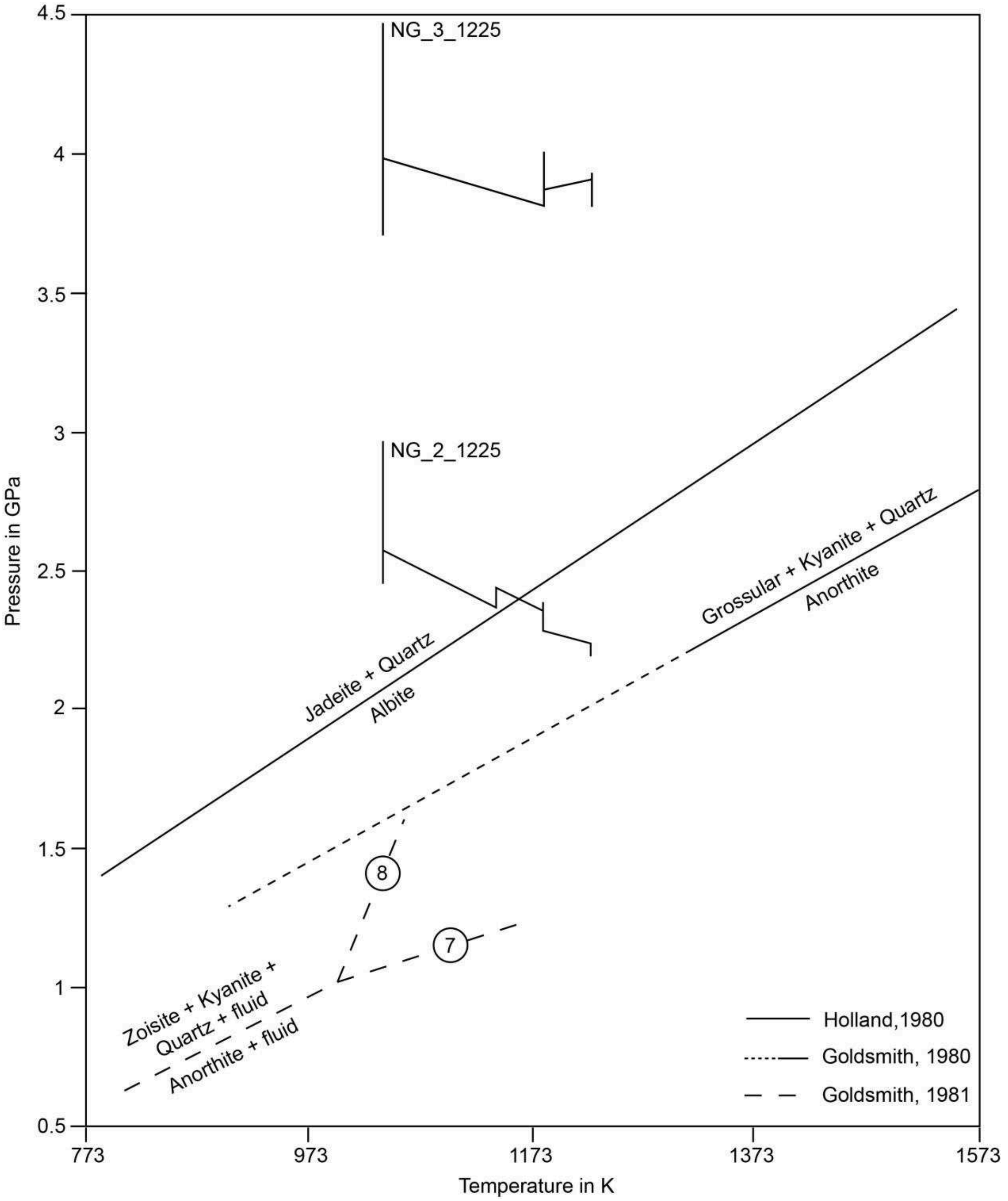

Figure 74: Mean stress-temperature curves of both granulite experiments superimposed on the P-T pseudosection showing the different breakdown reactions of the plagioclase components albite and anorthite. Phase boundary marked with 7 shows the reaction anorthite + fluid ↔ liquid and with 8 zoisite + kyanite + quartz + fluid ↔ liquid.

The fact that the eclogite-facies reaction products of plagioclase are forming bands, along which dissected and displaced crystals are found, implies a link between the growth of these phases and brittle failure. However, the sample NG_3_1225, which exhibits a much higher degree of eclogitization was with 9 AEs rather “silent” during deformation compared to NG_2_1225, where 87 AEs were recorded and which demonstrates a much lower degree of eclogitization.

4.2.3 Evidence of partial melting

Another microstructural observation is the loss of pyroxene grains from the starting material and the appearance of melt pockets. Some of these pockets show quench textures and idiomorphically shaped garnet crystals (Figures 67D; 68). These structures can only form because of the onset of partial melting. Due to the number of pockets found in the sample which is in the same range as the estimated amount of pyroxene present in the starting material, there seems to be a link between the disappearance of pyroxenes, partial melting and appearance of these pockets. Based on thermodynamic calculations on the natural granulite, only the lower pressure experiment NG_2_1225 crossed the solidus (dark blue line in Figure 75), but quench textures in pockets were also found in the high-pressure run NG_3_1225. Both experiments reveal large stress drops at around 12 % axial stress. These stress drops together with the subsequent temperature increase could have caused local decompression melting that mostly affected the pyroxene grains from the starting material.

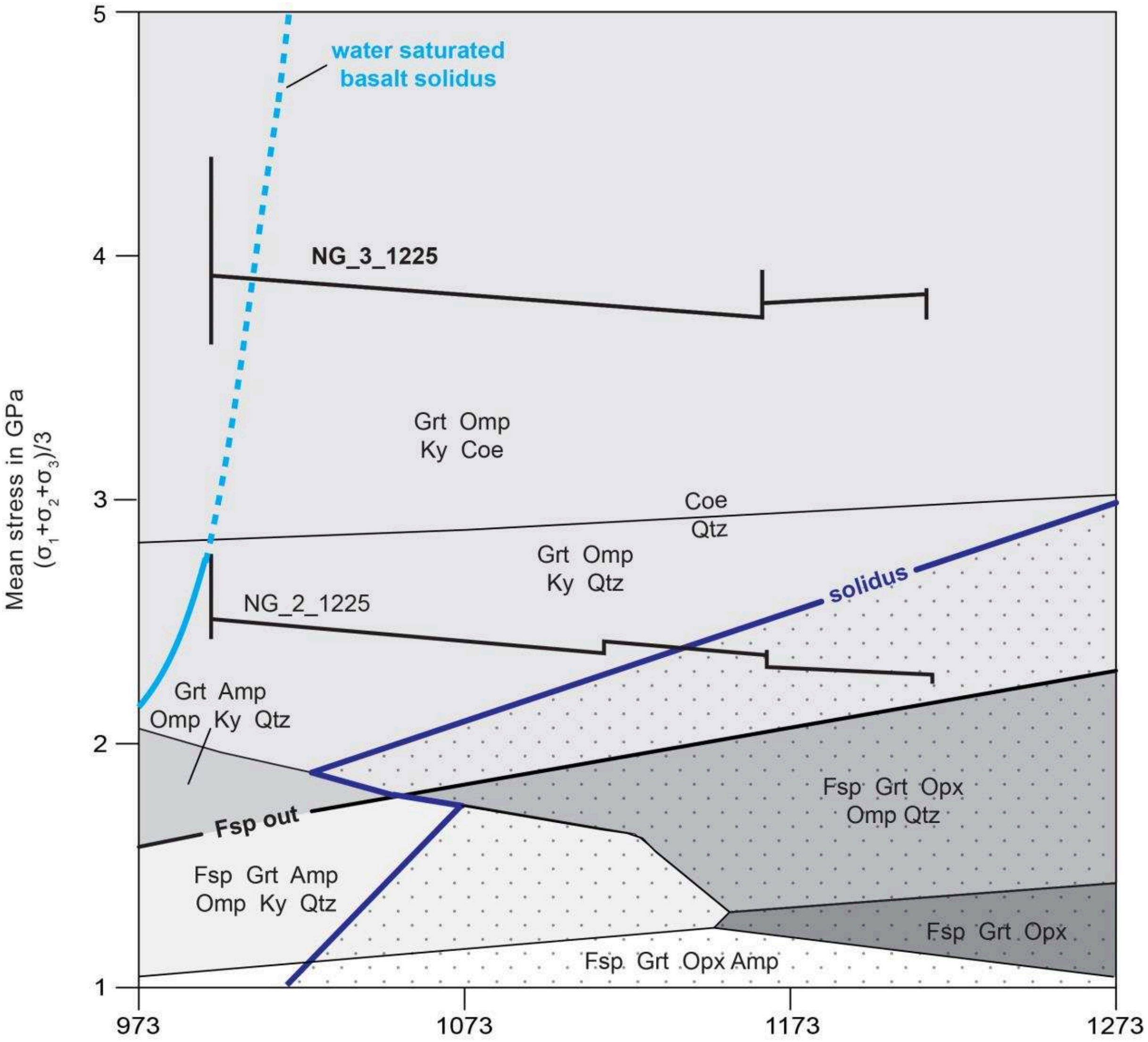

Figure 75: Mean stress-temperature curves superimposed on the P-T pseudosection (NCFMASH model system) of the natural rock. Thermodynamic calculations were performed using Theriak Domino. Bulk rock composition from Kühn (2002). Light blue curve represents the water saturated basalt solidus and the dark blue solid line the calculated solidus of the mafic granulite.

Another explanation would be that the water saturated basalt solidus was crossed during deformation and that only the pyroxenes, showing a similar chemical composition relative to MORB (Wei & Clarke, 2011), were partially melted (light blue line in Figure 75). The solidus curve is very steep in the investigated P-T range and this could explain that the stress drops occurred at around the same temperature/strain regardless of the difference in confining pressure.

Based on the microstructural observations it cannot be deciphered if partial melting was caused by stress drop or the presence of a melt triggered the stress drop in the samples. However, it appears that the stress drop in the high-pressure sample is not accompanied by AEs implying either slow rupture or overall softening of the sample. The duration of the stress drops were around 10 min and therefore stress decrease could have occurred slowly (Figures 60; 61).

4.2.4 Plagioclase breakdown at high-pressure

The poorly crystalline material forming patches in the samples is interpreted as plagioclase breakdown product. Reconstructive metamorphic reactions require the breaking and the formation of bonds between chemical components. Therefore the whole process can be divided into different stages, first the decomposition of the reactant/s and later the formation of the product phase/s. The rate at which these steps occur highly depends on several parameters, e.g. presence of fluids, temperature, pressure etc. Reaction rates increases in the presence of fluid and with higher temperature. Therefore, in these water under saturated samples reaction kinetics are expected to be rather sluggish. Hence, the occurrence of these poorly crystalline patches could represent the incomplete reaction of the plagioclase breakdown. This reaction also involves a decrease in grain-size of the plagioclase crystals (Figure 64). Another observation is that these structures are always associated with an increase in porosity (Figures 63; 64; 69; 70). As already mentioned above, the decomposition reactions of both plagioclase components are accompanied by a negative volume change (-14 % An breakdown, and -17 % Ab breakdown; Table 2) and this will cause the formation of porosity in the sample and as a result the nucleation of microcracks due to deformation. Zones of higher porosity, in NG_2_1225 in the vicinity of a fracture, are oriented at around 45° with respect to the maximum compression axis (Figures 62B) and located along the borders and in the corners of both samples (Figure 69).These are regions where the stress is expected to be highest and as a result plagioclase will be highly metastable. The extent in microcrack formation due volume decrease during plagioclase breakdown could explain the discrepancy between both experimental runs regarding the total number of AEs, as a result of microcracking or fast rupture. During the deformation of the sample NG_2_1225, which shows large areas of high porosity and a small fracture (Figure 62) many AEs were recorded (Figure 60) compared to sample NG_3_1225 which was rather silent (Figure 61) and which exhibits a lower amount of zones with increased porosity (Figure 65B).

4.2.5 Bursts of acoustic emissions

Two bursts of AEs were recorded during deformation of both samples (Figures 60; 61). Both bursts could derive from the formation of microcracks due to plagioclase breakdown where the first burst represents the sudden breakdown of plagioclase due to its metastability under high-pressure and the second the thermal reactivation of the plagioclase decomposition. The samples are rather dry and reaction kinetics are hampered. Therefore the increase in temperature may have supported the plagioclase breakdown in this water under saturated environment.

4.2.6 High-pressure faulting of granulites – one possible scenario

Combining all observations together the most plausible scenario to explain the microstructures would be that fracturing at HP/HT was caused by plagioclase decomposition involving a pronounced volume decrease. Stress drops on these fractures and in their surroundings could cause an influx of fluids (adhesion water) and may cause partial melting of some phases (pyroxenes from the starting material). Later the fluids and the presence of melt could enhance the eclogitization along the fractures (Cz-bands). The discrete formation of the plagioclase breakdown products Cz and Ky is in good agreement with the observed textural evolution monitored using the powder-diffraction pattern (Figures 60; 61). Based on the total number of AEs, which is around 10 times higher in the sample that reveals a low degree of eclogitization (NG_2_1225), it seems that the higher amount of eclogitization rather softens then embrittles the rock. The breakdown of plagioclase and the formation of eclogite appear to be two competing processes and their rates will control the overall rheology of the sample.

4.3 LINK TO NATURAL OBSERVATIONS

4.3.1 Geophysical observations – Tibet-Himalaya collision zone

Relocation of seismic events in the Tibet-Himalaya continent-continent collision zone reveal, that intermediate depth seismicity occurs in regions that are partially eclogitized (Hétenyi et al., 2007; Liang et al., 2011). Seismicity seems to occur especially in regions of the lower continental crust that are expected to show only lower amount of eclogitization (Figure 76). Areas that should be highly eclogitized do not exhibit seismic activity. The lack of seismic activity in these area matches well with the rather low AE activity in the sample that underwent pronounced eclogitization.

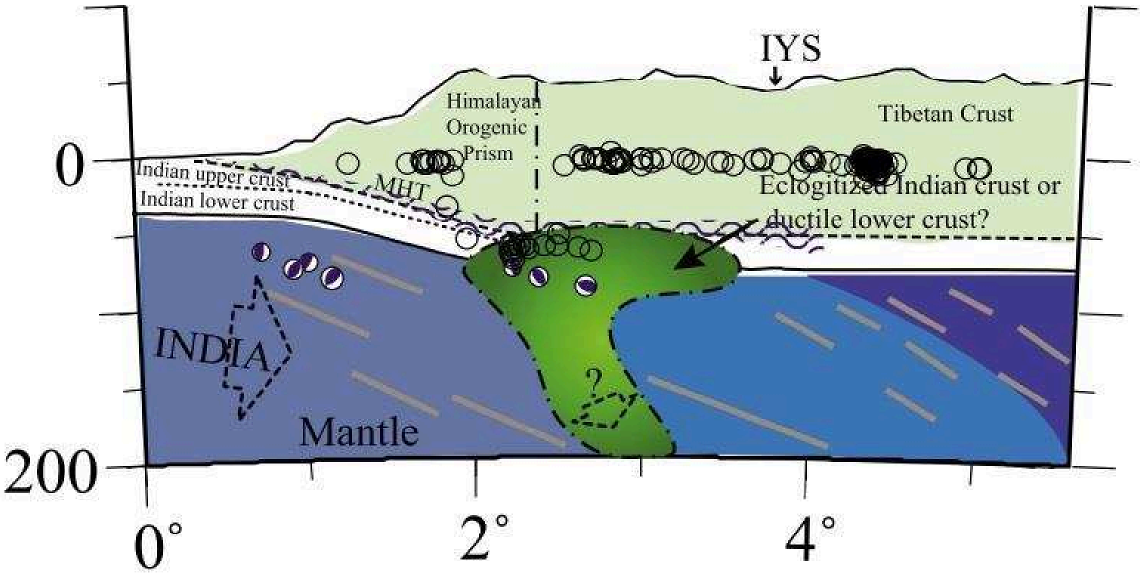

Figure 76: Modified from Liang et al. (2011). Cross-sectional view of the Tibet-Himalaya continent-continent collision zone. Relocations of intermediate-depth events reveal a good correlation between partially eclogitized areas of the lower continental crust.

4.3.2 FIELD OBSERVATIONS - ANCIENT SEISMIC FAULTING AT INTERMEDIATE-DEPTH IN THE BERGEN ARCS, SW NORWAY

During Caledonian orogeny (480-380 Ma) the continental crust along the complex scandinavian margin of the Iapetus Ocean was partly subducted and stacked into a series of allochthons on top of the Baltica shield (Corfu et al, 2014). The collisional stage caused large scale deformation of the lower crustal rocks (Andersen et al., 1990; Jamtveit et al, 1990), which was partly preserved in the Bergen Arcs in SW Norway. The Bergen Arc anorthositic to gabbroic granulites are part of the Lindås nappe, which underwent eclogite facies partial re-equilibration at 430 ± 3 Ma (Glodny et al, 2008) and limited subsequent amphibolite facies overprint. These rocks demonstrate discrete eclogitization in an intricate network of ductile shear zones and pseudotachylites (Figures 77; 78), both formed under eclogite-facies conditions and range from cm to dm scale in size (Boundy et al., 92; Raimbourg et al., 2007). Pseudotachylites (PST) are believed to represent fossilized evidence of ancient earthquakes (Sibson, 1975) and therefore their occurrence implies brittle failure at high-pressure/high-temperature (HP/HT) conditions. The close spatial relation of PSTs quenched under eclogite-facies conditions and eclogite shear zones in the Bergen Arcs, implying a change in deformation regime over short distances, has puzzled several geologists in the past.

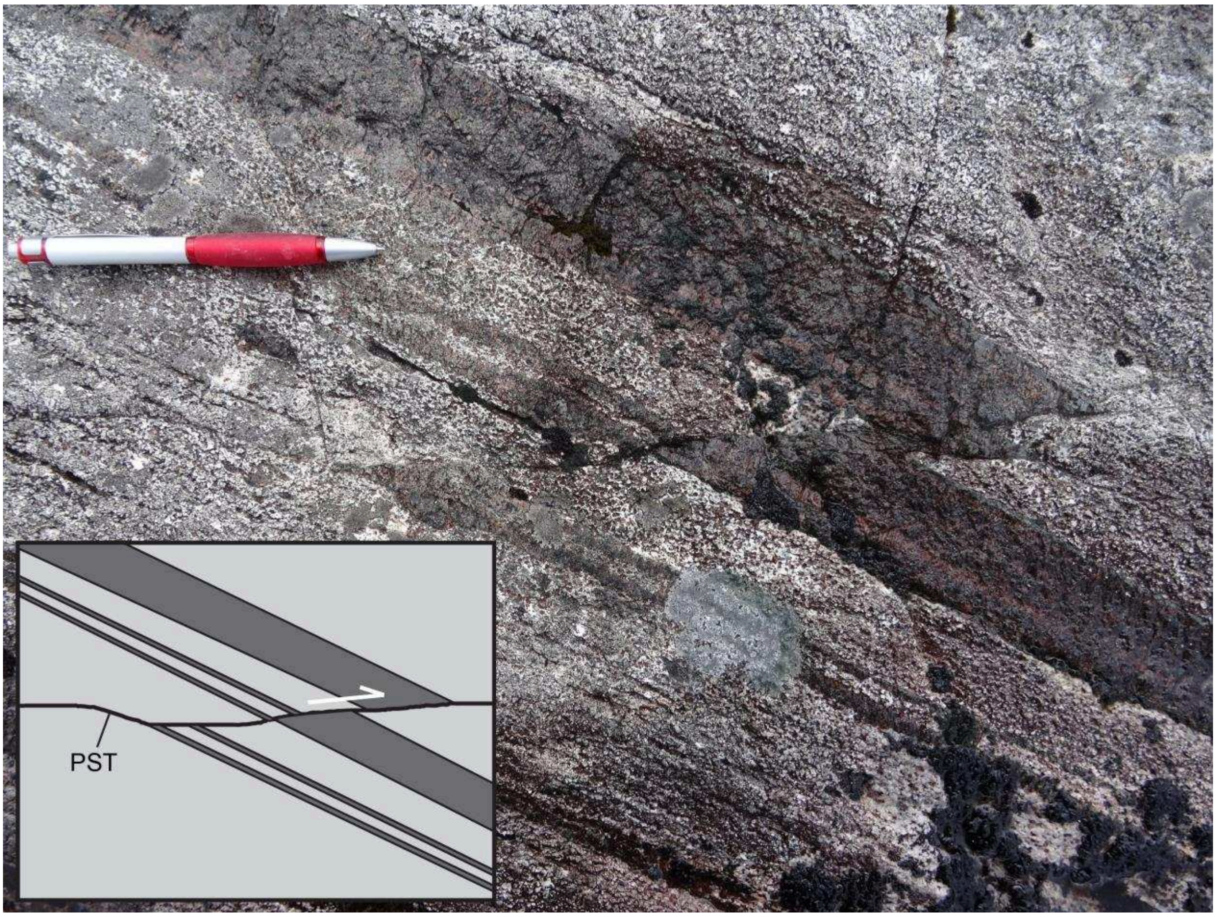

Figure 77: Natural pseudotachylite dissecting and displacing mafic veins on Holsnøy in the Bergen Arcs, SW Norway.

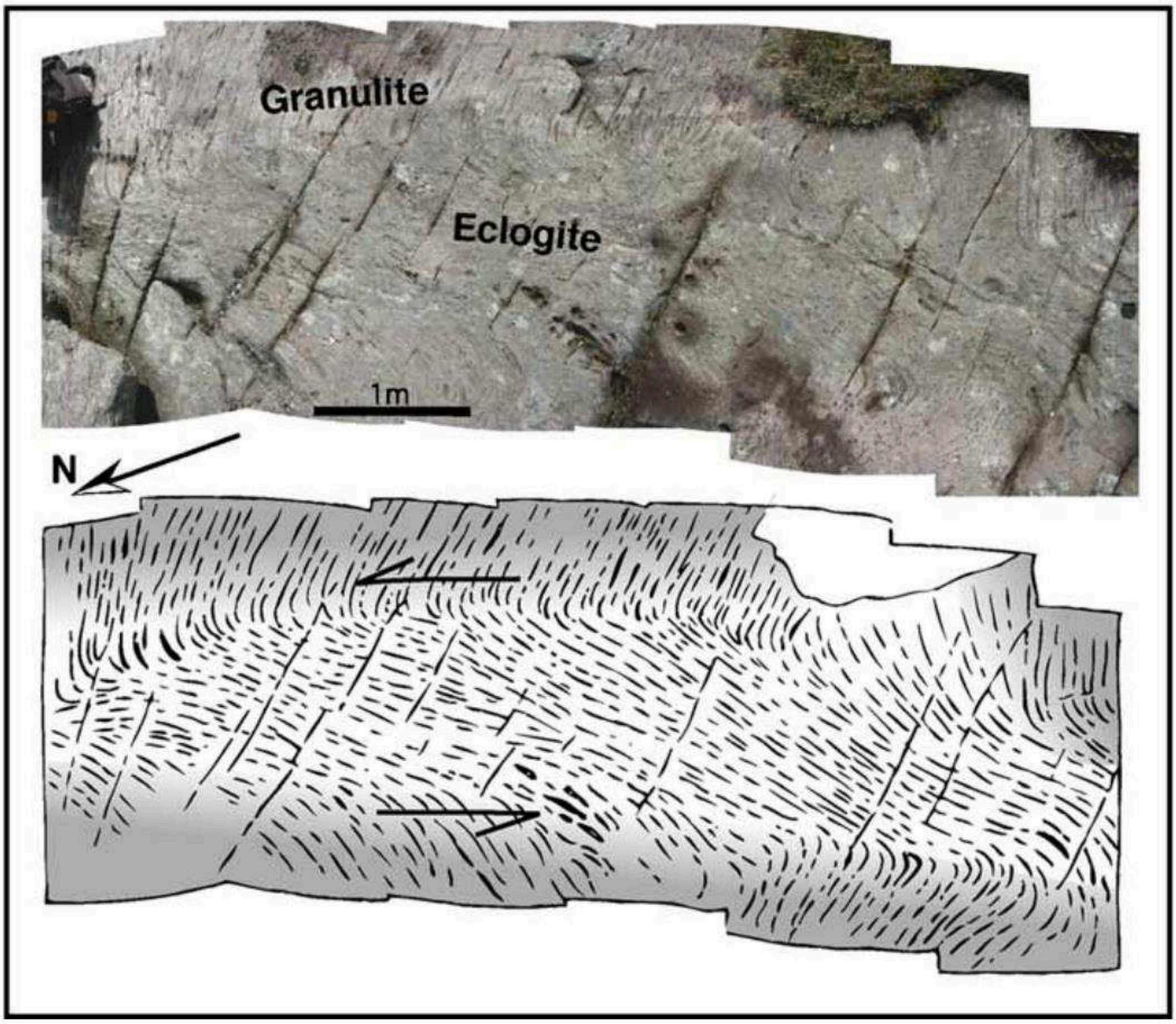

Figure 78: From Jolivet et al. (2005). Photograph and schematic drawing of an eclogite shear zone in granulites of the Bergen Arcs.

One possible explanation that is that metamorphic reactions assisted fracturing of the granulite at HP/HT conditions (Jolivet et al., 2005). Afterwards eclogitization due to fluid infiltration proceeded. If larger areas were transformed to eclogite the rock becomes ductile and forms eclogite shear bands or zones (Jamtveit et al., 2000; Jolivet et al., 2005; Figure 79).

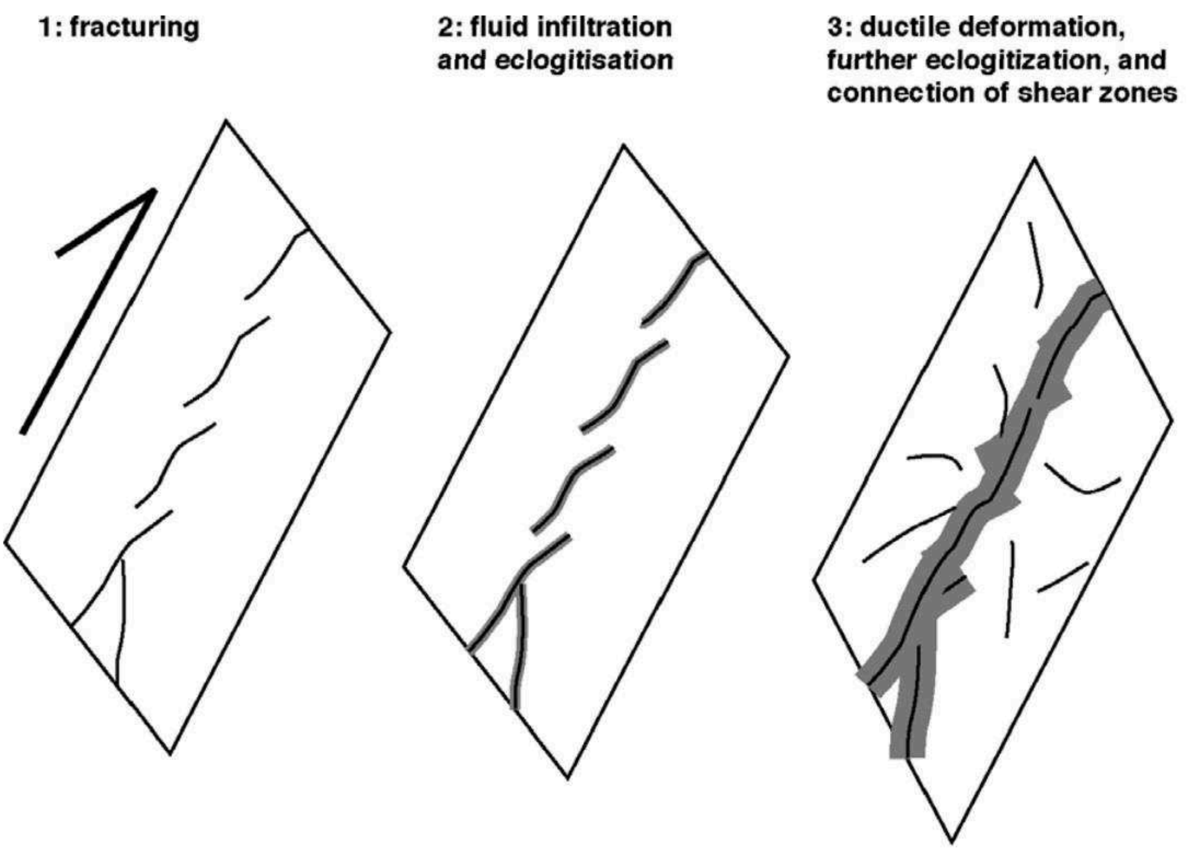

Figure 79: From Jolivet et al. (2005). Schematic drawing showing the evolution from brittle to ductile deformation due to the eclogitization of granulite.

The experimental results on granulite deformation also demonstrate that the decomposition of plagioclase causes fracturing of the rock (ductile-brittle transition). Later with ongoing eclogitization the deformation regime changes again from brittle to ductile. Therefore, the conclusions based on the experimental results presented in this chapter match very well with large scale observations of natural eclogitized granulites.

4.4 CONCLUSION

The experimental results demonstrate that there is a link between plagioclase breakdown and ductile-brittle transition at HP/HT conditions. Weakening occurs due to pronounced densification during plagioclase decomposition in conjunction with grain-size reduction of the remnant plagioclase crystals and the formation of a poorly crystalline low-frictional material. Ongoing eclogitization of the granulite samples seem to change the rheology again to favor ductile deformation. These observations based on laboratory experiments on small samples are in good correlation with geophysical observations and natural structures in the field. Thus, this leads to the conclusion that the formation of intermediate-depth earthquakes in nature may be governed by the same underlying mechanism as small “lab-earthquakes”, mainly the densification during eclogitie-facies metamorphic reactions.

However, only two deformation experiments on granulite powders were performed in the D-DIA. Although both samples show striking microstructures that highlight the role of plagioclase breakdown on faulting, more experiments have to be performed to prove this hypothesis which is based on preliminary results.

“Selig sind die Vergesslichen, denn sie werden

auch mit ihren Dummheiten fertig.“

- *Friedrich Nietzsche*

V THERMODYNAMIC CONSTRAINTS ON THE FORMATION OF INTERMEDIATE AND DEEP EARTHQUAKES

In this chapter two experiments on almost pure phases, glaucophane and tremolite, will be presented. The motivation behind the use of almost monophase starting materials was to highlight the impact of volume and enthalpy change during eclogite-facies metamorphic reactions. The experimental results will be discussed and linked to the formation of intermediate and deep seismicity. The main part of this chapter is represented by the experimental investigation of two high-pressure model reactions i) tremolite ↔ 2 diopside + talc and ii) the HP breakdown of glaucophane ↔ 2 jadeite + talc. The following discussion will also include the thermodynamics of other previously presented eclogite-facies metamorphic reactions and their influence on triggering and/or supporting seismic events.

5.1 EXPERIMENTAL RESULTS

5.1.1 Hydrostatic experiment on tremolitite as starting material

The microstructure of the static piston-cylinder experiment performed at approximately 2 GPa and 823 K (Figure 80) on tremolitite, comprising almost exclusively tremolite, is shown in Figure 81. Although the experiment was conducted in the stability field of Di and Tlc (after Kirby, 1987; Figure 80) there is no microstructural evidence that the reaction Tr ↔ 2 Di + Tlc took place. Based on the other P-T pseudosections after Jenkins et al. (1991) and Charnosky et al. (1993) the experimental run was conducted within the stability field of tremolite. The sample consists exclusively of the starting material minerals Tr, the Mn-enriched Tr and only minor amount of Ap (Figure 81).

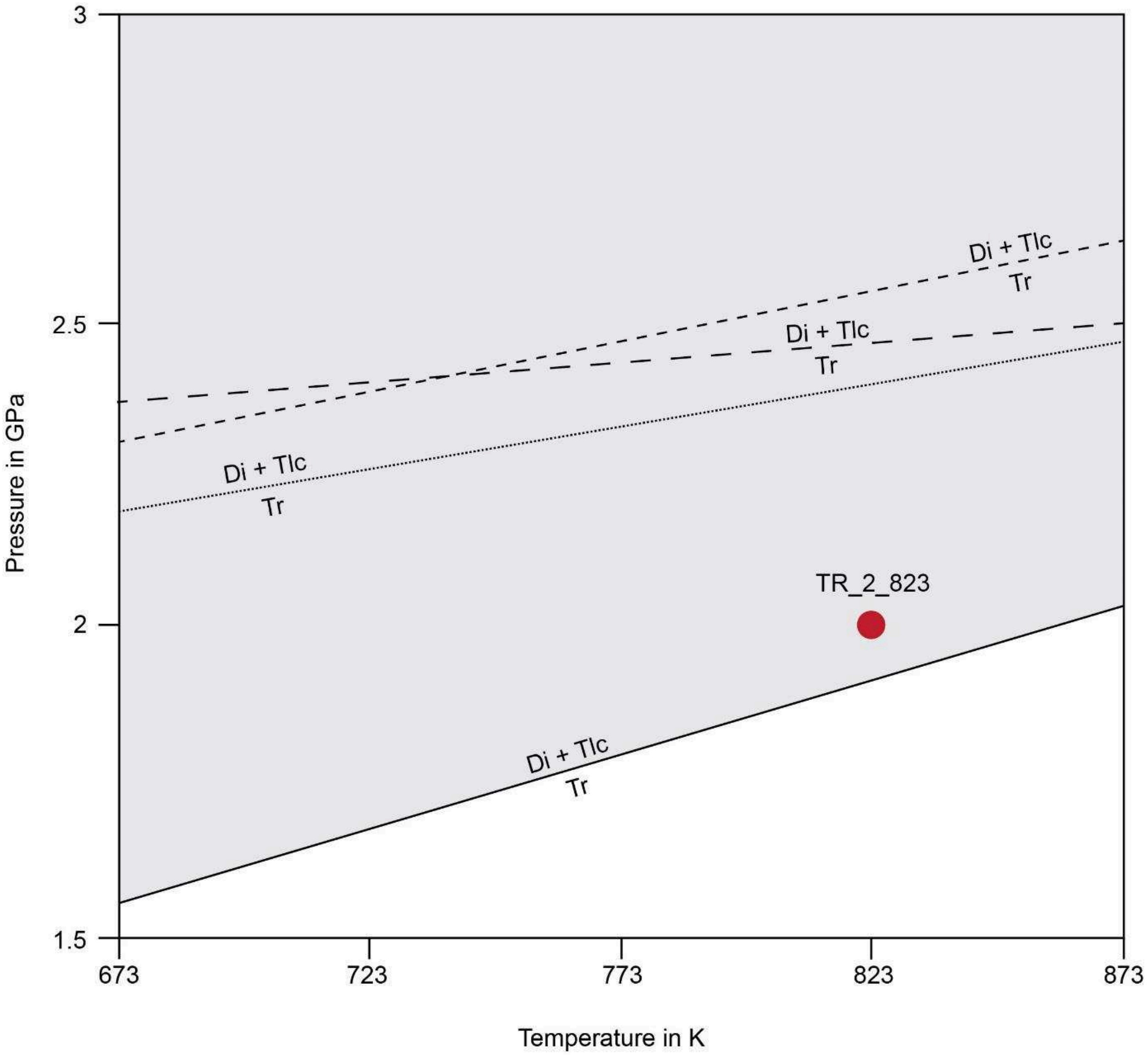

Figure 80: P-T conditons of the hydrostatic experiment TR_2_823.

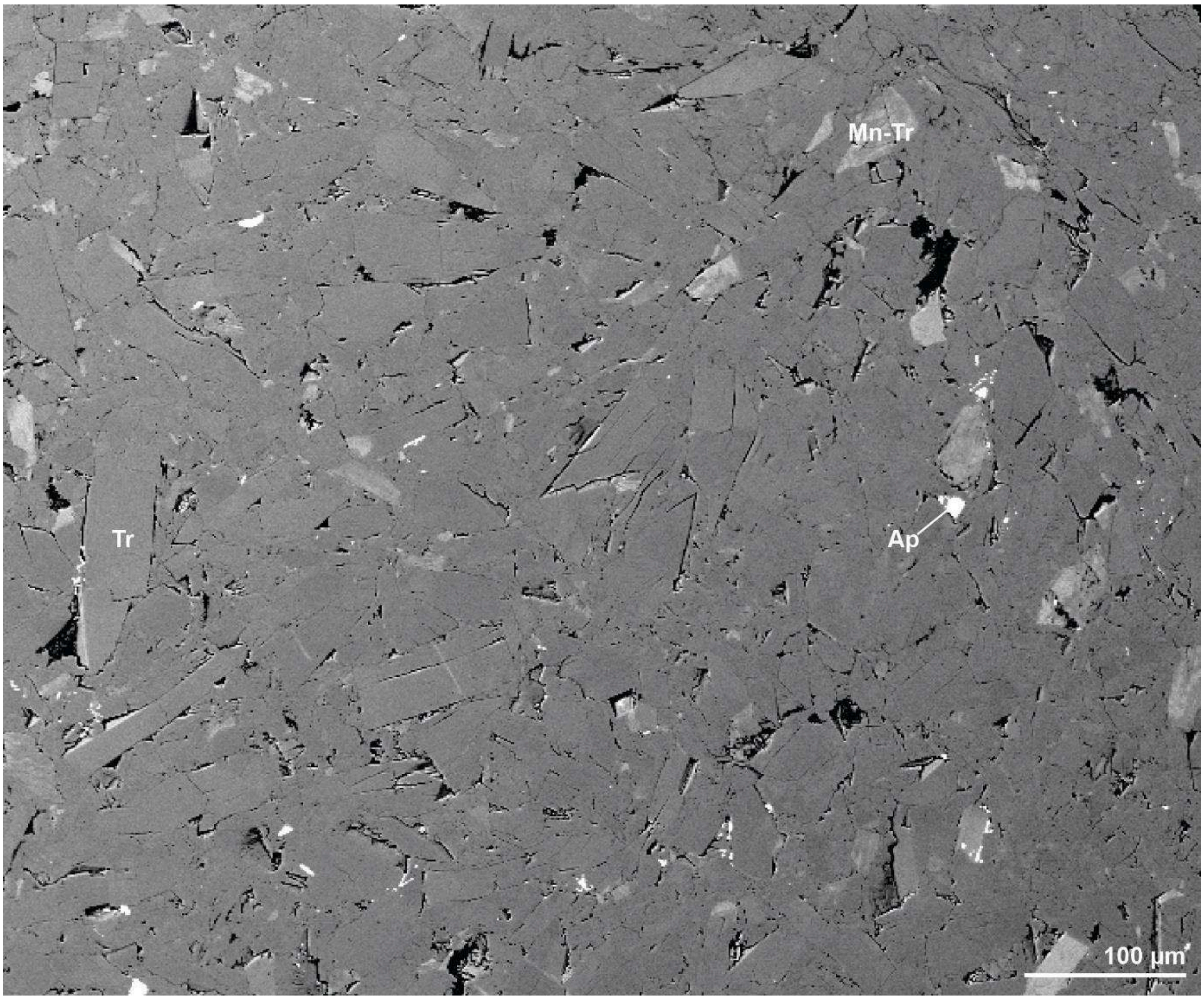

Figure 81: Microstructure of the static experiment using the tremolite starting material. The microstructure reveals, that it exclusively consists of tremolite with minor grains appearing brighter in BSE mode due to an enrichment in Mn.

5.1.2 D-DIA deformation experiments

Both sample materials were deformed using the D-DIA apparatus. Depending on the stability of either glaucophane or tremolite the experiments were performed under different confining pressures and temperatures (Table 15).

Table 15: Experimental conditions of the D-DIA experiments on two different amphiboles.

Sample	Experiment #	Starting material	P_c [GPa]	T range [K]	Strain rate [s^{-1}]	Maximum strain [%]
GLS_3_1043	D1815	Gln-powder	≈ 3	≈ 656-1043	$\approx 3\cdot10^{-5}$	≈ 39
TR_2_838	D1621	Tre-powder	≈ 2	≈ 740-838	$\approx 5\cdot10^{-5}$	≈ 42

Mechanical data, XRD observations, and acoustic emissions

GLS_3_1043

The differential stress on glaucophane (blue line in Figure 82) increases during the first stage of deformation until about 14 % axial strain then decreases due to the increase in temperature (black line in Figure 82). From the beginning of the deformation experiment the Jd (-221), the most intense peak of Jd, grows in the powder diffraction pattern until around 22 % then decreases very rapidly to approximately 35 % axial strain (green line in Figure 82). At the end of the experiment there is either no more Jd in the sample or its content lies beyond the detection limit for the XRD. Due to the low-symmetry of both phases, glaucophane and jadeite (or clinopyroxene in general), there are many peak overlaps in the powder diffraction pattern, which makes it difficult to observe the growth or the disappearance of a peak (Figure 38 under 2.4).

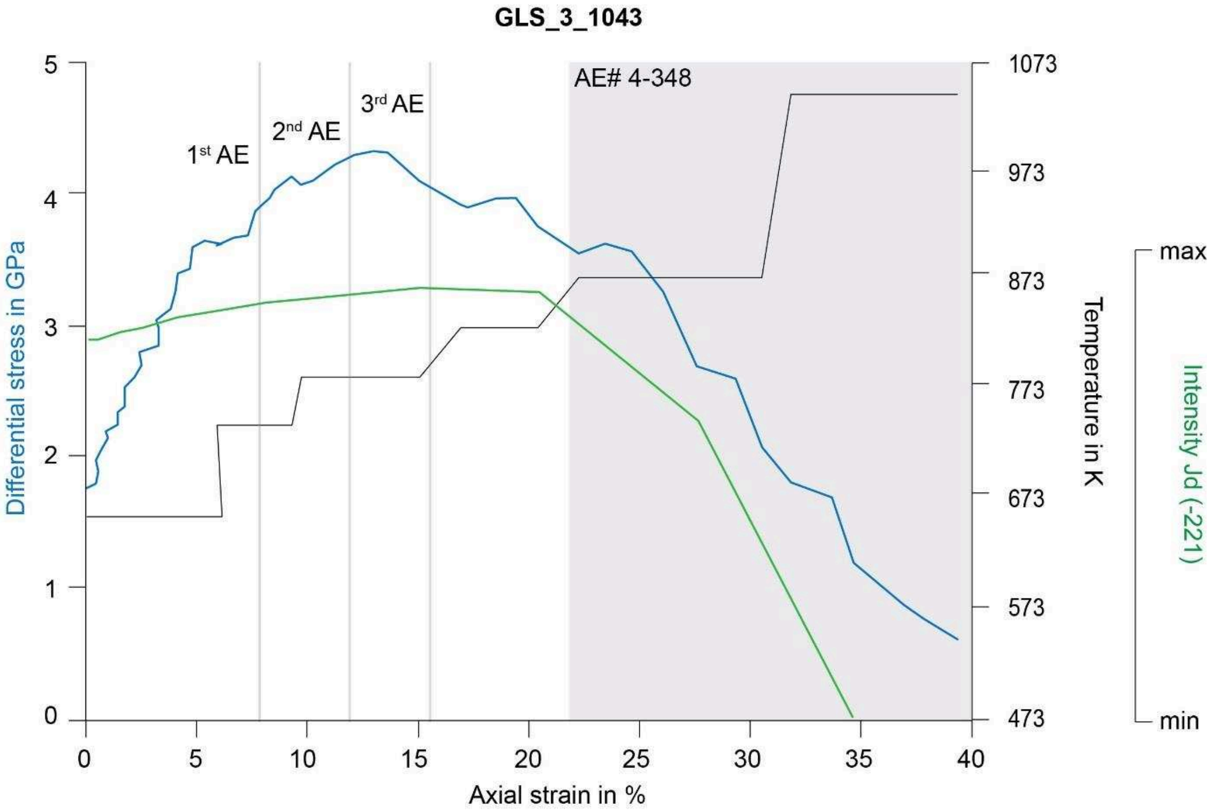

Figure 82: Differential stress (blue line), temperature (black line), and intensity of Jd (-221)(green line) vs. axial strain in %. The grey bars at around 8, 12, and 15.5 % axial strain mark the occurrence of the first three acoustic emissions and the grey rectangle from 22 % until the end of the experiment shows the area of the recorded AE-swarm with AE # 4-348.

In total 348 AEs were recorded during deformation. The three grey bars mark the positions at which the first three AEs occurred and the grey rectangle displays the stress-strain range in which a high-strain/high-temperature AE-swarm was recorded (Figure 83). The first emission was recorded at around 740 K and an axial strain of about 8 % (Figure 82), but most of the events occurred after heating up to about 875 K(Figures 82; 83). Most of the AEs are rather small with a magnitude $M_{AE} < 1$ (Figure 83). Only two bigger events with M_{AE} 1.6 and 1.4, respectively, were recorded during deformation. The M_{AE} 1.6 event coincides with a heating step from around 780 to 830 K and the M_{AE} 1.4 emission was recorded 18 min. after heating to the maximal temperature of approximately 1043 K (Figure 83). There are bursts of AEs while increasing the temperature (dashed lines in Figure 83), but there are also many AEs recorded between the heating steps and their intensity increase with increasing temperature (Figure 83).

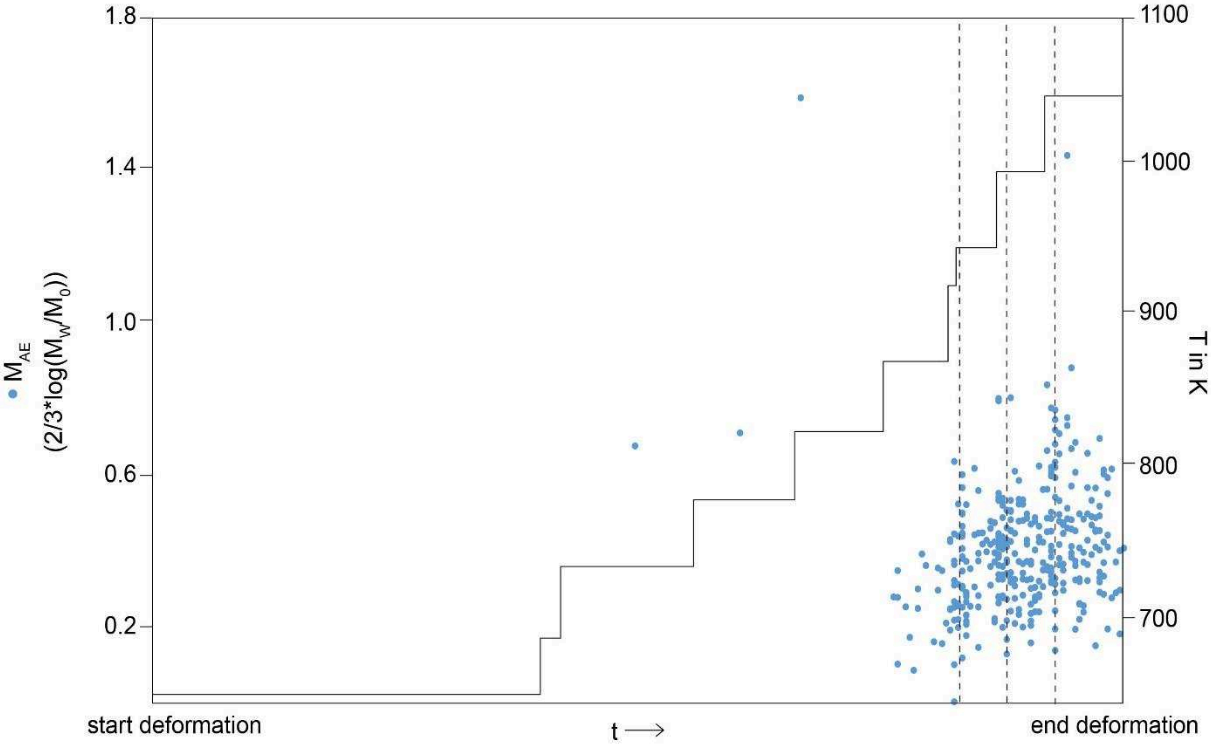

Figure 83: Magnitude of AE (M_{AE}; each blue spot corresponds to one recorded event) and temperature (black line) over time plot presenting the energy of each event and their occurrence during deformation of the sample GLS_3_1043.

The k-T plot (Figure 84) shows that most of the events are dominated by a shear or deviatoric component pointing to double-couple (center of the plot) or compensated linear vector dipole (CLVD, along the T-axis) as source mechanism (Figure 84). Since almost all AEs are not much larger than the recorded electrical noise signal, it is very difficult to pick the first P-wave arrivals and their polarization, used for the calculation of the source mechanism (explanations in section 2.4).

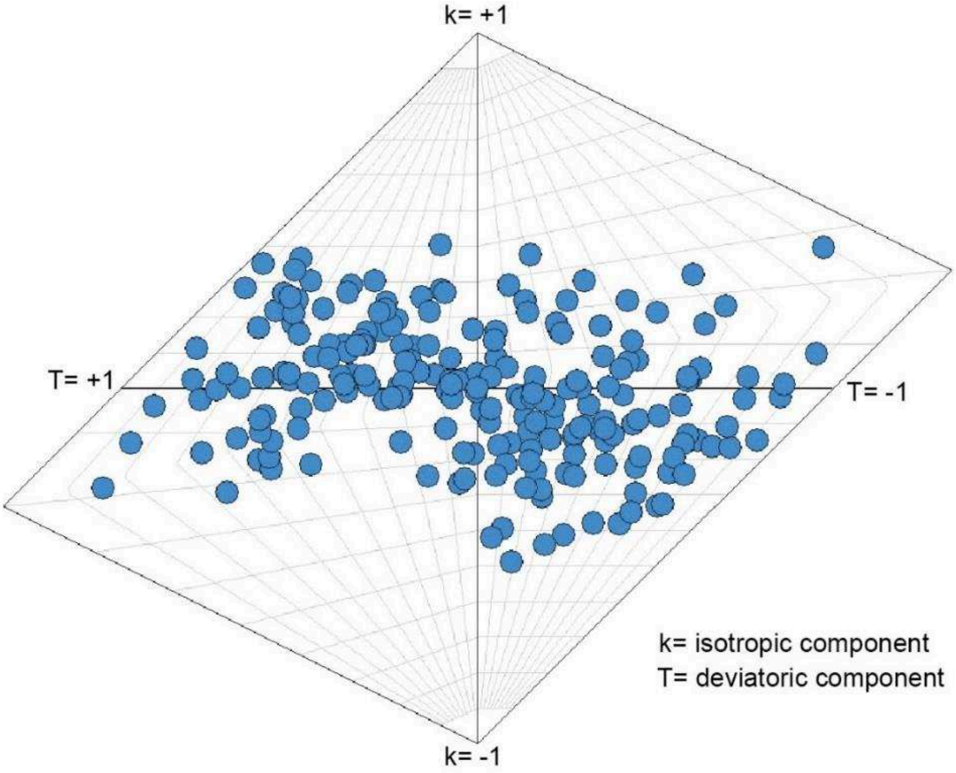

Figure 84: K-T plot for the glaucophane experiment GLS_3_1043 with k as isotropic component (k=+1 *"explosive" and k= -1 "implosive") and T as deviatoric or shear component.*

A plot of the total number of AEs shows that the events in the glaucophane experiment GLS_3_1043 follow rather well the Gutenberg-Richter law (Figure 85), which states that there are 10 times more earthquakes of $M_w \leq 1$ relative to events with $M_w \leq 2$, and 100 times more than $M_w \leq 3$ events (b-value= 1) (Gutenberg & Richter, 1956).

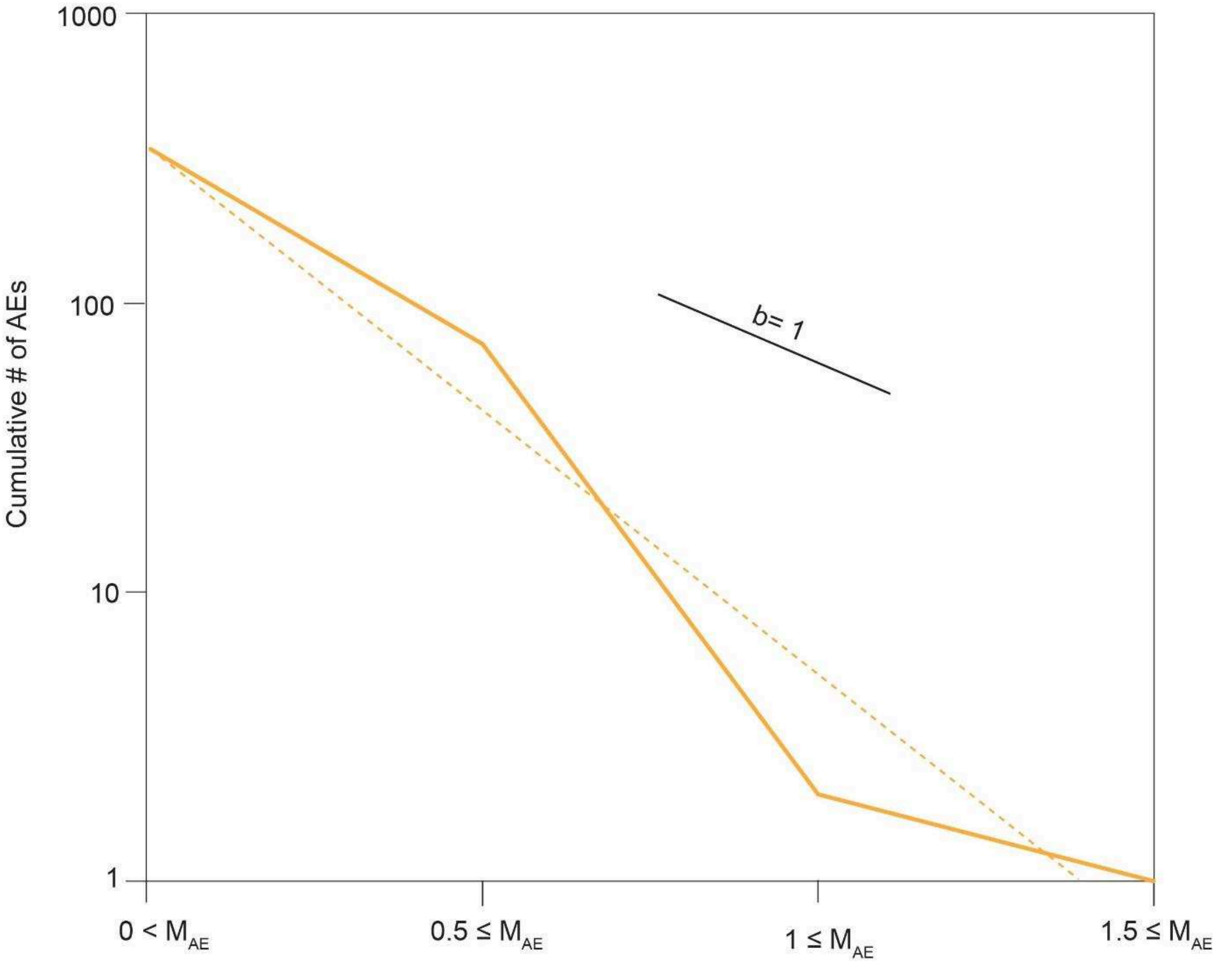

Figure 85: The cumulative number of AEs over magnitude diagram shows a Gutenberg-Richter distribution for the events recorded during the deformation of the glaucophane experiment.

TR_2_838

The differential stress on tremolite (grey line in Figure 86) increases during deformation to until 15 % axial strain and then decreases to the end of the experiment due to the stepwise heating of the sample (Figure 86). It was not possible to calculate the differential stress for tremolite between 10 and 15 % axial strain, because of the complexity of the diffraction pattern of the tremolite experiments. Monitoring the disappearance or the appearance of phases was also not possible due to many peak overlaps in the powder-diffraction pattern (Figure 38 and explanations in section 2.4). The grey bars mark the positions of the eight AEs recorded while deforming the sample. Due to the quality of the signal of the events and the small number of recorded AEs it was neither possible to calculate their source mechanisms nor to investigate if the events follow a Gutenberg-Richter distribution. The magnitude of the AEs increased during the experimental run with the smallest AE at the beginning and the biggest at the highest temperature at the end of deformation (Figure 87).

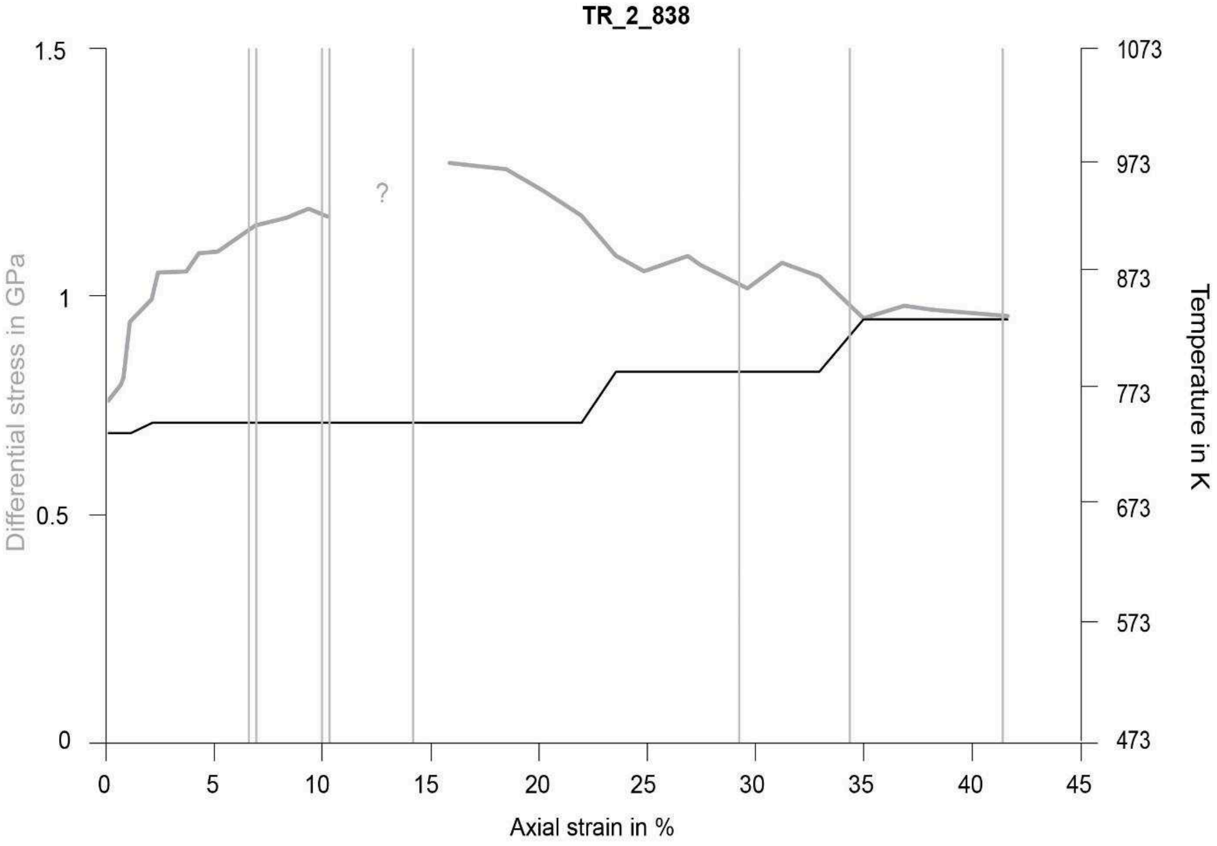

Figure 86: Differential stress (grey line) and temperature (black line) vs. axial strain in %. Due to an insufficient quality of the powder diffraction images it was not possible to calculate the differential stress on tremolite between around 11-16 % axial strain. This region is marked with a question mark. The grey bars highlight the occurrence of the recorded AEs during deformation.

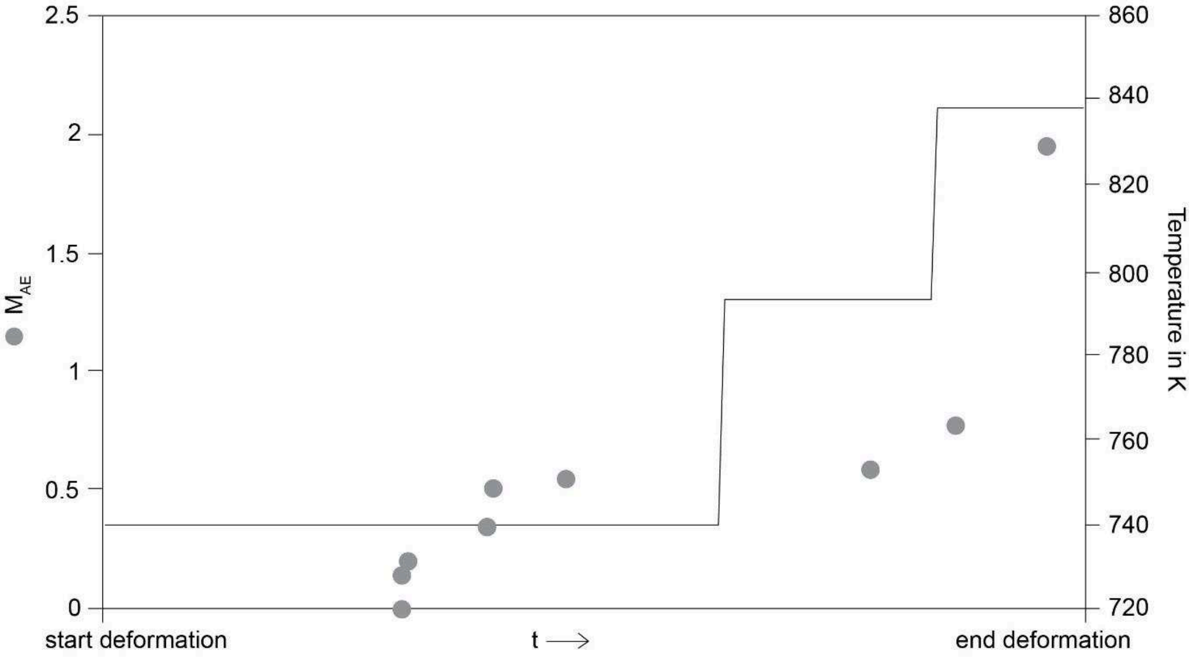

Figure 87: Magnitude of AE (M_{AE}; each grey spot represents an event) and temperature (black line) over time.

Microstructural and chemical analysis

GLS_3_1043

After deformation the glaucophane sample GLS_3_1043 is completely cross-cut by many fractures (Figure 88A). Due to the wide main fractures (Figure 88), sample preparation was challenging and unfortunately most of the material next to or filling out these fractures was lost. Several narrower fractures are oriented parallel to these bigger fractures (Figure 88B) and along some of them, either sheared (Figure 88C) or dissected and displaced crystals (Figure 88D) can be found in the microstructure. The sheared mineral, which appears dark in BSE mode, was analyzed as small albite crystal, deriving from the starting material, now showing tiny needles enriched in Na (Figure 88C). Due to the small grain size of these needles a phase identification using the SEM was not possible. The brighter zones, often along glaucophane crystals, were identified as actinolite (Figure 88B).

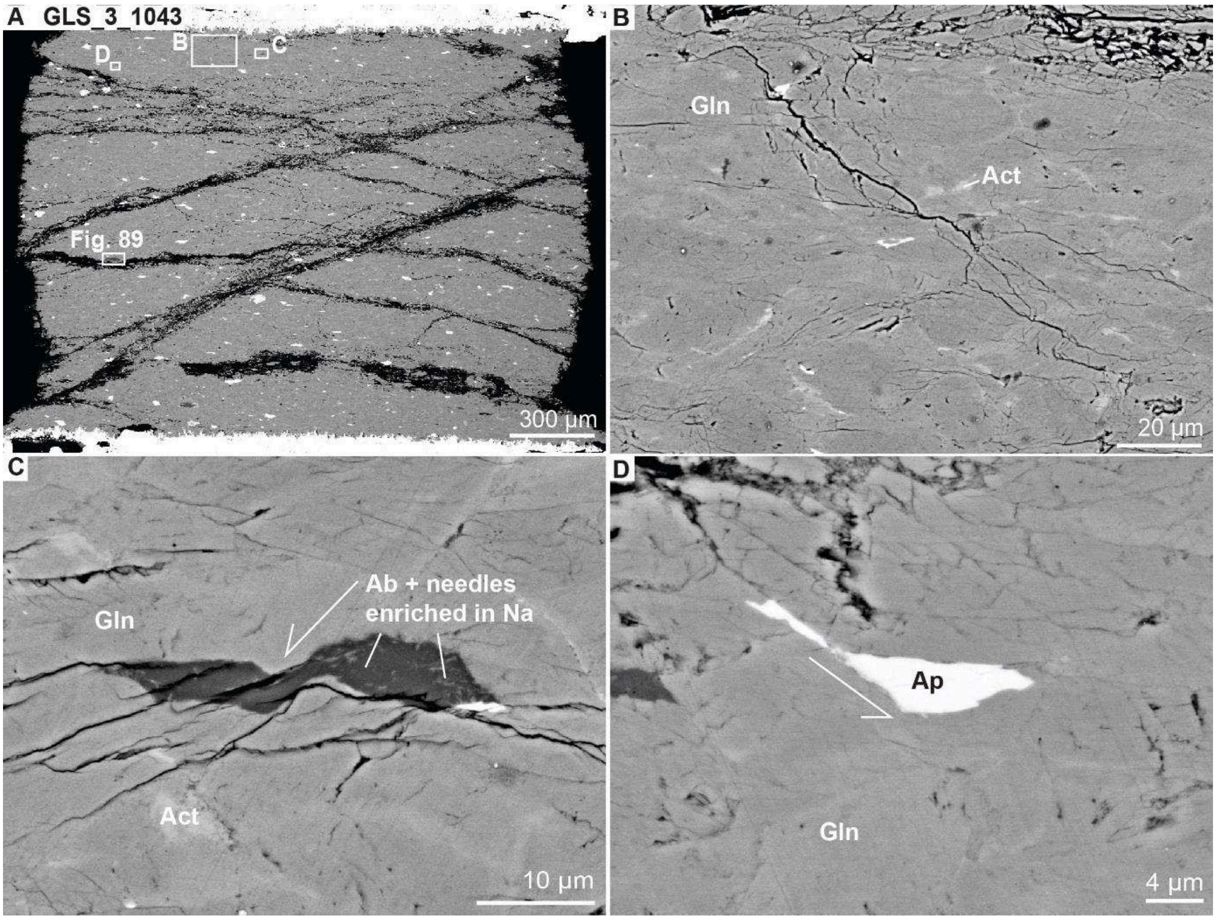

Figure 88: A) Overview of the glaucophane sample GLS_3_1043 after deformation, showing fractures cross-cutting the entire sample. The white rectangles mark the positions of the high magnification images presented in B, C, D, and of Figure 89. B) Microstructure showing a narrow fracture along the maximum shear stress direction. The sample consists almost exclusively of glaucophane with some areas identified as actinolite. C) Small albite grain sheared along a narrow fracture showing small needles enriched in Na. D) Apatite crystal dissected and displaced along a fracture. All presented images were taken in BSE mode at the SEM.

A white rectangle in the overview image (Figure 88A) marks the position of the area selected for an element distribution map (Figure 89). This region was chemically mapped and the Na- and Si-maps demonstrate that the idiomorphic crystals in this “pocket”-like structure are clearly enriched in Na together with many small grains enriched in Si (Figure 89). Raman analyses of two different areas (red spots in Figure 89) exhibit that this pocket is composed of a mixture of albite, appearing as darker material in BSE mode, which incorporates idiomorphic jadeite crystals, quartz grains, but also glaucophane. The appearance of this structure resembles the sheared albite grain in Figure 88C. All albite grains found on the exposed surface show variable amounts of jadeite needles and are randomly distributed in the whole sample.

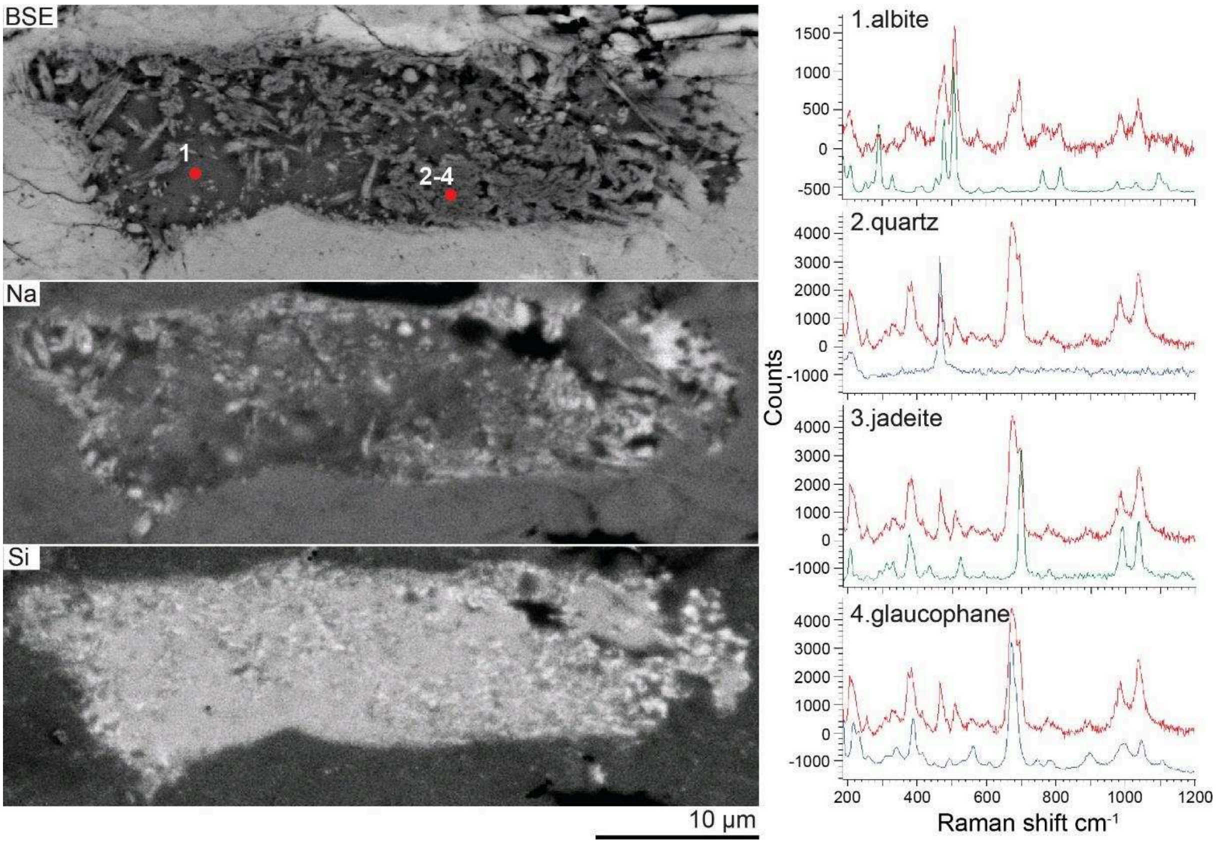

Figure 89: Albite crystal in BSE mode (top) and the corresponding Na (middle) and Si (bottom) distribution maps. The BSE image shows the position chosen for Raman analyses (right hand side). Analysis 1 demonstrates that the analyzed area mostly consists of albite. The area selected for the analysis 2-4 shows, that this region is composed of a mixture of quartz, jadeite, glaucophane, and albite.

TR_2_838

The tremolite sample TR_2_838 is also completely cross-cut by fractures after deformation (Figure 90A) and the microstructure shows dissected and displaced crystals along fractures (Figure 90C). Often fractures cut through grains, appearing darker in BSE mode (Figure 90) and identified as talc (Figure 91). In many places it seems that the propagation of the fracture is linked to the occurrence of talc (Figure 90D), which is not restricted to a certain area or direction but rather randomly distributed. The brighter contrast of some crystals (Figure 90C, D), also identified as tremolite, derive from a slightly different chemical composition, with brighter tremolite grains enriched in Mn relative to the main tremolite. There is no evidence for the growth of diopside during deformation neither in the powder diffraction pattern nor in the microstructure.

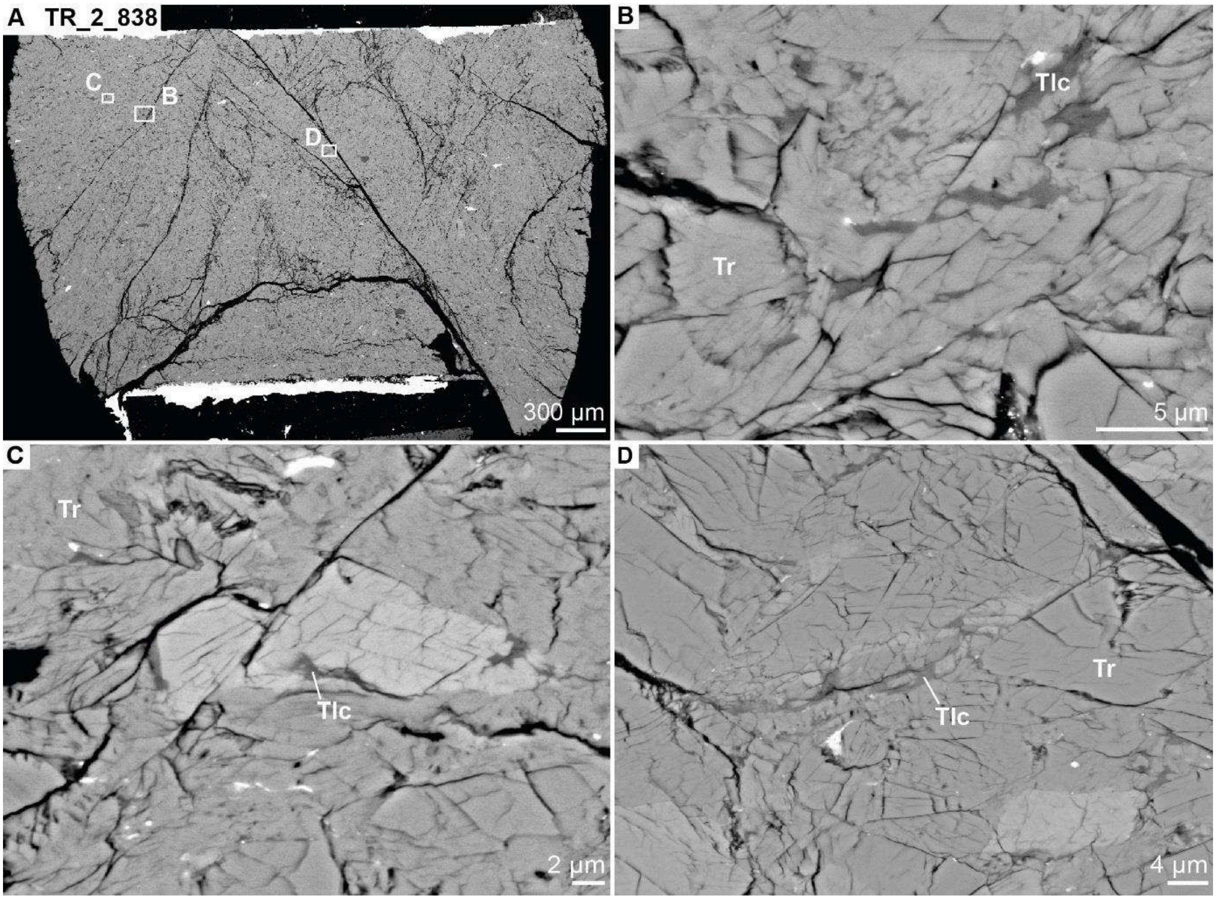

Figure 90: A) The overview image of the sample TR_2_838 exhibits, that the sample is completely cross-cut by conjugated fractures after deformation. The white rectangles B, C, and D show the locations for higher magnification images. B) The darker grey material was analyzed by Raman spectroscopy and identified as talc. C) Mn-rich tremolite displaced along a fracture. D) Fractures are often associated with the appearance of talc. Often they cut through or along (B) these newly formed phase and sometimes it seems that they progress where talc previously grew in the sample. All images were taken in BSE mode at the SEM.

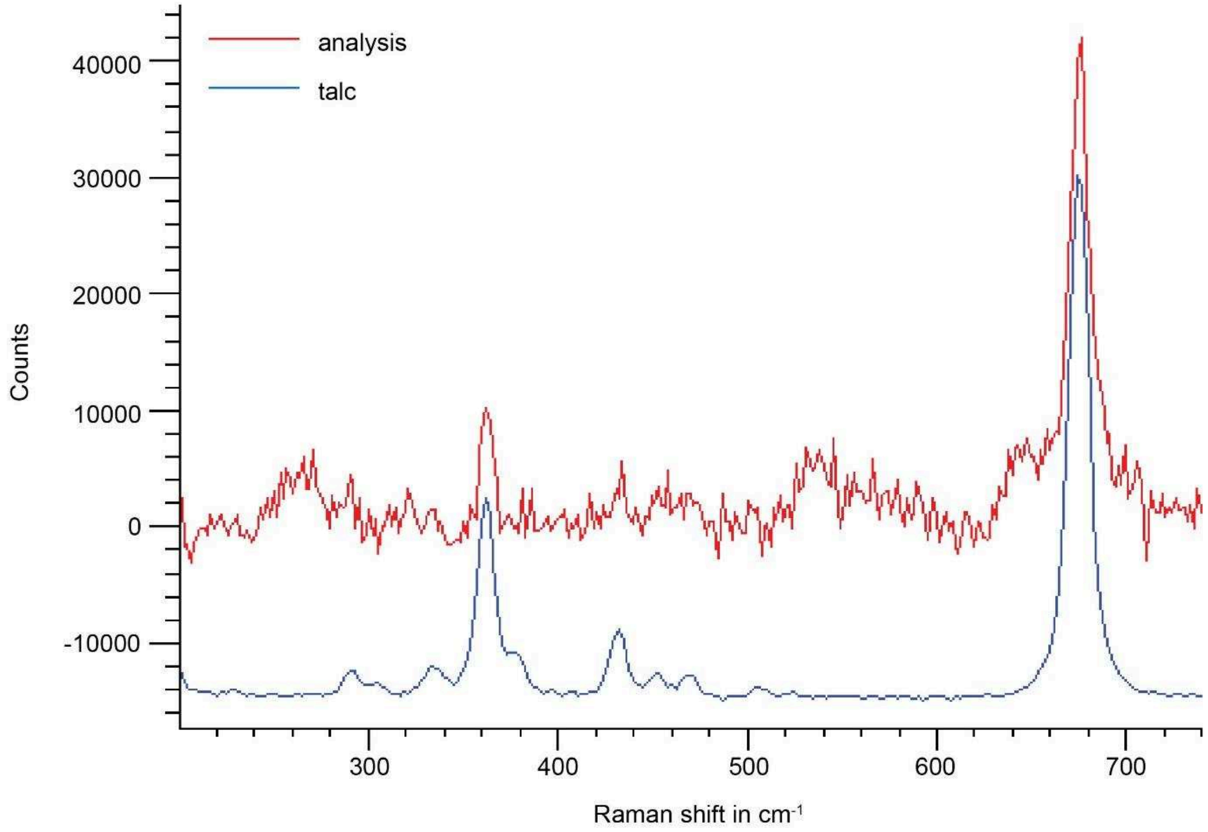

Figure 91: Raman analysis of the newly grown phase identified as talc in the tremolite experiment TR_2_838.

5.2 DISCUSSION

5.2.1 High-pressure faulting of glaucophane

During the first stage of deformation the (-221) peak of jadeite grows in the powder diffraction pattern, but there are neither microstructural evidences nor XRD observations for the growth of talc. The evolution of the jadeite diffraction peak (-221) is very similar to that of Omp (-221) in the blueschist experiments, where Omp (-221) intensity first increases and later decreases (Figure 4 in chapter III). However, secondary omphacite can be found along the shear fractures in the blueschist samples (Figure 7c in chapter III). Due to the loss of material during preparation of sample GLS_3_1043, it was not possible to examine neither the vicinity of most of the fractures nor the fracture filling material, which is expected to host the reaction products in case there is a link between the metamorphic reaction and the brittle fracturing of the sample at high-pressure conditions. Due to the resemblance of the Jd (-221) and the Omp (-221) evolution during deformation, it is believed that jadeite, or clinopyroxene in general, was present along the fractures in sample GLS_3_1043, as Omp2 in the Lws-blueschist samples, and was lost during preparation. Idiomorphic jadeite crystals, sometimes accompanied by very small quartz grains, can be found in albite grains derived from the starting material. By looking at the modified P-T pseudosection, the P-T path (solid blue line in Figure 92) of the the sample lies within the stability field of Jd + Tlc. Additionally, the high-pressure breakdown reaction of albite was added to the pseudosection (fine dashed line in Figure 92). This metamorphic reaction takes place at much lower P-T conditions relative to the HP breakdown reaction of glaucophane and the experimental path of the sample largely overstepped the albite breakdown reaction (Figure 92).

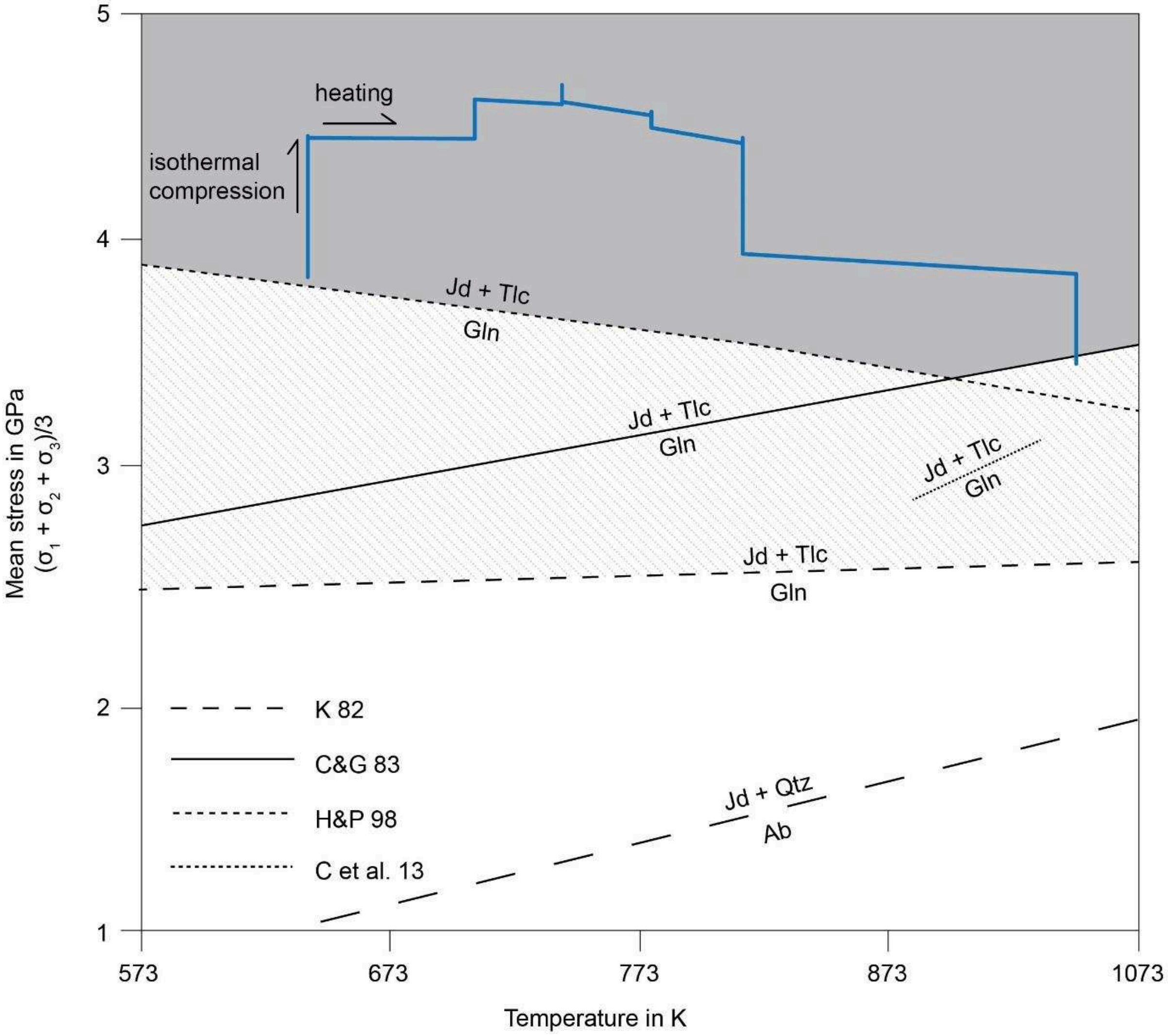

Figure 92: Mean stress vs. temperature plot showing that the P-T path (blue line) the glaucophane sample experienced lies within the stability field of jadeite and talc. Also some small albite crystals were found in the starting material and the P-T pseudosection demonstrates that the reaction albite ↔ jadeite + quartz was highly overstepped.

A possible explanation for the occurrence of jadeite and quartz in albite grains and the lack of talc and jadeite associated to glaucophane could be explained by the difference in metastability of both phases under the prevailing experimental conditions. Both breakdown recations of glaucophane and albite, are accompanied by a negative volume change with around -2.4 and -17 %, respectively (Table 2 in chapter I). Therefore the overstep or the metastability with increasing pressure will have a huge influence on their reaction rates. The overstep of reaction is more pronounced for the albite breakdown reaction relative to glaucophane breakdown at elevated pressure, which should lead to a higher reaction rate of albite.

5.2.2 HIGH-PRESSURE FAULTING OF TREMOLITE

Based on the calculated P-T pseudosection after Kirby (1987) (solid black line in Figure 93) the sample was deformed within the stability field of diopside and talc. Three other phase stability diagrams demonstrate that tremolite is stable at even higher pressures (Jenkins et al., 1991; Chernosky et al., 1993). The observation that tremolite remained stable under the experimental conditions of the static experiment could either show that the phase stability diagram from the publication of Kirby (1987) is not suitable here or that tremolite did not break down to form diopside and talc due to sluggish reaction kinetics. Experimental studies on either quartz or tremolite (Richter et al., 2016, Kirby, 1987) demonstrate that σ_1 is a critical parameter for mineral reactions to occur, and that the high-pressure breakdown reactions of either quartz (quartz ↔ coesite) or tremolite (tremolite ↔ 2 diopside + talc) can be induced only by increasing the principal compressive stress. This could also act as possible explanation for the occurrence of talc in the deformation experiment. Due to a continuous increase of σ_1 and in consequence also of σ_m while deforming the sample, it possibly entered the stability field of diopside + talc during deformation (Figure 93).

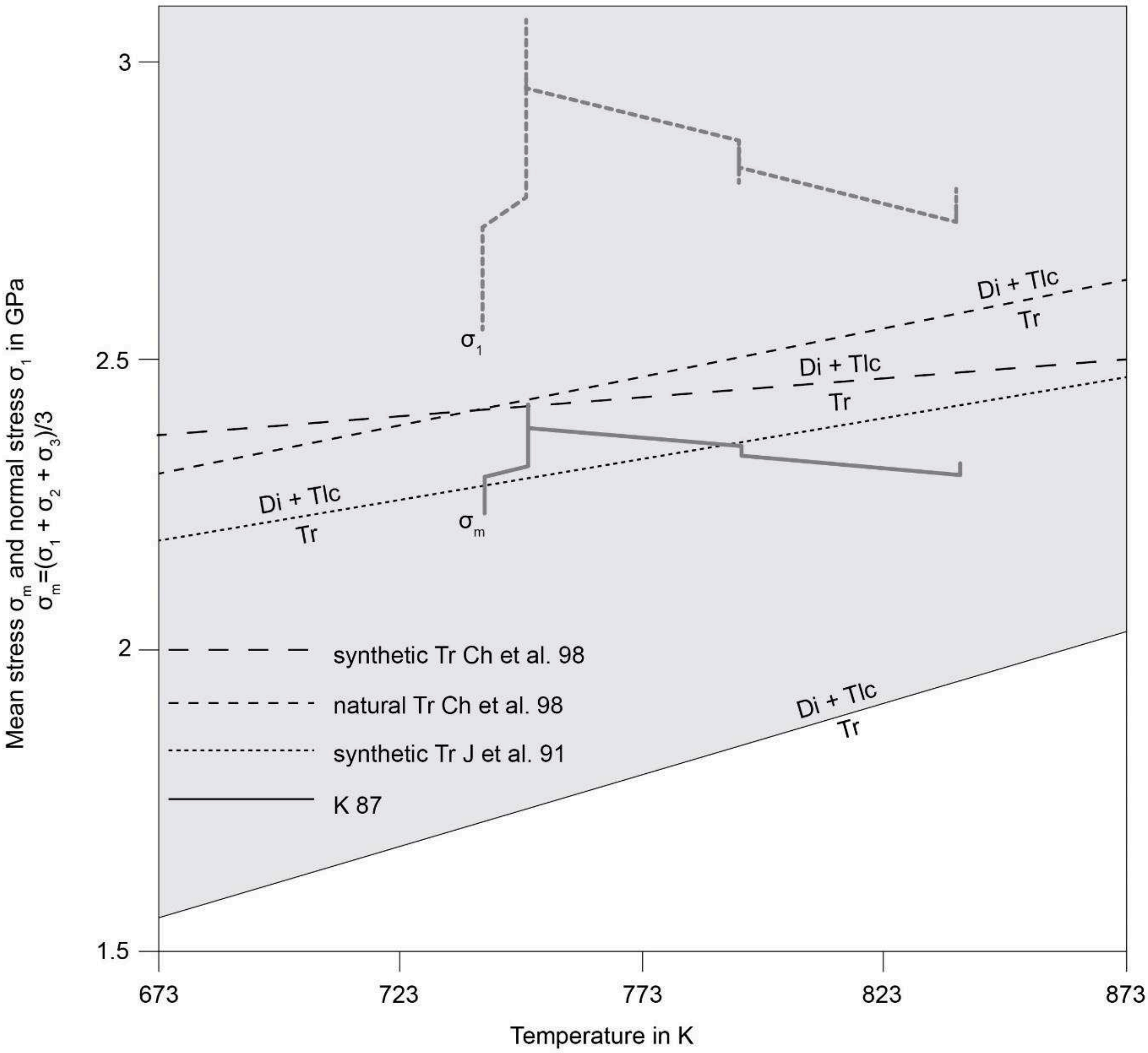

Figure 93: Mean normal and principal normal stress vs. temperature plot showing the influence of both stresses on the phase stability. Due to the increase in σ_1 the sample could enter the stability field of diopside and talc, although the confining pressure P_c (≈ 2 GPa) lies beyond this phase boundary (except for the phase diagram from Kirby, 1987).

5.2.3 BRITTLE FAILURE OF AMPHIBOLES UNDER HIGH-PRESSURE CONDITIONS

Both samples show bulged out sample borders, which implies that the samples were deformed within the ductile regime (Figures 88A; 90A) (Paterson & Wong, 2005). However, both microstructures reveal fractures cross-cutting the entire sample, which dissect and displace crystals (Figures 88D; 90C) implying brittle failure. During deformation of the glaucophane sample, 348 AE events were recorded in total, exhibiting double-couple or CLVD source mechanisms (Figure 84). The events follow a Gutenberg-Richter distribution (Figure 85), which suggests that our observations can be up scaled from the laboratory to natural conditions. While deforming the tremolite sample only eight events were recorded and due to this small number it was not possible to make a significant relation between the total number of events and their magnitude.

Densification as weakening mechanism

It is somehow surprising, that although the reaction enthalpies as well as the degree in volume change for the breakdown of glaucophane and tremolite are very similar, 348 events were recorded during the deformation of glaucophane and only eight while deforming tremolite. A possible explanation could be that the breakdown of albite was observed instead of the one of glaucophane. Both reactions, the breakdown of glaucophane and the decomposition of albite, will produce jadeite. Microstructural observations demonstrate that the reaction albite giving jadeite and quartz at higher pressure took place (Figure 89). In contrast, there is no evidence for the formation of talc neither in the diffraction pattern nor in the microstructure of the sample. The change in volume from glaucophane and tremolite to either jadeite or diopside and talc is rather small, around -1.2 or -2 % (Table 1). Though the densification during the reaction albite to jadeite and quartz is with approximately -17 % (Table 2) much higher. The reaction's slope is also positive in the investigated P-T range (Figure 94) and the reaction enthalpy is with ≈ -13.9 $kJ.mol^{-1}$ (calculated using the thermodynamic database of Holland & Powell, 1998) exothermic, which means that additional heat will be produced while the reaction takes place. The dependency of c_p on temperature changes was not taken into account. The pronounced densification during albite breakdown, observed in the GLS_3_1043 sample, relative to the expected volume decrease of the tremolite breakdown could explain the difference in total number of recorded AEs. This could imply a link between the degree in volume decrease and the "seismic activity" during deformation. Although this reaction involves a large volume decrease, it is not surprising that the radiation pattern of the AEs still dominated by the deviatoric component due to the overprint of the overall stress-field acting on the sample (Kirby, 1987). The solid-solid reaction of albite ↔ jadeite + quartz proceeds in the absence of water. This characteristic additionally highlights that the formation of mechanical instabilities leading to brittle failure is not necessarily related to the presence of water.

Influence of metastability and temperature on reaction rates

Another possible reason for this huge discrepancy in AE-activity could be the degree of metastability of the reacting phase. Unfortunately, the experimental studies on the high-pressure stabilities of glaucophane and tremolite vary a lot in the investigated P-T range (Figures 92; 93). Therefore, for the discussion of the degree of metastability on high-pressure faulting, the stabilities of Carman & Gilbert (1983) for glaucophane and of Chernosky et al. (1998) for natural tremolite were taken for the comparison (Figures 92, 93). Based on the mean stress over temperature curve the glaucophane stability was overstepped by around 1.5 GPa at lower temperatures and with approximately 500 MPa at higher temperatures (Figure 94). Based on tremolite stability of Chernosky et al. (1998) only regions of the sample dominated by σ_1 entered the stability field of Di + Tlc (Figure 94). The heating curves of both experiments were also different. The glaucophane sample GLS_3_1043 was quenched at much higher temperature of approximately 1043 K relative to the run TR_2_838, which was stopped at a temperature of around 838 K. Most of the AEs of the experiment GLS_3_1043 were recorded at higher temperatures from around 850 K. It is therefore possible that the higher temperatures the glaucophane sample experienced enhanced reaction kinetics. If the reaction progress scales with the AE activity this would imply that increasing temperature will increase the reactions kinetics and the densification leading to the formation of microcracks, assuming that this is the source of the AEs, and finally to brittle failure. Therefore, the differences in metastability and maximum temperature between glaucophane and tremolite during deformation could also explain the discrepancy of number of AEs recorded in both runs.

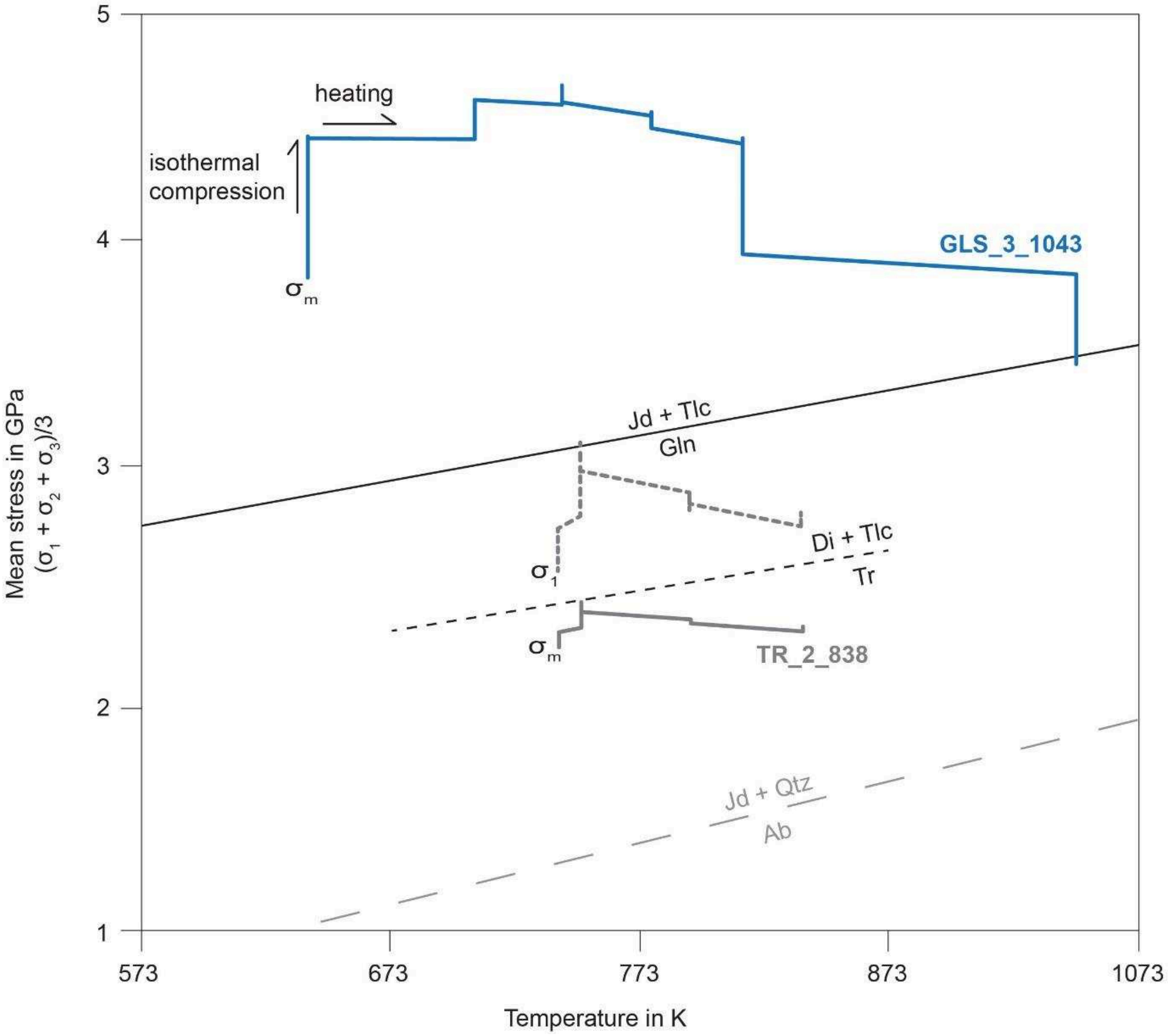

Figure 94: Mean stress-temperature curves of GLS_3_1043 (blue line) and TR_2_838 (grey solid line together with the maximum stress over temperature evolution of TR_2_838 (dashed grey line) and the breakdown reactions of both amphiboles after Carman & Gilbert (1983) for glaucophane and Chernosky et al. (1998) for tremolite. During deformation the glaucophane breakdown is highly overstepped at lower temperatures. Based on the experimentally investigated stability of tremolite after Chernosky et al. (1998) the sample only entered the stability field of Di and Tlc in highly stressed regions (grey dashed line).

5.2.4 GEOLOGICAL SIGNIFICANCE

It is not expected that large amounts of pure tremolite descend in subduction zones, although it is reasonable to assume that large volumes in blueschists of the down going oceanic crust may be almost exclusively composed of glaucophane. Therefore the reaction glaucophane ↔ 2 jadeite + talc occurring during the transition from blueschist to eclogite represents a potential candidate to explain the formation of intermediate-depth seismicity within the descending oceanic crust.

Although it is questionable if the reaction glaucophane ↔ 2 jadeite + talc took place during the glaucophane experiment, there is instead good microstructural and XRD evidence that the breakdown of albite giving jadeite + quartz, which was largely overstepped at the prevailing experimental conditions, occurred during deformation. This reaction has a high geological significance since plagioclase feldspars are common minerals of both the continental and oceanic crust. During orogeny, feldspar-rich rocks, e.g. anorthosites, will be thickened and stacked and due to the changing P-T conditions, the albite component of feldspar will become unstable to form jadeite and quartz. Feldspars are not only very common in the continental crust, but also present in minor amounts in the oceanic crust. In either case, glaucophane or albite breakdown, both reactions are accompanied by volume decrease and the liberation of heat (Table 2). Based on the presented experimental results it is clear that eclogite-facies metamorphic reactions involving densification can trigger high-pressure faulting accompanied by small laboratory earthquakes which follow the Gutenberg-Richter distribution (Figure 85).

5.2.5 ENERGY CONSIDERATIONS FOR METAMORPHIC REACTIONS TO SUPPORT DEEP SEISMICITY

Based on the slip weakening model (Rice, 1980) the total mechanical energy (ΔW) released during an earthquake is dissipated into fracture energy (E_G), radiated energy (E_R), and frictional heat (E_H) (Figure 95). In the schematic drawing in Figure 95, stress versus slip per rupture unit surface area (the blue trapezoid area) represents the total mechanical energy liberated during the seismic event. Rupture initiates at σ_0. During slip to a critical displacement d_c, frictional stress on the fault plane linearly decreases with increasing slip to the final stress σ_1. From this point onwards, the frictional stress remains constant until the final slip D is reached (solid black line in Figure 95).

The seismic moment can be calculated according to

$$M_o = \mu D A \tag{14}$$

with μ the elastic shear modulus, A as ruptured surface area, and D as the displacement along the fracture. The seismic energy E_S, i.e. the total mechanical energy excluding the frictional heat term, per unit surface area:

$$E_S = (E_G + E_R)A = \frac{\Delta\sigma}{2} Ad = \frac{\Delta\sigma}{2\mu} M_o \tag{15}$$

where $\Delta\sigma$ is the stress drop during rupture (Kanamori, 1977). In the following, the total mechanical energy and the fracture energy will be calculated based on microstructural observations and compared qualitatively with the energy liberation during example breakdown reactions under eclogite-facies conditions.

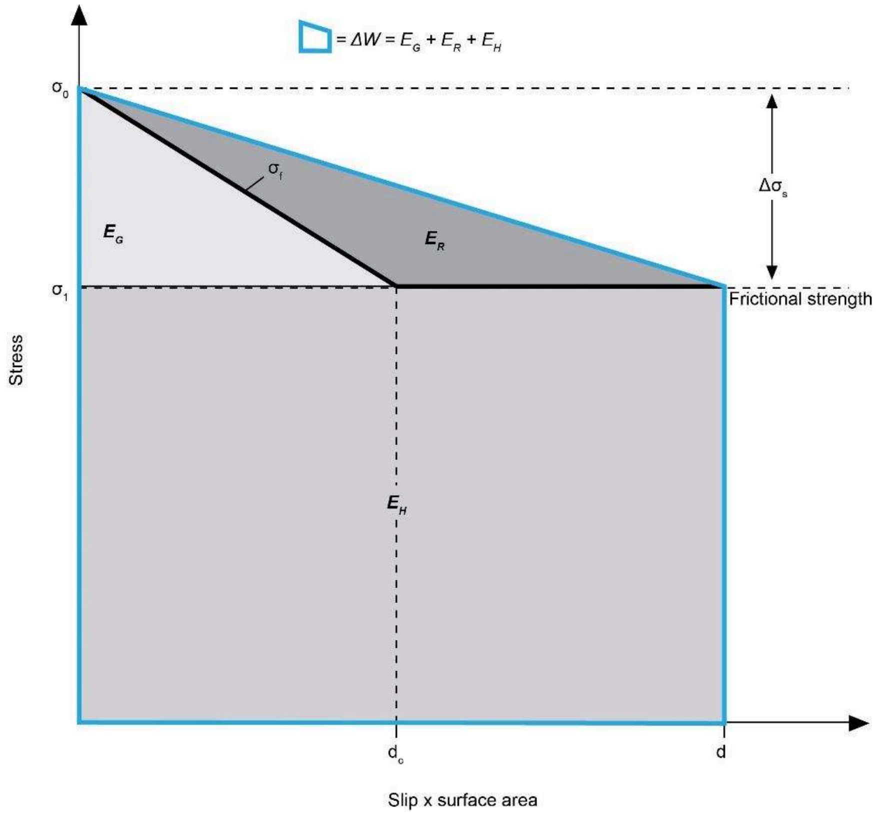

Figure 95: Schematic drawing of the slip weakening model demonstrating the expected energy partitioning released during an earthquake.

Frictional energy (E_H) will not be discussed in detail, because it is expected that under such high pressure–temperature conditions, microcracking is inhibited and thus, fracture energy linked to microcrack damage is a negligible term in the energy balance. In such conditions, fracture energy, i.e. the weakening term of the energy budget, is in fact related to thermal processes so that heat and fracture energy are undistinguishable, and E_G is mainly released in the form of frictional heat (Di Toro et al. 2011; Passelègue et al. 2016; Nielsen et al. 2016). We expect that, from empirical laboratory to field scaling laws recently published by Passelegue et al. (2016), E_G lies in the range of 10^{-1}J/m^2 approximately for micrometric slips.

Glaucophane breakdown – seismicity in blueschists

The sample GLS_3_1043 is almost a monophase material, therefore the shear modulus of glaucophane was applied with μ= 67.3 GPa (Bezacier et al., 2010) to calculate the seismic moment M_0. To estimate the rupture area, an exposed fracture exhibiting displaced crystals, shows a total displacement of $D \approx 5$ µm. Assuming the rupture is through-going (i.e. it breaks the sample from end to end) yields as estimate of the rupture area $A \approx 3$ mm^2. A value of 100 MPa is a reasonable average value for the stress drop (Prieto et al., 2012), compatible with our differential stress-strain curves during deformation (Figures 82; 86). This leads to an estimated seismic moment $M_0 \approx 1$ J and a resulting seismic energy $E_S \approx 10^{-3}$ J.

Considering now a 1 m^3 cube made of pure glaucophane, the complete reaction into jadeite and talc would release approximately 35 MJ/m^3 of heat (reaction enthalpy $\Delta_R H$ per unit volume). In our case, the sample size is much smaller, approximately 10 mm^3 (for the detailed description of the sample size please see chapter II). It consists of around 95 % glaucophane (starting material) which gives a reacting volume of around 9.5 mm^3 that could liberate a total heat of approximately ≈ 0.3 J. The mineral heat released by reaction enthalpy, $\Delta_R H$, around a fracture can simply be written as

$$E_M = \Delta_R H A w, \tag{16}$$

where w is the fracture thickness. Assuming now that all the mineral transformation energy is transformed into seismic energy, yields a fracture thickness of ≈ 7 µm. In other words, there is the same amount of energy released seismically by the fracture producing a 100 MPa stress drop over 5 µm sliding, than the heat released by the mineral transformation of Gln into Jd + Tlc within a fracture 7 µm thick. However, most of the seismic energy is released into elastic waves (Kanamori and Brodsky 2004). If we now consider that the mineral heat is the source of weakening, i.e. E_M equal to the fracture energy E_G, and using the estimate from empirical laboratory to field scaling laws, recently published by Passelègue et al. (2016), for the fracture energy E_G (i.e. 10^{-1}J/m^2 for micrometric slips), we find a transformed zone thickness around the fault in the range of 3 nm. In other words, this time the same amount of heat is released if a much narrower volume of Gln transform into Jd + Tlc than the surface energy needed for weakening and gliding. Therefore, the heat released during the reaction is enough to explain weakening (and radiation) over extremely thin fractures, which is compatible with our microstructural and nanostructural observations. There is no shear modulus available for tremolite. Since the reaction enthalpy for the glaucophane and tremolite breakdown are very similar, ≈ -8.9 kJ.mol-1 and ≈ -7.6 kJ.mol-1 (Table 1), respectively, as well as the fault geometries based on microstructural observations, the energy liberation during tremolite breakdown will lead to similar energy values.

Plagioclase breakdown – seismicity in granulites

The thermodynamic properties of the albite and the anorthite breakdown reactions (≈ 12.8 kJ.mol^{-1} for albite and ≈ -10 kJ.mol^{-1} for anorthite; Table 2) as well as their shear moduli are very similar (Pabst et al., 2015) and will consequentially lead to similar energy values. An imaginary cube of albite of 1 m^3 in size that transforms to jadeite and quartz at higher pressure would liberate an energy of ≈ 132 MJ/m^3 (reaction enthalpy $\Delta_R H$ per unit volume). The granulite samples were also not pure and contained around 5 % other phases (please see chapter II for the description of the starting materials) and the plagioclase shows no pure albite end-member composition. Nevertheless, our sample could liberate a total mineral heat of approximately 4 J. Assuming a displacement of D≈ 5 µm, rupture area A≈ 3 mm^2, and a stress drop $\Delta\sigma \approx 100$ MPa, and following the same reasoning as above, the fracture thickness estimate would be approximately 3.5 times smaller, i.e. between 1 nm (using fracture energy estimates) and 2 µm (using seismic energy estimates). Again, the heat released by the reaction on fractures, with thickness compatible with our microstructural observations, is enough to explain both weakening and radiation.

Although some assumptions, e.g. on the stress drops and the rupture area, were made the results show that a non-negligible amount of energy will be released during the breakdown of plagioclase (alibite and anorthite component), glaucophane, and tremolite at high-pressure. This energy supply would be available for deformation, e.g. fracturing of the sample, seismic radiation, and local heating or even melting of the rock. As for the experiment GLS_3_1043 the total number of AEs for the granulite and blueschist experiments also follows the Gutenberg-Richter distribution (Figure 96).

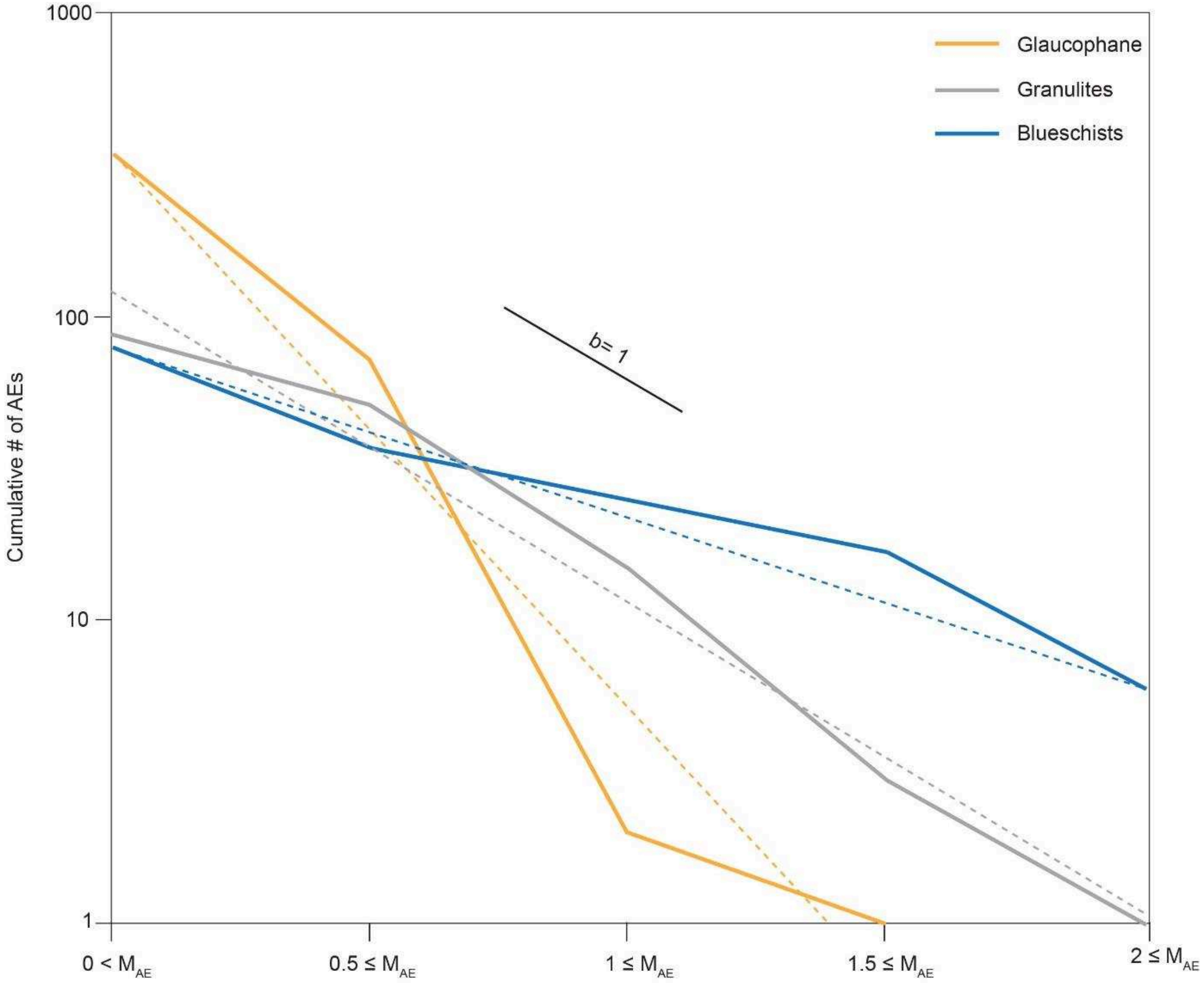

Figure 96: Cumulative number of AEs over magnitude diagram shows a Gutenberg-Richter distribution for the granulite and blueschist experiments.

5.2.6 Link to deep earthquakes – olivine to spinel transition

The phase transition olivine-spinel was also experimentally investigated on its potential to cause brittle failure (Green & Burnley, 1989; Burnley et al., 1991; Schubnel et al. 2013). Due to experimental limitation in reaching pressures as high as to investigate the natural silicate olivine-spinel transition (≈ 13-24 GPa; Helffrich & Wood, 1996) an analog reaction with structurally identical olivine germanates (Mg_2GeO_4) was used for the experimental studies (Ross & Navrotsky, 1987; Akaogi et al., 1989; Green & Burnley, 1989; Schubnel et al., 2013). The Mg_2GeO_4 phase transition occurs at much lower pressures than the transition in natural Mg_2SiO_4 (Figure 97).

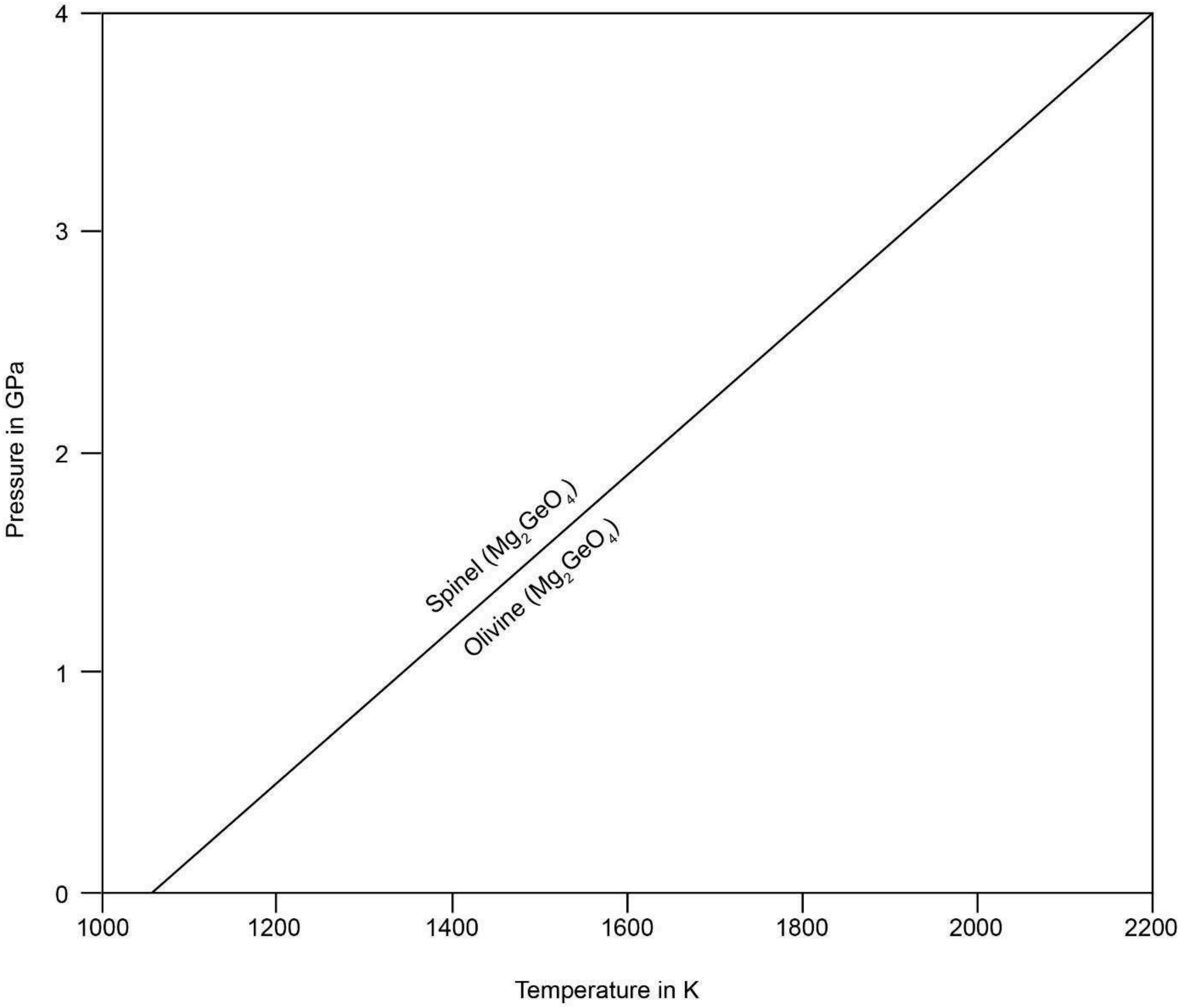

Figure 97: Modified after Ross & Navrotsky (1987). P-T pseudosection for olivine germanate (Mg_2GeO_4) exhibiting their high-pressure stability and the transition from olivine to spinel structure.

The phase transition olivine-spinel (silicates) is exothermic, releasing approximately 14 kJ.mol^{-1} (Ross & Navrotsky, 1987) and accompanied by a negative volume change of around 8 %, respectively (Table 16). The molar volumes used to calculate the volume changes for olivine and spinel (silicates) derive from Holland & Powell 1998 and for the germanate analogs from Navrotsky (1973). Since the olivine-spinel silicates are structurally identical to the germanates the relative volume change from olivine to spinel structure is very similar (Table 16). The Clapeyron slope for the phase boundaries are positive within the investigated P-T space.

Table 16: Thermodynamic data for olivine and spinel (silicates) and their germanate analogs.

Phase	V_m (from Holland & Powell, 1998) [cm^3/mol]	Reaction	ΔH_R [kJ.mol^{-1}]	ΔV [%]
Ol, olivine (forsterite)	45.9	Ol↔ Sp	≈ -14	≈ -8.8
Sp, spinel	42.2			
Mg_2GeO_4 (ol-structure)	45.9*			≈ -8.3
Mg_2GeO_4 (sp-structure)	42.4*			

*From Navrotsky (1973)

Using the reaction enthalpy of the olivine-spinel phase transition to calculate the energy release, it follows, that the energy liberation will be approximately 302 MJ if a 1 m^3 cube of olivine (silicate) reacts to spinel. High-pressure deformation experiments on olivine (germanate) demonstrate, that the reaction product spinel can be found as nanocrystalline material filling out the fractures (Burnley et al., 1991; Schubnel et al., 2013) or so called “anticracks” (Green & Burnely, 1989). These observation point towards transformational faulting as possible weakening mechanism under high-pressure conditions.

5.3 CONCLUSION

Every presented reaction in this chapter involves densification and the liberation of heat. Microstructural observations and energy considerations demonstrate that metamorphic reactions could be able to weaken the sample due to a negative volume change and additionally support the reaction because of the release of heat during progress. The transition from olivine to spinel, believed to trigger deep seismicity, shows the same characteristics. Therefore it might be possible that densification in conjunction with the liberation of heat might be a common weakening mechanism for both, intermediate and deep earthquakes.

VI FINAL CONCLUSION

All presented experimental results demonstrate that brittle failure of various natural rock samples can be triggered due to eclogite-facies metamorphic reactions in the laboratory. These observations are independent of the press type, D-DIA or Griggs apparatus, or the starting material, powder or intact rock, used for the deformation experiments. Our results point out that the only requirement for high-pressure faulting is the negative volume change during reaction. In most cases the metamorphic reactions are also accompanied by grain-size reduction, which can additionally weaken the rock. The experimental results on blueschist samples reveal that intermediate-depth seismicity in the subducting oceanic crust can be triggered due to the breakdown of glaucophane. Deformation experiments on granulite samples demonstrate that the breakdown of plagioclase, especially of the anorthite component, weakens the sample to enable brittle failure in rocks of the lower continental crust in continent-continent collision zones. The occurrence of pseudotachylites in these rather dry rocks could therefore be explained by the decomposition of plagioclase during eclogitization. Glaucophane and plagioclase breakdown are exothermic reactions and will liberate heat as they progress that can support the reaction progress. The small lab-earthquakes follow the Gutenberg-Richter law and the microstructures of the samples reveal good correlations to natural geophysical and field observations. Therefore we conclude that seismicity in nature is controlled by the same underlying mechanisms as in the laboratory. Densification as weakening mechanism in conjunction with grain-size reduction in the absence of larger amounts of fluids represents a viable process to enable brittle failure in high-pressure/high-temperature rocks. Intermediate and deep earthquakes reveal many similarities implying a common process that causes their nucleation. Since the theory of densification during metamorphic reactions can act as a trigger to enable brittle failure is independent of the rock type, it could therefore explain the formation of intermediate-depth earthquakes in lower crustal rocks as well as deep seismicity in Earth’s mantle.

VII PERSPECTIVES

Further investigation on intermediate-depth seismicity in subduction zones

As already mentioned, intermediate-depth seismicity in cold subduction zones seems to correlate very well with the expected eclogitization of lawsonite-bearing blueschist (Figure 4; Hacker et al., 2003; Kita et al., 2006). Although less abundant, intermediate-depth seismicity is also recorded in warm subduction zones, e.g. SW Japan. Due to the higher temperatures in the descending oceanic crust, the prograde metamorphism path of the basaltic oceanic crust will cross the stability field of epidote-blueschist instead of lawsonite-bearing blueschist (Figure 98).

This thesis experimentally investigated the influence of metamorphic reactions during eclogitization of lawsonite-bearing blueschist to better understand the formation of intermediate-depth earthquakes in cold subduction zones. Our experimental results show that the breakdown of glaucophane seems to play the key role in the formation of intermediate-depth seismicity in the oceanic crust. However, it would be interesting to also perform deformation experiments on the eclogitization of epidote-blueschists to strengthen this hypothesis and to complete the experimental study on intermediate-depth seismicity in the oceanic crust in subduction zones.

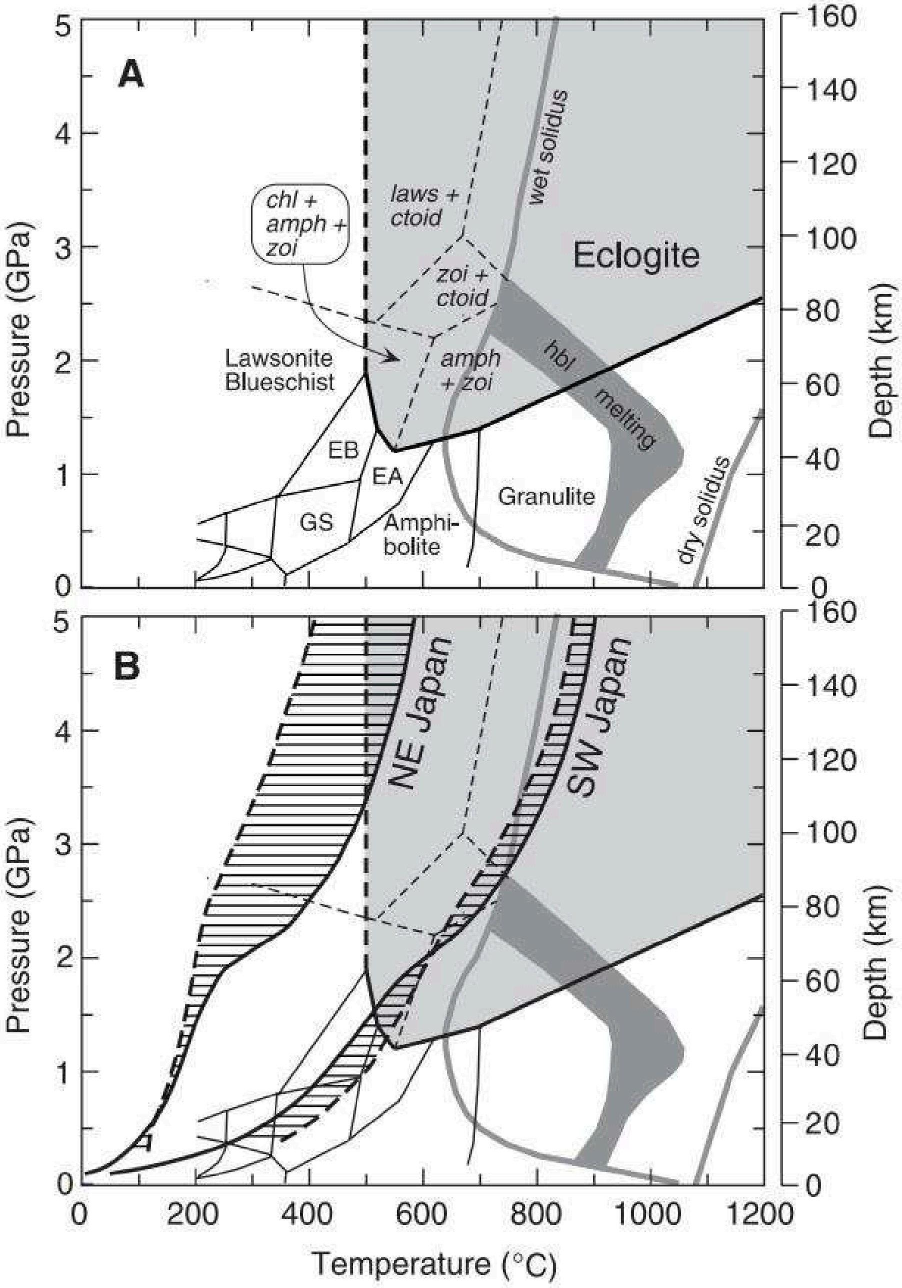

Figure 98: From Peacock & Wang (1999). A) P-T pseudosection shows the stability fields of different metabasalts and B) the expected P-T paths of the oceanic crust in either cold (NE Japan) or warm (SW Japan) subduction zones.

Influence of scapolite breakdown on brittle failure in granulites

Although considered to be nominally anhydrous, the Bergen Arc granulites reveal the presence of some hydrous phases, e.g. scapolite. This mineral, consisting of the volatile components sulphur and carbon, is forming vein networks in granulite of several mm – cm in thickness locally following pseudotachylites (discussion with Håkon Austrheim). Since the breakdown of scapolite will liberate volatile components it is expected to influence the eclogitization of the host rock granulite, which can be linked to the formation of pseudotachylites. After discussions with Håkon Austrheim and Bjørn Jamtveit at the PGP at University of Oslo we agreed that experimental investigations are of necessity to better understand the role of scapolite breakdown on the evolution of the Bergen Arcs granulites.

Application for a Feodor-Lynen fellowship of the Alexander von Humboldt Stiftung

AN EXPERIMENTAL STUDY OF MASS TRANSFER AND MICROSTRUCTURAL DEVELOPMENTS IN WALL ROCKS DURING INTERMEDIATE DEPTH EARTHQUAKES IN THE PRESENCE OF FLUIDS: IMPLICATIONS FOR THE ONSET OF RETROGRADE METAMORPHISM AND SHEAR ZONE DEVELOPMENT

INTRODUCTION

Unequivocal evidence for seismic slip rates along ancient faults is rare and usually related to frictional melting and the formation of pseudotachylites (Sibson, 1975). Pseudotachylites located in high-pressure (HP) rocks reveal brittle failure in rocks that for a long time were believed to be able to deform by ductile mechanisms only, under the prevailing pressure (P) and temperature (T) conditions. However, compared to the abundance of earthquakes located at deep crustal levels, pseudotachylites found in lower-crustal rocks are surprisingly rare (Kirkpatrick & Rowe, 2013). Based on this discrepancy together with field and microstructural observations, it has been suggested that brittle precursors initiated the development of ductile shear zones where ductile flow processes obliterated any evidence of localized slip (Guermani & Pennacchioni, 1997; Kirkpatrick & Rowe, 2013). This is further supported by numerical models of the rheology of brittle and ductile shear bands that have demonstrated that shear zones that have undergone large amounts of hydration and retrograde metamorphism can only have formed in the wake of an earlier brittle event (Mancktelow, 2006). Such findings imply that the rarity of brittle structures may often reflect that such structures are re-worked and overprinted by subsequent development into ductile shear bands or shear zones. Recently, there have however been reports of microstructures that are interpreted to reflect wall rock fragmentation processes and associated fluid mediated transport during deep crustal earthquakes (Austrheim et al., 2017). Some of these may survive later stage ductile deformation and thus have the potential to provide information about the presence of brittle precursors to shear zones and associated retrograde metamorphism even in the absence of pseudotachylites. However, to understand the conditions under which these structures form, the mechanisms of their formation, and their implications for the development of ductile shear and associated retrograde metamorphism require the performance of experiments under controlled conditions. This is the focus of the proposed project.

WALL ROCK DAMAGE DURING DEEP CRUSTAL EARTHQUAKES

Field observations accompanied by numerical models have so far indicated a strong link between seismic events, fluid influx, and the onset of retrograde metamorphism. Ductile deformation is observed to overprint earlier brittle structures (Guermani & Pennacchioni, 1997; Jamtveit et al. 2000, 2016; Mancktelow, 2006; Kirkpatrick & Rowe, 2013). The Bergen Arcs in Norway provide unique field exposures where pseudotachylites quenched under eclogite-facies conditions are found in the same area as eclogite shear zones. Both structures are located in nominally anhydrous granulites. Phase assemblages in pseudotachylites and shear zones are very similar, implying development under comparable P-T conditions. However they demonstrate formation within different deformation regimes. A striking and interesting observation is the presence of hydrous minerals, (epidote group minerals, amphiboles and phengite) as well as carbonates (dolomite) in the pseudotachylites. This suggests an influx of external fluids during seismic slip.

A recent microstructural study shows that pervasive fragmentation associated with dilatant deformation around fault zones triggered the migration of fluids and solutes into the fault wall rocks during seismic slip (Austrheim et al., 2017). This caused hydration of the host granulites, and the production of eclogites. Eclogite production was associated with a change in the rheology of the rock manifested by a dramatic reduction in rock strength. Further deformation therefore lead to the development of eclogitic shear zones, which often completely obliterate ay evidence of an initial stage of brittle deformation. The conditions and mechanisms under which the microstructures associated with wall rock alteration form is however not understood.

AN EXPERIMENTAL APPROACH

To understand the mechanisms and conditions controlling wall rock damage and associated microstructures during deep crustal earthquakes, this postdoctoral project aims to experimentally investigate the impact of seismic deformation on wall rocks at conditions representative of the deep crust in the presence of fluids. Combining experimental rock mechanics with metamorphic petrology will help to better understand natural processes by comparing the laboratory results with natural observations with focus on the Bergen Arcs eclogites. The key questions to be addressed are:

What wall rock microstructures, fluid movements, and mass transfer are generated by seismic slip events at deep crustal conditions?

What is the impact of the presence of fluids and the available amount of this phase?

How and to what extent are the wall rock changes controlling the transition from brittle deformation to ductile shear?

What is the role of seismic deformation for the onset of retrograde metamorphism?

Can microstructures and associated changes from the brittle stage be recognized throughout subsequent shear zone development?

If so, can some well studied shear zones, reflecting ductile deformation, be interpreted as re-worked brittle structures?

METHODS – FIELD WORK, DEFORMATION EXPERIMENTS & ANALYTICAL METHODS

The Bergen Arcs in Norway represent a unique place with optimal outcrop conditions to study high-pressure/high-temperature (HP/HT) rocks and their rheology change due to fluid infiltration during eclogitization. The anticipated project would include a field work at Holsnøy, the Bergen Arcs, SW Norway, to collect material for the experiments and to extensively study the natural structures we intend to reproduce in the lab.

For this postdoctoral project a set of state-of-the-art high-pressure deformation experiments is planned using a Griggs apparatus. A big advantage of this press over the piston cylinder apparatus, widely used in experimental petrology, is the ability to deform samples. The Earth is a dynamic system in which most of its areas are exposed to an anisotropic stress field. The highest goal for experimental geoscientists should always be to compare their laboratory results with observations from the field. Therefore deformation experiments represent a better approach to understand natural structures than static piston cylinder experiments.

The experimental work will be performed in the rock mechanics laboratory at Ecole Normale Supérieure Paris under the supervision of Dr. Alexandre Schubnel. There, a new Griggs apparatus was constructed, which can go up to confining pressures of around 5 GPa and temperatures of approx. 1200 °C. Since the experiments have to be performed at granulite- to eclogite-facies conditions, the P-T limits of this press are ideal for the anticipated experimental work.

The solid-medium Griggs apparatus is mainly designed based on the original drawings after Griggs (1960s). The Griggs rig is very similar to a piston cylinder press with the difference that an additional deformation piston can be moved independently to create an anisotropic stress field in the sample (Rybacki et al., 1998). First, both pistons, the confining pressure and the deformation piston, are moved together until the prescribed load is reached. Confining pressure on the sample is generated due to the progression of both pistons. During advancement the confining pressure piston crushes a weak solid pressure medium, in most cases salt, surrounding the sample. Then the deformation of the sample can be initialized by further moving the deformation piston to compress the sample. An electrical current flowing through a graphite furnace placed in the sample assembly allows heating. Temperature is measured and controlled by two Ni/CrNi thermocouples situated next to the sample.

During my Ph.D. I had the chance to support my supervisor, Alexandre Schubnel, to set up this new machine and to perform the first deformation experiments. Experimental work can be very time-consuming, especially if the experimental setup and procedure are completely unknown. Regarding the limited time during postdoctoral projects, the already existing experience on this press and other deformation apparatus will help to decrease the number of experimental failures and as a result could increase the outcome of this planned research project.

In order to answer the presented questions above, the deformation experiments require a more sophisticated sample assembly that allows the influx of fluids into the sample. A possible experimental procedure is presented in the following:

Drill cores of the natural intact granulite will serve as starting material. These drill cores will be placed in capsules made of gold. Nobel metals are often used in experimental geoscience to avoid chemical interaction between the sample and the capsule, but also to prevent reactions between the capsule and the surrounding pressure-medium. Together with the sample a distinct amount of a selected hydrous phase, acting as fluid source, will be filled into the gold capsule. Welding of the capsule will hamper the released fluid to easily escape from the sample. The amount of added hydrous phase can easily be adjusted to additionally test the impact of the amount of liberated fluid during the experimental run. First the granulite drill core will be fractured under low-pressure and low-temperature (LP/LT) conditions. Afterwards, load and temperature will be increased to the prescribed P-T conditions (granulite- to eclogite-facies conditions). During syndeformational heating the added hydrous phase will break down and liberate a fluid phase. This liberated fluid phase will preferentially flow into low-permeability zones, previously formed during LP/LT fracturing, and there it will react with the sample. To better understand the interplay of fluids with brittle fractures under HP/HT conditions the deformation experiments will be stopped at different P-T-ε conditions. This will allow us to compare the microstructural evolution of brittle faults at various stages.

A detailed microstructural and chemical analysis of the samples after deformation is required, which will mostly take place at the host university - the University of Oslo. The samples will be investigated using optical polarization microscopy, but also scanning electron microscopy (SEM), electron microprobe analysis (EMPA), electron backscattered diffraction (EBSD), and Raman spectroscopy. If necessary, additional nanostructural analysis can be conducted using transmission electron microscopy (TEM). The goal of an extensive microstructural and chemical investigation will be to find structures in the deformation samples comparable to those observed in the natural samples from the Bergen Arcs. This will help to decipher the chronology of events operated under different P-T conditions during metamorphism. The evolution of brittle structures under controlled laboratory conditions will facilitate the interpretation of natural structures.

Résumé

L’origine de la sismicité intermédiaire est discutée dans la communauté scientifique depuis des décennies. L’occurrence des séismes sous des conditions élevées en pression et température ne peut pas être expliquée par les modèles classiques qui reposent sur le comportement fragile des matériaux. Les observations géophysiques combinées aux calculs thermodynamiques montrent que dans les zones de subduction, une partie des tremblements de terre du plan Wadati-Benioff supérieur peut être corrélée avec l’éclogitisation des schistes bleus de la croûte océanique. Ces interprétations, basées sur la géophysique et la modélisation thermodynamique, sont supportées par la présence des pseudotachylites dans les roches de haute pression sur le terrain. La motivation de cette thèse est d’établir un lien entre les réactions métamorphiques pendant l’éclogitisation des schistes bleus/granulites et la formation des séismes intermédiaires en utilisant des méthodes expérimentales (D-DIA et Griggs). Les résultats expérimentaux sur tous les échantillons testés démontrent que la densification pendant les réactions d’éclogitisation joue un rôle clé dans l’activation des mécanismes fragiles, mis en lumière par l’enregistrement d’émissions acoustiques pendant les expériences. Pour les expériences réalisées sur les échantillons de schistes bleus, la transition ductile-fragile est associée à la dégradation thermique du glaucophane pendant la réaction lawsonite-éclogite. Ce résultat est en accord avec la relocalisation et la fréquence de la sismicité intermédiaire dans la partie supérieure du plan Wadati-Benioff. Les résultats préliminaires sur la déformation des granulites montrent que les évènements fragiles enregistrés à haute pression et haute température sont associés à la dégradation thermique des plagioclases, qui induit par une importante réduction de volume. Ces résultats sont également en accord avec les observations géophysiques et géologiques. La distribution des émissions acoustiques enregistrées pendant les expériences révèlent des lois de Gutenberg-Richter similaires à celles observées pour les tremblements de terre naturels. Grace aux corrélations entre nos résultats expérimentaux et les connaissances sur les séismes intermédiaires naturels, nous concluons que les mécanismes expliquant la sismicité pendant nos expériences peuvent expliquer la formation des séismes intermédiaires naturels. Nous proposons ainsi que le processus de densification pendant les réactions d’éclogitisation, qui est associé à une réduction de la taille des grains, est un mécanisme d’affaiblissement commun qui peut expliquer la sismicité intermédiaire.

Mots Clés

Séismes intermédiaires, éclogitization, densification, expériences en déformation, émissions acoustiques

Abstract

The origin of intermediate-depth seismicity has been debated for decades, because its formation at elevated depths cannot be explained by classic rock fracture and friction theory. Geophysical and field observations demonstrate that intermediate-depth earthquakes occur in hydrous rocks of the subducting oceanic crust as well as in nominally anhydrous rocks of the lower continental crust. n subduction zones the eclogitization of blueschist correlates very well with the relocation of intermediate-depth earthquakes forming the upper Wadati-Benioff plane and in continent-continent collision zones seismicity is recorded in areas of partially eclogitized granulites. The aim of this thesis is to experimentally investigate the potential of metamorphic reactions during eclogitization on the formation of intermediate-depth earthquakes in the oceanic and the continental crust. For the deformation experiments (D-DIA and Griggs) natural samples, were selected to study the eclogitization of blueschist and granulite in the laboratory. Experimental results on all investigated samples demonstrate that densification during eclogite-facies reaction plays a key role to enable faulting accompanied by acoustic emissions in the laboratory. In blueschist samples the breakdown of glaucophane during the transition from lawsonite-blueschist to lawsonite-eclogite acts as trigger for brittle failure. This is in good agreement with the relocation and frequency of natural intermediate-depth earthquakes of the upper Wadati-Benioff-plane. The preliminary results on granulite deformation show that the breakdown of plagioclase, accompanied by a pronounced volume decrease, weakens the sample to enable brittle failure at high-pressure/high-temperature conditions. Also these results match very well with geophysical and field observations. Gutenberg-Richter distribution of the acoustic emissions reveal that the events recorded during deformation follow the same physical law as earthquakes in nature. Together with the good correlation to natural observation we conclude that natural seismic events are caused by the same underlying mechanisms as our small lab-earthquakes. Based on the experimental results on various natural rock samples we propose densification in conjunction with grain-size reduction during eclogitization as a common weakening mechanism for intermediate-depth earthquakes in lower crustal rocks.

Keywords

Intermediate-depth seismicity, eclogitization, densification, deformation experiments